



Lewandowski, Karol (2020) *Numerical investigation of bone adaptation to exercise and fracture in Thoroughbred racehorses*. PhD thesis.

<http://theses.gla.ac.uk/81627/>

Copyright and moral rights for this work are retained by the author

A copy can be downloaded for personal non-commercial research or study, without prior permission or charge

This work cannot be reproduced or quoted extensively from without first obtaining permission in writing from the author

The content must not be changed in any way or sold commercially in any format or medium without the formal permission of the author

When referring to this work, full bibliographic details including the author, title, awarding institution and date of the thesis must be given

Enlighten: Theses

<https://theses.gla.ac.uk/>
research-enlighten@glasgow.ac.uk

NUMERICAL INVESTIGATION OF BONE
ADAPTATION TO EXERCISE AND FRACTURE
IN THOROUGHBRED RACEHORSES



KAROL LEWANDOWSKI

DIVISION OF INFRASTRUCTURE AND ENVIRONMENT
JAMES WATT SCHOOL OF ENGINEERING

UNIVERSITY OF GLASGOW

*SUBMITTED IN FULFILMENT OF THE REQUIREMENTS FOR THE DEGREE OF
DOCTOR OF PHILOSOPHY*

FEBRUARY 2020

Abstract

Third metacarpal bone (MC3) fracture has a massive welfare and economic impact on horse racing, representing 45% of all fatal lower limb fractures, which in themselves represent more than 80% of reasons for death or euthanasia on the UK racecourses. Most of these fractures occur due to the accumulation of tissue fatigue as a result of repetitive loading rather than a specific traumatic event. Despite considerable research in the field, including applying various diagnostic methods, it still remains a challenge to accurately predict the fracture risk and prevent this type of injury. The objective of this thesis is to develop computational tools to quantify bone adaptation and resistance to fracture, thereby providing the basis for a viable and robust solution.

Recent advances in subject-specific finite element model generation, for example computed tomography imaging and efficient segmentation algorithms, have significantly improved the accuracy of finite element modelling. Numerical analysis techniques are widely used to enhance understanding of fracture in bones and provide better insight into relationships between load transfer and bone morphology. This thesis proposes a finite element based framework allowing for integrated simulation of bone remodelling under specific loading conditions, followed by the evaluation of its fracture resistance.

Accurate representation of bone geometry and heterogeneous material properties are obtained from calibrated computed tomography scans. The material mapping between CT-scan data and discretised geometries for the finite element method is carried out by using Moving Least Squares approximation and L_2 -projection. This is then used for numerical investigations and assessment of density gradients at the common site of fracture.

Bone is able to adapt its density to changes in external conditions. This property is one of the most important mechanisms for the development of resistance to fracture. Therefore, a finite element approach for simulating adaptive bone changes (also called bone remodelling) is proposed. The implemented method is based on a phenomenological model of the macroscopic behaviour of bone based on the thermodynamics of open systems. Numerical results showed that the proposed technique has the potential to accurately simulate the long-term bone response to specified training conditions and also improve possible treatment options for bone implants.

Assessment of the fracture risk was conducted with crack propagation analysis. The potential of two different approaches was investigated: smeared phase-field and discrete configurational mechanics approach. The popular phase-field method represents a crack by a smooth damage variable leading to a phase-field approximation of the variational formulation for brittle fracture. A robust solution scheme was implemented using a monolithic solution scheme

with arc-length control. In the configurational mechanics approach, the driving forces, and fracture energy release rate, are expressed in terms of nodal quantities, enabling a fully implicit formulation for modelling the evolving crack front. The approach was extended for the first time to capture the influence of heterogeneous density distribution. The outcomes of this study showed that discrete and smeared crack approximations are capable of predicting crack paths in three-dimensional heterogeneous bodies with comparable results. However, due to the necessity of using significantly finer meshes, phase-field was found to be less numerically efficient.

Finally, the current state of the framework's development was assessed using numerical simulations for bone adaptation and subsequent fracture propagation, including analysis of an equine metacarpal bone. Numerical convergence was demonstrated for all examples, and the use of singularity elements proved to further improve the rate of convergence. It was shown that bone adaptation history and bone density distribution influence both fracture resistance and the resulting crack path. The promising results of this study offer a novel framework to simulate changes in the bone structure in response to exercise and quantify the likelihood of a fracture.

Acknowledgements

Firstly I should thank my supervisors Doctor Łukasz Kaczmarczyk, Doctor John Marshall, and Professor Chris Pearce for the constant support they provided throughout my PhD. The help from Łukasz with implementing my models in MoFEM has been invaluable. I believe that his passion and commitment to his work motivated me to do my best and develop not only as a researcher but also as a software engineer enthusiast. I thank him for always believing in me and supporting me in various ideas. I am grateful to John for introducing me into the world of veterinary science, biomechanics, horseracing, and for providing a great deal of support even after leaving academia. Chris's insightful guidance and his in-depth knowledge in many fields of engineering were an enormous help to me during this doctoral project. I should also thank Professor Tim Parkin and Doctor Tariq Alzidjali, who worked with me and provided CT scans of the equine bones.

Secondly, I wish to thank my family for all their help and encouragement during my PhD, in particular, my mother, Barbara. She pushed me to perform to my best and guided me at the beginning when things were not going so smoothly.

Finally, I would like to thank my friends: Andreea Pantiru, Irene Rizzo, Persa Chowdhury, and Ken Fabian Petersen, for all the adventures, laughter, and joy in my spare time as well as much-needed moral support. A special mention to my dear colleagues from the office: Zahur, Szymon, Pradeep, Ignatios, Hoang, Christophe, Arthur, and Andrei. Thanks to all of you, I really enjoyed my PhD research life in academia.

Declaration

I declare that this thesis is a record of the original work carried out by myself under the supervision of Doctor Łukasz Kaczmarczyk, Doctor John Marshall and Professor Chris Pearce in the James Watt School of Engineering at the University of Glasgow, United Kingdom. This research was undertaken from November 2015 to February 2020. The copyright of this thesis belongs to the author under the terms of the United Kingdom Copyright acts. The due acknowledgement must always be made of the use of any material contained in or derived from this thesis. The thesis has not been presented elsewhere in consideration for a higher degree.

Karol Lewandowski

Table of Contents

Nomenclature	1
1 Introduction	6
1.1 Motivation and objectives	6
1.2 Thesis overview	8
2 Literature overview	10
2.1 Introduction	10
2.2 Fractures of the equine 3rd metacarpal	11
2.2.1 Anatomy of equine 3rd metacarpal bone	12
2.2.2 Fractures in Thoroughbred racehorses	13
2.2.3 Bone material properties	15
2.2.4 Horse Kinematics	17
2.3 Computational modelling of bones	20
2.3.1 Bone remodelling	20
2.3.2 Bone fractures	21

2.4	Summary	25
3	Bone imaging and material mapping	26
3.1	Introduction	26
3.2	Least-squares mapping	28
3.2.1	L2 projection	29
3.2.2	Comparison with literature	30
3.3	Moving Least Squares Approximation	31
3.3.1	Computational implementation	31
3.3.2	MWLS mapping examples	32
3.4	Partial Volume Artifacts	34
3.5	Assessment of bone density gradient	37
3.5.1	Quantitative Computed Tomography	37
3.5.2	Bone segmentation and 3D FE model generation	39
3.5.3	Density mapping	40
3.5.4	Results	40
3.6	Summary	41
4	Bone remodelling	42
4.1	Introduction	42
4.2	Continuum formulation for bone	43

4.2.1	Conservation of mass	44
4.2.2	Conservation of momentum	45
4.2.3	Constitutive equations	45
4.2.4	Strong form	47
4.2.5	Weak form	48
4.2.6	Time discretisation	49
4.2.7	Spatial discretisation	49
4.2.8	Linearisation	50
4.2.9	Tangent operator	51
4.3	Benchmark problems	53
4.3.1	Parameter sensitivity	53
4.3.2	Influence of the mass flux	55
4.3.3	Size effect	57
4.3.4	Numerical efficiency	58
4.4	Bone remodelling and topology optimisation	59
4.4.1	Bike frame	60
4.4.2	Three-dimensional L-shaped crank	62
4.5	Summary	64
5	Phase-field fracture	65
5.1	Introduction	65

5.2	Phase-field representation	66
5.2.1	Continuum formulation	68
5.2.2	Strain energy density split	68
5.2.3	Degradation function	69
5.2.4	Strong form	70
5.2.5	Weak form	71
5.2.6	Derivation of projection tensors	72
5.2.7	Comparison of the methods	75
5.3	Arc-length control	76
5.4	Benchmark problems	77
5.4.1	One-dimensional bar	77
5.4.2	Notched plate	78
5.4.3	Plate with an eccentric hole	84
5.5	Summary	86
6	Configurational force driven fracture mechanics	87
6.1	Introduction	87
6.1.1	Material force concept	87
6.1.2	Material forces in fracture mechanics	89
6.2	Energy consistent framework for crack propagation	90

6.2.1	Preliminaries	90
6.2.2	First and second laws of thermodynamics	91
6.2.3	Fracture process	93
6.2.4	Density field	94
6.2.5	Discretisation	94
6.2.6	Arc-length control	97
6.2.7	Linearised system of equations	97
6.2.8	Crack topology resolution	98
6.2.9	Singularity element	99
6.3	Benchmark problems	99
6.3.1	Stress intensity calculations	99
6.3.2	Configurational forces in a heterogeneous body	102
6.3.3	Crack propagation in heterogeneous two-dimensional plate	105
6.4	Summary	107
7	Numerical investigations	108
7.1	Simulation of proximal femur adaptation	108
7.1.1	Proximal femur example	109
7.1.2	Proximal femur in presence of an implant	110
7.2	Comparison of smeared and discrete approaches for fracture	111

7.2.1	Differences and similarities	113
7.2.2	Comparative numerical examples	115
7.3	Fracture resistance of MC3 bone following adaptation	120
7.3.1	Metacarpal adaptation	120
7.3.2	Fracture risk and energy release of equine metacarpal	124
7.3.3	Fracture energy release in bone using CT scan data	126
7.3.4	Fracture energy release in bone using simulated density data	128
7.4	Crack propagation in MC3 bone	128
7.5	Summary	131
8	Conclusions	134
8.1	Limitations and future work	137
A	Moving Weighted Least Squares basis functions	139
B	Topology optimisation	142
B.1	Implementation	142
B.2	Density filtering	143
B.3	Numerical examples	144
B.4	Summary	146
C	Arc-length based on the internal and the dissipated energy rates	147
C.0.1	Algorithmic treatment	149

D One-dimensional Quarter Point Element

152

Bibliography

154

Nomenclature

Abbreviations

ADOL-C Automatic Differentiation by OverLoading in C++

CPU Central Processing Unit

CT Computed Tomography

DEXA Dual-energy X-ray absorptiometry

DOF Degree of Freedom

FDM Finite Difference Method

FE Finite Element

FEM Finite Element Method

FX Fractured condyle

GRF Ground Reaction Force

HU Hounsfield units

LS Least-squares

MC3 3rd metacarpal bone

MOAB Mesh-Oriented datABase library

MoFEM Mesh Oriented Finite Element Method library

MRI Magnetic Resonance Imaging

MUMPS MUltifrontal Massively Parallel sparse direct Solver

MWLS Moving Weighted Least Squares

NFX Non-fractured contralateral condyle

PDE Partial Differential Equation

PETSc The Portable, Extensible Toolkit forScientific Computation

K_2HPO_4 Dipotassium phosphate

QCT Quantitative Computed Tomography

SIMP Solid Isotropic Material with Penalisation

STL Stereolithography file format

TOP Topology Optimisation

VTK Visualization Toolkit format

XFEM eXtended Finite Element Method

Greek symbols

δ_{ab}	Kronecker delta
$\dot{\mathcal{E}}^D$	Rate of dissipated energy
ψ	Elastic energy
η	Numerical damping coefficient
$\partial\Gamma$	Crack front domain
Γ	Discrete crack surface
γ_l	Crack surface density function
γ	Surface energy
χ	Position in reference (mesh) configuration
Ξ	Map from reference to material configuration
\mathcal{H}	History parameter
\mathcal{L}	Lagrangian
λ_l	Length scale parameter
λ_b	Lagrange multiplier in topology optimisation
λ, μ	Lamé constants
Λ	Diagonal matrix
$\lambda_1, \lambda_2, \lambda_3$	Eigenvalues
ν	Poisson's ratio
ω	Resulting vector of shape functions for MWLS
Ω_t	Current spatial domain
Φ	Map from reference to spatial configuration
φ	Map from material to spatial configuration
Ψ	Elastic energy density
ψ_0^{neo}	Elastic Neo-hookean free energy
Ψ^{pot}	Energy potential
ρ	Density
\mathbf{r}_τ	Residual vector of arc-length control for crack surface
Σ	Eshelby stress tensor
Φ	Shape function
σ_g	Standard deviation
$\boldsymbol{\varepsilon}$	Small strain tensor
$\boldsymbol{\sigma}$	Cauchy stress tensor
τ	Arc-length load factor
$\Delta\tau^D$	Increment of dissipated energy

$\Delta\tau^U$	Increment of internal energy
$\dot{\mathcal{U}}$	Rate of internal energy
φ_i	Weight for Gaussian Smoothing
ξ	Natural coordinates

Roman symbols

a	Vector of unknown coefficients for MWLS
A_Γ	Crack surface area
$\mathbf{A}_{\partial\Gamma}$	Crack front orientation
A	Matrix of weighted basis functions coefficients for MWLS
a	Switch ratio for energy based arc-length control
A	Domain surface
b ₀	Body force
\mathcal{B}_0	Reference material domain
$\partial\mathcal{B}_0$	Boundary of reference material domain
b	Exponent controlling rate of bone remodelling
B	Matrix of weighted basis functions for MWLS
B _□	Element shape function derivative
\mathcal{B}_t	Current material domain
c	Bone remodelling rate (growth velocity)
C	Right Cauchy-Green deformation tensor
\mathbb{D}	4th order elasticity tensor
d	Phase-field variable
d_{mi}	Influence domain radius
$g(\cdot)$	Degradation function
ΔA_Γ	Increment of the crack surface area
\mathcal{D}_{max}	Dissipation
e	Basis vector
F	Deformation gradient
\mathcal{F}	Newtonian force
f _l	Global force vector
f ^{ext}	Global vector of external forces
f ^{inh}	Fictitious inhomogeneity material force
f ^{int}	Global vector of internal forces
f^{top}	Desired volume fraction
g	Gravity acceleration
G	Configurational force
$\tilde{\mathbf{g}}^h$	Vector of nodal Griffith forces at the crack front

g_s	Gaussian smoothing filter
\mathbf{g}^ρ	Bilinear form of residual of mass conservation
\mathbf{g}^u	Bilinear form of residual of linear momentum balance
g_c	Griffith energy release rate
h	Effective element size
\mathbf{H}	Gradient of material map Ξ
\mathbf{h}	Gradient of spatial map Φ
$H(\cdot)$	Heaviside function
\mathbb{I}	4th order unit tensor
\mathbb{I}^s	4th order unit symmetric tensor
\mathbb{I}	Identity matrix
i_{\max}	Maximum number of iterations in topology optimisation
J	Jacobian
J_c	Cost function
\mathbf{K}_e	Element stiffness matrix
k	Order of approximation for MWLS
K_I	Mode I stress intensity factor
\mathbf{K}_l	Global stiffness matrix for Least Squares problem
$\mathbf{K}_T, \mathbf{K}^{\square\square}$	Tangent stiffness matrix
L	Crack front curve
l_0	Material length scale
m	Algorithmic exponent for bone remodelling
m^{top}	Move limit
n	Porosity exponent
n_w	Number of points located within the domain of influence
\mathbf{N}_{\square}	Element shape function
\mathbf{N}	Crack normal vector
\mathbf{n}	Unit normal vector
\mathbf{p}	Vector of basis functions for MWLS
p_l	Local order of approximation
p_g	Global order of approximation
\mathbf{P}_v	Matrix of eigenvectors
p^{top}	Penalisation coefficient
$\phi(\cdot)$	Arc-length function
Φ^{MWLS}	Approximation function derived from MWLS
\mathbf{P}	First Piola-Kirchhoff stress tensor
\mathbb{P}	4th order projection tensor

q	Number of approximation functions for MWLS
r	Radius
R^2	Correlation coefficient
R_0	Mass conductivity coefficient
ρ_0^*	Reference density
ψ_0^*	Reference free energy
\mathbf{r}^ρ	Residual of mass conservation
\mathbf{r}^u	Residual of linear momentum balance
\mathbf{R}	Mass flux
$\rho^{h,MWLS}$	Density approximation derived from MWLS
\mathcal{R}_0	Locally created mass
s	Cubic degradation function coefficient
S	Inclusion surface
t	Time
Δt	Time increment
\mathbf{t}	Traction
\mathcal{T}	Triangles on surface of the current material configuration $\partial\mathcal{B}_t$
\mathbf{u}	Displacement vector
\mathbf{u}_g	Generalised displacement
\mathbf{v}	Global vector of approximated discrete field
v	Arbitrary discrete field
v^h	Approximation of arbitrary discrete field
V	Domain volume
V_e	Element volume
\mathbf{W}	Displacement vector in material domain
\mathbf{w}	Displacement vector in spatial domain
$w(\cdot)$	1D weight function
\mathbf{X}	Position in material configuration
\mathbf{x}	Position in spatial configuration
\mathbf{X}_t	Position in MWLS domain
E	Young's modulus
$\mathbf{Z}^{\text{front}}$	Matrix of crack tangent vectors

Chapter 1

Introduction

1.1 Motivation and objectives

In the UK, approximately 60% of horse fatalities at racecourses are associated with a fracture, with the distal limb the most commonly affected site (Parkin et al., 2004). Most of these fractures occur due to the accumulation of tissue fatigue, as a result of repetitive loading (Parkin et al., 2005), rather than a specific traumatic event. Remodelling is the on-going complex biological process of replacing old bone tissue by new bone and thus repairing the fatigue damage (Hughes et al., 2017). The bone repair is overwhelmed by load-induced bone densification that also increases brittleness (Loughridge et al., 2017). Racehorses experience extreme bone remodelling, with intense exercise and excessive loading of the metacarpal bones resulting in maladaptation. The location of 3rd metacarpal fractures is remarkably consistent across a large number of racehorses, crack initiation presenting from the lateral sagittal groove of the distal condyle of the leading forelimb (Jacklin and Wright, 2012; Parkin et al., 2006).

Despite considerable research in the field, including applying diagnostic methods such as radiography (Bogers et al., 2016; Crijns et al., 2014; Loughridge et al., 2017), magnetic resonance imaging (Tranquille et al., 2017) and biomarkers (McIlwraith, 2005), it remains a challenge to accurately predict the fracture risk and prevent this type of significant injury. The purpose of this thesis is to develop a finite element based framework allowing for integrated simulation of an equine 3rd metacarpal remodelling under specific exercise regime (boundary conditions), followed by the evaluation of its fracture resistance. Such an approach may help to understand better the correlation between exercise intensity, bone adaptation, and fracture risk, ultimately improving the welfare of the racehorse. The current veterinary practice is based mostly on experience and intuition without the support of computational models. The efficient

and robust numerical tools based on the finite element method can not only assist practitioners in decision making regarding training regimes but also support of orthopaedic surgeons in finding the most reliable treatments for patient-specific fractures. The principle aim of the framework is to utilise methods that have low-complexity, require a minimum number of parameters, can be easily automatised and at the same time provide high accuracy, robustness and generality. These features are essential to fit in efficient patient-specific modelling routines capable of handling many patients within a limited time frame. A schematic of the proposed modelling framework is depicted in Figure 1.1.

The procedure of building successful finite element models for analysing bones always has to start with the acquisition of accurate geometry and density data (material properties). Since the local bone stiffness is directly related to the local mineral density of the bone, the radiopacity values from CT scanning can be mapped onto finite element mesh. In the first step of building the framework, methods for mapping bone density are introduced, as shown in Figure 1.1a). The resulting finite element bone model with proper heterogeneous density distribution is a starting point for a comprehensive investigation of adaptation and fracture propensity. Bone's ability to adapt its density in response to external loading is crucial for maintaining mechanical integrity and resistance to fracture. Consequently, there is a strong correlation between stress fractures and the adaptation process (Hughes et al., 2017). Simulation of the adaptation process can provide important insights into the macroscopic morphology of bone and changes as a result of intense athletic training. Therefore, to improve the predictive capability of the framework, a numerical method for simulating long term bone response to applied loading is included as a second step in the pipeline.

In recent years, the main focus in bone mechanics was in the use of different strength criteria for the onset of failure. The most commonly adopted ones were based on stress or strain measures assuming the bone failure under the von Mises, the Drucker-Prager or, maximum principal stress yield criteria (Keyak et al., 2005; Schileo et al., 2008; Yosibash et al., 2010). However, these criteria are merely designed to assess the criticality of a preexisting fracture, and they cannot model propagation and the post-failure response of the bone. In general, crack propagation can be modelled by a discrete or smeared approach. In the discrete approach, the crack is represented explicitly on the mesh, whereas in the smeared approach, the crack is distributed over a damage zone with a finite width. The potential of these two different techniques is explored in this thesis using the state of the art developments of phase-field and configurational mechanics for smeared and discrete approaches, respectively. The phase-field approximation has been used in the past to analyse crack propagation in heterogeneous materials (Hirshikesh et al., 2019). In contrast, the method to include varying material properties in configurational force driven approach has not been explored before. The most robust implementation is used as the last step of the proposed framework to assess bone resistance to fracture, including the bone's history of adaptation.

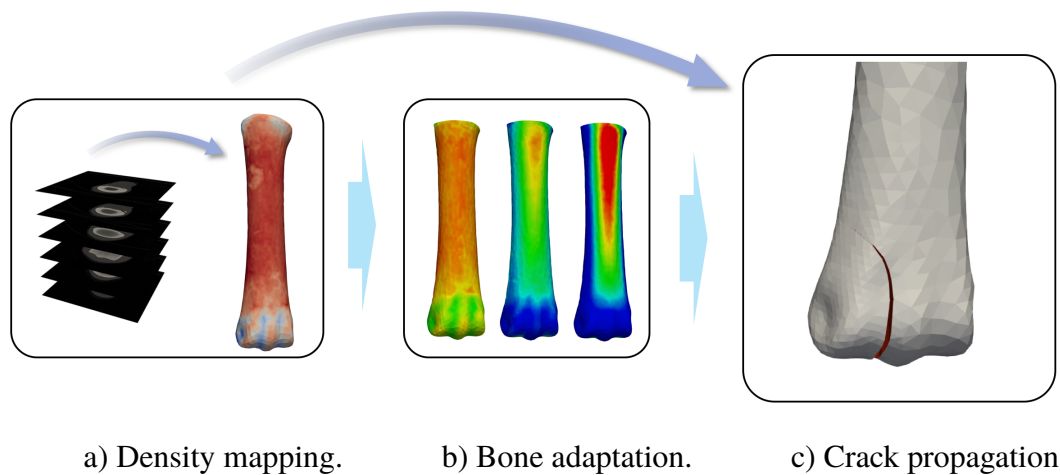


Figure 1.1: Framework for estimating bone fracture resistance. a) density data derived from Computed Tomography (CT) imaging mapped onto finite element mesh. b) bone adaptation simulation. c) assessment of fracture resistance and crack propagation analysis.

Another essential aspect of building numerical bone models is the measurement or estimation of forces exerted on the bones, typically obtained using pressure films or musculoskeletal modelling methods (Brama et al., 2001; Pang et al., 2012). However, it is out of the scope of this thesis, and boundary conditions will be based on the literature findings.

In summary, the goal of this study is to develop a robust numerical tool for the estimation of a fracture risk in response to training regimes. The main objectives are the following:

- Implementation of an efficient strategy for building bone patient-specific finite element models from widely available medical imaging methods.
- Identification of material properties necessary for an accurate numerical representation of the equine bone stiffness.
- Building a numerical model to predict adaptation of bone density in response to loading exercise.
- Investigation of the initiation and propagation of fracture in MC3 bones using state of the art finite element tools.
- Estimate maximal exercise loading to predict and prevent fatal injuries in racehorses.

1.2 Thesis overview

This thesis comprises of different aspects related to the proposed numerical framework for analysing bone propensity to fracture. In Chapter 2, a brief literature overview is presented

with emphasis on the origins of the equine bone fractures and numerical techniques for analysing bones. Chapter 3 introduces two novel techniques for mapping CT-scan data onto finite element meshes. The numerical and imaging setups are characterised. Subsequently, the continuum formulation and numerical aspects of the bone remodelling model are presented in Chapter 4. Two approaches for approximating bone fracture are considered in this thesis: The first one - the smeared phase-field method is covered in Chapter 5. In Chapter 6, the main novelty of this thesis is presented - implicit formulation for crack propagating in heterogeneous materials using the configurational force-driven approach. In Chapter 7, implemented bone remodelling formulation is tested on a practical problem of proximal femur adaptation, followed by a comparative study for both crack propagation approaches. All the components are subsequently brought together into a single framework, and its performance is demonstrated using a series of numerical examples. The different aspects of the code are investigated. Finally, in the last Chapter 8, concluding remarks are depicted to summarise research contributions. Limitations and future directions of the research are outlined.

Throughout this thesis, matrix-vector notation will be used; all matrices and vectors are distinguished by bold-faced characters. For 4th order tensors a calligraphic font is utilised.

Chapter 2

Literature overview

This chapter includes a brief literature overview and is divided into two parts. In the first section, the fracture mechanism of the equine metacarpal bones is addressed. The literature on the material properties of bone and horse kinematics are discussed. The second section focuses on different numerical theories for simulating both bone remodelling and fracture developed in the past.

2.1 Introduction

Racehorses are trained very intensively to develop the speed and stamina required for racing. Thanks to adaptation, the structure of their bones changes every day. However, a consequence of the adaptation process is increased bone density and stiffness. Tissue accumulates in particular regions, causing increased bone stiffness and fragility. In the UK, a catastrophic fracture of the equine 3rd metacarpal bone (MC3) is the main reason of euthanasia or death of horses on the racetrack. Many factors influence the propensity for injuries such as bone density, training, type of ground surface, or direction of a race. In order to examine the relationship between these factors and fragility sophisticated computational approach of bone loading, adaptation and fracture has to be developed.

A schematic drawing in Figure 2.1 shows the steps involved in building subject-specific finite element models. The first step is the generation of a finite element mesh. Geometry is usually obtained based on CT or MRI scans provided by clinicians. Acquired images are segmented and discretised. Subsequently, material property mapping is conducted over all elements in the mesh. The methods for assigning the properties are discussed in Chapter 3. Material properties can be determined by mechanical testing and from microscale images, which is briefly discussed in Section 2.2.3. Musculoskeletal modelling supplies information on forces

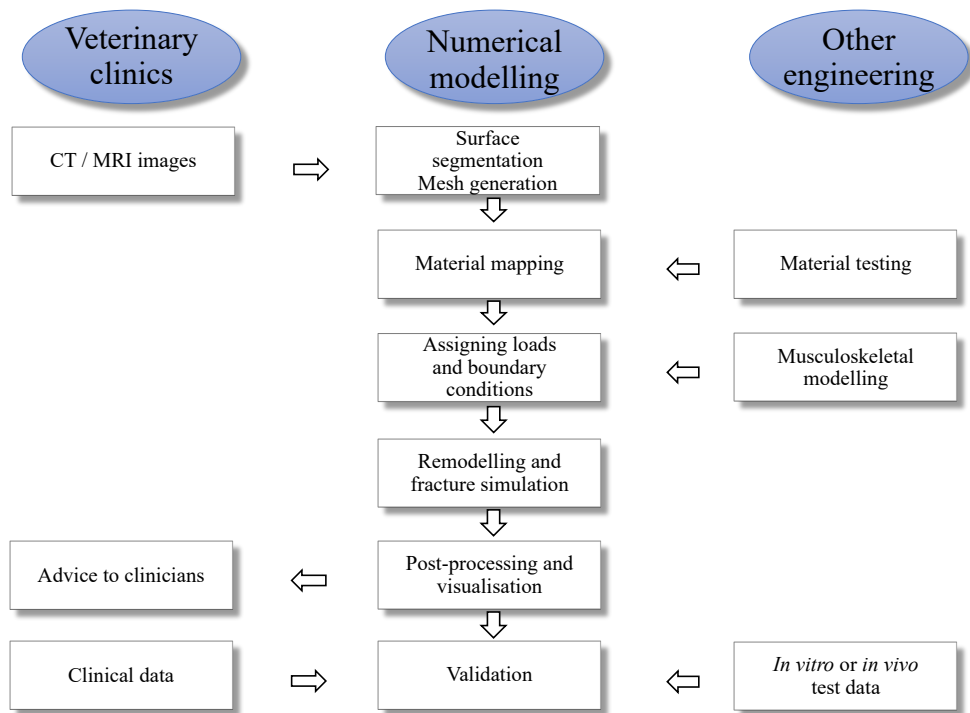


Figure 2.1: Steps involved in construction, analysis, and validation of a patient-specific FE model of bone (Poelert et al., 2013).

in joints, tendons, and ligaments during gait of a subject, giving the data used as loading and boundary conditions for numerical bone models (see Section 2.2.4).

In order to build an efficient framework capable of handling many subjects within a limited time frame, the numerical methods used therein have to be of low complexity, require a minimum number of parameters while maintaining high accuracy and robustness. In the proposed framework, two subsequent analyses will be conducted: bone remodelling and fracture. Numerical methods available in the literature regarding these two phenomena are discussed in Section 2.3.

2.2 Fractures of the equine 3rd metacarpal

Bone is a remarkable living material. It is heterogeneous, consisting of dense cortical bone and porous trabecular bone. The bones of the young horses develop following a basic genetic template. However, it is only when the bone is subjected to mechanical loading that the process of modelling or adaptation results in the development of the mature bone structure and shape. When bone then accumulates micro-damage, it is removed by cells called osteoclasts and subsequently replaced with new bone by building cells - osteoblasts. This ongoing replacement of old bone tissue by new bone tissue is called remodelling. The racehorse is an extreme example of this process in which strenuous exercise and excessive loading result

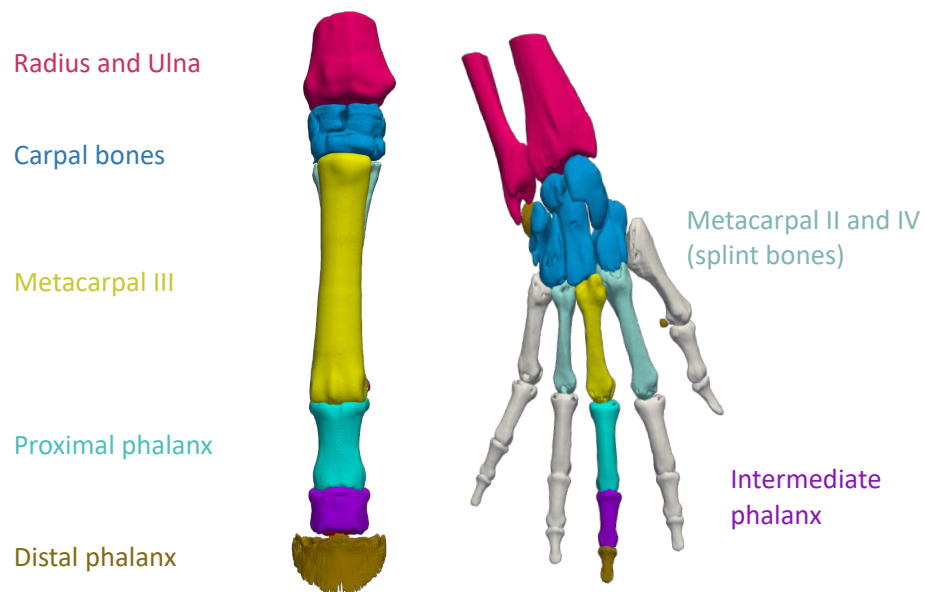


Figure 2.2: Comparison of the equine and human forelimb. It can be noticed that the limbs are of different structure and function.

in maladaptation in MC3 bone. A combination of dense bone adjacent to micro-cracks can ultimately propagate into a fatigue fracture – a lateral condylar fracture.

2.2.1 Anatomy of equine 3rd metacarpal bone

Horses (*Equus caballus*) are odd-toed ungulates. They bear the weight of their bodies on odd-number of toes, which in the horse is one hoof that surrounds the distal phalanx. The distal hindlimb and forelimb are very similar in their structure. This study considers one particular bone from the front limb – the 3rd metacarpal (MC3). The placement of this bone with comparison to a human arm is presented in Figure 2.2. It can be noticed that only the MC3 is not reduced in the horse. Metacarpal II and IV are approximately one-third shorter, also known as splint bones.

In contrast to the human arm, metacarpals I and V are absent in the horse limb. Proximally the metacarpals articulate with the small carpal bones, whereas distally MC3 articulates with proximal phalanx. Together with the proximal sesamoids, they form a metacarpophalangeal (fetlock) joint (Budras et al., 2003). This joint is especially prone for injury because of the extensive range of motion, the relatively small surface area (450 mm^2 , whereas in human tibiofemoral joint - 700 mm^2) compared to body size and the magnitude of forces that occur during a high-speed gallop. The mean contact stress in the equine fetlock can be more than 10 times higher than that estimated for the human knee during walking (Harrison et al., 2014). The metacarpal is a stiff, well-developed bone due to its function. It bears loads transferred through the whole limb. The shape of the bone with essential elements is presented in Figure 2.3 below. The distal articular surface has two condyles separated by a sagittal ridge, which articulates with the proximal phalanx groove to limit the fetlock to only the sagittal

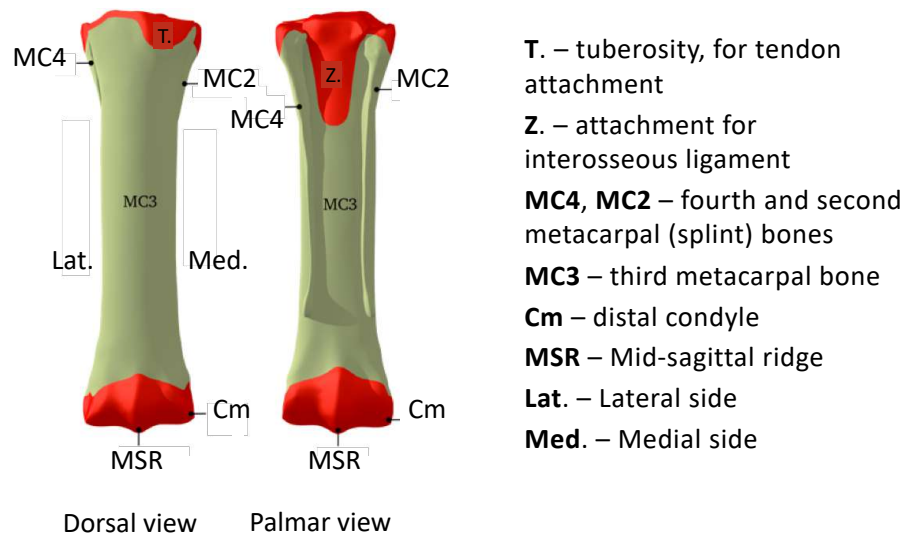


Figure 2.3: Anatomy of MC3 bone. Right forelimb.

plane movement. The proximal aspect of metacarpal III has articular facets on its palmar side, where the splint bones link. The dorsal side of the proximal end has a tuberosity for muscular attachment. It is worth to note that tuberosity can be used as a straightforward indication of the side of the limb in CT imaging (medial or lateral).

2.2.2 Fractures in Thoroughbred racehorses

Two different fracture mechanisms can be distinguished. The first one appears when accidental load causes critical stress over the strength that bone tissue has achieved during growth and adaptation (traumatic fracture). The second type of fracture is produced by creep or fatigue. Bone often bears more or less constant loads for long periods of time and cyclic loads that may produce microdamage. If the accumulation of microdamage is faster than repair by remodelling, microcracks can multiply to produce macrocracks leading to a complete fracture. Clinically, this is often called a stress fracture. It usually occurs in individuals who have increased repetitive-type physical activities such as soldiers, ballet dancers, joggers, athletes, and racehorses (Doblaré et al., 2004).

Catastrophic failure of the equine distal limb is the most common cause of euthanasia of Thoroughbred racehorses on the racetrack. Fractures of the 3rd metacarpal and metatarsal are responsible for about 25% of cases that end in euthanasia of racehorses in California and the UK. Most frequently, the site of fracture is the lateral condyle (Jacklin and Wright, 2012; Parkin et al., 2005). Almost all lateral condylar fractures originate from the mid to mid axial site of the lateral condyle and traverse toward the lateral cortical bone (Figure 2.4a). In contrast to medial condylar fractures, lateral fractures rarely spiral into the diaphysis (shaft) of

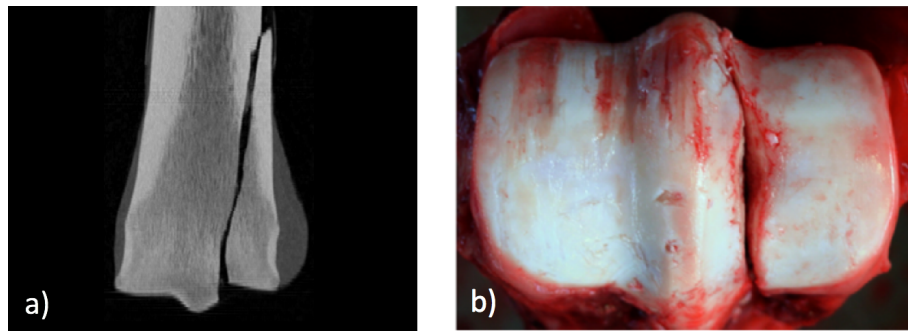


Figure 2.4: Common metacarpal bone damage in racehorses. a) radiograph of typical fracture subchondral bone b) palmar view of MC3 with a fracture that has propagated from the lateral sagittal groove (Harrison et al., 2014).

the MC3. Medial condylar fractures nearly always extend toward the axial aspect of the MC3 (Mc Turlough, 2014).

There have been numerous studies investigating possible risk factors for fractures of racehorses. Some of them like age, gender, and genetics are hard to control. In contrast, others related to training and racing can be reduced through proper training, gait modifications, and biomechanical alterations (e.g., horseshoes). Exact statistics differ between tracks and types of racing. Investigations based on hoof ground reaction forces by Setterbo et al. (2009) indicated that synthetic surfaces have the potential for injury reduction in Thoroughbred racehorses. The distribution of injury between right and left forelimbs varies - Parkin et al. (2006) found that horses were 6.3 times more likely to injure the leading forelimb. This study will focus on fatigue fractures, which are usually the result of bone adaptation. Prolonged intense loading suppresses remodelling, leaving modelling as the only process of maintaining bone strength. Racehorses with fatigue fractures of the distal MC3 may have reduced porosity associated with suppressed remodelling while continued adaptive modelling will result in higher densities on the subchondral bone (Whitton et al., 2010). Cross-sections of distal condyles from 3rd metacarpal and metatarsal (usually less loaded than MC3 from forelimb, therefore can be considered as equivalent for less trained horse) are presented below in Figure 2.5.

It can be noticed that MC3 is characterised by areas of high bone density adjacent to areas of increased porosity (in the sagittal ridge) that create large density gradients within condyle (Riggs and Boyde, 1991). Such gradients may lead to concentration of shear forces, which can cause localisation of cracks (Figure 2.5c) and further catastrophic fracture. The sagittal ridge is not directly loaded during functional weight-bearing, as shown in contact areas investigations (Brama et al., 2001). Therefore, in this region, a low correlation between bone density and horse exercise may be expected. Also, joint-pressure measurements confirm that areas of high load are associated with increased subchondral density (Easton and Kawcak, 2007).

In addition to fractures of the condyles, it is worth to mention fatigue fracture of the dorsal cortex diaphysis of MC3, which is a component of 'bucked shins' disease. It occurs in 70%

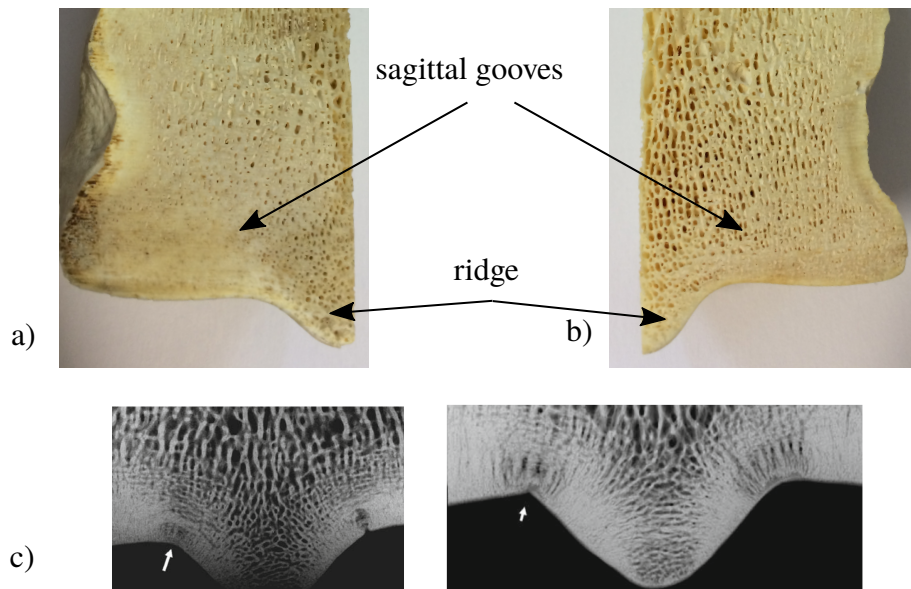


Figure 2.5: Cross-sections of subchondral bone. a) distal MC3 from a training horse showing high porosity at sagittal grooves compared with b) less loaded (adapted) metatarsal bone c) Radiographs of sections through the condylar surface of MC3, showing fracture localization at high-density gradients (Firth et al., 2016).

of the population of young thoroughbred horses in training. Bucked shins are the result of high-strain cyclic fatigue caused by repeated compression loads on a bone that has not remodelled enough to tolerate the stress placed on it. Stressed bone forms a new weaker layer of bone at the point of stress. However, only 10% of horses with this syndrome were found to have a stress fracture (Nunamaker and Ruggles, 2010).

2.2.3 Bone material properties

Bones are the basic elements of the skeletal system. They are built of dense connective tissue and determine the shape of the body. Most bones have support functions that allow them to maintain an upright position. Some of them protect other organs against traumas. Another mechanical function of bones, connected through the joints, is to enable the body movement. Together with the muscular system, bones constitute a complex mechanism that ensures the motor functions of the body. In order to fulfil their important role, they must have sufficient mechanical strength. Thanks to their internal structure, external shape and ability to adapt, they are very effective structures from an engineers' point of view. A biological function of bone is the storage of calcium and phosphorus. Another vital role, is the production of blood cells in the red marrow within the cavities of individual bones.

Bone tissue is a highly complex multi-scale material, with varying properties on its many length scales. It is naturally occurring, with properties adapted to its local environment during growth, making bone tissue an unpredictable material to work with that certainly can not be described in terms of a single value for a particular materials property.

The structure of all bones consists of the same essential components. These include mineral, carbonated hydroxyapatite, the framework protein type I collagen, many other so-called non-collagenous proteins and water. The material of bones has a hierarchical structure that changes at different length scales (Sharir et al., 2008). It is also a heterogeneous and anisotropic material, as its composition, structure, and mechanical properties vary in space. The combination of these attributes makes bone tissue a challenging material to model numerically.

Equine MC3 bone, in particular, has exceptional properties compared to other mammals bones. Maximum physiological strain taking place during extreme activity is generally between 0.0015% and 0.0030% whereas, in racehorses, the compressive strain can reach approximately 0.0078% when measured during fast-galloping on a treadmill (Sharir et al., 2008).

The proper assignment of material properties is essential for FE models. Many empirical relationships between isotropic Young's modulus and bone density are available in the literature. Due to simplification of bone isotropy, they are widely used in FE analyses (e.g. in Eberle et al. (2013)). Helgason et al. (2008a) reviewed numerous density-elasticity relations. A large spread in the predicted Young's modulus was reported. That indicates complexity in the experimental techniques needed to measure the mechanical properties in material like trabecular bone. Usually, in order to determine mechanical properties, a bone specimen is cut out of a whole bone and loaded in a testing machine between the two anvils as presented in Figure 2.6b) (Les et al., 1994). Recording of load-displacement data allows for the calculation of parameters like Young's modulus. Many different testing set-ups have been applied over the years. Both three and four-point bending tests have been employed to investigate the mechanical performance of entire bone specimens (Figure 2.6a)). However, bending tests, in general, better serve as a validation of FE analyses predictions (Taddei et al., 2007; Trabelsi and Yosibash, 2011). Another effective method for verification of numerical results is modal analysis (Scholz et al., 2013). Natural frequencies after bone excitation are measured (by laser vibrometry or accelerometers) and compared with FEM predictions that can be accomplished by simple solving of an eigenvalue problem.

When anisotropy is considered, the values achieved in the testing described above are inadequate. The fully anisotropic bone-matrix material tensor can be obtained at the microlevel by ultrasonic (Rho, 1996) or nanoindentation (Fan et al., 2002) methods. The use of ultrasonic waves for analysis of bones is a well-known technique. Elastic properties can be obtained from velocity measurements of transverse and longitudinal waves propagating in particular directions in the bone specimens. The relations between velocity and elastic properties originate from the theory of small amplitude wave propagation in solids. In nanoindentation method, a hard tip, often made of diamond, is pressed into a sample with unknown properties. The load placed on the indenter tip is increased as the tip penetrates further into the specimen. This technique enables the measurement of mechanical properties with a low resolution and allows the measurement of properties in several different directions at the microstructural level.

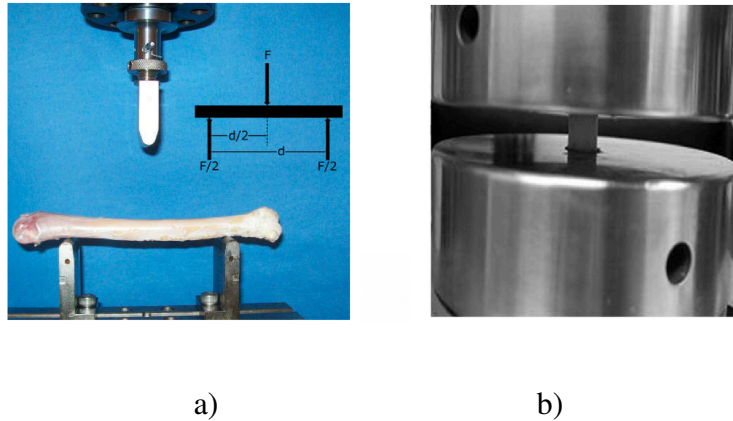


Figure 2.6: Simple bone testing techniques. a) 3-point bending of deer metacarpal bone (Hovagimian et al., 2011). b) trabecular bone compression between two anvils (Leahy et al., 2010).

Another relatively new method to achieve full stiffness tensor for bone is computational homogenisation. Based on segmented microCT scans of trabecular specimens, a FE model is built assuming the isotropy at the micro-level. Young's modulus is usually achieved from nanoindentation of a single trabecula. Subsequently, specimens are numerically loaded and from their response fully homogenised stiffness tensor can be computed (Pahr and Zysset, 2008).

Once anisotropic properties are obtained, material trajectories need to be determined in order to apply well-oriented elasticity tensor to finite elements. It was found in several studies (e.g. Tabor and Rokita (2007)) that this might be a hard venture since trabecular bone morphology cannot be determined by using clinical (non-micro CT) tomography scanning. Many researchers presented techniques that help to assess the aforementioned trajectories. For example, Trabelsi and Yosibash (2011) applied a micro-mechanical approach to overcome this limitation. Trajectories were determined either by the assumption that they follow outer surface geometry or principal strains. However, the results of FE analyses with both orthotropic and simple isotropic material properties were very similar. They remained in good agreement with tests conducted on femur bones with simple loading configuration (typical femur head load simulating stance position). Equine MC3 is mainly axially loaded; therefore, it is probable that including anisotropy will not significantly affect the results.

2.2.4 Horse Kinematics

The equine forelimb experiences very large loads during locomotion. The extreme extension of the metacarpophalangeal joint (fetlock) results in the storage and release of the elastic strain energy in the long flexor tendons and the suspensory apparatus. This mechanism makes the distal forelimb act like a passive spring (Harrison et al., 2010). However, such energy

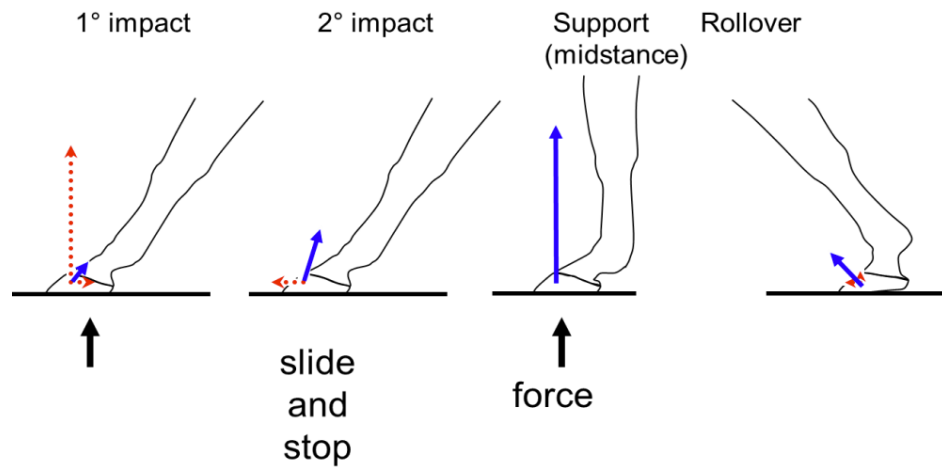


Figure 2.7: Phases of the stance: blue vector represents Ground Reaction Force (GRF) and red vector - accelerations (vertical and horizontal) (adopted from Thomason and Peterson (2008)).

storage requires relatively high forces to be developed by tendons and transferred through contact in the fetlock joint. Numerous studies have estimated ligament and tendon strain, bone strains with strain gauges (Merritt et al., 2006), and joint surface pressure distribution in the metacarpophalangeal joint and surrounding structures. Determining muscle and joint loading *in vivo* is challenging and limited for practical and ethical reasons. Contact pressures in the horse have only been measured *ex vivo* with the use of pressure mapping sensors (Easton, 2012) or sensitive films (Brama et al., 2001). Both strains and contact pressures were found to grow with the increasing loading.

Indirect methods, like musculoskeletal modelling, are potentially more potent than invasive experiments. Models of the musculoskeletal system enable the study of neuromuscular coordination, analysis of athletic performance, and estimation of loads. A musculoskeletal model consists of rigid body segments connected by joints. Muscles span these joints and generate forces and movement. Such models enable to study the effects of musculoskeletal geometry, joint kinematics, and muscle-tendon properties on the forces and joint moments that the muscles can produce (Delp et al., 2007). Dynamic simulations are divided into two types: inverse and forward. An inverse dynamic approach is useful for studying experimental data, whereas forward dynamics may be used to perform simulated tests. By means of inverse dynamic simulations, joint moments and forces, muscle forces and strains in the equine forelimb during swing phase and stance phase of a gait can be derived. A forward approach typically uses simplified equine models and focuses on general locomotion modelling of the entire horse.

During galloping, the highest forces and accelerations occur during the stance phase of the forelimb stride and can be divided into four parts (see Figure 2.7). Approximately the first 7% of the duration of stance is the primary impact when the hoof hits the ground causing high decelerations, and the ground reaction force (GRF) increases. Secondary impact accounts for the next 5-30% of the stance phase and is characterised by the first stage of the loading of

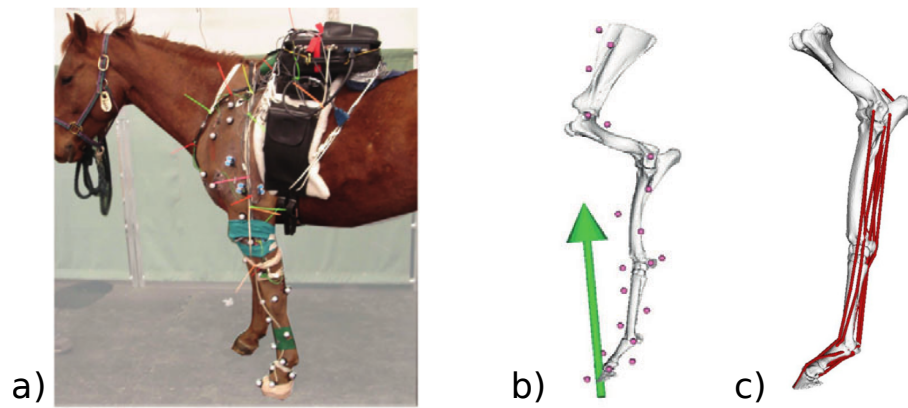


Figure 2.8: a) Horse loaded with markers and accelerometers for gait experiments. b) The kinematics from markers and ground reaction forces (can be determined by use of force plate or special horseshoe) c) Final musculoskeletal model with wrapped tendons and ligaments (Harrison et al., 2014).

the horse's mass with the leg as it becomes steady placed on the ground. During this phase, there is a significant increase in force and strain due to a substantial increase in horizontal acceleration and rapidly increasing GRF. The third stage of the stance, midstance, stands for 30-90% of the stance following impact depending on the speed and gait.

During midstance, the full body weight of the horse is loaded on the limb, and peak vertical GRFs are achieved. An extremely high vertical GRF occurs during midstance upwards of 2.5 times the body weight. The angle of the metacarpophalangeal joint (fetlock) at midstance can be close to 90%. It has been reported that during midstance, MC3 is primarily in axial compression exerted by resultant forces applied by the proximal sesamoid bones and proximal phalanx (Merritt et al., 2010). Breakover is the final stage of the stance (85-100%) where the hoof lifts at the heels and push off from the ground unloading the limb (Thomason and Peterson, 2008).

Many researchers have reported the magnitudes of resultant forces transmitted by the fetlock joint (Harrison et al., 2010; Merritt et al., 2006, 2010; Setterbo et al., 2009). However, there was only one study found, that attempted to estimate the magnitudes and locations of maximum cartilage pressures (Harrison et al., 2014). Sophisticated subject-specific finite element model of fetlock joint was developed. Bone, muscle and cartilage geometries were obtained from a cadaver forelimb using MRI and CT. Tendon and ligament strains, bone kinematics, and hoof forces were determined from *in vitro* mechanical experiments on a cadaver limb. Gait analysis was performed to measure joint kinematics and hoof loading. Example configuration of such tests is presented in Figure 2.8. Although the model had several limitations (e.g. bones modelled as rigid bodies), the results of analyses were in satisfactory agreement with previous studies. It was also reported that models were relatively insensitive to the magnitude of muscle-tendon forces; thus bone kinematics and net joint torques measured from a gait analysis experiment can be used with the application of a generic rigid body musculoskeletal model to determine individual muscle - tendon forces.

Overall, all of these studies only investigated a few components at once. The variations in loading schemes between different studies make it difficult to determine the correlations of data from the literature. The number of animals used in the experiments was usually small, and the same subjects may not have been used in all analyses. There is also no data reported about gait experiments conducted at racing speeds. In summary, while building biomechanical finite element models, some simplifications are inevitable.

2.3 Computational modelling of bones

2.3.1 Bone remodelling

Bones can adapt their local density when subjected to mechanical loading. They can change their morphology within days as a result of continuous microstructural tissue turnover and regeneration. Such an adaptation process results in the densification of the bone in regions of high loading levels and resorption of the material in regions of low loading levels. The first attempts to describe the mechanism that governs the relationship between bone morphology and its external mechanical loads were carried out more over than a century ago. The father of modern biomechanics - Julius Wolff formulated his phenomenological so-called Wolff's Law (Wolff, 1870). He postulated the existence of mathematical laws according to which bone adapts its trabecular structure to external stimuli.

Bone remodelling has a substantial impact on human lives. As previous studies showed (Menzel and Kuhl, 2012), because of adaptation astronauts in space lose their bone density, too stiff orthopaedic implants may develop local loss of bone structure, and dental implants can become loose over time. Athletes in asymmetric sports like tennis often develop much denser leading arm, which can cause constantly recurring pain. Therefore, the functional adaptation of bones found much interest of researchers from different disciplines, including computational mechanics. However, the mass exchange is an uncommon issue in classical mechanics; thus, the application may be problematic if only standard continuum mechanics tools are considered.

Numerous approaches to bone remodelling (Podshivalov et al., 2014) have been utilised over the years. Generally, they can be divided into two main categories: mechanistic and phenomenological (Poelert et al., 2013). The first one was initially proposed by Frost (Frost, 1987). This concept assumed that the minimum effective strain has to be exceeded in order to trigger bone adaptation process. The new material configuration responds differently to the mechanical environment, inducing a feedback loop between bone mechanical properties and biological activity. This theory clarifies the foundations of Wolff's theory. However, in numerical studies, phenomenological approach was found to be more widely

used (Hazelwood et al., 2001). Simulations usually assume that the functional stimulus for adaptation is stress, strain energy or a related factor such as damage. Some investigations were based on optimality criterion postulating that the tissue adaptation process tries to maintain the structural integrity of the bone while minimising the required mass (Jacobs et al., 1995). This technique is widely used in engineering, e.g. to determine the optimal shape of structures. Another category of models assumed that adaptation is driven by healing micro-cracks and damage in bone tissue (Doblaré et al., 2004).

Multi-scale approaches in 3D have also been investigated for the bone remodelling problem, where the macro-scale domain is characterised by homogeneous material properties and passes information down to the micro-scale Podshivalov et al. (2014). However, such methods require many parameters on different levels that may be difficult to obtain and validate. Moreover, multi-scale analyses are still computationally expensive for modelling large scale problems, like entire bones.

In relatively new approaches, non-constant mass is characterised by single-phase material within an open-system mechanics framework that allows for local energy-driven creation of mass (Kuhl et al., 2003). Constitutive parameters used in such models, in particular those related to the local creation of mass, can be experimentally determined by means of CT-scanning (Zadpoor, 2013). Nevertheless, accurate data acquisition for subject-specific studies is a very troublesome task. Many researchers conducted remodelling simulations without taking into consideration heterogeneity and anisotropy of material as well as complex loading patterns including forces from muscles, tendons or ligaments (Kaczmarczyk and Pearce, 2011; Kuhl and Steinmann, 2003; Pang et al., 2012; Podshivalov et al., 2014). However, some studies have shown that even with high uncertainty of the used data, like geometry, loading conditions or model parameters (Campoli et al., 2014), the results from state of the art bone remodelling analyses are comparable with bone density levels measured experimentally (Pang et al., 2012).

2.3.2 Bone fractures

Subject-specific finite element modelling has commonly been used to assess the stresses and fracture risk of bones (Chen et al., 2010; Helgason et al., 2008a; Taddei et al., 2007; Trabelsi et al., 2009; Yosibash et al., 2010). The two main components of subject-specific FE models: model geometry and material properties, can be derived from computed tomography (CT) datasets (Knowles et al., 2016). Generation of the three-dimensional (3D) geometry of a bone segment from CT data might be complicated and time-consuming depending complexity of the considered bone.

Bone tissue is a natural composite material with a hierarchical structure across the scales. On macroscale bone consist of a very dense cortical bone or porous trabecular bone. The most

common approximation of such a complex structure assumes that the bone material is elastic, isotropic and highly heterogeneous, which still makes the modelling of fracture a challenging task.

In context of fractures, bone tissues developed a number of microstructural mechanisms to increase its resistance and ultimately prevent failures. The stress/strain curve for bone typically exhibits a linear elastic phase followed by an inelastic region where the material yields followed by sudden catastrophic failure in the form of a fracture (Gupta and Zioupos, 2008). Through a number of experiments by Ritchie et al. (2005) and co-workers identified four major toughening mechanics occurring in cortical bone: crack deflection, crack bridging by collagen fibres, ligament bridging and diffuse micro-cracking. These phenomena have been further classified into two classes: intrinsic and extrinsic due to different toughening effects that they incorporate. Intrinsic corresponds to microstructural damage processes that act ahead of the crack tip. The experimental studies showed that so-called 'cement lines' provide weaker crack path than surrounding microstructure, resulting in an inelastic behaviour. The second class, extrinsic mechanisms operate behind the crack tip, restraining it from opening further. The experiments showed that collagen bridging is responsible for increased fracture toughness as the crack continues to propagate in bone specimens. Therefore, it can be concluded that in order to fully capture bone tissue behaviour one has to take into account at least two dissipative phenomena; diffuse cracking that reduces bone stiffness ahead of the crack front and energy release due to advancing fracture plane. However, in particular cases the fracture processing zone can be so small with respect to the size of the specimen, that such mechanisms can be neglected. Classical linear elastic fracture mechanics (LEFM) theory assumes that yielding zone is infinitely small (which is true only for some materials), therefore all the dissipated energy is consumed to create new crack surfaces. Materials that exhibit significant dissipation at the crack front in the form of plasticity or diffused cracking cannot be characterised solely using the linear theory. Moreover, structures made of such materials demonstrate so called 'size effect', where small specimens have much higher nominal strength than large ones Bazant (2000). In order to further consider implications of this phenomenon, three specimens with deep notches in the middle, made from e.g. bone tissue are presented in Figure 2.9a). The nominal strength (maximum stress) of these geometrically similar beams can be presented against the characteristic (dimensionless) size D of the specimen ($1, D, D'$) as presented in Figure 2.9b). On the log-log scale, the LEFM failures are represented by a straight line of slope $-1/2$, while plasticity and other strength-based failure criteria correspond to a horizontal line. The presented power laws characterize so called deterministic (energetic) size effect. Clearly, for both classical approaches: strength-based and LEFM, exist only a specific range of the specimens sizes in which they are applicable (the closest to experiments). The size effect curve for nonlinear fracture mechanics bridges these two theories, representing a transition from one to another. Such formulation introduces a characteristic length scale of the microstructure, making it appropriate for much larger range of sizes and accurate failure estimation.

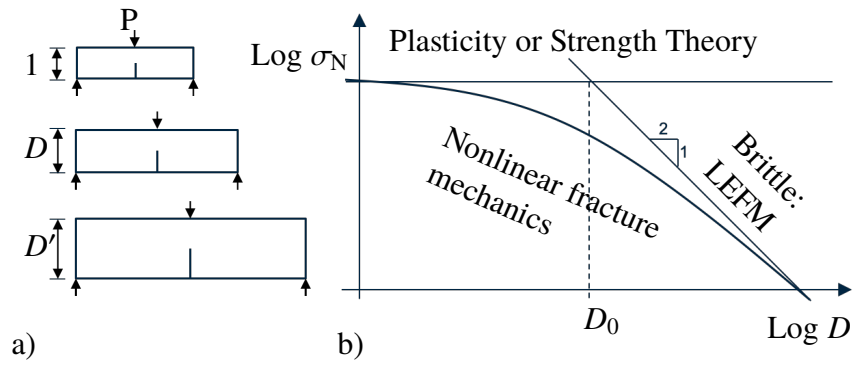


Figure 2.9: a) Beam specimens of different sizes. b) Size-effect (scaling) power laws for limiting cases: plasticity theory, linear elastic fracture mechanics (LEFM), transitional curve for nonlinear fracture mechanics. (Adopted from Bažant (1999))

The whole bone tension tests also exhibit ductile to brittle transition (Gupta and Zioupos, 2008) due to intrinsic and extrinsic microstructural mechanisms mentioned before. Consequently, when the considered specimens are relatively small with respect to the size of the fracture processing zone, as seen in Figure 2.9b), the LEFM alone will vastly overestimate the strength of the material (left side of the graph). Therefore, it is evident that in case of bones, the formulation has to include the influence of microstructural effects, like e.g. collagen bridging and diffuse cracking. One simple computational method to include characteristic length scale into LEFM, is scaling of the Griffith energy g_c parameter according to Irwin's characteristic material length (Bažant, 1999; Irwin, 1958):

$$\ell_0 = \frac{E g_c}{\sigma_0^2} \quad (2.1)$$

where E is Young's elastic modulus and σ_0 is yield stress. ℓ_0 approximately characterizes the length of the fracture processing zone. The above formula can be used to adjust the Griffith energy parameter when the characteristic length scale is known, e.g. from experiments. Such idea combines the concepts of strength or yield with linear fracture mechanics, which is essential to properly capture deterministic size effect and predict the failure load for quasibrittle materials like bones.

Various theories exist in the literature regarding failure criteria for bone tissue, and it is now standard practice for researchers to estimate fracture risk within the framework of FEM. In particular, subject-specific FEM models can potentially quantify the risk of failure under a given loading scenario. In recent years, the main focus in bone mechanics was in the use of different strength criteria for the onset of failure. The most commonly adopted ones were based on stress (Keyak et al., 2005) or strain measures (Schileo et al., 2008) assuming the bone failure under the von Mises, the Drucker-Prager or maximum principal strain and maximum principal stress yield criteria (Yosibash et al., 2010). The experimental validations for such simplified models show that they have a significant spread in the predicted failure. The percentage error in the majority of studies report is between 10%

and 20% (van den Munckhof and Zadpoor, 2014). This variation is explained perhaps by their focus on the local initiation of failure, rather than the complete failure mechanism. The fracture process of bone is critical, particularly in the case of fatigue fractures (Gupta and Zioupos, 2008). Limitations in previous studies (e.g. use of 2D geometry (Bettamer et al., 2017), assuming homogeneous bone properties (Gasser and Holzapfel, 2007)), can also explain why an appropriate model for bone fracture has not been developed previously.

The numerical modelling of fracture can be divided into two categories: smeared and discrete approaches. The smeared method, or continuum damage, incorporates a damage parameter into the model that controls the strength of the material. An advantage of this approach is that it does not require interface tracking since the damage parameter varies continuously over the domain (see, e.g. de Borst et al. (2004)). Damage approaches were applied to model trabecular bone damage and fracture in the past (e.g. in Hambli et al. (2012); Hambli (2013a)). Various implementations of the method showed that it can reproduce force-displacement curves obtained experimentally in the ovine vertebra or proximal femur bones (Harrison et al., 2013; Hambli et al., 2012). However, the inherent disadvantage of damage models is high mesh dependency or spread of the diffused crack over large zones. The lack of failure localisation can be addressed by various regularisation methods (see, e.g. Londono et al. (2017)).

Closely related to continuum damage models are the phase-field models which have become extremely popular over the last decade. The major promise behind these models is that they can overcome some of the limitations presented in the other methods. With phase-field, the fracture can be described purely with partial differential equations as regularised energy minimisation problem (Miehe et al., 2010b). Thanks to the introduced length scale parameter l_0 , phase-field produces realistic narrow crack bands, which in the limit $l_0 \rightarrow 0$ should reproduce a discrete crack. The promising results with this method have been presented for simulating fracture in humerus bone with heterogeneous material properties (Shen et al., 2019).

In discrete models for fracture, the geometrical discontinuity is modelled by modifying the geometry of the domain. One of the popular approaches within this family of methods is exploiting the partition of unity concept like, e.g. the eXtended Finite Element Method (XFEM). XFEM uses enrichment of the standard finite element shape functions with expressions derived from benchmark analytical solutions which decouple the crack path from the underlying discretisation (Belytschko and Black, 1999). This approach is robust and has been applied to bone fracture problems in the past (Gasser and Holzapfel, 2007; Feerick et al., 2013). However, it is often limited to simple crack paths and using homogeneous material properties. Lattice element approach (also known as rigid body spring networks) have also been used to model discrete crack paths for concrete with low computational cost (Bolander and Saito, 1998; Grassl and Jirásek, 2010). Another novel discrete approach in an isogeometric analysis that introduces knot insertions that lower the order of continuity to introduce cracks in the considered domain (Hosseini et al., 2014).

In cohesive zone models, the problem of discontinuity in the displacement field is undertaken

using a priori assumptions regarding the location of potential cracks. Special interface elements are defined at the beginning of the analysis, which allows for the creation of cohesive or traction-free boundaries. Ural and Mischinski (2013) analysed crack propagation in human distal radius using such approach, where cohesive elements were inserted along the expected crack path, which substantially limits the ability of the approach to model complex fracture profiles.

One of the simplest methods which can simulate fracture problems is the element deletion method. It has been used, e.g. in Hambli (2013b) to analyse human proximal femur. In this approach, there is no need to represent sharp discontinuities since fractured elements are expressed by a set of elements with zero stress. This method requires modifications in constitutive equations based on the element size, which causes spurious mesh dependency. Generally, simulating bone fracture using a discrete family of methods is extremely difficult. Most of the approaches exhibit bias from the original mesh, require intensive remeshing which is computationally expensive (especially in complex geometries of bones) or are limited to homogeneous material cases. Recent advancements in the field of configurational mechanics promise to overcome these issues. In Kaczmarczyk et al. (2017), a thermodynamically consistent approach was presented with equilibrium at the crack front expressed entirely in terms of nodal material forces. The results from example problems showed that the method is robust, efficient, predicts crack paths without bias from the original mesh, and unlike most the methods does not introduce any new parameters like length scale. However, the approach has not been utilised yet to simulate fracture propagation in solids with inhomogeneities like bones.

2.4 Summary

This chapter presented a brief overview of the literature regarding equine metacarpal bone fractures, possible methods of data acquisition for related finite element models, techniques and approaches used in numerical modelling of bone adaptation and bone fractures. The observations made in this chapter are an essential prerequisite, which enables the choice of numerical methods used in the developed framework described in the following chapters.

Chapter 3

Bone imaging and material mapping

In this chapter, two methods for efficient approximation of bone CT scan data onto finite element meshes are presented. The first approach is a simple but robust L_2 -projection. The method is subsequently used for determining density gradients from CT-scans of 18 horses from three different cohorts. The second presented method is Moving Weighted Least Squares approximation. It provides the same capability of approximating the noisy CT-scan data onto the smooth field as L_2 -projection and also allows for the computation of derivatives. This feature will be later exploited in configurational force driven crack propagation framework discussed in Chapter 6. Additionally, a Partial Volume Artifacts correction technique is proposed for improved accuracy. The performance of both methods is tested on simple examples.

3.1 Introduction

The first step when building finite element models for analysing bones is to generate accurate geometry from three-dimensional imaging techniques like computed tomography (CT) or magnetic resonance imaging (MRI). Many studies in the past have established that experimentally validated bone FEM models require both high resolution in meshing and heterogeneous material mapping of bone density (Pakdel et al., 2016). The most widely adopted and validated method for patient-specific finite element modelling of bone is BONEMAT program (Viceconti et al., 2004). The algorithm implemented therein interpolates the CT-scan data (radiopacity) of the voxels mapped from the CT image to the volume of the FEM mesh, assigning the density and elastic modulus to each individual element. This results in a constant density within elements leading to a very noisy distribution of material properties with unrealistically sharp gradients. However, as it will be shown later in Chapter 6

for efficient and accurate simulation of crack propagation, the heterogeneities within the body should be smooth. Moreover, smoothly varying density allows for calculations of gradients which can help to identify potential points of crack initiation.

It is hypothesised that changes in subchondral bone mineral density, induced by the repetitive cyclical loading in racehorses, are increasing the propensity of fatal injuries such as lateral condyle fracture of 3rd metacarpal bones. Many researchers over the years reported significantly higher bone mineral density at the distal articulating surface in bones of trained horses or with an already fractured limb (Loughridge et al., 2017; Riggs et al., 1999; Whitton et al., 2010). Some of them observed the presence of associated high-density gradient at the parasagittal grooves. However, such gradients have never been quantified. They may be predisposing the site of the fracture, since rapid changes in mechanical properties within the bone may lead to concentration of shear forces, causing the localisation of micro-cracks (Riggs and Boyde, 1999). In this section, numerical tools based on Finite Element Method for mapping CT data and subsequently determining density gradients from CT scans are presented. Developed techniques are utilised to characterise gradients at the sagittal grooves of the third metacarpal bone in racehorses with and without lateral condylar fractures.

In FEM simulations, each finite element in the mesh is assigned with material properties. In the case of analysing bones, it is beneficial to utilise CT scan data that was used to generate the geometry. Each voxel (3D pixel) of a CT scan contains information about measured radiopacity in so-called Hounsfield units (HU), which are directly related to the average stiffness of the bone part enclosed by the voxels. Depending on this relation HU values of a CT image can be used for density mapping and for determining elastic properties based on density-elasticity relationships. It was shown that the apparent density can be related to the mechanical properties of the bones using power-laws.

Subsequently, such relationships can be used to correlate bone density to Young's modulus. Poisson's ratio is usually assumed to be constant $\nu = 0.3$ in hard tissues. It is not clear which power-law relationship is the most accurate. Many proposed relationships in the literature often significantly differ from each other (Helgason et al., 2008a). Some of them have already been used in FEM, validated by experiments and resulted in satisfactory agreement (Eberle et al., 2013). However, there was only one relation found, that considered equine MC3 (Les et al., 1994). Over three hundred bone specimens from the MC3 were harvested in that study. Subsequently, CT scans, along with a Cann-Genant K_2HPO_4 calibration phantom were obtained (Cann and Genant, 1980). The specimens were compressed until failure to estimate elastic modulus, which resulted in the following empiric relation.

$$E = 15100 \cdot \rho_{QCT}^{2.25} \text{ [MPa]} \quad (3.1)$$

Where ρ_{QCT} is dipotassium phosphate K_2HPO_4 equivalent density. Equation 3.1 will be used throughout this thesis to translate density data into elastic modulus.

Another important issue regarding the assignment of density and mechanical properties is whether one single value should be assigned to every element or rather vary within the same

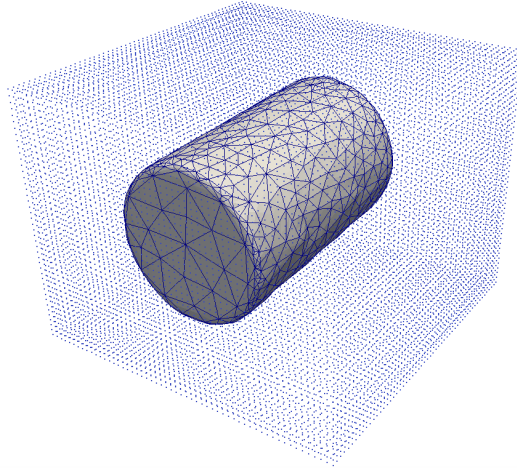


Figure 3.1: Example data set: Finite Element mesh inside voxels lattice from MetaIO file.

element. A comparison between both approaches showed that the single-value approach results in slightly more accurate simulation results as compared to the modified method (Helgason et al., 2008a). Surprisingly, regardless of the discontinuous field of densities (and further elastic modulus) and a limited number of different material properties, numerical outcomes were in better agreement with experiments for the less accurate approach. It shows that methods employing non-constant distribution of material properties within element still need to be improved. As was previously shown, the choice of the mapping algorithm might be critical (Poelert et al., 2013) for estimating stresses. Therefore, in this study new approaches for this application are proposed: L_2 -projection and MWLS approximation.

3.2 Least-squares mapping

The framework developed in this study allows for reading generated meshes from VTK file format and CT scans data from MetaIO files (Ahrens et al., 2005). Example dataset presented in Figure 3.1. MetaIO files consist of a regular grid of equally spaced points depending on slice thickness and resolution of a CT scan. They represent voxels with assigned HU values. Within those points, previously generated tetrahedral mesh is placed. The algorithm used by most of the researches detects voxels inside each finite element and assigns a user-defined grey value for mapping material properties over mesh (Taddei et al., 2007). In the method implemented for this study voxels around each Gauss integration point are collected into sampling cubes. Every finite element has defined integration points whose quantity and placement inside tetrahedral is correlated with the order of integration. Range of collection is defined as the *cube size* parameter presented in Figure 3.2. For each Gauss integration point of the finite element, a sampling cube is created, and subsequently, data from all consisted voxels is collected. In the next step, HU values are translated into densities by using relation presented later in Equation 3.12 and then assigned onto integration point. The representative

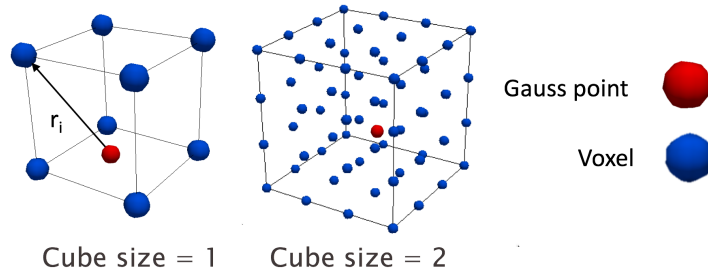


Figure 3.2: Sampling cube around Gauss point for two example sizes. r_i is the distance from the Gauss point to voxel. Cube dimensions are correlated with voxel size.

value from all the voxels surrounding an iteration point is calculating with 1D Gaussian blur equation:

$$g_s(r) = \frac{1}{\sqrt{2\pi}\sigma_g} \exp \frac{-r^2}{2\sigma_g^2} \quad (3.2)$$

where r is distance from the integration point presented in Figure 3.2 and σ_g is the standard deviation, typically 2. Next, the function is normalised:

$$\varphi(r) = \frac{g_s(r)}{\sum_{i=1}^n r_i} \quad (3.3)$$

Values of densities from voxels ρ^* are smoothed into one value ρ by multiplying by weight φ_i :

$$\rho = \sum_{i=1}^n \varphi_i \rho_i^* \quad (3.4)$$

Gaussian smoothing reduces the noise from CT scan data. It was found that for typical CT-scan datasets, a number of 3-4 voxels for the sampling cubes width is sufficient. Furthermore, with the values of densities defined at the integration point level, an L_2 projection a.k.a Least Squares method (LS), is applied to approximate the values into finite elements' nodes with a minimum error on the entire domain.

3.2.1 L_2 projection

L_2 -projection is a simple projection of an arbitrary function into a finite element space. It is often used in the context of FEM analyses when the internal variables need to be projected from the integration points into nodes, like, e.g. plastic strain in plasticity models.

To approximate a given field, $v(\mathbf{X})$, with L_2 -projection, the following L_2 norm has to be minimised:

$$\min J_c(\mathbf{v}^h) : \quad J_c(\mathbf{v}^h) = \frac{1}{2} \|\mathbf{v}^h - v\|^2 \quad (3.5)$$

where v^h is the approximated value of v . v can be considered here as density acquired from CT scan data stored at the integration points. Using standard FEM discretisation, the minimisation of J_c with respect to v_h leads to the following linear system of equations:

$$\mathbf{K}_l \mathbf{v} = \mathbf{f}_l \quad (3.6)$$

where \mathbf{K}_l is the global stiffness matrix, and \mathbf{v} is the vector of approximated values. The system in Equation 3.6 is calculated on a global level such that:

$$\begin{aligned} \mathbf{f}_l &= \sum_{e=1}^n \int_{\Omega} \Phi^T v \, dV_e \\ \mathbf{K}_l &= \sum_{e=1}^n \int_{\Omega} \Phi^T \Phi \, dV_e \end{aligned} \quad (3.7)$$

Additionally, the matrix \mathbf{K}_l can be augmented with the Laplacian term as follows:

$$\mathbf{K}_l = \sum_{e=1}^n \int_{\Omega} \Phi^T \Phi + \lambda_l \nabla_{\mathbf{X}} \Phi^T \nabla_{\mathbf{X}} \Phi \, dV_e \quad (3.8)$$

where λ_l is a length scale parameter, which helps to control the strength of the smoothing. It is worth to note that in the form presented in Eq. 3.8, the projection becomes weighted H_1 -projection. However, since parameter λ_l is optional, the applied projection is called L_2 -projection throughout the thesis.

3.2.2 Comparison with literature

To validate the performance of proposed L_2 -projection, a randomly selected healthy MC3 bone from veterinary school CT-scan database is used as an example. The geometry is segmented with a simple threshold filter and subsequently discretised into relatively coarse mesh consisting of 7554 tetrahedral elements. For assigning the voxel data onto integration points, a sampling cube of size $3 \times 3 \times 3$ was chosen. Additionally, a slight smoothing was introduced with $\lambda_l = 0.1$. The outcomes of the projection of HU values directly (without translating to density) are depicted in Figure 3.3b).

In widely used programs like BONEMAT for bone density assignment, all CT scan voxels that fall inside each mesh element volume are averaged (Zannoni et al., 1999) or integrated into one constant value throughout the element (Taddei et al., 2007; Helgason et al., 2008a). Results of such procedure are presented in Figure 3.3a). The comparison of the two approaches reveals that proposed the L_2 -projection method results in smooth and far less noisy data assignment on the finite element mesh. Although, it still has to be validated experimentally, with strain gauges whether this method can better represent the mechanical response, i.e. stress and strains of the bones.

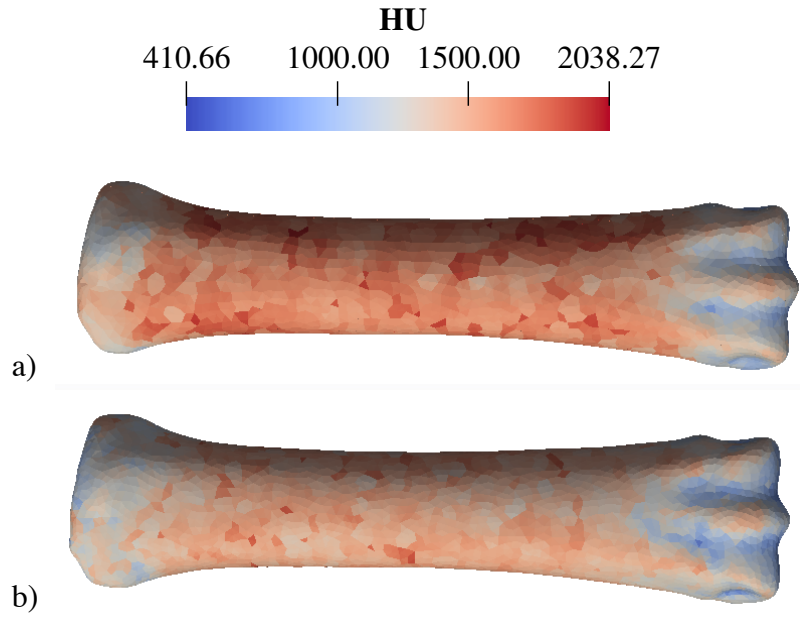


Figure 3.3: Mapped HU voxel data on FEM tetrahedral mesh for equine metacarpal bone mode. a) Bonemat V3 (Taddei et al., 2007) b) Method proposed in this study.

3.3 Moving Least Squares Approximation

The Moving Weighted Least Squares (MWLS) method is used to construct interpolation functions on a set of points to approximate a given spatially varying discrete field (in this case the scalar density field), $v(\mathbf{X}_i)$, and is widely used for various meshless methods (Belytschko et al., 1996). In computer graphics, it is useful to reconstruct a surface from a set of points (Lancaster and Salkauskas, 1981) through downsampling or upsampling. Numerous studies have also attempted to utilise the method within the context of Element-Free Galerkin approach as trial and test functions (Belytschko and Tabbara, 1996; Wong et al., 2010; Ullah and Augarde, 2013).

In discrete fracture approach presented in this work, the nodal configurational forces $\tilde{\mathbf{G}}^h$ (see Eq. 6.27) are dependent on the gradient of elastic energy over the change of density, $\partial\Psi(\mathbf{X}, \rho)/\partial\mathbf{X}$ (see Section 6.2.5). Therefore, the approximation of a spatially smooth density field is important in order to evaluate the configurational forces at the crack front.

3.3.1 Computational implementation

The approximation of a given discrete scalar field $v(\mathbf{X}_i)$ with MWLS method at an arbitrary point \mathbf{X}_t can be calculated as follows:

$$v^h(\mathbf{X}_t) = \sum_{\alpha=1}^q \mathbf{p}_\alpha(\mathbf{X}_t) \mathbf{a}_\alpha(\mathbf{X}_t) = \mathbf{p}^T(\mathbf{X}_t) \mathbf{a}(\mathbf{X}_t) \quad (3.9)$$

where $v^h(\mathbf{X}_t)$ is the approximated value, $\mathbf{p}(\mathbf{X}_t)$ is the vector of complete basis functions, and $\mathbf{a}(\mathbf{X}_t)$ is the vector of unknowns. It should be noted that in the MWLS method, $\mathbf{a}(\mathbf{X}_t)$ is spatially varying rather than being constant as used in conventional Least Squares method. Moreover, q is the number of approximation functions that are built from Pascal's tetrahedron. The monomials are equal to the spatial coordinates X_t , Y_t and Z_t of the node. For maximum target order of approximation functions, k , the total number of non-orthogonal approximation functions is determined by the binomial coefficient as:

$$q = \binom{k+3}{3} = \frac{(k+3)!}{6k!} \quad (3.10)$$

In the current implementation, three types of basis functions are used:

$$\begin{aligned} \mathbf{p}^T(\mathbf{X}_t) &= \mathbf{p}^T(X_t, Y_t, Z_t) = [1], & q = 1 \text{ and } k = 0, \\ \mathbf{p}^T(\mathbf{X}_t) &= \mathbf{p}^T(X_t, Y_t, Z_t) = [1, X_t, Y_t, Z_t], & q = 4 \text{ and } k = 1, \\ \mathbf{p}^T(\mathbf{X}_t) &= \mathbf{p}^T(X_t, Y_t, Z_t) = [1, X_t, Y_t, Z_t, X_t Y_t, Y_t Z_t, Z_t X_t, X_t^2, Y_t^2, Z_t^2], & q = 10 \text{ and } k = 2 \end{aligned} \quad (3.11)$$

The derivation of the coefficients for functions in Equation 3.11 can be found in Appendix A

3.3.2 MWLS mapping examples

Here, validation of the implementation of the MWLS method (described in Section 3.3) is presented via two examples. The first example involves the mapping of an analytical scalar field onto the nodes of a mesh of a prism. For this case, the relative error between the analytical input scalar field and MWLS results are compared for three target orders of approximation of MWLS. In the second example, mapping of CT scan data of a bone onto a mesh is presented. For this challenging mesh geometry, results of the MWLS method are compared with the direct CT scan data as well as results of the Least Squares method.

Mapping of an analytical field

The analytical field ($f(\mathbf{x}) = x + y^2 + z^3$) is mapped onto the mesh nodes of the prism (see Figure 3.4a) using the proposed MWLS procedure described in 3.3. The analytical field $f(\mathbf{x})$ is evaluated at a discrete set of points, $v(\mathbf{x}_i)$, presented in Figure 3.4b. The FE mesh is placed within the discrete field (Figure 3.4b), and the spherical domains of influence of each mesh node are presented (reduced in size for clearer visual presentation) in Figure 3.4c. The size of the influence domain is determined by increasing its radius until matrix \mathbf{A} in Eq. A.4 is invertible for all mesh nodes. The approximated field data, with its gradient, is saved on corresponding nodes, as demonstrated in Figure 3.4c for $q = 10$. Subsequently, the relative

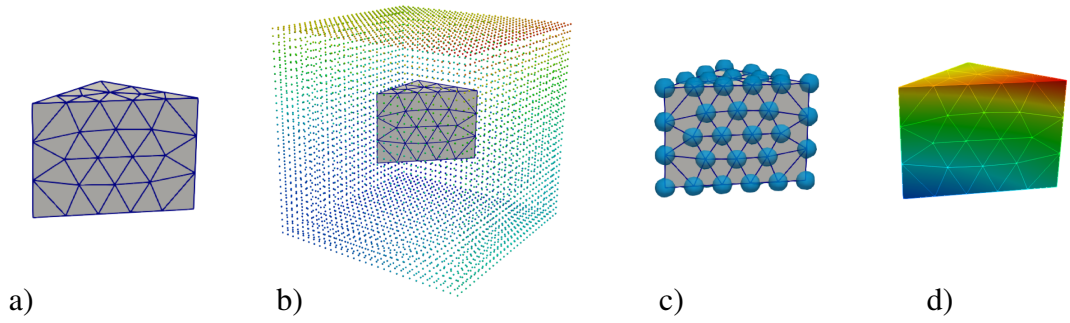


Figure 3.4: a) Finite element tetrahedral mesh. b) Mesh inside analytical discrete field $f(\mathbf{x}) = x + y^2 + z^3$. c) Mesh with corresponding nodes and spherical domain of influence. d) Outcomes of the approximation for $q = 10$.

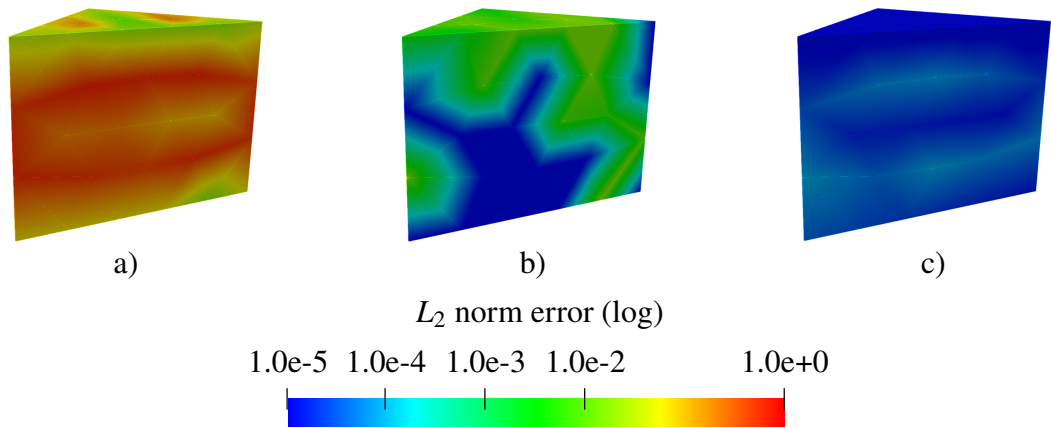


Figure 3.5: Contour plot of relative error of approximated gradient field for constant a), linear b) and quadratic c) basis functions. The logarithmic scale represents the magnitude of relative error.

approximation error between the norm of the analytical gradient of the given field $f(\mathbf{x})$ at the coordinates of each mesh node and the norm of gradient calculated with MWLS at the same node is evaluated and presented in Figure 3.5. The error is evaluated for three cases: constant ($q = 1$), linear ($q = 4$) and quadratic ($q = 10$) basis functions. It is clear from the presented results in Figure 3.5 that constant functions are not sufficient for evaluating the gradient. The maximum error for a linear and quadratic basis has values of 10^{-2} and 10^{-4} , respectively. These results are satisfactory for the application of mapping data fields onto the mesh and suggest correctness of the implementation.

Metacarpal bone

In this section, the results of density approximation from CT data are presented. Geometry and finite element mesh of an equine 3rd metacarpal bone were obtained in ScanIP (Synopsys Simpleware, Exeter) from medical 3D images. The CT data was subsequently used to approximate the density values onto the finite element mesh nodes by using the proposed

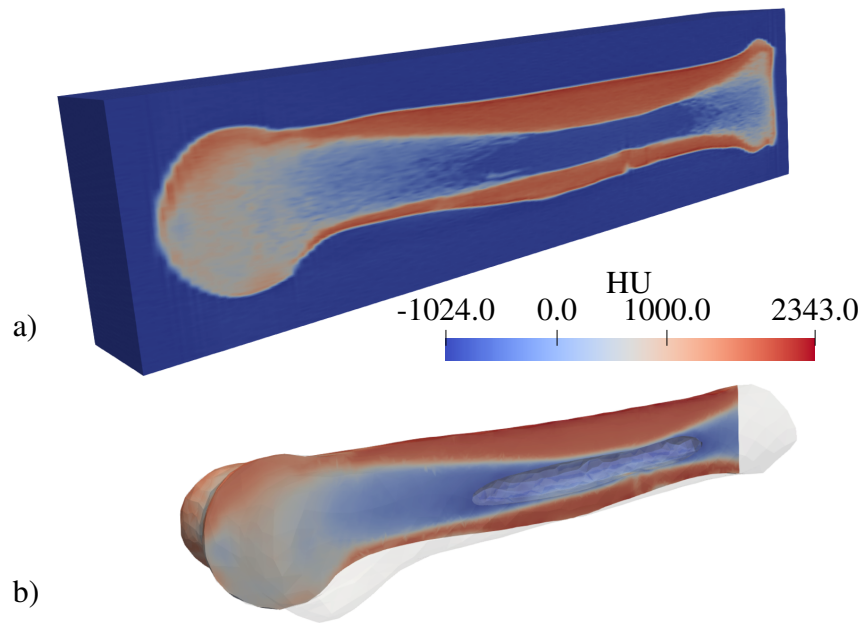


Figure 3.6: Comparison of CT data with the corresponding approximation. a) A cut-view along the $x - y$ plane for CT scan data and b) density mapped onto FE mesh.

MWLS method. The mesh consisted of 7554 tetrahedral elements. Results of the mapping procedures are presented in Figure 3.6. Comparison between the proposed MWLS method and the L_2 -projection (see Section 3.2.1) is shown in Figure 3.7 for both the density field and the density gradient field. The density pattern from both methods is very similar. The density field is continuous. However, classical finite elements used for L_2 -projection provides only C^0 -continuity resulting in piecewise continuous gradients. Density gradients resulting from the MWLS approximation are smooth, as required for the fracture propagation analysis.

3.4 Partial Volume Artifacts

A common problem arising from CT scanning is the generation of Partial Volume Artifacts (Adams, 2009). As a result, the voxel data can be averaged between two materials, for example, bone and soft tissue as presented in Figure 3.8. Each voxel in a CT image represents the attenuation properties of a specific material volume; if that volume is comprised of different materials (e.g. bone and soft tissue), then the resulting CT value is an average of their properties. Furthermore, all object boundaries are blurred to some extent, and thus the material in any one voxel can affect CT values of the surrounding voxels. It has been shown in the past that the reduction of partial volume effects can improve the effectiveness of bone finite element models acquired from CT data (Peleg et al., 2014). To eliminate mapping of spurious bone densities, some researchers proposed to either redefine data at any node on the mesh surface to data assigned on the nearest internal node (Helgason et al., 2008b; Chen et al., 2010) or resurface the mesh geometry (Peleg et al., 2014).

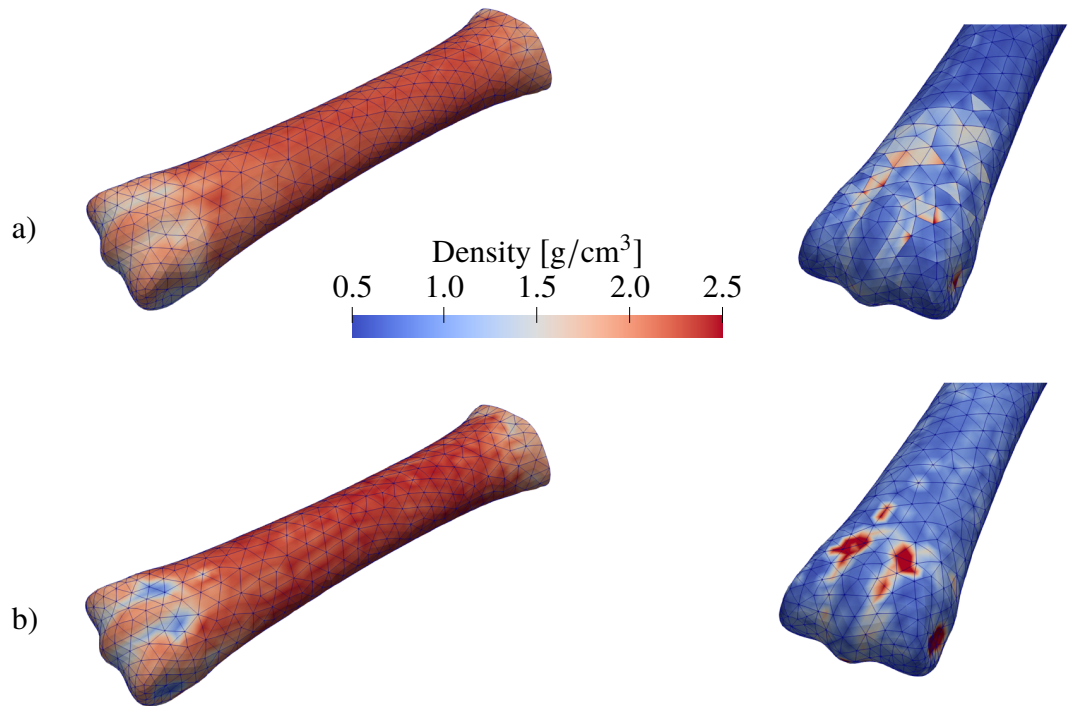


Figure 3.7: Mapping results of bone density (left) and magnitude of density gradient (right). a) Least Squares approximation. b) Moving Weighted Least Squares approximation.

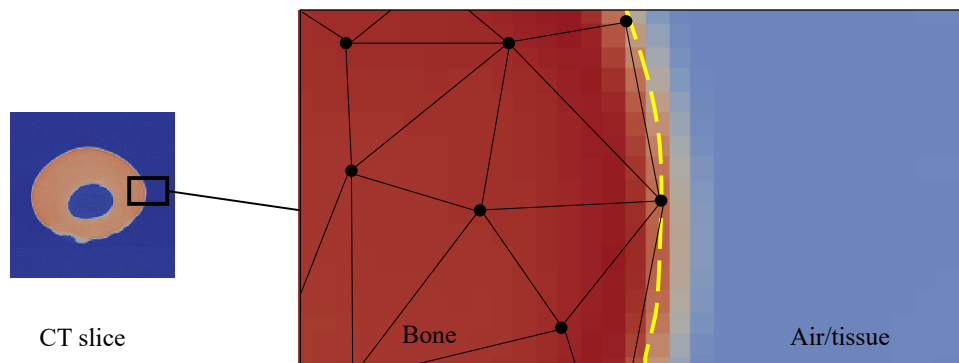


Figure 3.8: Example of Partial Volume Artifact at the interface of bone and soft tissue or air.

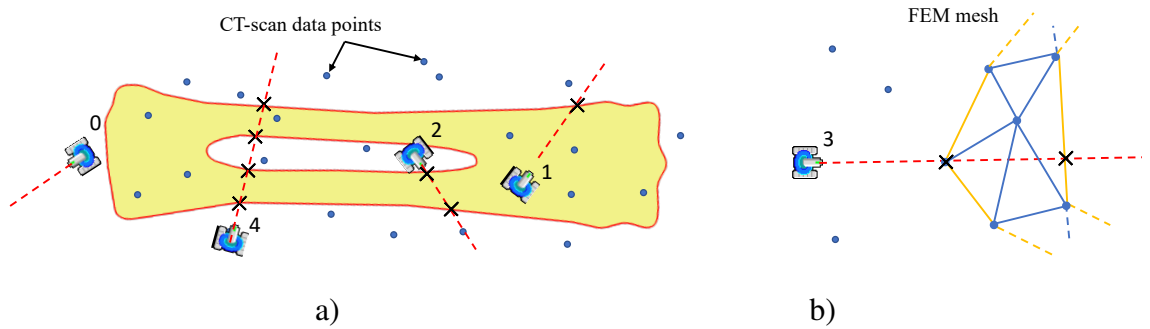


Figure 3.9: a) Random ray casting - a method for determining whether a point is outside the domain. b) A problem when the closest triangle is chosen for the casting direction.

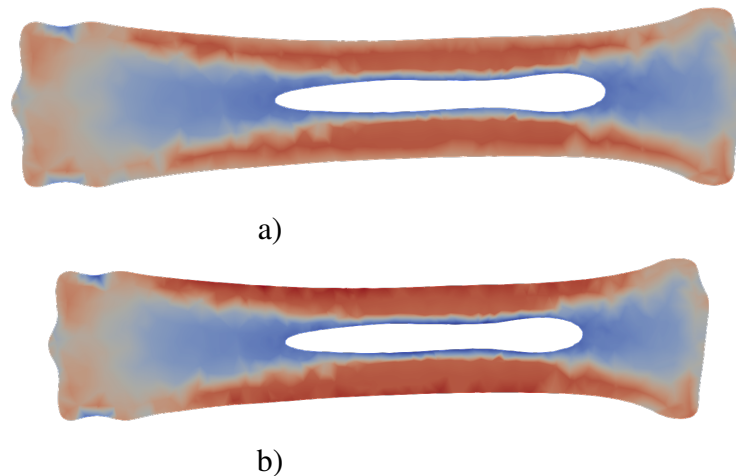


Figure 3.10: Cross-section of MC3 bone (coronal plane) with approximated CT-scan data a) with Partial Volume Artifacts b) without artifacts.

In this study, a more elegant solution is proposed; every considered CT scan data point positioned outside the geometry of the bone is simply removed from the domain of influence (MWLS) or sampling cube (LS). Thereby only points that fall inside the bone geometry are approximated.

Determining whether a given point is inside a polyhedron is a classic computer graphics problem. It can be solved by casting a ray originating from the given point to an arbitrary direction and determine the number of intersections of the ray with the triangles on the skin of FEM mesh. This was done using Mesh-Oriented datABase library (MOAB) functionality (Tautges et al., 2004). If the ray intersects an even number of triangles, then the point is outside the shape. A schematical depiction of this procedure is shown in Figure 3.9a). In MoFEM implementation standard C++ `rand()` function was used, however without the seed in order to ensure that the code remains deterministic. This procedure has to be performed only once for each domain of influence, and it can be easily parallelised.

Interestingly, the initial idea for making the procedure deterministic was to cast a ray from each considered voxel point towards the nearest triangle using MOAB functionality. However, due to FEM discretisation of the geometry, the ray was often cast exactly at the edge of two triangles, as presented in Figure 3.9b), returning not one, as expected, but two triangles. In such cases, the assumption on the even numbers of triangles was incorrect. The solution

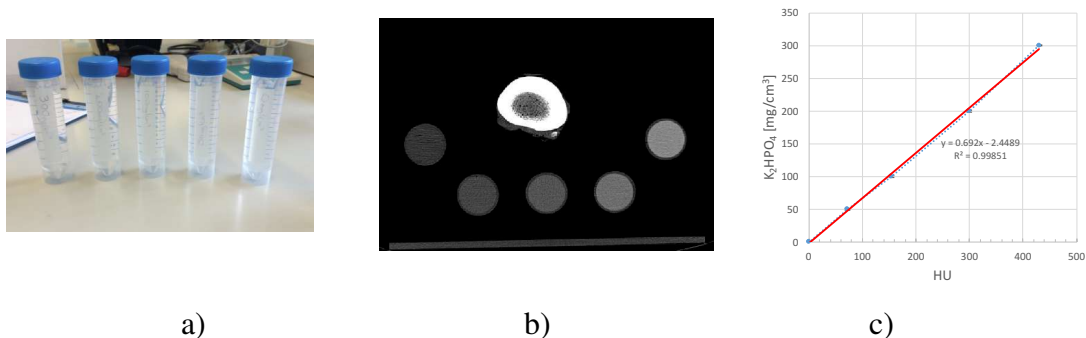


Figure 3.11: a) Five burettes containing solutions of dipotassium phosphate (K_2HPO_4). b) CT scan slice of bone's shaft and K_2HPO_4 calibration phantoms and c) the linear correlation of HU and phantom concentration.

turned out to be casting the ray in a random direction. According to measure theory, the probability of randomly picking a rational number from a given set is 0 (Grigoryan, 2008), which means that casting random number will never coincide with algebraic numbers generated with constrained Delaunay triangulation used by meshing software. Despite the fact that computer-generated random numbers are merely pseudo-transcendental, based on the author's experience, the method still never fails; hence the procedure will correctly identify points outside the discretised geometry.

The difference before and after applying the proposed methodology of removing outer points is demonstrated in Figure 3.10b). The effects of the removal of artifacts are most apparent at the bone's shaft. Without the correction (Figure 3.10a)), it is noticeable that bone density unrealistically decreases close to the outer boundary. The problem is eliminated after applying the proposed method.

3.5 Assessment of bone density gradient

In this section, the developed L_2 -projection mapping is applied for characterising gradients at the sagittal grooves of MC3 bone in racehorses with and without lateral condylar fractures.

3.5.1 Quantitative Computed Tomography

In order to accurately capture bone densities, Quantitative Computed Tomography (QCT) is typically used. QCT is a medical technique that adopts a standard X-ray Computed Tomography (CT) scanner with a calibration phantom to convert Hounsfield Units (HU) of the CT image to bone mineral density values (Adams, 2009). It has been established that QCT is an accurate tool for measuring bone density in MC3 (Drum et al., 2009). Usually, solid calibration phantoms are placed in a pad under the patient during scanning. They contain

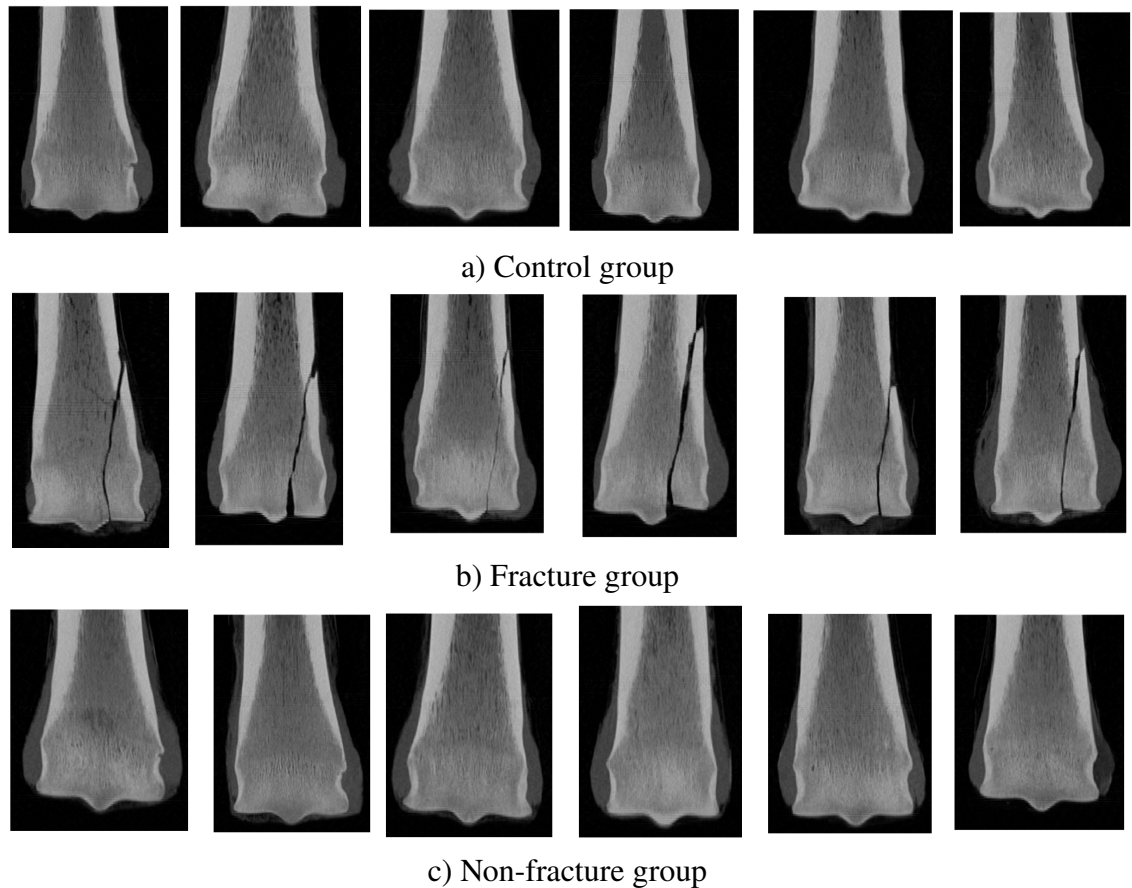


Figure 3.12: Coronal slices from CT scans used in this study. a) Control group b) fractured group (FX) and c) non-fractured contralateral condyle group (NFX).

materials that represent a number of different equivalent bone mineral densities. Calcium hydroxyapatite (CaHAp) or potassium phosphate (K_2HPO_4) are often employed as a reference. By normalizing the HU voxel values against the known density values, a relationship between CT image and bone density can be established. However, calibration between HU units and standard phantom requires the assumption that bone density remains linear beyond the density of phantom (Les et al., 1994).

CT images of the distal condyles of the third metacarpal bone were obtained from 18 Thoroughbred racehorses. The coronal slices of all the scans are presented in Figure 3.12. Third metacarpal bones were divided into 3 groups (6 of each) based on lateral condyle status: fractured (FX), non-fractured contralateral condyle (NFX) and control condyles from horses subjected to euthanasia for reasons unrelated to the third metacarpal bone (Control). NFX bones were harvested from horses with a developed fracture on the other side. Following Trabelsi et al. (2009), each bone was scanned with five burettes (calibration phantoms) containing different concentrations of K_2HPO_4 ranging from 0 to $300\text{mg}/\text{cm}^3$, see Figure 3.11a). A density value was calculated by using the resulting linear ($R^2 = 0.99$) correlation between Hounsfield units and phantom concentrations, as presented in Figure

3.11b). The obtained correlation is expressed as follows:

$$\rho_{QCT} = 0.69HU - 2.45[\text{kg/m}^3] \quad (3.12)$$

The cadaver limb specimens were placed on a table, and CT scanned transversely in the proximal-to-distal direction. Parameters for the scan were set at 120 kVp, 150 mAs of tube voltage and current, respectively. The resultant CT data comprised a 512 x 512 matrix array with voxel dimensions of 0.13 x 0.13 x 0.5 mm and consisted of 268 image slices.

3.5.2 Bone segmentation and 3D FE model generation

Using commercially available software ScanIP 7.0 (Simpleware Ltd., Exeter, UK), the distal end of each MC3 bone was segmented automatically using the same script for every specimen. First, in the procedure, all CT slices were resampled to cubic voxel sizes of $0.5 \times 0.5 \times 0.5$ mm. Bone tissue was separated from the surroundings by setting the threshold of 200 to 3000 HU units (similarly to Eberle et al. (2013)). Subsequently, to close the gaps in the bone and smooth the surfaces Recursive Gaussian Filter was applied with the value of $\sigma = 2.5$ in all directions. Finally, the segmented slices were converted into stereolithographic 3D (STL) representation of distal condyle, as presented in Figure 3.13.

Next, STL models were discretised with 2nd-order tetrahedral elements in Cubit (Sandia National Laboratories, Albuquerque, USA) with a constant element size of 3 mm. The resulting meshes of the distal condyles (Figure 3.13b)) comprised of 30,000 up to 40,000 elements depending on the height of cut-off in the diaphysis. In order to exclude the necessity

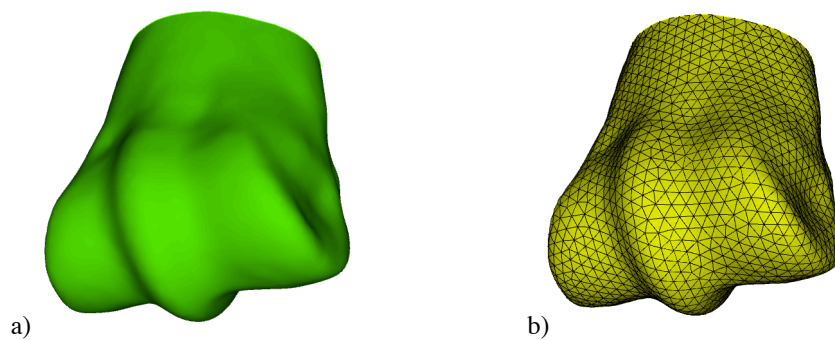


Figure 3.13: a) Stereolithographic representation of segment distal condyle from example CT dataset. b) Corresponding FEM mesh obtained in Cubit.

for manual processing of the slices, the fractured fragments of bones in the fracture group (FX) are excluded from the segmentation procedure. Therefore, it is not possible to estimate the density gradient within already fractured bones. To achieve this, CT scans of broken limbs would require 'stitchings' of fractured fragments, which is a very cumbersome task.

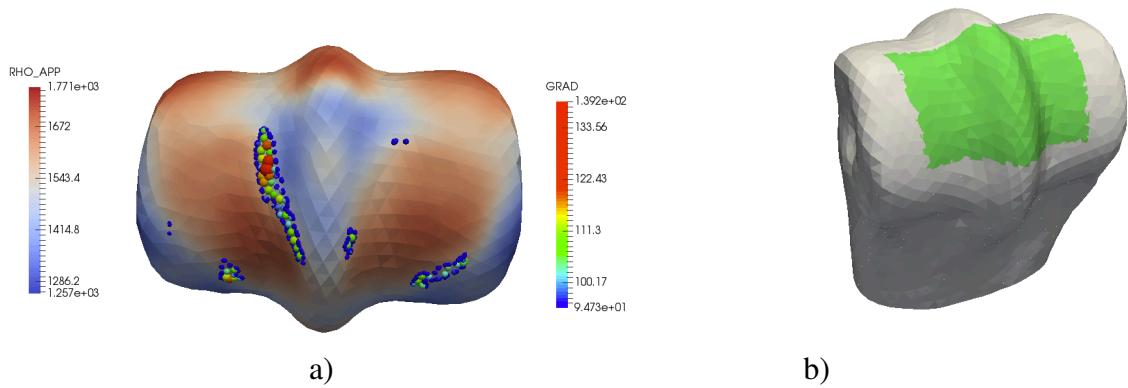


Figure 3.14: a) Mapping results of bone density on the articular surface. The colours on the bone indicate measured density. The spherical glyphs indicate high-density gradient values (magnitude). b) Site of the measurements (palmar site).

3.5.3 Density mapping

For the projection of the density data onto generated meshes, L_2 -projection method discussed in Section 3.2.1 was chosen. The sampling cube size was chosen to be $3 \times 3 \times 3$, and no additional smoothing was introduced ($\lambda_l = 0$). The relationship between the bone density ρ and the HU is taken based on measurements of the phantoms (see Figure 3.11b)). The density within elements is approximated by the polynomial shape functions of order 3 in this study. Next, over the entire domain, Least squares approximation problem is solved to produce a smooth and continuous density field. The spatial variation of density within the elements allows evaluating a gradient field of one order lower than the main field. Example results of density mapping with corresponding gradient magnitudes plot of equine distal condyle are shown in Figure 3.14. Finally, maximum subchondral bone density and gradient magnitude were assessed in 2 regions: from dorsal to the centre of sagittal on lateral and medial site (see Figure 3.14b)). All measurement were made in post-processing open-source program Paraview by using the clip tool and evaluating maximum value within a given region on the lateral or medial side.

3.5.4 Results

Figure 3.15a) provides a comparison of the mean bone density on lateral and medial site between the measured bones. It can be observed that bone density is much higher in the FX condyles compared to the NFX and control condyles; though, there is a high variation between the values. This difference may represent pathological changes in bone density that can increase the risk of lateral condylar fractures in racehorses. On the other hand, measured mean gradients (see Figure 3.15b)) present no significant differences between the groups and regions of the measurements. Horses with fractured limbs (FX) have the highest maximum density levels between the groups. No correlation is found between gradient and density for

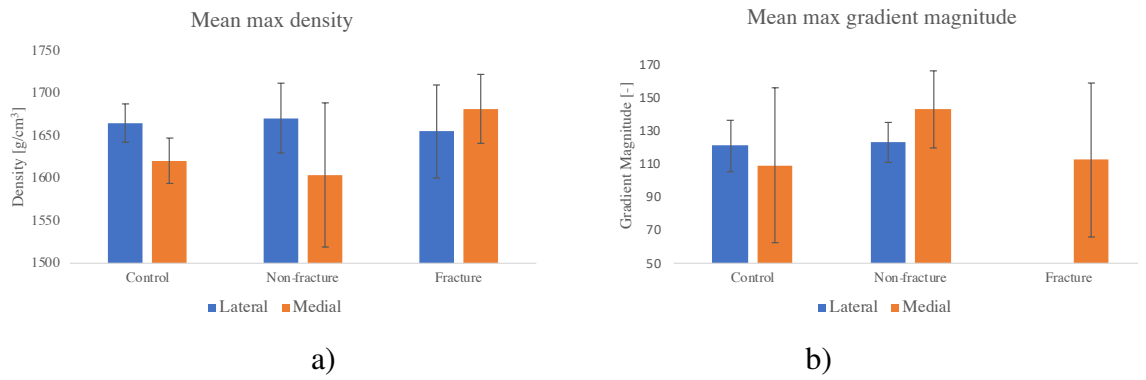


Figure 3.15: Measured mean bone density a) and gradients b) on the medial and lateral side for control, NFX and FX condyles from a CT scan dataset.

control and FX groups; however, a strong correlation ($R^2 > 0.5$) occurs for NFX group on both lateral and medial sites.

3.6 Summary

This chapter introduced two methods for mapping CT scan data onto finite element meshes: L_2 -projection using FEM approximation and meshless MWLS method. Validation of analytical field mapped on a simple mesh and comparison with LS method on mapping data from CT scanning was conducted and proved that both LS and MWLS can be suitable techniques for the approximation of density field, even with strong gradients. Moreover, MWLS allows for the computation of derivatives necessary for crack propagation. Nevertheless, the accuracy of the presented approaches still has to be validated experimentally, for example, in the prediction of strains in the loaded bone specimen. This study also introduced a new simple methodology for correcting Partial Volume Artifacts. The presented approach is robust and proved to effectively eliminate spurious low-density levels at the boundaries of the specimens.

A novel method in quantifying bone gradient is presented in this study. By integrating and mapping density data derived from CT scanning on a finite element mesh, a possible new risk fracture factor can be specified. A density gradient study was conducted on 18 equine bones divided into three categories: control, fractured and non-fractured. However, it was found that a larger body of specimens might be necessary to find significance and correlation between the groups. In the current small cohort, it was found that bones with fractures had the highest density levels on the medial side and a strong correlation was found between the maximum level of density and magnitude of the gradient in NFX horses.

Chapter 4

Bone remodelling

This chapter focuses on a phenomenological model for bone remodelling proposed by Kuhl and Steinmann (2003). It is based on open system thermodynamics which allows for the exchange of energy and mass with the environment, thus simulating the bone's natural ability to adapt to the mechanical conditions. Another important aspect of the model is treating the bone as a continuum. Simplifying the complex underlying micro-structure makes the approach attractive from the practical point of view since all the model parameters can be easily determined through macro-scale mechanical testing and CT-scanning. The governing equations describing the model are discretised and solved using FEM. The implementation is verified with numerous benchmark examples, providing a better understanding of the underlying theory and foundation for the numerical investigation that follows in Chapter 7.

4.1 Introduction

Stress fractures developing in racehorses' bones are strongly correlated with the remodelling process (Hughes et al., 2017). The bone's ability to repair micro-damage caused by cyclical loading is essential for maintaining mechanical integrity. One of the first mathematical theories for bone adaptation (Cowin and Hegedus, 1976), based on open system thermodynamics, has foundations in the theory of poroelasticity. Since this concept was introduced in the 1970s, it has become a popular area of interest within the field of modelling biomechanical processes. In this approach (unlike classical closed systems), energy, mass, momentum and entropy can cross the boundary of the body and be exchanged with its environment. Many derivations and enhancements of this approach have been developed over the years. For example, based on optimisation theory with an objective function where researchers were able to capture the functional adaptation of the bones (Harrigan et al., 1996; Jacobs et al.,

1995; Weinans et al., 1992). The general concept for density evolution within these approaches is to establish a mechanical stimulus as a trigger for bone adaptation. The stimulus may take the form of stress (Beaupre et al., 1990; Carter et al., 1996; Doblaré and Garcia, 2002), strains (Cowin and Hegedus, 1976) or strain energy density (Weinans et al., 1992; Kuhl and Steinmann, 2003; Kaczmarczyk and Pearce, 2011; O’Connor et al., 2017). In this contribution, functional adaptation of the equine 3rd metacarpal bone is modelled by using the approach proposed by Kuhl and Steinmann (2003). Over the years this model was proven to be stable (Kuhl et al., 2003), efficient (Kaczmarczyk and Pearce, 2011) and capable of producing quantitatively comparable results with Dual-energy X-ray absorptiometry (DEXA) scanning when combined with loading given from gait analysis (Pang et al., 2012). With this method, researchers have been able to simulate bone adaptation in human scapula (Liedtke et al., 2017), tibia (Pang et al., 2012), humerus (Taylor et al., 2009) and femur with various surgical implants (Ambrosi et al., 2011; O’Connor et al., 2017) and even explore its potential in topology optimization (Waffenschmidt and Menzel, 2012). One of the advantages of these phenomenological models is that they often require a small number of parameters which can be experimentally determined, for example by using CT imaging (Zadpoor, 2013). To the best of authors’ knowledge, to date, there is only one report of finite element modelling equine bones adaptation (Wang et al., 2016). A mechanistic micro-scale model of three-dimensional cortical bone remodelling was presented, and in-vivo equine data was applied. The model used the von Mises stress as a stimulus to control microstructural cortical bone remodelling. The main goal of the present study is to test the hypothesis that micro-damages and fracture can be modelled at macroscale by using clinically available CT-scanning data. The motivation for this work, is to generate subject-specific simulations to acquire meaningful insight into bone fracture resistance for veterinary practitioners. Additional emphasis on the robustness and efficiency of the implementation is addressed. Numerical methods used for medical research applications have to fit into heavily time-constrained subject-specific modelling frameworks in order to handle as many patients as possible (Poelert et al., 2013).

4.2 Continuum formulation for bone

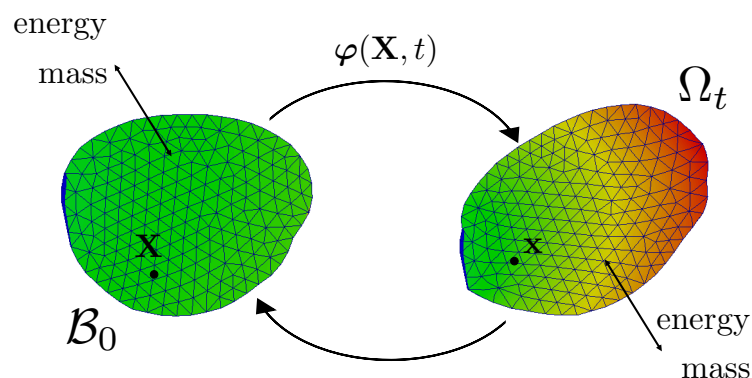


Figure 4.1: Kinematics of a continuum body in an open system.

4.2.1 Conservation of mass

Open system thermodynamics approach adopts the kinematics of finite deformations, and unlike in classical closed systems, energy and mass can cross the boundary of the body. Density field ρ evolves in the current material configuration \mathbf{X} and is defined as:

$$\rho = \rho(\mathbf{X}, t) \quad (4.1)$$

For the sake of generality, a nonlinear kinematic formulation was chosen. It is worth noting, that bone in the physiological range only experiences small strains. The motion of the body is characterised through the nonlinear deformation map $\varphi(\mathbf{X}, t)$, which at any given time t , maps the material coordinates \mathbf{X} in the material configuration \mathcal{B}_0 to its spatial position x in the current configuration Ω_t as presented in Figure 4.1. The physical displacement is:

$$\mathbf{u} = \mathbf{x} - \mathbf{X} \quad (4.2)$$

The deformation gradient and the corresponding right Cauchy-Green deformation, characteristic spatial strain measures take the following representation:

$$\mathbf{F} = \nabla_{\mathbf{X}}\varphi, \quad \mathbf{C} = \mathbf{F}^T\mathbf{F} \quad (4.3)$$

The determinant of the gradient introduces the Jacobian $J = \det(\mathbf{F}) > 0$, which defines volumetric changes. In the context of bone mechanics, the considered system is open i.e. the amount of matter contained in a body \mathcal{B}_0 can change as a result of natural growth. The mass of a reference body cannot be conserved as in classical closed systems. Considering that basic phenomenon, the rate of change of the time-dependent material density is in equilibrium with mass flux \mathbf{R} and the locally created mass \mathcal{R}_0 , expressed as:

$$\dot{\rho} = \nabla_{\mathbf{X}} \cdot \mathbf{R} + \mathcal{R}_0 \quad (4.4)$$

where ρ is mass density and \mathcal{R}_0 is the locally created mass (Kuhl et al., 2003). Although, the mass flux \mathbf{R} is well established in the literature, it is generally never used for practical computations (Pang et al., 2012; Liedtke et al., 2017). The mass flux vector can be considered as an equivalent to the heat flux vector in Fourier's law for heat conduction. Generally, \mathbf{R} is expressed as the spatial gradient of the density weighted by scalar R_0 , as follows:

$$\mathbf{R} = \mathcal{R}\nabla_{\mathbf{X}}\rho \quad (4.5)$$

where R_0 can be considered as mass conductivity. In the present work, it is assumed that the mass flux $\mathbf{R} = 0$ (unless otherwise stated), and hence only the local mass source \mathcal{R}_0 contributes to the changes in density.

4.2.2 Conservation of momentum

Bone adaptation is a mechanically driven process, whereby the density field evolves in response to the mechanical environment. Second governing equation, the conservation of linear momentum balances the density-weighted rate of change of the momentum with the momentum flux \mathbf{P} and the body force $\mathbf{b}_0 = 0$.

$$\rho \dot{\mathbf{v}} = \nabla_{\mathbf{x}} \cdot \mathbf{P} + \mathbf{b}_0 = 0 \quad (4.6)$$

where \mathbf{v} is the spatial velocity vector and \mathbf{P} is the first Piola-Kirchhoff stress:

$$\mathbf{P} = \frac{\partial \Psi(\mathbf{F}, \rho)}{\partial \mathbf{F}} = \left[\frac{\rho}{\rho_0^*} \right]^n \frac{\partial \Psi(\mathbf{F})}{\partial \mathbf{F}} \quad (4.7)$$

Since the time scale of the evolution in density is much larger than the time scale of the mechanical problem, the balance equation above is considered in a quasi-static sense, hence the momentum source $\mathbf{b}_0 = 0$.

4.2.3 Constitutive equations

Constitutive relation for the mass source was adopted following Harrigan and Hamilton (1993). Herein, local mass source \mathcal{R}_0 is governed by free energy density ψ_0 :

$$\mathcal{R}_0 = c \left[\left[\frac{\rho}{\rho_0^*} \right]^{-m} \psi_0 - \psi_0^* \right] \quad (4.8)$$

where ρ_0^* and ψ_0^* represent reference values of the density and free energy, respectively. As will be presented in future examples, both of these coefficients can vary spatially. Parameter ψ_0^* can be considered as a biological stimulus for remodelling. To better visualise its influence on density, a schematic graph is presented below: Biological stimulus essentially governs the threshold of free energy at which density is locally increasing or decreasing. The moment when free energy reaches the exact value of biological stimulus is referred as a biological equilibrium state, where for a given loading magnitude, density changes cannot be observed any more. Whether free energy weighed by relative density (driving force) has a value greater than biological stimulus ψ_0^* density locally increases, if its lower density degrades. Coefficient c in Equation 4.8 controls the rate of the remodelling process, and its unit is the time divided by the length squared. As proposed in (Waffenschmidt and Menzel, 2012), it can be beneficial to prescribe an upper and lower bound for bone density, thereby avoiding spurious or non-physical values. In this work, the parameter c , which is conventionally considered to

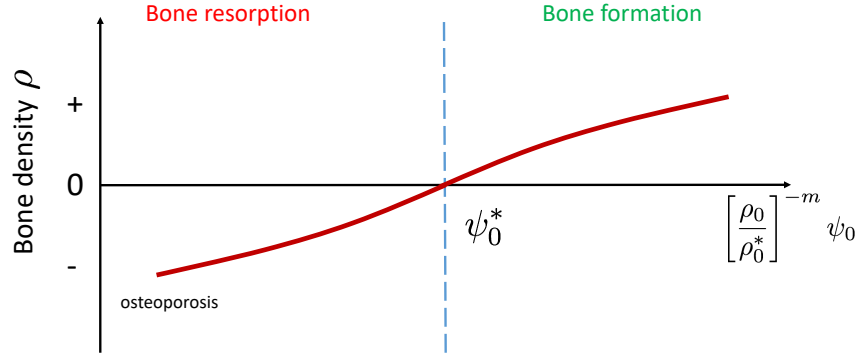


Figure 4.2: Influence of biological stimulus parameter. Whether free energy weighed by relative density (driving force $[\rho_0^*/\rho]^m \psi_0$) exceeds the defined biological stimulus ψ_0^* density locally increases, if its below it decreases.

be constant, is replaced by a bell function defined as:

$$c(\rho) = \frac{1}{1 + [(\rho - \rho^{\text{mid}})/(\rho^{\text{max}} - \rho^{\text{mid}})]^{2b}} \quad (4.9)$$

with $\rho^{\text{mid}} = \frac{\rho^{\text{max}} + \rho^{\text{min}}}{2}$

ρ^{max} and ρ^{min} where ρ^{max} and ρ^{min} are the maximum and minimum values of ρ , and ρ^{mid} is their average. The bell function (4.9) is illustrated in Figure 4.3 for different values of the integer exponent, b . Its application and influence on the overall results are elaborated in Section 7.1. Furthermore, exponent m is a dimensionless scalar, introduced to guarantee

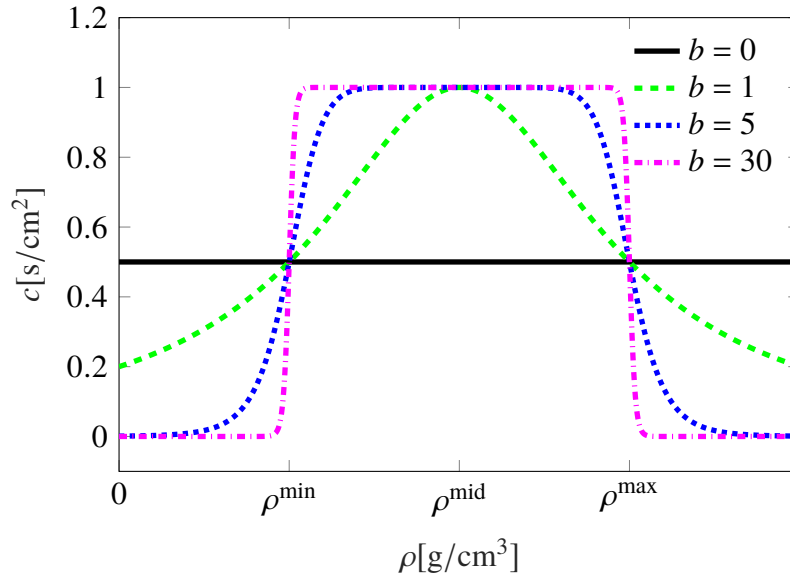


Figure 4.3: Bell function plotted for different values of the integer exponent b . As $b \rightarrow \infty$, bell-shape curve becomes infinitely steep at ρ^{min} and ρ^{max} .

uniqueness and stability (Harrigan and Hamilton, 1993) . In the context of porous materials

like bones, the free energy is equal to:

$$\psi_0 = \left[\frac{\rho}{\rho_0^*} \right]^n \psi_0^{\text{neo}}, \quad (4.10)$$

where the elastic free energy (Helmholtz) ψ was chosen to be of Neo-hookean type, which can be expressed in terms of the right Cauchy-Green deformation tensor:

$$\psi_0^{\text{neo}} = \frac{\mu}{2} [\text{tr}(\mathbf{C}) - 3] - \mu \ln(\sqrt{\det \mathbf{C}}) + \frac{\lambda}{2} \ln^2(\sqrt{\det \mathbf{C}}) \quad (4.11)$$

μ and ν are the Lamé constants. Moreover, the exponent n typically varies between $1 \leq n \leq 3.5$ depending on the porosity of the material (Gibson, 2005).

4.2.4 Strong form

Equations 4.6 and 4.4 represent the strong form of the bone remodelling model. They hold for the entire domain and must be satisfied at every point within that domain. The residuals of linear momentum balance (\mathbf{r}^u) and mass conservation (\mathbf{r}^ρ) on the domain \mathcal{B}_0 can be stated as follows:

$$\mathbf{r}^\rho = \dot{\rho} - \nabla_{\mathbf{X}} \cdot \mathbf{R} - \mathcal{R}_0 \quad (4.12)$$

$$\mathbf{r}^u = \rho \dot{\mathbf{v}} - \nabla_{\mathbf{X}} \cdot \mathbf{P} \quad (4.13)$$

The boundary $\partial \mathcal{B}_0$ of the material domain can be divided into Dirichlet boundary pairs $\partial \mathcal{B}_0^\rho$ and $\partial \mathcal{B}_0^u$, where the density ρ and displacements u are the initial conditions and also Neumann boundary pairs of $\partial \mathcal{B}_0^R$ and $\partial \mathcal{B}_0^\sigma$, where the mass flux and tractions are prescribed respectively. As the essential and natural boundary conditions cannot be assigned simultaneously, the division is subjected to the following requirements:

$$\begin{aligned} \partial \mathcal{B}_0^\rho \cup \partial \mathcal{B}_0^R &= \partial \mathcal{B}_0 \quad \text{and} \quad \partial \mathcal{B}_0^\rho \cap \partial \mathcal{B}_0^R = \emptyset \\ \partial \mathcal{B}_0^u \cup \partial \mathcal{B}_0^\sigma &= \partial \mathcal{B}_0 \quad \text{and} \quad \partial \mathcal{B}_0^u \cap \partial \mathcal{B}_0^\sigma = \emptyset \end{aligned} \quad (4.14)$$

The boundary conditions for the mass flux and the tractions are given by:

$$\begin{aligned} \mathbf{R} \cdot \mathbf{n} &= \tilde{R} \quad \text{on } \partial \mathcal{B}_0^R \\ \mathbf{P} \cdot \mathbf{n} &= \tilde{\mathbf{t}} \quad \text{on } \partial \mathcal{B}_0^\sigma, \end{aligned} \quad (4.15)$$

with \mathbf{n} denoting vector normal to $\partial \mathcal{B}_0$. Furthermore, boundaries on the solution for initial density and displacements are as follows:

$$\rho = \tilde{\rho} \quad \text{on } \partial \mathcal{B}_0^\rho$$

$$\mathbf{u} = \tilde{\mathbf{u}} \quad \text{on } \partial\mathcal{B}_0^u, \quad (4.16)$$

where $\tilde{\mathbf{u}}$ and $\tilde{\rho}$ are imposed values for displacements and densities, respectively.

The initial condition for the density is generally given by:

$$\rho(\mathbf{X}, t = 0) = \rho_0^* \quad (4.17)$$

However, in this contribution non-uniform, initial distribution is also investigated in Section 7.3.1, where the starting density is obtained through mapping CT-scan data as described in Chapter 3.

4.2.5 Weak form

For the finite element discretisation, the strong form has to be transformed into the weak form of the partial differential equations. The solution of the weak form equations is required to hold in a weighted residual sense in the domain, hence much easier to satisfy with the FEM formulation. The residual statements in Equations 4.12, 4.13 and the corresponding Neumann boundary conditions are tested by the scalar- ($\delta\rho$) and vector-valued ($\delta\mathbf{u}$) functions, respectively. Following Galerkin, weighting function tests that the equation is satisfied in an average sense, rather than at each point of the domain. In the presented model, these functions are in H_1 space, which means that the gradient of function has to be square-integrable. The residuals of the balance of mass \mathbf{g}^ρ and momentum \mathbf{g}^u are expressed as follows:

$$\begin{aligned} \mathbf{g}^\rho(\rho, \mathbf{u}, \delta\rho) &= 0 \quad \forall \delta\rho \quad \text{in } H_1(\mathcal{B}_0) \\ \mathbf{g}^u(\rho, \mathbf{u}, \delta\mathbf{u}) &= 0 \quad \forall \delta\mathbf{u} \quad \text{in } H_1(\mathcal{B}_0) \end{aligned} \quad (4.18)$$

After performing integration by parts, applying Green's formula and inserting the boundary conditions, the weak form of the balance of mass residual \mathbf{g}_ρ and \mathbf{g}_u are given by:

$$\begin{aligned} \mathbf{g}^\rho &= \int_{\mathcal{B}_0} \delta\rho \dot{\rho} dV + \int_{\mathcal{B}_0} \nabla_{\mathbf{X}} \delta\rho \cdot \mathbf{R} dV - \int_{\partial\mathcal{B}_0^R} \delta\rho \tilde{R} dA - \int_{\mathcal{B}_0} \delta\rho \mathcal{R}_0 dV \\ \mathbf{g}^u &= \int_{\mathcal{B}_0} \delta\mathbf{u} \rho \dot{\mathbf{v}} dV + \int_{\mathcal{B}_0} \nabla_{\mathbf{X}} \delta\mathbf{u} \cdot \mathbf{P} dV - \int_{\partial\mathcal{B}_0^\sigma} \delta\mathbf{u} \tilde{\mathbf{t}} dA \end{aligned} \quad (4.19)$$

4.2.6 Time discretisation

For the time discretisation of the governing equations, implicit backward Euler method is utilised. A time step is defined as $\Delta t = t_{n+1} - t_n$, where t_{n+1} denotes the next and t_n the current time step. It is assumed that the primary unknowns ρ_n and u_n are known at the actual subinterval t_n , and hence equilibrium can be calculated. In the backward Euler time integration scheme, any first-order material time derivative can be expressed for example as:

$$\dot{\rho} = \frac{1}{\Delta t} [\rho_{n+1} - \rho_n] \quad (4.20)$$

At this point, to numerically solve the system of equations, a monolithic scheme is chosen, also referred as the node-based approach, where both balance equations are evaluated simultaneously. The choice is motivated by the fact, that the staggered approach with local Newton iterations becomes very computationally expensive for large scale problems with a high order of approximations (Kuhl et al., 2003), which are one of the most important features exploited in MoFEM (Kaczmarczyk et al., 2020).

4.2.7 Spatial discretisation

For spatial discretisation, the domain of interest \mathcal{B}_0 is partitioned into n_{el} finite elements \mathcal{B}_0^e . The geometry of each subdomain is interpolated in terms of the local basis functions Φ . The Galerkin method is used for approximation of density and displacement fields.

$$\begin{aligned} \rho &\approx \rho^h = \sum_{i=1}^{n_{el}} \Phi_i^\rho \rho_i & \mathbf{u} &\approx \mathbf{u}^h = \sum_{j=1}^{n_{el}} \Phi_j^u \mathbf{u}_j \\ \delta \rho &\approx \delta \rho^h = \sum_{i=1}^{n_{el}} \Phi_i^\rho \delta \rho_i & \delta \mathbf{u} &\approx \delta \mathbf{u}^h = \sum_{j=1}^{n_{el}} \Phi_j^u \delta \mathbf{u}_j, \\ \nabla_{\mathbf{X}} \rho &\approx \nabla_{\mathbf{X}} \rho^h = \sum_{i=1}^{n_{el}} \nabla_{\mathbf{X}} \Phi_i^\rho \rho_i & \nabla_{\mathbf{X}} \mathbf{u} &\approx \nabla_{\mathbf{X}} \mathbf{u}^h = \sum_{j=1}^{n_{el}} \nabla_{\mathbf{X}} \Phi_j^u \otimes \mathbf{u}_j \\ \nabla \delta \rho &\approx \nabla \delta \rho^h = \sum_{i=1}^{n_{el}} \nabla_{\mathbf{X}} \Phi_i^\rho \delta \rho_i & \nabla \delta \mathbf{u} &\approx \nabla \delta \mathbf{u}^h = \sum_{j=1}^{n_{el}} \nabla_{\mathbf{X}} \Phi_j^u \otimes \delta \mathbf{u}_j, \end{aligned} \quad (4.21)$$

where n_{el} are the global nodes. Φ^ρ and Φ^u are the shape functions for displacement and density fields respectively and $\rho, \mathbf{u}, \delta \rho, \delta \mathbf{u}$ are the nodal values of the respective quantities. With the above relations at hand, the discrete balance equations can be rewritten as:

$$\mathbf{r}_{n+1}^\rho = \sum_{e=1}^{n_{el}} \int_{\mathcal{B}_0} \Phi \frac{\rho_{n+1} - \rho_n}{\Delta t} dV + \int_{\mathcal{B}_0} \nabla_{\mathbf{X}} \Phi^T \cdot \mathbf{R}_{n+1} dV - \int_{\partial \mathcal{B}_0^R} \Phi \tilde{\mathbf{R}}_{n+1} dA - \int_{\mathcal{B}_0} \Phi \mathcal{R}_{0n+1} dV$$

$$\mathbf{r}_{n+1}^u = \sum_{e=1}^{n_{el}} \int_{\mathcal{B}_0} \Phi^u \rho \frac{\mathbf{v}_{n+1} - \mathbf{v}_n}{\Delta t} dV + \int_{\mathcal{B}_0} \nabla_{\mathbf{x}} \Phi^T \cdot \mathbf{P}_{n+1} dV - \int_{\partial \mathcal{B}_0^s} \Phi \tilde{\mathbf{t}}_{n+1} dA \quad (4.22)$$

Note that in the above equation and the following, superscript ρ and u from shape functions Φ is dropped for readability.

4.2.8 Linearisation

The non-linear coupled system of Equations 4.19 can be solved efficiently by means of iterative Newton-Raphson method at each time step. Equations 4.13, 4.12 are expressed as a truncated Taylor series expansion, whereby the residuals at the next iteration ($i + 1$) have the following form:

$$\begin{aligned} \mathbf{r}_{i+1}^\rho &= \mathbf{r}_i^\rho + dR^\rho = 0 \\ \mathbf{r}_{i+1}^u &= \mathbf{r}_i^u + dR^u = 0 \end{aligned} \quad (4.23)$$

thus the iterative residua dR^ρ and dR^u take the form:

$$\begin{aligned} dR_{i+1}^\rho &= \frac{\partial R_i^\rho}{\partial \rho} \Delta \rho + \frac{\partial R_i^\rho}{\partial \mathbf{u}} \Delta \mathbf{u} \\ dR_{i+1}^u &= \frac{\partial R_i^u}{\partial \rho} \Delta \rho + \frac{\partial R_i^u}{\partial \mathbf{u}} \Delta \mathbf{u} \end{aligned} \quad (4.24)$$

With the above definitions, iterative stiffness matrices can be expressed:

$$\begin{aligned} \mathbf{K}^{\rho\rho} &= \frac{\partial R^\rho}{\partial \rho} & \mathbf{K}^{\rho u} &= \frac{\partial R^\rho}{\partial \mathbf{u}} \\ \mathbf{K}^{u\rho} &= \frac{\partial R^u}{\partial \rho} & \mathbf{K}^{uu} &= \frac{\partial R^u}{\partial \mathbf{u}} \end{aligned} \quad (4.25)$$

Calculating the derivatives, results in the following representations:

$$\begin{aligned} \mathbf{K}^{\rho\rho} &= \sum_{e=1}^{n_{el}} \int_{\mathcal{B}_0^e} \Phi^T \frac{1}{\Delta t} \Phi dV - \int_{\mathcal{B}_0^e} \Phi^T \frac{\partial \mathcal{R}_0}{\partial \rho} \Phi dV + \int_{\mathcal{B}_0^e} \nabla_{\mathbf{x}} \Phi^T \cdot \mathbf{R} \nabla_{\mathbf{x}} \Phi dV \\ \mathbf{K}^{\rho u} &= \sum_{e=1}^{n_{el}} - \int_{\mathcal{B}_0^e} \Phi^T \frac{\partial \mathcal{R}_0}{\partial \mathbf{F}} \cdot \nabla_{\mathbf{x}} \Phi dV \\ \mathbf{K}^{u\rho} &= \sum_{e=1}^{n_{el}} \int_{\mathcal{B}_0^e} \nabla_{\mathbf{x}} \Phi^T \cdot \frac{\partial \mathbf{P}}{\partial \rho} \Phi dV \\ \mathbf{K}^{uu} &= \sum_{e=1}^{n_{el}} \int_{\mathcal{B}_0^e} \Phi^T \frac{1}{\Delta t^2} \mathbb{I} \Phi dV + \int_{\mathcal{B}_0^e} \nabla_{\mathbf{x}} \Phi^T \cdot \frac{\partial \mathbf{P}}{\partial \mathbf{F}} \cdot \nabla_{\mathbf{x}} \Phi dV \end{aligned} \quad (4.26)$$

Note that balance of momentum is usually evaluated in a quasi-static sense, taking the simple form of $\nabla_{\mathbf{x}} \cdot \mathbf{P} = 0$; hence the mechanical forces can be interpreted as an average daily loading and consequently, all the terms in Equations 4.22, 4.26 related to changes in velocity vanish. By assembling all the matrices and vectors, global system of equations can be derived:

$$\begin{bmatrix} \mathbf{K}_{\rho\rho} & \mathbf{K}_{\rho u} \\ \mathbf{K}_{u\rho} & \mathbf{K}_{uu} \end{bmatrix} \begin{bmatrix} \Delta\rho \\ \Delta\mathbf{u} \end{bmatrix} = \begin{bmatrix} \mathbf{r}^\rho \\ \mathbf{r}^u \end{bmatrix} \quad (4.27)$$

The system is subsequently solved at each time step using the Newton-Raphson method.

4.2.9 Tangent operator

The partial derivatives in Equations 4.26 are trivial to compute, except for derivative of Piola stress $\partial\mathbf{P}/\partial\mathbf{F}$. The result of which is a fourth-order elasticity tensor \mathbb{D} . It is well-known that derivation of such operators and the following implementation into the code can be troublesome and error-prone. Therefore, in this study, automatic differentiation is utilised by means of ADOL-C library (Walther, 2009). ADOL-C is an open-source C++ library that applies the operator overloading technique to compute derivatives of arbitrary functions. The independent variables subject to differentiation are defined using a special type *adouble*, and all variables which depend on the independent variable are also be defined using this type. Constants are considered passive and can be defined using standard types such as *double*. To generalize the implementation and fully utilise ADOL-C library, the desired fourth-order tensor \mathbb{D} is directly derived from elastic free energy (Eq. 4.11) by calculating automatic Hessian operator as follows:

$$\frac{\partial^2 \psi_0^{\text{neo}}}{\partial \mathbf{F}^2} = \mathbb{D} \quad (4.28)$$

Using ADOL-C significantly speeds-up the implementation process and simplifies the debugging. The additional advantage is the flexibility; since the tangent operator can be directly obtained from the energy function, it is straightforward to explore more sophisticated constitutive models, like for example include fibres into the material (Eberlein et al., 2001). However, for commonly used compressible Neo-Hookean model, the tangent operator can be found in the literature (Kuhl, 2004). The representation of the analytical solution for fourth-order tangent operator \mathbb{D} requires the introduction of the non-standard dyadic products $\bar{\otimes}$ and $\underline{\otimes}$. Their definition can be expressed component-wise as follows:

$$\begin{aligned} \{\bullet \bar{\otimes} \circ\}_{ijkl} &= \{\bullet\}_{ik} \{\circ\}_{jl} \\ \{\bullet \underline{\otimes} \circ\}_{ijkl} &= \{\bullet\}_{il} \{\circ\}_{jk} \end{aligned} \quad (4.29)$$

Finally, the fourth-order tangent is specified:

$$\mathbb{D} = \frac{\partial \mathbf{P}}{\partial \mathbf{F}} = \lambda \mathbf{F}^{-t} \otimes \mathbf{F}^{-t} + \mu \mathbb{I} \otimes \mathbb{I} + [\mu - \lambda \ln(\det(\mathbf{F}))] \mathbf{F}^{-t} \otimes \mathbf{F}^{-1} \quad (4.30)$$

where μ and ν are the Lamé constants. With analytical solution at hand, it is beneficial to investigate the numerical efficiency of the automatic differentiation approach. Two simple problems are computed for that purpose: one with small number degrees of freedom (843 DOFs) calculated on 1 processor and second one significantly larger (35532 DOFs) calculated on 24 cores. The total CPU time with distinction to solver and assembly time for these two cases is shown in Figure 4.4. It can be noticed that analyses using automatic differentiation are about 25 % slower than the analytical formulation due to increased assembly time. However, for bigger problems with a larger number of elements, the overall assembly time will have much less computational cost in comparison to solver time; therefore, the difference between the two implementations should decrease. Nevertheless, considering how greatly ADOL-C simplifies the implementation process and how much flexibility it provides, it can be recommended for implementing highly nonlinear problems. Especially where the analytical solution of the derivative is difficult to obtain. In conclusion, calculating the tangent stiffness matrix from the

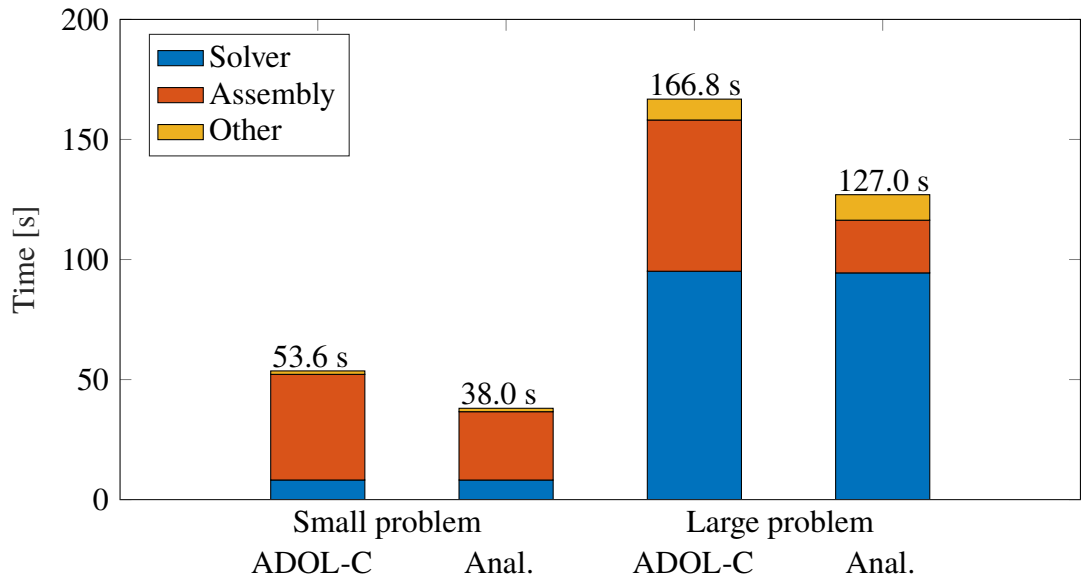


Figure 4.4: Runtime for two simple problems. Time distribution in a different part of the code for ADOL-C and analytically obtained tangent operator.

constitutive relations can be troublesome. However, the use of automatic differentiation helps to simplify this process, speeds up the implementation and reduces the possibility of errors at the cost of a minor increase in the assembly time.

4.3 Benchmark problems

To validate the implementation, the results of the simple benchmark problems are compared with the literature.

4.3.1 Parameter sensitivity

Consider a simple one-dimensional, homogeneous tension test, similarly to Kuhl and Steinmann (2003) as presented in Figure 4.5. The following values of parameters are used: elasticity

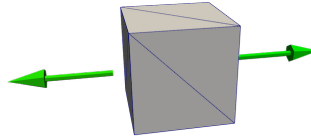


Figure 4.5: One-dimensional model problem under tension.

modulus $E = 1$, Poisson's ratio of $\nu = 0$. The reference density is chosen to be $\rho_0^* = 1$ and energy stimulus is $\psi_0^* = 1$. To ensure uniqueness and stability of the solution, exponents of growth are $m = 3$ and $n = 2$. Time integration is performed with time steps of $\Delta t = 0.1$. The specimen was axially loaded by multiple step loading function (line f) as illustrated in Figure 4.6 below. The corresponding mechanical response proves the high nonlinearity of the problem. The time-dependent nature of the balance of mass is visualised above. Curves

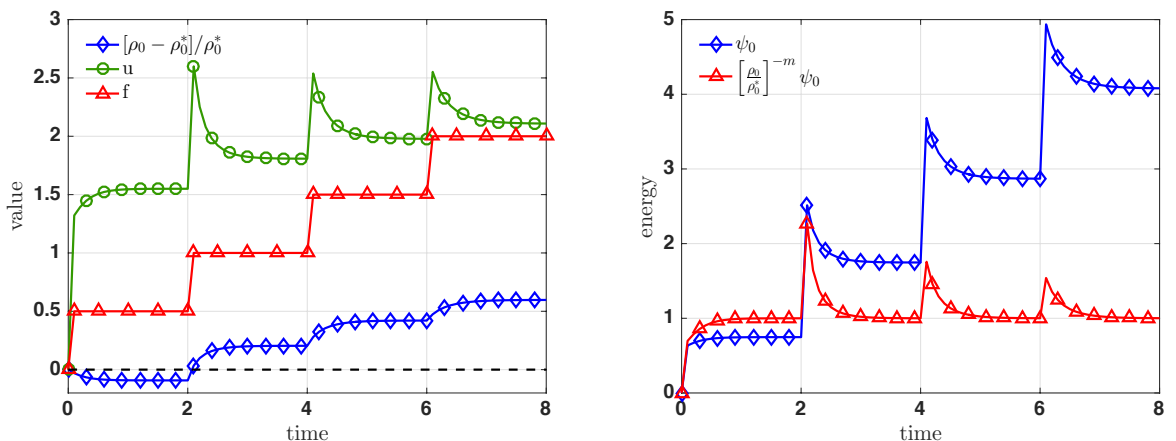


Figure 4.6: One-dimensional model problem. Evolution of density ρ_0 , displacements u and energy values ψ and relative energy $[\rho_0/\rho_0^*]^{-m} \psi$.

of primary unknowns demonstrate the relaxation towards biological equilibrium, the state when density converges to a final value for particular loading magnitude. Figure 4.7a) depicts

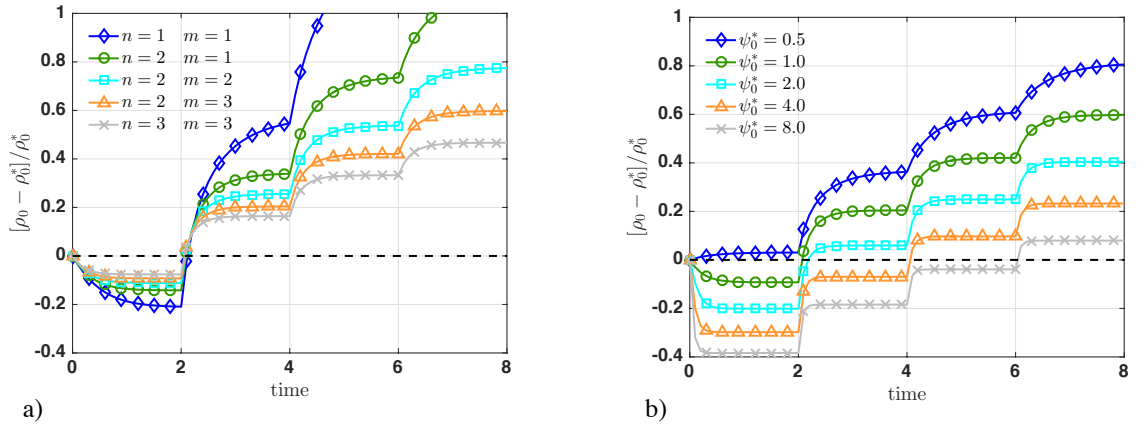


Figure 4.7: Parameter sensitivity with respect to algorithmic exponents n, m and biological stimulus ψ_0^* .

the sensitivity of the relative changes in density $(\rho - \rho_0^*) / \rho_0^*$ with respect to combinations of algorithmic exponents m and n . The relative density differs significantly from one other, even when the difference $n - m = -1$ stays the same and is proportional to the reference free energy ψ_0^* as presented in Equation 4.8. This is because of stress-driven loading, as stated in Equation 4.10, where the porosity exponent n contributes to the definition of the energy density. Figure 4.7b) illustrates the influence of the larger values of ψ_0^* initially drives the density to decrease, whereas smaller ones, as expected, result in increased density formation. An

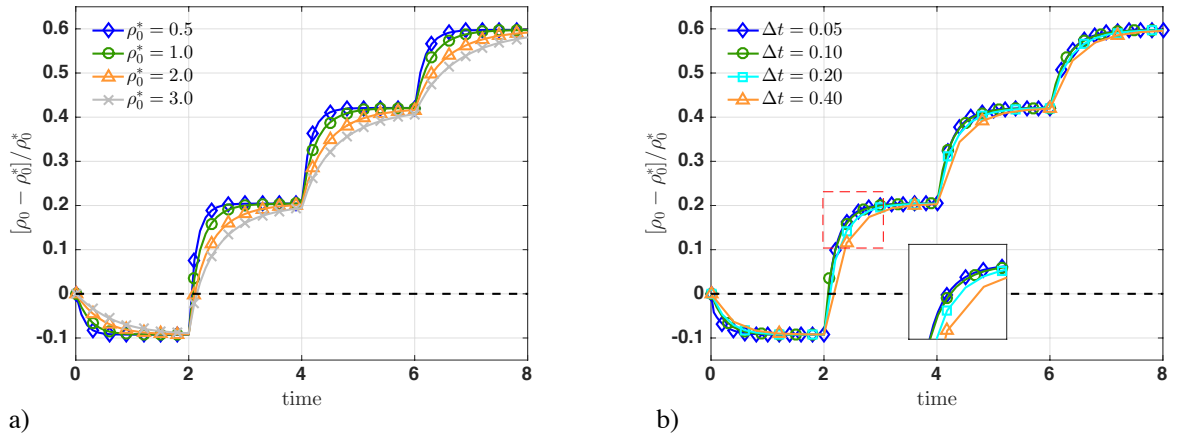


Figure 4.8: Parameter sensitivity with respect to reference density ρ_0^* and time step Δt .

interesting phenomenon can be observed in Figure 4.8a) b), where the influence of reference density ρ_0^* and time step Δt is considered. It turns out that for given exponents $m = 3$ and $n = 2$, the value of relative density at equilibrium state is insensitive to the reference density ρ_0^* parameter and the time step size Δt as well. Finally, the impact of the coefficient c that governs the growth velocity as specified in Equation 4.8 is tested (Figure 4.9). It is clear that for higher values of c the equilibrium is achieved sooner with no impact on the final solution. In summary, simulations perfectly match the results reported by Kuhl and Steinmann (2003).

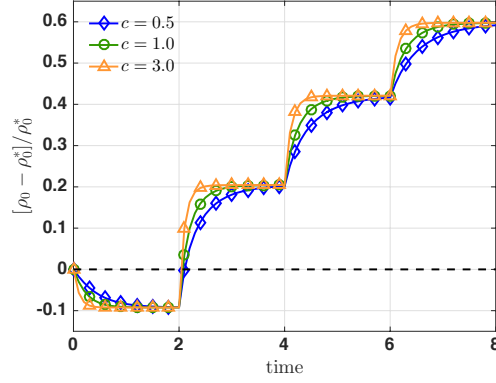


Figure 4.9: Parameter sensitivity with respect to the density evolution velocity c .

4.3.2 Influence of the mass flux

In the subsequent examples, the sensitivity of the solution is investigated with respect to the mass flux. Unlike in previous simulations wherein the mass flux was assumed to vanish in the balance of mass Equation 4.4, here, it has the following form:

$$\frac{\partial \rho}{\partial t} = \nabla_{\mathbf{x}} \cdot \mathbf{R} + \mathcal{R}_0 \quad \text{with} \quad \mathbf{R} = R_0 \nabla_{\mathbf{x}} \rho, \quad (4.31)$$

where R_0 is the mass conduction coefficient. Subsequently, to illustrate the implications of using this parameter, another one-dimensional problem is considered similarly to Kuhl and Steinmann (2003), and Kaczmarczyk and Pearce (2011). A unit length bar with length to width ratio of 1% is modelled with a unit load that generates approximately 250% stretch. The parameters are chosen to be: $E = 1$ and $\nu = 0.2$ for Young's modulus and Poisson ratio, respectively. The remodelling-related coefficients are $\rho_0^* = 1$, $\psi_0^* = 2$, $c = 1$, $n = 2$ and $m = 3$. To guarantee convergence within the global Newton iteration, the load is applied in ten steps of 0.1 and then is held constant for another 50 time steps of Δt until the solution converges to the equilibrium state. Additionally, to trigger a discontinuous solution, target energy (biological stimulus) ψ_0^* is increased in five discrete steps of $\Delta \psi_0^* = 0.25$ from the middle, see Figure 4.10. Such distribution is inducing density jumps, as the lower values of this

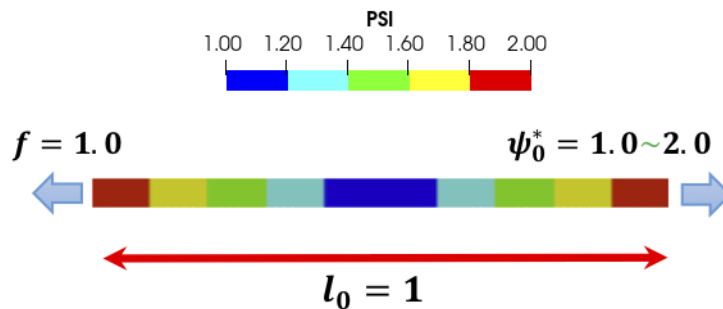


Figure 4.10: Discontinuous model problem. Loading and stepwise varying biological stimulus ψ_0^* from the value of 1.0 in the middle up to the value of 2.0 at both ends of the specimen.

parameter are compensated with a significant increase in density, as illustrated in Figure 4.11. Note that the geometry of the bar in figures is stretched in one plane for visualisation purposes.

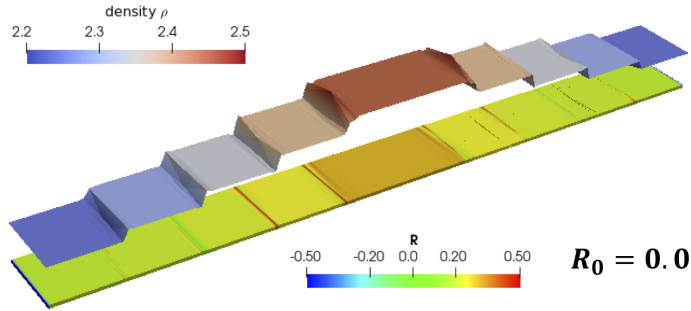


Figure 4.11: Discontinuous model problem at equilibrium state with reference free energy parameter distribution imposed. The upper plot depicts density. Contour plot below shows the mass source (Eq. 4.8).

Furthermore, it can be observed that the developed method can handle discontinuities very well. Moving on, the influence of the mass conduction coefficient R_0 is investigated. The simulation

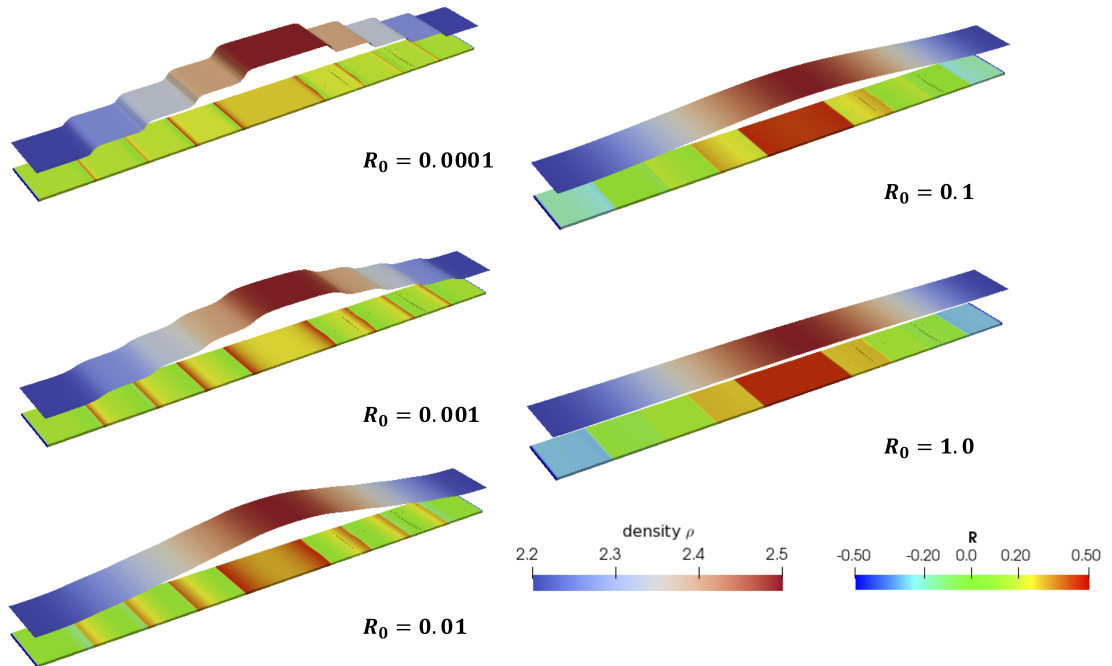


Figure 4.12: Parameter sensitivity with respect to coefficient R_0 that induces the mass influx.

with $R_0 = 0$ results in oscillations close to the density jump. However, by introducing the mass influx, the density profiles are smoothed. $R_0 = 1.0$ decreases the gradients almost to zero resulting in constant density distribution. Since the mass conduction coefficient R_0 is operating on a Laplacian term, an additional length scale is introduced into the formulation. It has an analogous interpretation as the gradient parameter in gradient enhanced continuum mechanics (Gitman et al., 2010). In summary, including mass influx can be beneficial to handle discontinuities in the system and help to control the density levels.

4.3.3 Size effect

In the next example, the effect of smoothing the density distribution will be utilised, to capture the characteristic size effect of bone microstructure. To study the formation of microstructures, following Kuhl and Steinmann (2003), example bone geometry with loading, as presented in Figure 4.14, is considered. The geometry and the magnitude of applied forces have been scaled by a factor of 0.5 and 2.0. The parameters are chosen to be: $E = 100$ MPa and $\nu = 0.2$ for Young's modulus and Poisson ratio, respectively. The remodelling-related coefficients are $\rho_0^* = 1$, $\psi_0^* = 2\text{N/mm}^2$, $c = 1\text{d/cm}^3$, $n = 2$ and $m = 3$. The predicted density distribution is

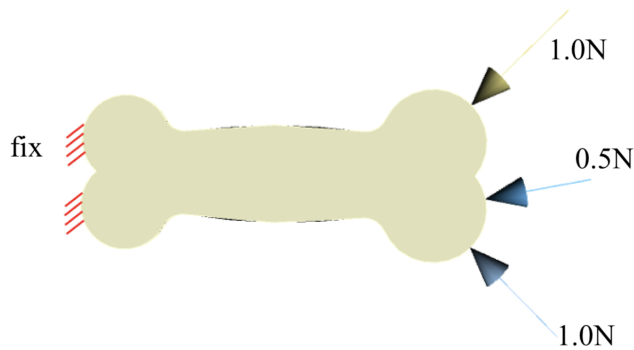


Figure 4.13: Loading conditions for bone size effect study.

identical for the different bone size, as presented in Figure 4.13a). However, incorporation of previously studied mass flux \mathbf{R} with conduction coefficient $R_0 = 0.1$ significantly influences the density pattern, see Figure 4.13b). The larger structure of bone is characterised by the formation of sharp, truss-like structures while the small bones show almost homogeneous density distribution. Therefore, it is evident that by using mass conduction coefficient R_0 the microstructural size effects can be simulated.

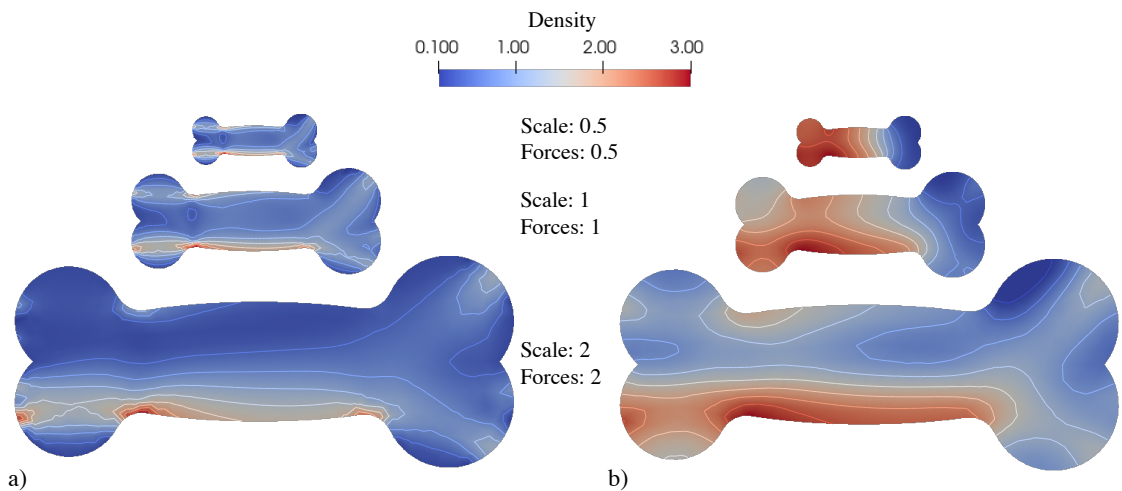


Figure 4.14: Development of microstructures predicted by the model with b) and without a) the mass flux \mathbf{R} .

4.3.4 Numerical efficiency

As previously stated in Section 4.1, numerical frameworks for medical research applications aim for maximum efficiency in order to analyse large cohorts of patients in a limited amount of time. In this subsection, a potential improvement in the developed model's performance will be briefly investigated.

Returning to the coupled system of Equations 4.4 and 4.6 solved in this work, it is worth noting that they are a slight modification of well-known heat equation and nonlinear elasticity problems. These two PDEs can be classified as parabolic and elliptic, respectively. The elliptic part will be of special interest here, as for this type of equations iterative multigrid solvers can be applied. Multigrid methods are one of the most efficient numerical algorithms for solving sparse systems of linear equations (Bruaset and Tveito, 2006). In many cases of elliptic PDEs, multigrid can have a remarkable complexity of $O(n)$ to solve a large linear system with n degrees of freedom. For comparison, in case of dense matrices, a well-known direct Gaussian elimination method typically will require n^3 floating-point operations in order to solve the same dense system. A multigrid method is constructed from a series of consecutive discretisations (grids) where the problem is solved starting from the coarse grid, and subsequently, the errors are transferred onto finer grids. In typical FEM discretisations building multiple levels of grids often can be troublesome.

However, in MoFEM (Kaczmarczyk et al., 2020), grids can be easily constructed with hierarchical approximation bases (Ainsworth and Coyle, 2003) at very low cost. In order to deliver multigrid solver functionality into bone remodelling implementation, a fieldsplit preconditioner from PETSc (Balay et al., 2018) package is utilised. Fieldsplit provides block solver functionality, i.e. allows for dividing a problem and apply different preconditioners and solvers to the appropriate parts of the system. As derived earlier, in bone remodelling model, the global tangent stiffness matrix has the following block-like structure:

$$\begin{bmatrix} \mathbf{K}_{\rho\rho} & \mathbf{K}_{\rho u} \\ \mathbf{K}_{u\rho} & \mathbf{K}_{uu} \end{bmatrix} \quad (4.32)$$

Subsequently, in order to use fieldsplit, the following multiplicative preconditioner is applied to the original matrix:

$$\begin{pmatrix} I & 0 \\ 0 & \mathbf{K}_{uu}^{-1} \end{pmatrix} \begin{pmatrix} I & 0 \\ -\mathbf{K}_{u\rho} & I \end{pmatrix} \begin{pmatrix} \mathbf{K}_{\rho\rho}^{-1} & 0 \\ 0 & I \end{pmatrix} \quad (4.33)$$

The inverse of block matrices: \mathbf{K}_{uu}^{-1} and $\mathbf{K}_{\rho\rho}^{-1}$ is then obtained by internal Krylov preconditioners which can be of different, more suitable types, like for example aforementioned multigrid.

Moving on, the scalability of the implementation with fieldsplit is investigated. Example 10 time steps of a bone remodelling problem is solved on a high-performance parallel computer system. The mesh consists of 33,000 finite elements and 113,000 degrees of freedom. MUMPS (Amestoy et al., 2001) direct solver is utilised in two ways: first on the global system

and second separately on each field (density and displacement). Solving the problem on

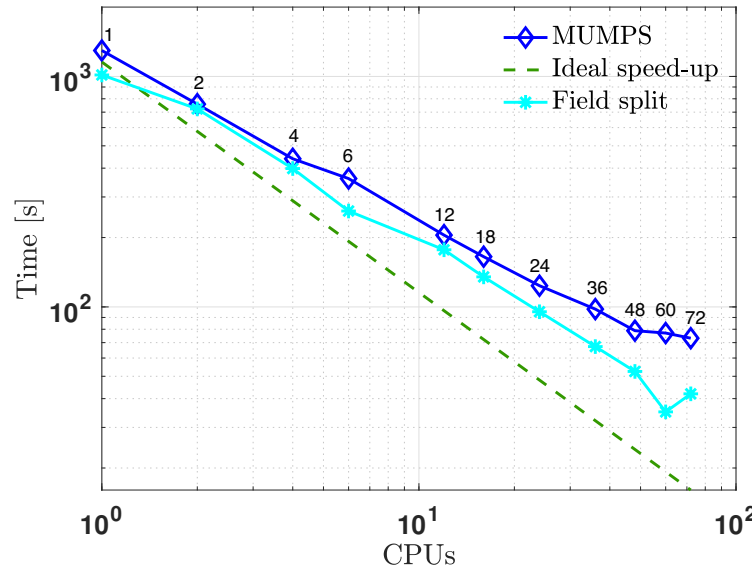


Figure 4.15: Scalability of bone remodelling implementation for two solver cases.

multiple CPUs demonstrates a speed-up in computation time for both cases, as shown in Figure 4.15. However, since fieldsplit divides the problem into smaller ones, the direct solver scales slightly better and saturates (no longer decreases computational time) at around 60 CPUs, in comparison to 48 CPUs when used on a global system. Overall, in both variants, the total time from a single CPU is reduced by a factor of 20, which means that this particular the medium-sized problem can be solved in less than two minutes which is rather acceptable for practical applications. Ultimately, in the future, it is planned to implement a multigrid solver on the elliptical part (\mathbf{K}_{uu}^{-1}) and fully take advantage of MoFEM's hierarchical approximation bases.

4.4 Bone remodelling and topology optimisation

The following section moves on to compare two conceptually different approaches for structural design: a classical topology optimisation (TOP) and implemented bone remodelling formulation. The comparison is motivated by the work of Kuhl et al. (2003) and followers (e.g. (Waffenschmidt and Menzel, 2012)) who applied an algorithm for the functional adaptation of hard tissues to find the optimal arrangement of material in various structures. Such class of problem is often used as benchmark for bone remodelling implementations.

A typical engineering problem seeks to maximise the structural stiffness within a domain to most efficiently use the given space and the material, while at the same time fulfil particular constraints like for example volume fraction. The solution for such problems is far from trivial due to many local minima. Therefore, numerous numerical methods have been implemented

Material parameters		Bone remodelling		Topology optimisation	
E	1000 MPa	c	1.0 d/cm ²	f^{top}	0.3
ν	0.3	Δt	0.01 d	m^{top}	0.2
		ρ_0^*	0.1 g/cm ³	p^{top}	3
		ψ_0^*	0.5 N/mm ²	λ_l	0.3
		m	3	i^{max}	40
		n	2		

Table 4.1: Material parameters used for bike frame optimization.

to approximate this problem (Bendsøe and Sigmund, 2003). One of the most commonly used is the SIMP approach (Solid Isotropic Material with Penalization) (Bendsøe, 1989). In SIMP, the material properties of each discretisation element in the design domain are relative to the densities, which varies from 0 to 1. Additionally, the densities are raised to some power, similarly to bones, where the material properties are found to fit the power-law of the density (Helgason et al., 2008a). This approach gained its popularity due to exceptional robustness and ease of implementation. The slight modification has been implemented in MoFEM and is described in details in Appendix B. Classical optimisation techniques are not the only ones considered for structural design. To date, several studies have investigated the bio-inspired approaches, for example, genetic algorithms (Hajela and Lee, 1995), cellular automaton (Tovar et al., 2006) or neural networks (Yildiz et al., 2003). The bone remodelling formulation presented in this work has also been proven to qualitatively match the expected optimal designs (Liedtke et al., 2017; Kuhl, 2004). However, it has never been directly compared side by side with the results of the topology optimisation itself.

4.4.1 Bike frame

Three simple examples of rectangular panels are considered, following Kuhl and Steinmann (2003). The bone remodelling approach and SIMP TOP are utilised to find the most effective shape of the bike frame for certain loading conditions. Material and model parameters are presented in Table 4.1 below. The design domain of a rectangular shape with 1 unit in length and 0.5 height and three different loading cases are depicted in Figure 4.16a). Geometry is discretised with 2717 quadratic tetrahedral elements. The mass flux \mathbf{R} is assumed to be suppressed. The load is applied in a single step load in the first time step and held constant thereafter. For topology optimisation, the maximal volume fraction is set to 30%, the penalty parameter is equal to 3 and the length scale coefficient $\lambda_l = 0.3$. The rest of the parameters are purely algorithmic, as described in Appendix B. i^{max} is the maximum number of iterations. The simulations of bone remodelling are continued until the density distribution is completely adapted (biological equilibrium). The resulting density patterns are demonstrated in Figure 4.16 for bone remodelling b) and topology optimisation c). For bone remodelling, the regions of resorption, i.e. where ($\rho < \rho_0^*$) are blanked, whereas for TOP,

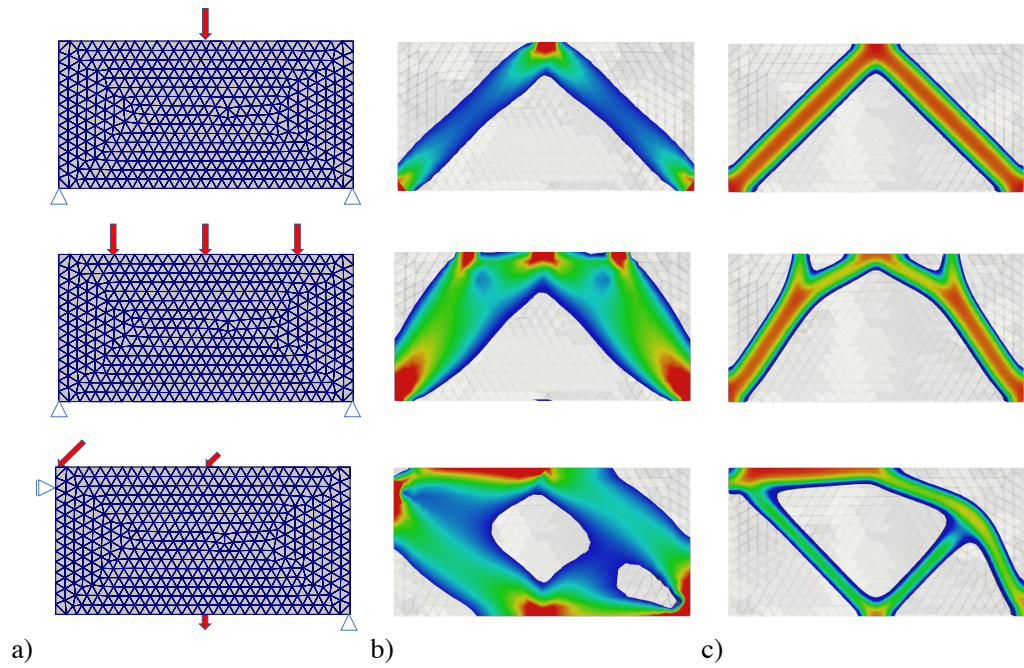


Figure 4.16: Topology optimization - a) geometry, discretisation and loading conditions. b) Resultant density distributions at equilibrium state. Regions of resorption ($\rho < \rho_0^*$) are blanked. c) Resultant geometry from topology optimisation $f^{\text{top}} = 0.3$.

the threshold for density is chosen such that the resulting volume matches the desired target f^{top} . In both cases, the simulation captures the densification effects and clearly identifies the main load-bearing regions, while degrading material in regions that do not take part in transferring loads. Both formulations will produce unstable checker-board solutions without regularisation, in case of remodelling it is exponent m (Eq. 4.8), and in TOP typically various different filtering techniques are utilised (Lazarov and Sigmund, 2011; Sigmund and Maute, 2013). The algorithm in TOP tends to form sharper contours with a truss-like structure, which is very desired for engineering purposes. Moreover, the width of these truss elements can be easily controlled with the filtering parameter, in this case, λ_l . On the other hand, in bone remodelling, the parameter to control *smoothness* of the resulting distribution is the mass conduction coefficient R_0 as was previously presented in Section 4.3.2. The demonstrated examples shown that by introducing the mass conduction (mass flux), the solution of the density can be smoothed out, even to a homogeneous state. However, the inverse of this process is not possible in this model. Choosing the negative value of R_0 will result in Helmholtz-like equation, rendering the system of matrices to be ill-conditioned and ultimately loss of convergence within the Newton iterations. Interestingly, it can be noticed that in TOP the truss elements have consistently high density along their length in distribution produced. Whereas in remodelling, mass is added only locally, in the vicinity of the applied boundary conditions. Moving on, it is worth to remark that TOP is insensitive to the material properties like Young's modulus, the magnitude of the force or the scale of the structure, the result will remain the same. In contrast, in bone remodelling, all the material related parameters: Young's modulus E , the reference density ρ_0^* and biological stimulus ψ_0^* have a significant

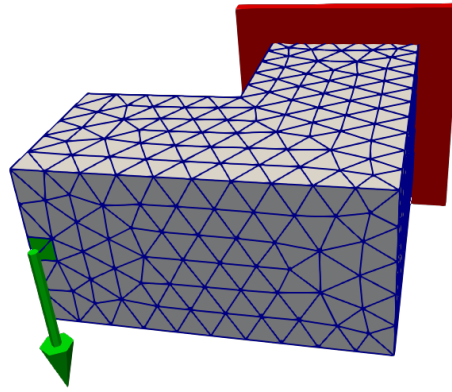


Figure 4.17: Crank optimisation example. Geometry, discretisation and loading conditions. The backside is clamped. Height = 100mm, Length=200mm, width=200mm. Applied pressure $\tau_l = 1.5\text{N/mm}^2$ on a rectangular area of 400mm^2

Parameter		Parameter	
E	3800 MPa	c	0.4
ν	0.3	m	3.0
ρ_0^*	1.0 g/cm ³	n	2.0
ψ_0^*	0.01 N/mm ²		

Table 4.2: Set of material parameters used for the bone remodelling L-shaped crank calculations.

impact on the result and if not chosen carefully, since the problem is highly nonlinear, it can lead to divergence.

4.4.2 Three-dimensional L-shaped crank

In the next example, following Waffenschmidt and Menzel (2012), an L-shaped crank structure is analysed. The geometry, discretisation to 3597 quadratic tetrahedral elements and boundary conditions are depicted in Figure 4.17 below. The material parameters used for bone remodelling are shown in Table 4.2 below. The adaptive time step size Δt is utilised. For TOP, the model parameters are the same as in the previous example (Table 4.1). In this analysis, the loading for bone remodelling is applied in two variants: first - full load in one step and held constant thereafter and second: the load is applied in four even steps. In both cases, the analysis is continued until biological equilibrium is achieved. The resulting evolution of the total energy over time and the produced geometries are demonstrated in Figure 4.18 below. The difference between the two results is significant. The crank that was loaded in one step achieved noticeably higher stiffness and therefore the resulting topology is more developed. Additional confirmation of this remark can also be found based on the graph in Figure 4.18, where it is evident that the model loaded in a stepwise manner has higher total energy and thus displacements as well. This interesting observation has not been reported before regarding this model. As it turns out, the bone remodelling is highly history (path)

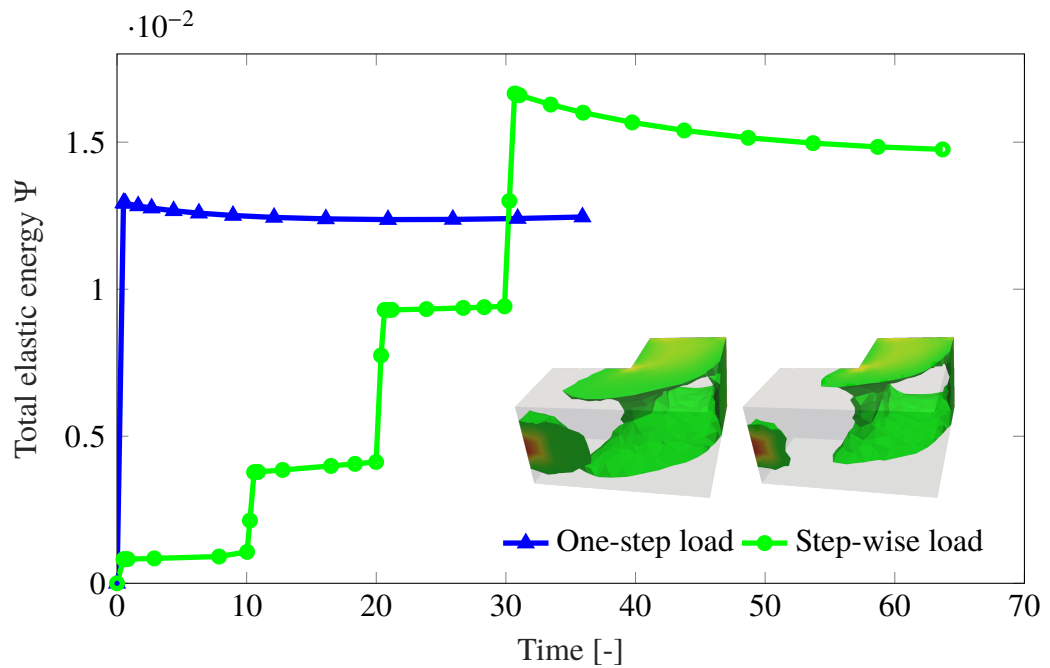


Figure 4.18: The evolution of total elastic energy for one-step and multiple-step loaded crank. The resulting isosurfaces with $\rho \geq \rho_0^*$.

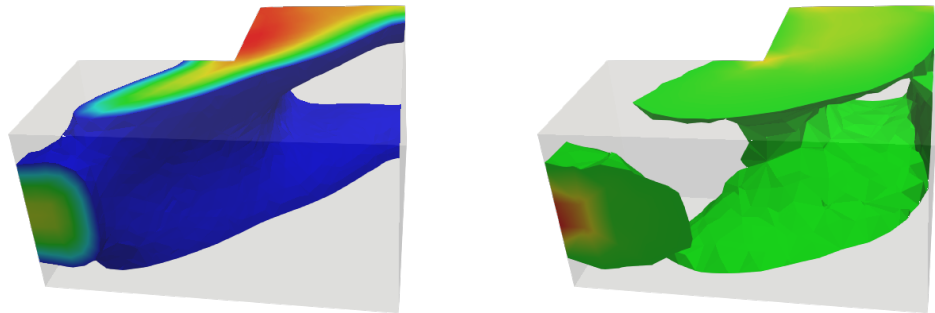


Figure 4.19: Resulting geometry from topology optimisation (left) and bone remodelling (right).

dependent problem. Finally, the converged crank shape simulated with the bone model along with the one obtained from TOP is presented in Figure 4.19. It is clear that shape attained from TOP maintains structural integrity and resembles a sharp, truss-like geometry to minimise the deformation and volume. In comparison, the model reacted with a box-like section to torsion loading arising at the clamped boundary. On the other end of the model, the density clearly increased, but there is no connection with the rest of the formation. It is worth noting that the blanked resorbed "bone" regions still contribute to the load-bearing capacity of the structure. The results of this investigation show that bone remodelling can be applicable for designing structures with materials with an easily controlled material density like, for example, with additive manufacturing methods. The density could be interpreted as the refinement of the infill material, locally increased in the particular regions of the domain. As for classical structural design, bone remodelling fails in comparison with well establish

topology optimisation. The resulting geometry simulated with bone density growth only resembles an optimal design obtained with TOP. The parameters which are used for density bone growth have biological sense but are difficult to interpret when used for engineering design. Based on the examples, it can be concluded that bone remodelling model is most suitable for simulating growth. Overall, the presented phenomenological model tries to mimic nature's universal ability to adapt to external conditions. However, based on the observations, nature only tends to evolve to states that are "good enough", but not necessarily optimal (Milo, 2019).

4.5 Summary

In this chapter, a numerical framework for bone remodelling simulation was presented. All the parameters used in the model has been tested against various benchmark problems. It has been shown that the implementation is correct in comparison with the literature. Two different methods of obtaining the tangent stiffness matrix were demonstrated and compared. Particular attention was given on the application of density growth model into structural design problems and similarities with the topology optimisation method. The practical application of the presented formulation with numerical examples of human and equine bones is provided in Chapter 7.

Chapter 5

Phase-field fracture

This chapter introduces to smeared crack approach with phase-field for crack propagation. Phase-field is a popular formulation for solving fracture mechanics problems with only PDEs. It is based on potential energy approximation of Griffith brittle fracture functional. Some details of the implementation are closely elaborated, i.e. derivation of tangent stiffness matrix and arc-length control method. The main goal is to deliver a simple, robust method for simulating fracture in heterogeneous materials like bones, thus providing cross-validation of the novel developments presented in Chapter 6. The performance of the implementation is verified with several benchmark problems.

5.1 Introduction

The prediction of failure mechanisms in structures due to micro-cracks and their possible propagation by using numerical methods has been continuously the subject of considerable attention in science over the years. First significant work in the fracture mechanics was introduced by Griffith (Griffith, 1921), wherein based of thermodynamics the effect of crack formation was described by surface energy that is required for the creation of new crack surfaces. Many numerical methods are available to solve the problem of fracture initiation and growth. Such methods may be divided into two categories: discrete and diffused approach. Discrete crack models initially were limited to describe crack formation only on element boundaries (Ngo and Scordelis, 1967). More recently, in the presence of automatic mesh generators, the extended finite element method (XFEM) separated the crack path from underlying mesh, see, e.g. (Belytschko and Black, 1999) where XFEM is applied to brittle fracture. Another novel approach in isogeometric analysis field introduces knot insertions that lower the order of continuity to introduce cracks in solids (Hosseini et al., 2014). The

continuum damage, or diffused crack, the approach incorporates a damage parameter into the model that controls the strength of the material. An advantage of this approach is that it does not require interface tracking since the damage parameter varies continuously over the domain with further improvement by a gradient approach (see, e.g. de Borst et al. (2004)). Closely related to continuum damage models are the phase-field models. The numerical solution of this model is based on an approximate energy potential, inspired by the image segmentation method developed by Mumford and Shah (1989). The study in de Borst and Verhoosel (2016) showed that the diffusion equation for the phase-field can be considered as a special case a gradient-damage model.

In the phase-field method, the fracture problem can be described purely by partial differential equations. The initially proposed variational method based on energy minimisation by Francfort and Marigo (1998) gained a rapid increase in popularity since it has been revisited by Miehe et al. (2010b) by introducing new way of crack regularisation. Miehe et al. (2010b) proposed a thermodynamically consistent framework for crack propagation along with the efficient numerical implementation in multi-field finite element method formulation. It has been proven that this method is robust and can accurately and efficiently capture the crack propagation process. Moreover, a number of phenomena that are difficult to capture in discrete crack models, like crack branching, merging and nucleation are solved straightforwardly (Kuhn and Müller, 2010).

To date, phase-field has been successfully applied, e.g. to dynamic problems (Borden, 2012), cohesive fracture (Vignollet et al., 2014), ductile fracture (Miehe et al., 2016), functionally graded materials (Hirshikesh et al., 2019) and more. An extensive review of phase-field for fracture can be found in (Egger et al., 2019). More recently, phase-field has also been used for simulation of crack propagation in bones (Nguyen et al., 2017; Shen et al., 2019), which is of particular interest of this thesis. It is important to note that the presented phase-field formulation, is restricted to geometrically linear setting, similarly to the vast majority of literature which utilises phase-field for brittle fracture. Another reasoning behind this choice is the efficiency, since the additional nonlinearity could significantly increase the computation time. Moreover, as previously mentioned in Section 4.2.1, bone even of extreme athletes like racehorses experiences only small strains up to 0.002% (Davies and Merritt, 2004), which is within the range of applicability of small strain formulation. Extension to finite strain kinematics is straightforward if necessary, as presented e.g. in Clayton and Knap (2014).

5.2 Phase-field representation

Consider one-dimensional bar under tension with a discrete crack at $\mathbf{x} = 0$ as presented in Figure 5.1a). The underlying idea of phase-field is to approximate the discontinuity Γ with a scalar damage phase-field Γ_I representing the smooth crack (see Figure 5.1b)). The

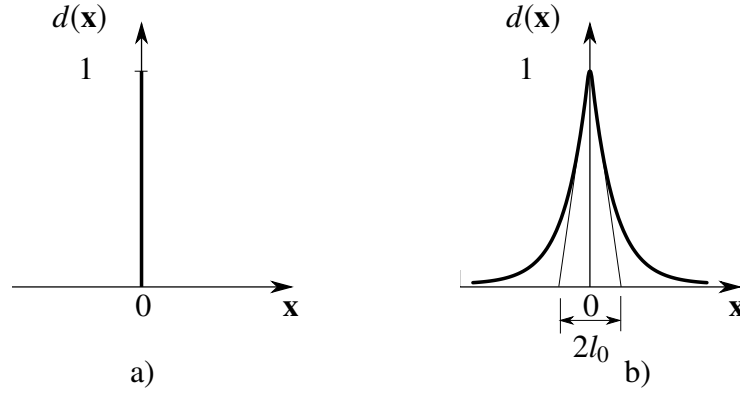


Figure 5.1: a) Schematic representation of a discrete crack with Dirac delta function and b) phase-field (smeared) representation of a crack with the length parameter l_0 .

approximated discrete crack Γ can be expressed as a smeared crack Γ_l with the exponential function as follows:

$$d(x) = \exp\left(-\frac{|\mathbf{x}|}{2l_0}\right) \quad (5.1)$$

The phase-field variable $d \in [0, 1]$ indicates damage in the material, where $d = 0$ characterises intact material and $d = 1$ means fully broken. Therefore, it has to satisfy the following boundary conditions:

$$d(0) = 1, \quad (5.2)$$

$$d(\pm\infty) = 0 \quad (5.3)$$

The first and the second derivatives of the phase-field function (5.1) with respect to x can be derived as follows:

$$\begin{aligned} \frac{dd}{d\mathbf{x}} &= -\frac{\text{sgn}(\mathbf{x})}{2l_0} \exp\left(-\frac{|\mathbf{x}|}{2l_0}\right), \\ \frac{d^2d}{d\mathbf{x}^2} &= -\frac{1}{4l_0^2}d \end{aligned} \quad (5.4)$$

With the above definitions, for $\mathbf{x} \neq 0$, it can be demonstrated that Equation 5.1 is the solution of the differential equation:

$$d - 4l_0^2 \frac{d^2d}{d\mathbf{x}^2} = 0 \quad (5.5)$$

Following (Miehe et al., 2010a), the discrete crack surface Γ can be expressed as the quadratic functional:

$$\Gamma = \int_{\Gamma} dA = \int_{\Omega} \underbrace{\frac{1}{4l_0} \left(d^2 + 4l_0^2 \left(\frac{dd}{d\mathbf{x}} \right)^2 \right)}_{\gamma_l} dV = \Gamma_l \quad (5.6)$$

The minimisation of this functional renders the phase-field smeared crack representation as given in Equation 5.1. The integrand of Equation 5.6 - γ_l can be interpreted as a crack surface density function. The extension to multi-dimensions renders the following expression:

$$\gamma_l = \frac{1}{4l_0} \left(d^2 + 4l_0^2 |\nabla d|^2 \right) \quad (5.7)$$

5.2.1 Continuum formulation

Let assume small strains, where elastic energy density is given by the Hooke's law for an isotropic linear elasticity, $\psi_{el}(\boldsymbol{\varepsilon}) = \frac{1}{2}\lambda \text{tr} \boldsymbol{\varepsilon}^2 + \mu \text{tr} [(\boldsymbol{\varepsilon})^2]$, where λ and μ are the Lamé constants. In the regime of small deformations, where the current spatial domain is indistinguishable from the reference material domain, the infinitesimal strain tensor has the following form:

$$\boldsymbol{\varepsilon} = \frac{1}{2} \left((\nabla \mathbf{u})^T + \nabla \mathbf{u} \right), \quad (5.8)$$

where \mathbf{u} denotes the displacement vector. The potential energy of the brittle fracture in the Griffith sense (Griffith, 1921) can be expressed in the following form:

$$\Psi^{\text{pot}} = \int_{\Omega} \psi^{el}(\boldsymbol{\varepsilon}) dV + \int_{\Gamma} g_c dA, \quad (5.9)$$

where ψ^{el} is the elastic strain energy density function and the fracture energy contribution is the critical energy release rate g_c . It is a well-known material parameter, which indicates the amount of energy necessary for unit advancement of the crack surface area. Using phase-field and previously presented surface energy density function γ_l in Equation 5.7 the fracture energy contribution can be expressed by:

$$\int_{\Gamma} g_c dA \approx \int_{\Omega} g_c \gamma_l dV \quad (5.10)$$

5.2.2 Strain energy density split

Next, it is assumed that the elastic energy can be additively decomposed into a damaged and intact part, $\psi_0 = \psi_0^+ + \psi_0^-$, so that the degradation function g only acts on the damaged part (Miehe et al., 2010b):

$$\psi^{el}(\boldsymbol{\varepsilon}, d) = g(d)\psi^+(\boldsymbol{\varepsilon}) + \psi^-(\boldsymbol{\varepsilon}) \quad (5.11)$$

This split is motivated by the fact that the tensile strain components contribute to the damage process that results in a fracture, while the compression strain components do not. Various forms of a split in the energy density have been investigated by Amor et al. (2009), for example, it has been demonstrated that volumetric-deviatoric split of the energy might be more suitable for a shear-type fracture. However, the most commonly used is a spectral decomposition of strain into positive (tension) and negative (compression) part. The strain tensor can be split as:

$$\boldsymbol{\varepsilon} = \mathbf{P}_v \boldsymbol{\Lambda} \mathbf{P}_v^{-1} \quad (5.12)$$

where \mathbf{P}_v consists of the orthonormal eigenvectors of $\boldsymbol{\varepsilon}$ and $\boldsymbol{\Lambda} = \text{diag}(\lambda_1, \lambda_2, \lambda_3)$ is a diagonal matrix of principal strains. Moving on, the positive and negative strains can be calculated as

follows:

$$\boldsymbol{\varepsilon}^+ = \mathbf{P}_v \boldsymbol{\Lambda}^+ \mathbf{P}_v^{-1} \quad (5.13)$$

$$\boldsymbol{\varepsilon}^- = \mathbf{P}_v \boldsymbol{\Lambda}^- \mathbf{P}_v^{-1} \quad (5.14)$$

where

$$\boldsymbol{\Lambda} = \text{diag}(\langle \lambda_1 \rangle, \langle \lambda_2 \rangle, \langle \lambda_3 \rangle) \quad (5.15)$$

$$\boldsymbol{\Lambda}^- = \boldsymbol{\Lambda} - \boldsymbol{\Lambda}^+ \quad (5.16)$$

and $\langle \cdot \rangle$ is the Macaulay bracket defined as:

$$\langle \mathbf{x} \rangle = \begin{cases} \mathbf{x} & \mathbf{x} > 0 \\ 0 & \mathbf{x} \leq 0 \end{cases} \quad (5.17)$$

With the above split defined, the tensile (damaged) ψ^+ and compressive (intact) ψ^- energy have the following forms:

$$\begin{aligned} \psi^+(\boldsymbol{\varepsilon}) &= \frac{1}{2} \lambda \langle \text{tr} \boldsymbol{\varepsilon} \rangle^2 + \mu \text{tr} \left[(\boldsymbol{\varepsilon}^+)^2 \right] \\ \psi^-(\boldsymbol{\varepsilon}) &= \frac{1}{2} \lambda (\text{tr} \boldsymbol{\varepsilon} - \langle \text{tr} \boldsymbol{\varepsilon} \rangle)^2 + \mu \text{tr} \left[(\boldsymbol{\varepsilon} - \boldsymbol{\varepsilon}^+)^2 \right] \end{aligned} \quad (5.18)$$

Note that in case of small strains, where $\boldsymbol{\varepsilon}$ is a symmetric matrix, the matrix of eigenvectors \mathbf{P}_v is orthogonal; hence its inverse can be simply computed as: $\mathbf{P}_v^{-1} = \mathbf{P}_v^T$.

5.2.3 Degradation function

Similarly to the damage mechanics concepts, in Equation 5.11 a degradation function $g(d)$ is introduced, which must satisfy the following conditions:

$$g(0) = 1, \quad g(1) = 0, \quad g(d) > 0 \text{ for } d \neq 0, \quad g'(0) = 0, \quad g'(1) > 0 \quad (5.19)$$

These requirements are implied to provide damage propagation and set the upper constraint of the phase-field $d = 1$. A simple quadratic degradation function that meets the restrictions has the form:

$$g(d) = (1 - d)^2 \quad (5.20)$$

Such form of the function $g(d)$ is the most widely used in the literature. However, many different formulas can be utilised (Kuhn et al., 2015). Borden (Borden, 2012) proposed a cubic function:

$$g(d) = s((1 - d)^3 - (1 - d)^2) + 3(1 - d)^2 - 2(1 - d)^3 \quad (5.21)$$

where $s > 0$ determines the slope of g at $d = 1$. Implications of choosing either of those functions have been investigated in (Borst et al., 2015; Vignollet et al., 2014). Essentially, using the cubic function can reduce the accumulation of strain elastic energy before reaching critical strain; it is an issue that can be observed with classical 2nd order functions. The additional parameter s can significantly alter material behaviour, and it has to be carefully calibrated.

5.2.4 Strong form

Finally, the potential Ψ_l^{pot} can be derived by substituting Equations 5.10, 5.11, 5.20, 5.7 into potential energy (Eq. 5.9) renders the diffused form of the potential energy for brittle fracture:

$$\Psi_l^{\text{pot}} = \int_{\Omega} g(d)\psi^+ + \psi^- + g_c \left[\frac{d^2}{4l_0} + l_0 |\nabla d|^2 \right] dV \quad (5.22)$$

In the equilibrium state of the above potential Ψ_{pot}^l must be a minimum, which leads to the following strong form:

$$\begin{aligned} \nabla \cdot \boldsymbol{\sigma}(\boldsymbol{\varepsilon}, d) &= 0 \quad \mathbf{x} \in \Omega \\ \boldsymbol{\sigma} \mathbf{n} &= \bar{\mathbf{t}} \quad \mathbf{x} \in \Gamma_t \\ \mathbf{u} &= \bar{\mathbf{u}} \quad \mathbf{x} \in \Gamma_u \\ g_c \left(\frac{d}{2l_0^2} - 2\Delta d \right) &= \frac{dg}{dd} \mathcal{H} \quad \mathbf{x} \in \Omega \\ \nabla d \cdot \mathbf{n} &= 0 \quad \mathbf{x} \in \Gamma \end{aligned} \quad (5.23)$$

where the history parameter:

$$\mathcal{H}(t) = \max_t \psi^+(t) \quad (5.24)$$

ensures irreversibility such that cracks can only grow (Miehe et al., 2010b). Alternatively, it can also be imposed by setting $d = 0$ when d becomes close to zero as reported by (Bourdin et al., 2008) or by a penalty term to the phase-field equation as described in (Miehe et al., 2010a). Further, in the strong form (5.23) $\bar{\mathbf{t}}$ and $\bar{\mathbf{u}}$ are the boundary tractions and displacements, respectively, such that $\Gamma_t \cup \Gamma_u = \Gamma$ and $\Gamma_t \cap \Gamma_u = \emptyset$. The Cauchy stress can be expressed as follows:

$$\begin{aligned} \boldsymbol{\sigma}(\boldsymbol{\varepsilon}, d) &= g(d) \frac{\partial \psi^+}{\partial \boldsymbol{\varepsilon}} + \frac{\partial \psi^-}{\partial \boldsymbol{\varepsilon}} \\ \boldsymbol{\sigma}(\boldsymbol{\varepsilon}, d) &= g(d) [\lambda \langle \text{tr} \boldsymbol{\varepsilon} \rangle \mathbb{I} + 2\mu \boldsymbol{\varepsilon}^+] + \lambda \langle -\text{tr} \boldsymbol{\varepsilon} \rangle \mathbb{I} + 2\mu \boldsymbol{\varepsilon}^-, \end{aligned} \quad (5.25)$$

where \mathbb{I} is an identity matrix.

5.2.5 Weak form

The weak form is derived by the standard Galerkin method. Approximation of the field variables and their derivatives are the following:

$$\begin{cases} \mathbf{u}(\mathbf{x}) = \mathbf{N}_u(\mathbf{x})\mathbf{u}^h \\ d(\mathbf{x}) = \mathbf{N}_d(\mathbf{x})d^h \end{cases} \quad \begin{cases} \boldsymbol{\varepsilon}(\mathbf{x}) = \mathbf{B}_u(\mathbf{x})\mathbf{u}^h \\ \frac{\partial d(\mathbf{x})}{\partial \mathbf{x}} = \mathbf{B}_d(\mathbf{x})d^h \end{cases} \quad (5.26)$$

The resulting set of nonlinear equations is subsequently linearised and solved simultaneously using a Newton-Raphson iterative scheme. At each iteration i the following linear system of equations is solved:

$$\begin{bmatrix} \mathbf{K}^{dd} & \mathbf{K}^{du} \\ \mathbf{K}^{ud} & \mathbf{K}^{uu} \end{bmatrix}_i \begin{bmatrix} \delta d \\ \delta \mathbf{u} \end{bmatrix}_{i+1} = \begin{bmatrix} -\mathbf{f}_d^{\text{int}} \\ \mathbf{f}^{\text{ext}} - \mathbf{f}_u^{\text{int}} \end{bmatrix}_i \quad (5.27)$$

with

$$\begin{aligned} \mathbf{f}_d^{\text{int}} &= \int_{\Omega} \left[g_c \left(\frac{1}{2l_0} \mathbf{N}_d^T \mathbf{N}_d + 2l_0 \mathbf{B}_d^T \mathbf{B}_d \right) d + \frac{dg}{dd} \mathcal{H} \mathbf{N}_d^T \right] dV \\ \mathbf{f}_u^{\text{int}} &= \int_{\Omega} \mathbf{B}_u^T \frac{\partial \boldsymbol{\sigma}}{\partial \boldsymbol{\varepsilon}} \mathbf{B}_u \mathbf{u} dV = \int_{\Omega} \mathbf{B}_u^T \boldsymbol{\sigma} dV \end{aligned} \quad (5.28)$$

$$\begin{aligned} \mathbf{K}^{dd} &= \int_{\Omega} g_c \left(\frac{1}{2l_0} \mathbf{N}_d^T \mathbf{N}_d + \mathbf{B}_d^T \mathbf{B}_d \right) + \frac{d^2g}{dd^2} \mathcal{H} \mathbf{N}_d^T dV \\ \mathbf{K}^{du} &= \int_{\Omega} \frac{dg}{dd} \mathbf{N}_d \frac{\partial \mathcal{H}}{\partial \boldsymbol{\varepsilon}} \mathbf{B}_u dV \\ \mathbf{K}^{uu} &= \int_{\Omega} \mathbf{B}_u^T \frac{\partial \boldsymbol{\sigma}}{\partial \boldsymbol{\varepsilon}} \mathbf{B}_u dV \\ \mathbf{K}^{ud} &= \int_{\Omega} \mathbf{B}_u^T \frac{\partial \boldsymbol{\sigma}}{\partial d} \mathbf{N}_d dV \end{aligned} \quad (5.29)$$

where

$$\begin{aligned} \frac{\partial \boldsymbol{\sigma}}{\partial d} &= \frac{dg}{dd} (\lambda \langle \text{tr} \boldsymbol{\varepsilon} \rangle \mathbb{I} + 2\mu \boldsymbol{\varepsilon}^+) \\ \frac{\partial \mathcal{H}}{\partial \boldsymbol{\varepsilon}} &= \begin{cases} \lambda \langle \text{tr} \boldsymbol{\varepsilon} \rangle \mathbb{I} + 2\mu \boldsymbol{\varepsilon}^+ & \mathcal{H} \geq \psi^+(t) \\ 0 & \mathcal{H} < \psi^+(t) \end{cases} \end{aligned} \quad (5.30)$$

Partial derivative $\partial \boldsymbol{\sigma} / \partial \boldsymbol{\varepsilon}$ represents the fourth-order elasticity tensor, which can be expressed as follows:

$$\frac{\partial \boldsymbol{\sigma}}{\partial \boldsymbol{\varepsilon}} = \lambda [g(d)H(\text{tr} \boldsymbol{\varepsilon}) - H(-\text{tr} \boldsymbol{\varepsilon})] \mathbb{I} \otimes \mathbb{I} + 2\mu (g(d) - 1) \mathbb{P}^+ + \mu (\mathbb{III} + \mathbb{III}^s), \quad (5.31)$$

where $H(\cdot)$ is a Heaviside function, \mathbb{III} and \mathbb{III}^s are fourth-order unit tensors such that, for an arbitrary second-order tensor \mathbf{A} :

$$\begin{aligned} \mathbb{III} : \mathbf{A} &= \mathbf{A} \\ \mathbb{III}^s : \mathbf{A} &= \mathbf{A}^{\text{sym}} \end{aligned} \quad (5.32)$$

Furthermore, \mathbb{P}^+ is a projection tensor that has the following property:

$$\mathbb{P}^+ : \boldsymbol{\varepsilon} = \boldsymbol{\varepsilon}^+ \quad (5.33)$$

The computation of such tensors is far from trivial, and it is elaborated further in Section 5.2.6. The monolithic solution scheme is chosen since unlike the staggered scheme, it is insensitive to the size of load increments and therefore, can be significantly faster (Vignollet et al., 2014). It is worth to note that the resulting regularised free energy functional (Eq. 5.6) is non-convex with respect to simultaneously the displacement and the phase-field. Therefore, the monolithic scheme might be very unstable at the crack initiation. The phenomenon of crack length function being discontinuous in time is often referred as *brutal crack* propagation (Bourdin, 2007). A few different approaches have been proposed to approach the problem of non-convexity (Gerasimov and De Lorenzis, 2016; Wick, 2017). However, this is not within the scope of this study.

Moving on, with consistent tangent stiffness matrix as presented in Equation 5.27 monolithic scheme attains quadratic convergence rate of Newton iterations. Nevertheless, the Newton-Raphson method is insufficient after a limit point is reached, e.g. snap-back or unstable behaviour. For such complex cases, the arc-length method can be used, as proposed, e.g. in (May et al., 2016).

5.2.6 Derivation of projection tensors

This section described three different methods for obtaining the projection tensor introduced in tangent stiffness matrix for phase-field (Equation 5.31). The projection tensor \mathbb{P}^+ from Equation 5.33 can be calculated with matrix differentiation as follows:

$$\mathbb{P}^+ = \frac{\partial \boldsymbol{\varepsilon}^+(\boldsymbol{\varepsilon})}{\partial \boldsymbol{\varepsilon}}. \quad (5.34)$$

However, as it was presented in Equation 5.13, the positive strain tensor is obtained through spectral decomposition, which is difficult to differentiate. Theoretically, it is possible to compute the roots of characteristic polynomial $\det(\boldsymbol{\varepsilon} - \lambda \mathbb{I}) = 0$. However, in practice, the algorithms for calculating the roots of cubic polynomials are known to be numerically inefficient and prone to truncation errors (Eberly, 2014). Typically, eigenvalues and eigenvectors for matrices larger than 2x2 are found with iterative algorithms. Therefore, the automatic differentiation technique with ADOL-C library presented in Section 4.2.9 also cannot be applied. Ultimately, for the non-trivial task of computing tensor \mathbb{P}^+ , three different methods have been chosen:

- Centered Finite Difference method

- Complex-variable method (complex-step)
- The algorithm for the partial derivatives of the eigenvectors with respect to the strain tensor proposed by (Miehe, 1998).

Centered Finite Difference

One of the simplest methods for calculating derivatives of mathematical functions $f(x)$ is the finite difference method (FDM). This two-point formula computes the slope of a nearby secant line. As the small perturbation h approaches zero, the secant approaches the tangent line. To increase the accuracy for small values of h the secant line is calculated at points $(x + h, f(x + h))$ and $(x - h, f(x - h))$, which also known as Centered Finite Difference method. The approximation of the derivative of the positive small strain tensor $\boldsymbol{\varepsilon}^+$ can be derived as follows:

$$\mathbb{P}_{ijkl} = \frac{\partial \boldsymbol{\varepsilon}_{ij}^+}{\partial \boldsymbol{\varepsilon}_{kl}} \approx \frac{\boldsymbol{\varepsilon}_{ij}^+(\boldsymbol{\varepsilon} + h \mathbf{e}_k \otimes \mathbf{e}_l) - \boldsymbol{\varepsilon}_{ij}^+(\boldsymbol{\varepsilon} - h \mathbf{e}_k \otimes \mathbf{e}_l)}{2h} \quad (5.35)$$

Note that, for legibility, Leibniz's notation has been replaced with index notation. \mathbf{e} is the basis vector, and the tensor product $\mathbf{e}_k \otimes \mathbf{e}_l$ results in a tensor which has the (k, l) element equal to unity. An h parameter is usually a small number around 10^{-8} . The Finite Difference method is very general and simple to implement. However, in numerical calculations constrained by machine precision, Finite difference method turns out to be very sensitive to the value of h . Due to truncation errors, the accuracy of the calculated slopes deteriorates very quickly (See Table 5.1). This issue can be resolved by using the complex variables (Squire and Trapp, 1998).

Complex-variable method

In contrast to the previous method, a small perturbation h is replaced with a complex number ih ($i = \sqrt{-1}$). This alternative of Finite Difference method is often called Complex Step Differentiation. Similarly to Equation 5.35 the approximate derivative has the form:

$$\mathbb{P}_{ijkl} = \frac{\partial \boldsymbol{\varepsilon}_{ij}^+}{\partial \boldsymbol{\varepsilon}_{kl}} \approx \frac{Im(\boldsymbol{\varepsilon}_{ij}^+(\boldsymbol{\varepsilon} + ih \mathbf{e}_k \otimes \mathbf{e}_l))}{h} \quad (5.36)$$

where $Im(\cdot)$ represents the imaginary part. The formula in Equation 5.36 above is almost as simple to implement as finite difference and does not suffer from truncation errors.

Following (Squire and Trapp, 1998), to further prove the advantage of using complex number, lets consider simple scalar valued function $f(x) = x^{9/2}$ at $x_0 = 1.5$ and compute its derivatives using both methods presented previously. Table 5.1 below shows the absolute errors for different values of h , ranging from 0.1 to 10^{-19} . As shown in Table 5.1, Finite Difference

h	Finite Difference (Eq. 5.35)	Complex Step (Eq. 5.36)
1.00e-01	2.293689646259029e+00	1.205407314009328e-01
1.00e-02	2.182181061612667e-01	1.205606223422251e-03
1.00e-03	2.171300728445757e-02	1.205608212728748e-05
1.00e-04	2.170215376157358e-03	1.205608270993253e-07
1.00e-05	2.170107647749830e-04	1.205606281473592e-09
1.00e-06	2.169935328311112e-05	1.205435751217010e-11
1.00e-07	2.180744331781170e-06	1.207922650792170e-13
1.00e-08	6.687969289487228e-08	0.000000000000000e+00
1.00e-09	1.487965164415073e-06	3.552713678800501e-15
1.00e-10	2.952926937638267e-06	0.000000000000000e+00
1.00e-11	4.736184791909182e-05	3.552713678800501e-15
1.00e-12	1.196087939661084e-03	3.552713678800501e-15
1.00e-13	2.012019413314192e-02	7.105427357601002e-15
1.00e-14	3.788376252714443e-02	3.552713678800501e-15
1.00e-15	1.827290918843122e+00	3.552713678800501e-15
1.00e-16	1.860081273425976e+01	0.000000000000000e+00
1.00e-17	1.860081273425976e+01	3.552713678800501e-15
1.00e-18	1.860081273425976e+01	3.552713678800501e-15
1.00e-19	1.860081273425976e+01	7.105427357601002e-15

Table 5.1: Absolute error of calculated derivative for $f(x) = x^{9/2}$ for different values of h using Finite Difference Method and Complex Step.

method reaches the minimum error of $\sim 6.688 \cdot 10^{-8}$ half way through the sequence of h and then the accuracy starts to deteriorate. Complex Step, on the other hand, shows much lower error for smaller values of h and establishes full double precision accuracy for any $h < 10^{-8}$. This confirms that complex step method is accurate even for small values of h whereas the Finite Difference never achieves full accuracy.

Analytical algorithm for fourth-order isotropic tensor

Miehe (1998) presented an algorithm for the computation of fourth-order isotropic tensor functions. The functions that take arguments in the spectral form of symmetric second-order tensors represent a certain class of functions. The derivatives of these functions can be calculated by exploiting the knowledge of the eigenvectors; in particular the spin of the orthonormal base. The formula proposed by Miehe applied for the calculation of the fourth-order projection tensor \mathbb{P} can be expressed as:

$$\begin{aligned}
P_{ijkl}^+ &= \sum_{a=1}^3 \sum_{b=1}^3 H(\lambda_a) \delta_{ab} \mathbf{n}_{ai} \mathbf{n}_{aj} \mathbf{n}_{bk} \mathbf{n}_{bl} \\
&+ \sum_{a=1}^3 \sum_{b \neq a}^3 \frac{1}{2} \frac{\langle \lambda_a \rangle - \langle \lambda_b \rangle}{\lambda_a - \lambda_b} \mathbf{n}_{ai} \mathbf{n}_{bj} (\mathbf{n}_{ak} \mathbf{n}_{bl} + \mathbf{n}_{bk} \mathbf{n}_{al}),
\end{aligned} \tag{5.37}$$

where λ_a is the eigenvalue and \mathbf{n}_{ai} is the corresponding i -th component of the eigenvector \mathbf{n}_a , δ_{ab} is the Kronecker symbol. In order to avoid splitting the formula in Equation 5.37 into several cases for equal or nearly equal eigenvalues, the following perturbation is applied (Miehe, 1993).

$$\begin{cases} \lambda_1 = \lambda_1(1 + h) & \text{if } \lambda_1 = \lambda_2 \\ \lambda_3 = \lambda_3(1 - h) & \text{if } \lambda_2 = \lambda_3 \end{cases} \quad (5.38)$$

where h is a small number 10^{-8} . Thanks to this perturbation, the formula holds for all the cases of eigenvalues without the need for conditional statements.

5.2.7 Comparison of the methods

In this section, the previously proposed methods for computing the tangent stiffness matrix (see Section 5.2.6) are compared for their computational efficiency. A small phase-field test problem consisting of 949 degrees of freedom (DOFs) is considered. The first five loading steps are calculated. The runtime of the analyses is presented on the bar plot in Figure 5.2, with distinction to the time spent on matrix assembly and the linear solver. Unsurprisingly,

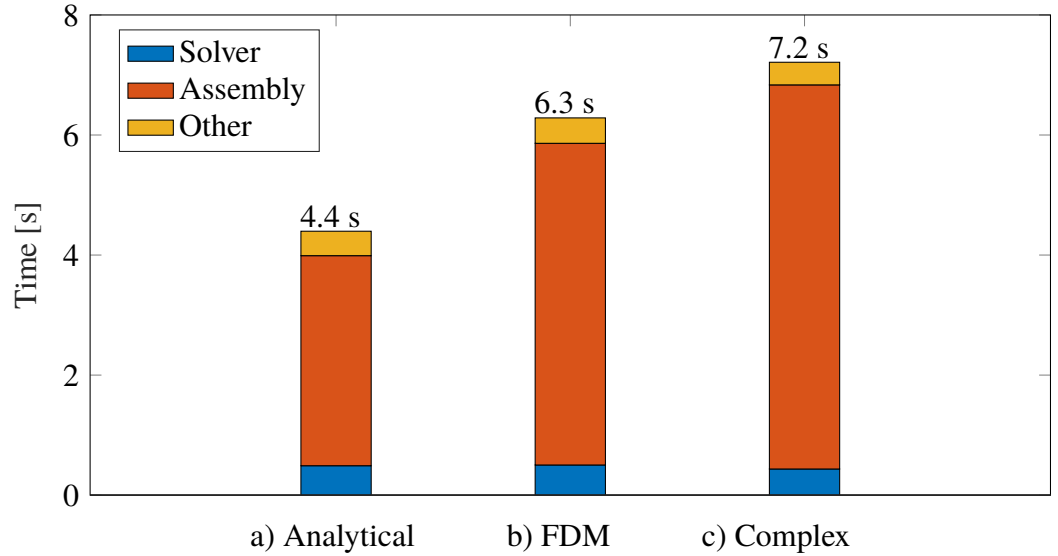


Figure 5.2: Runtime for a test problem with tangent matrix calculated using three formulas: a) Analytical, b) Finite Difference Method and c) Complex Step.

the complex step method is the slowest approach since complex multiplication quadruples the number of floating-point operations. Additionally, the perturbed matrix $\boldsymbol{\varepsilon}_{ij}^+(\boldsymbol{\varepsilon} + i h \mathbf{e}_k \otimes \mathbf{e}_l)$ is no longer real; thus it requires the computation of the inverse of the Hermitian matrix \mathbf{P}_v for eigendecomposition (see Equation 5.13). However, Complex Step method is only slightly slower than Finite Difference with the additional advantage of being more accurate and insensitive to small values of perturbation h . It is also worth to note that all the methods have enough accuracy to attain quadratic convergence for the Newton method.

In conclusion, the analytical formula found in the literature is the most efficient method for the calculation of the tangent stiffness matrix for phase-field. However, it was also shown that Complex Step method is a robust option for this task and most importantly it can be applied to a broad number of different constitutive equations without the advanced knowledge of the mathematical properties of the functions used therein.

5.3 Arc-length control

Newton's method cannot accurately predict the solution after a limit point is reached. Neither the force control nor displacement control is able to capture highly nonlinear equilibrium path as presented in Figure 5.3. If such snap-back or snap-through behaviour is to be expected, an alternative method should be used instead. Multiple different approaches have been proposed

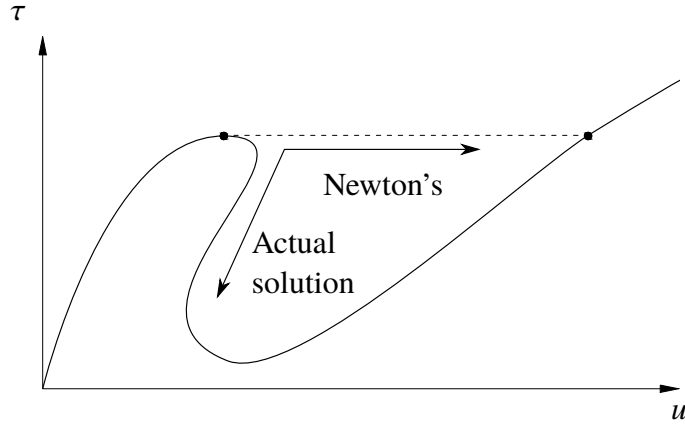


Figure 5.3: Newton's method limitation on an example of snap-back and snap-through behaviour.

in the past for tracing the equilibrium path in nonlinear problems. The most established method is the arc-length control approach, initially proposed by Riks (1979) and further improved by Crisfield (1982). Arc-length control provides an additional degree of freedom τ into the system (Equation 5.27), which is used as a multiplier on the external load vector $\mathbf{f}^{\text{ext}} = \tau \hat{\mathbf{f}}$. Additionally, the arc-length function $\phi^D = \phi^D(u, \tau)$ constraints the increments of load factor τ and displacements \mathbf{u} such that the load path can be traced. In general case, the complete set of equations that have to satisfy the equilibrium which can be written as:

$$\begin{bmatrix} \mathbf{f}^{\text{int}} - \tau \hat{\mathbf{f}} \\ \phi(\mathbf{u}, \tau) \end{bmatrix} = \begin{bmatrix} 0 \\ 0 \end{bmatrix} \quad (5.39)$$

The resulting new tangent stiffness matrix has the following form:

$$\begin{bmatrix} \mathbf{K}_T & -\hat{\mathbf{f}} \\ \frac{\partial \phi(\mathbf{u}, \tau)}{\partial \mathbf{u}} & \frac{\partial \phi(\mathbf{u}, \tau)}{\partial \tau} \end{bmatrix} \quad (5.40)$$

which consists of \mathbf{K}_T - the stiffness matrix, e.g. from Equation 5.27, $\hat{\mathbf{f}}$ - the load vector and the derivatives of arc length function (bottom row) with respect to displacement and load factor. The function ϕ in arc-length methods have to be related to a monotonically increasing quantity of the solid (Gutiérrez, 2004). For quasi-brittle materials that quantity can be energy release. In the absence of any healing effects, the failure always evolves at a positive rate. However, at the beginning of the loading or in case of solids which exhibit numerous snap-through points, the evolution of the failure can be very slow. In these cases, the controlled dissipation rate would have to be constantly adjusted in order to accurately follow the equilibrium path. In the recent publication by May et al. (2016), a new arc-length control method based on both rate of the internal and the dissipated energy has been introduced. The proposed therein approach requires only two parameters to automatically and precisely trace the equilibrium path by switching between dissipative and non-dissipative arc-length controls. The derivation of the approach can be found in Appendix C.

5.4 Benchmark problems

In order to verify the implementation of a phase-field model for brittle fracture, the results of several benchmark problems are investigated. The following factors are explored: p-convergence, length scale parameter l_0 and type of degradation function $g(d)$.

5.4.1 One-dimensional bar

Consider the one-dimensional unit length (1m) bar as depicted in Figure 5.4. The bar is fixed on one end and on the opposite end, pressure $\tau\hat{\mathbf{f}}$ is applied, where $\hat{\mathbf{f}} = 1$ Pa and τ is the arc-length multiplier.

The geometry is discretised with 24 linear tetrahedral elements which results in 57 degrees of freedom. Note that for this problem, the solution is homogeneous; therefore, it is considered to be one-dimensional. The material parameters are $E = 1$ Pa for the Young's modulus, Poisson's ratio $\nu = 0$, Griffith's energy $g_c = 1$ N/m, length scale parameter $l_0 = 0.25$ m. The parameters for the arc-length control are the following: initial load step $\Delta\tau_1^F = 0.15$ and ratio $a = 0.8$. The resulting load-displacement curve is presented in Figure 5.4. The phase-field and strain field are both uniform along the bar; therefore the analytical solution for stress can be computed straightforwardly with the given formula (Wu et al., 2018):

$$\boldsymbol{\sigma} = \left(\frac{g_c}{g_c + l_0 E \boldsymbol{\varepsilon}^2} \right)^2 E \boldsymbol{\varepsilon} \quad (5.41)$$

It can be noticed that the curve obtained with the finite element method perfectly matches

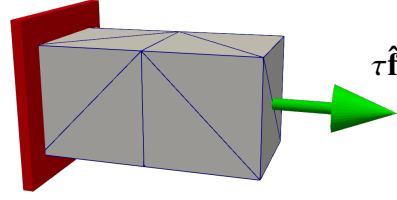


Figure 5.4: Bar subjected to tensile load $\tau \hat{\mathbf{f}}$.

with the analytical solution (see Eq. 5.41). This specific one-dimensional case is insensitive to order of approximation or the size of the element. However, it is important to note that such uniform solution for phase-field is only stable until stress is lower than critical stress $\sigma \leq \sigma_c$ (ascending part of the curve) (Pham et al., 2011).

5.4.2 Notched plate

In the next benchmark example, a square plate of unit length with a notch in the middle, as presented in Figure 5.6 is subjected to shear force. This is one of the most commonly used tests for phase-field fracture propagation, it has been analysed for example in (Vignollet et al., 2014; Miehe et al., 2010a; Borden, 2012; Wu, 2017; Liu et al., 2016). The material parameters are: $E = 210$ MPa, $\nu = 0.3$ and $g_c = 2.7 \cdot 10^{-3}$ N/mm. The top surface is loaded with uniform shear pressure $f = 1$ MPa and the bottom edge is fixed. Additionally, the top surface and the initial notch have constrained vertical displacements. To keep relatively small number of finite elements, the thickness of the plate was chosen to be 0.025 mm. The plain strain is enforced by constraining the displacements in the z -direction. In order to accurately capture the crack pattern, the mesh is refined where the crack is expected to propagate. The discretisation presented in Figure 5.7 using 17188 tetrahedral elements (16481 DOFs), results in an effective element size of $h \approx 0.012$ mm. Therefore, following (Borst et al., 2015) the length scale parameter is chosen to be $l_0 = 0.025$ mm, unless otherwise stated. The initial step size $\Delta\tau_1^F = 0.1$ N and the ratio a which controls switch for the arc-length $a = 1$. Figure 5.8 demonstrates the crack pattern attained using linear elements and length scale parameter $l_0 = 0.025$ mm. It is clear that the model is capable of tracking non-planar crack paths. The resulting load-displacement curve is depicted in Figure 5.9. Linear tetrahedral elements are well-known to suffer from shear locking (Zienkiewicz et al., 2000). Therefore, the results for 2nd-order elements are also presented for comparison. It can be noticed that linear elements exhibit only slightly higher stiffness until the post-failure region where it starts to differ noticeably. This can be explained by the fact that the used mesh refinement does not perfectly capture the crack path at the end of crack propagation, as can be observed from Figure 5.7 in comparison with Figure 5.8. In future developments, with adaptive mesh refinement, the

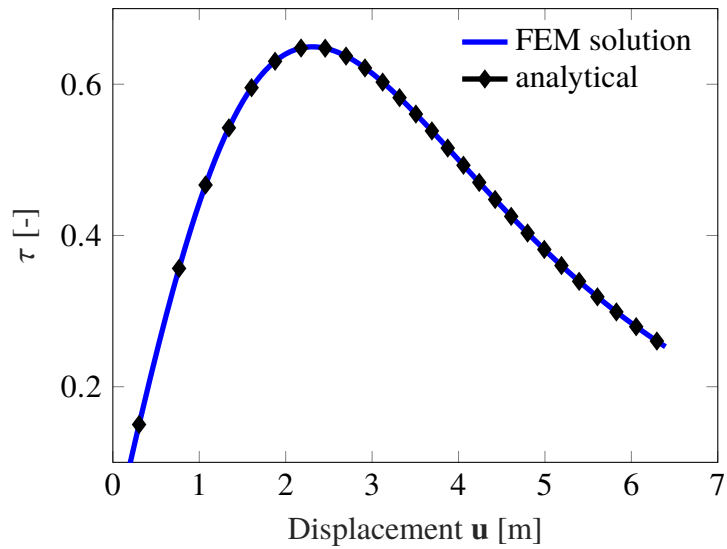


Figure 5.5: Load - displacement curve for the one-dimensional bar under tension with the comparison to the analytical solution.

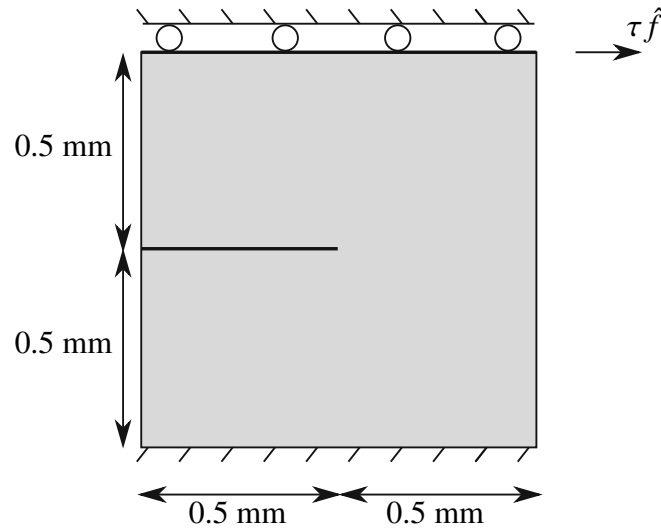


Figure 5.6: Geometry and boundary conditions for the notched plate shear test.

difference should be less apparent. Overall, the results with linear elements have satisfactory accuracy, and they are often the first choice due to their lower computational cost. Since, in this case, the considered plate is three-dimensional, unlike in the most examples in the literature, the results can be only compared qualitatively. Nevertheless, the outcomes are in good agreement with the results presented, e.g. in Miehe et al. (2010a).

In the following example, the influence of the length scale parameter l_0 is investigated. The same mesh as in Figure 5.7 is analysed with 3 different length scales: 0.05, 0.025 and 0.015 mm. From the load-displacements curves in Figure 5.11 it can be observed that decreasing length scale, results in increased critical force. Furthermore, results in Figure 5.10 shows that as expected for the smallest length scale parameter $l_0 = 0.015$ mm the sharpest crack pattern is attained. Clearly, in phase-field length scale l_0 does not only function as a regularising parameter but also influences the material properties like critical stress.

Several researchers, e.g. Hirshikesh et al. (2019) proposed to choose the length scale

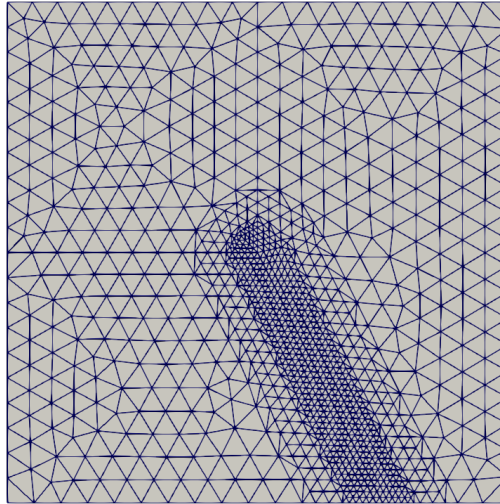


Figure 5.7: Finite element mesh consisting of 17188 tetrahedral elements, refined in the vicinity of the expected crack.

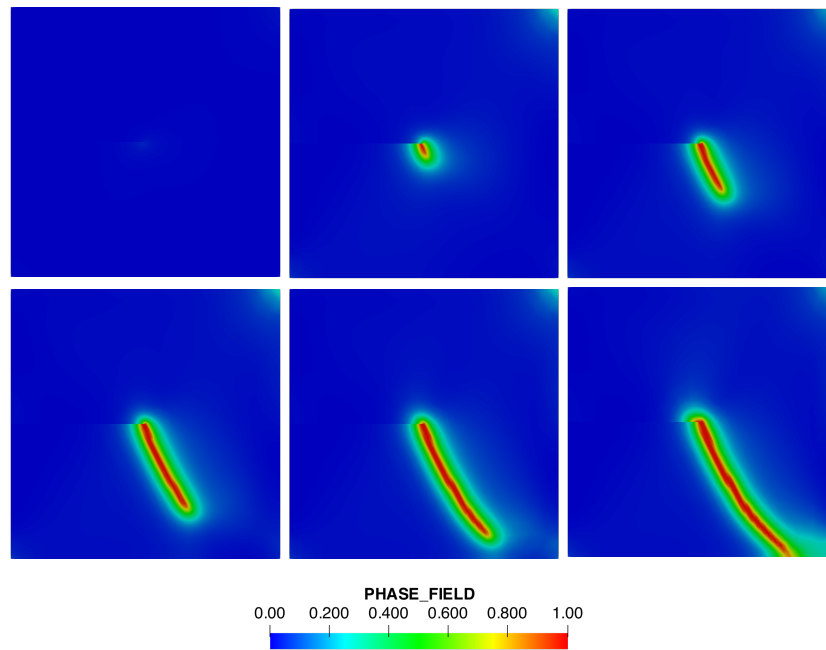


Figure 5.8: Phase-field contour plot represents crack patterns for the length scale $l_0 = 0.025$ mm.

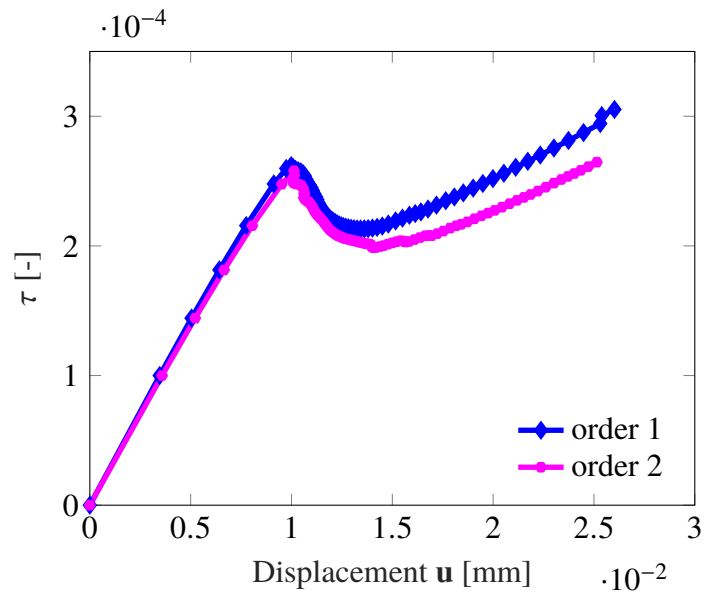


Figure 5.9: Load - displacement curve notched for plate example. Note that the displacement is measured in the top right corner of the plate.

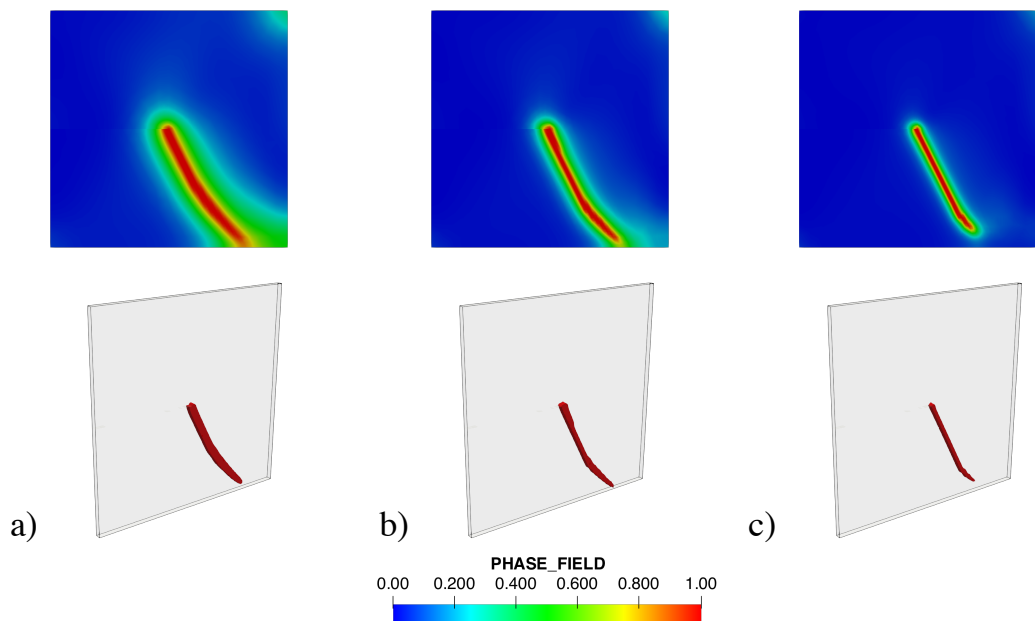


Figure 5.10: Influence of the length scale parameter for $l_0 = 0.05$ mm a), $l_0 = 0.025$ mm b), $l_0 = 0.015$ mm c). Iso-volumes below shows the phase-field variable $0.9 \leq d \leq 1$.

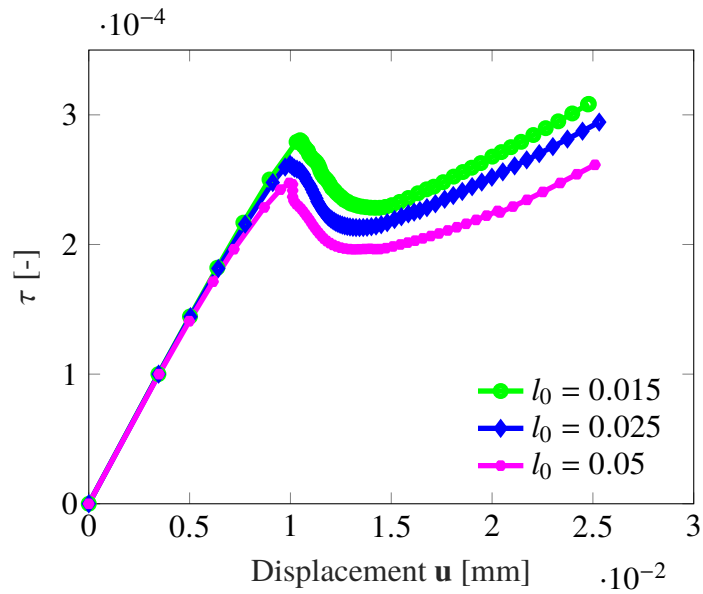


Figure 5.11: Influence of the length scale parameter l_0 on the load-displacement curve for constant mesh size.

parameter based on known critical stress σ_f parameter for brittle materials. In that approach, l_0 is obtained from homogeneous solution for a one-dimensional quasi-static problem. Computations with l_0 adjusted in such way reveal a good agreement with experiments as presented in Martínez-Pañeda et al. (2018).

Next example considers cubic degradation function as presented in Equation 5.21. From Figures 5.9 and 5.11, it can be found that the phase-field model using standard quadratic function exhibits slight softening behaviour before the failure. Such nonlinearity contradicts with linear elastic behaviour in brittle materials that phase-field intends to simulate. The source of such phenomenon is the damage that occurs not only in the expected localisation zones but in the entire domain. It is particularly apparent in Figures 5.8 and 5.10 at the top right corner of the plate where additional phase-field develops. One of the methods to mitigate that issue is to use cubic degradation function as proposed in Borden (2012). The disadvantage of this approach is that additional parameter s is introduced. Vignollet et al. (2014) demonstrated that for $s = 10^{-2}$ solution close to linear can be recovered. The results with quadratic and the cubic degradation functions for the notched plate are compared in Figure 5.13. Note that, since in the case of cubic degradation function much less dissipation is introduced, the ratio a parameter that governs the switch between arc-length controls had to be reduced to $a = 0.1$.

It can be observed that the cubic degradation function results in a more linear behaviour up to the peak force. Moreover, the snap-back behaviour is more apparent. The critical force attains higher value which can be particularly beneficial if the length scale l_0 is adjusted according to the critical stress σ_f . Using cubic degradation function would result in choosing larger l_0 , and therefore, a much coarser mesh is then necessary to accurately approximate the critical load as proposed in Miehe et al. (2010b). Furthermore, from the contour plots in Figure 5.12 it is clear that the phase-field is much less smeared, and unlike in quadratic function, additional

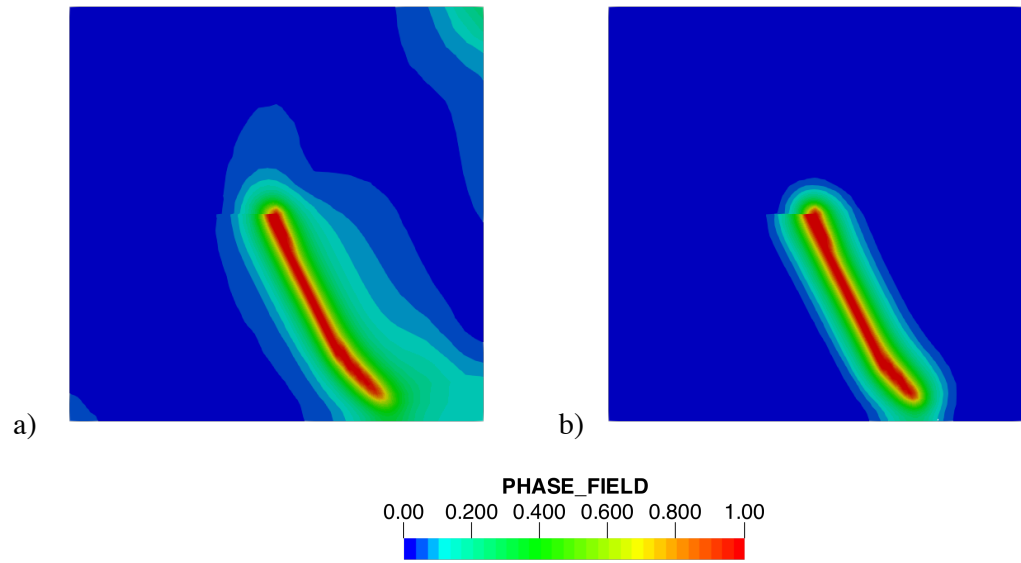


Figure 5.12: Comparison of the quadratic a) and cubic b) degradation functions on phase-field contours. Note that the scale on both contours is shifted to better visualise spurious damage in the entire domain with quadratic function a).

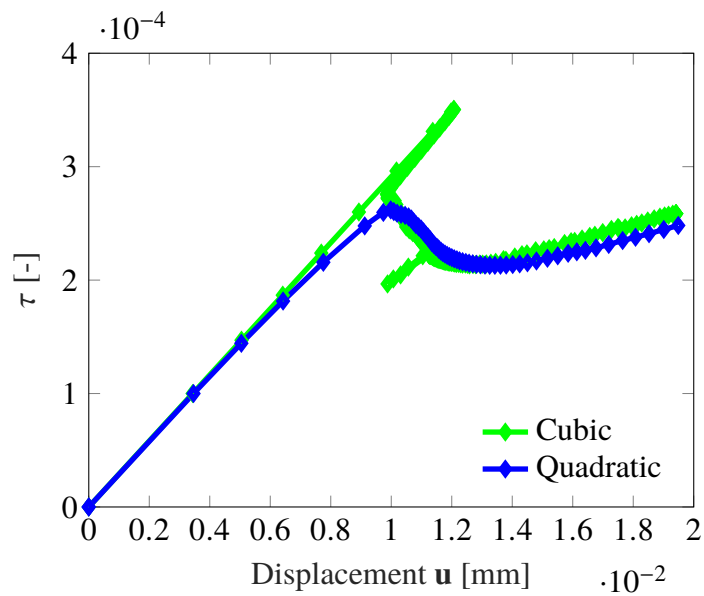


Figure 5.13: Load-displacement curves for the quadratic and cubic degradation functions. In Equation 5.21 parameter $s = 10^{-2}$.

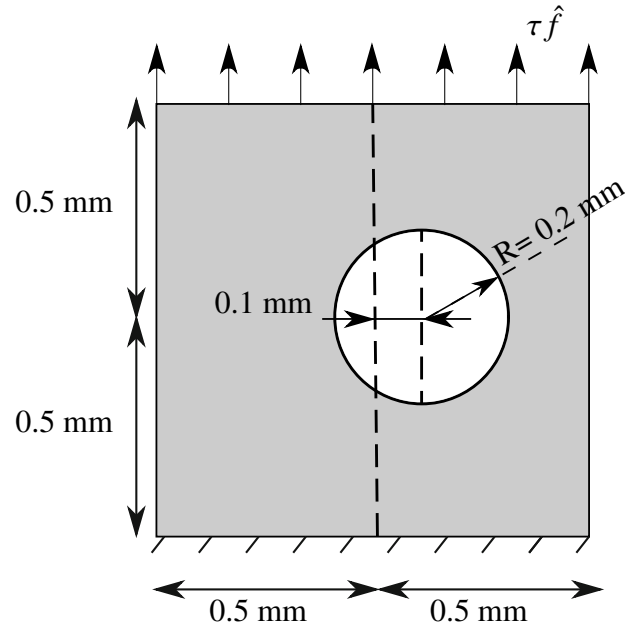


Figure 5.14: Geometry and boundary conditions for plate with hole example.

spurious localisation at the top right corner does not occur. A more in-depth investigation about degradation functions in phase-field models can be found in (Kuhn et al., 2015).

5.4.3 Plate with an eccentric hole

In this subsection, a numerical example is considered, which features multiple snap-back and snap-throughs to demonstrate the full capabilities of the implemented arc-length control algorithm. The geometry of the problem is inspired by the example presented in Lorentz and Badel (2004). The boundary conditions are shown in Figure 5.14. The mesh consists of 22,305 linear tetrahedral elements, refined in the expected crack propagation zone and the effective element size $h \approx 0.012\text{mm}$. Similarly, to the notched plate in the previous section, the geometry is extruded in the 3rd dimension to 0.025 mm. The plane strain is assumed. The material parameters are: $E = 210\text{ MPa}$, $\nu = 0.3$, $g_c = 2.7 \cdot 10^{-3}\text{ N/mm}$ and the length scale $l_0 = 0.025\text{ mm}$. Parameters for the arc-length are $\Delta\tau_1^F = 0.15\text{ N}$ and ratio $a = 0.25$. The evolution of the phase-field variable d is demonstrated in Figure 5.15. Figure 5.16 shows the τ load factor versus the displacement magnitude of the point taken from the upper middle of the plate. The circular markers correspond to the snapshots presented in Figure 5.16. The crack initiates from the left end of the narrower side of the plate and subsequently propagates to the free surface on the right side. After that, the structure starts another failure mode in which the left-hand side of the hole develops another crack. Note that no initial notches are introduced. In the phase-field model for brittle fracture, unlike in linear fracture mechanics (Kuna, 2013), nucleation can occur in the absence of stress singularities. As previously mentioned critical stress and crack initiation are related to the length scale parameter l_0 (see Amor et al. (2009) for more details). Overall, the results are in good agreement with the 2D case presented

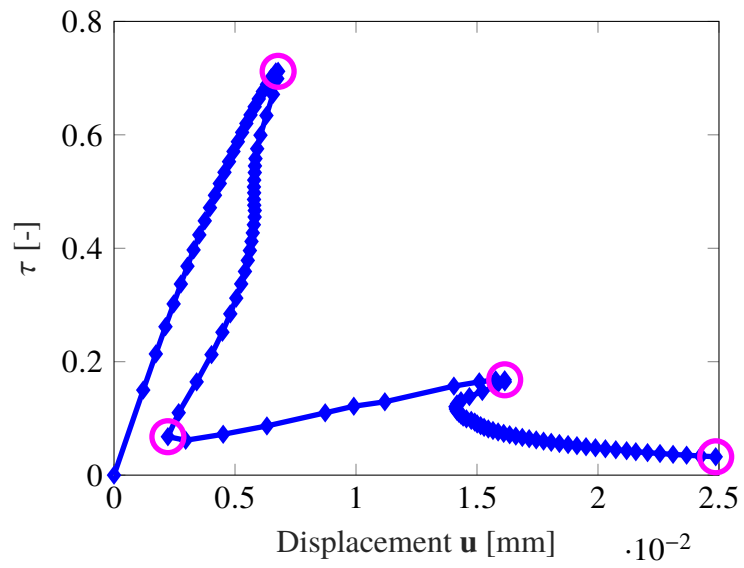


Figure 5.15: Load displacement curve for example with the eccentric hole example.

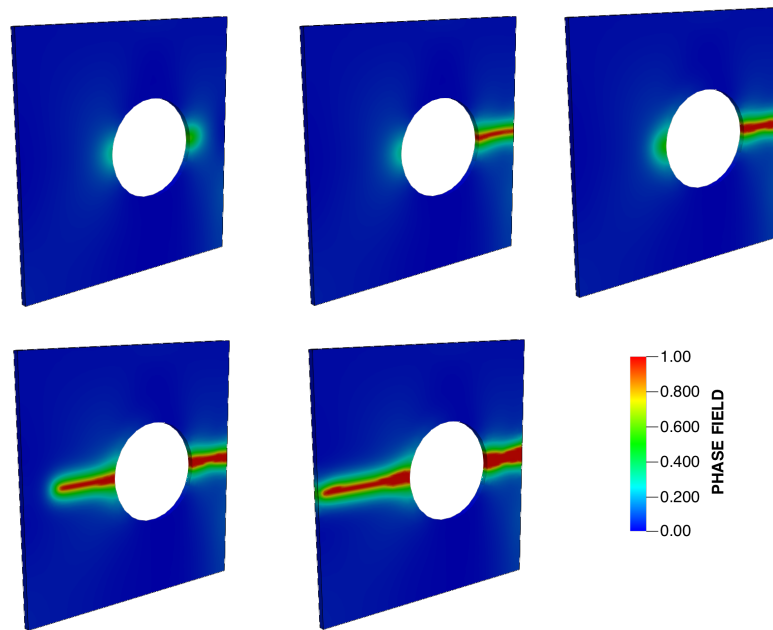


Figure 5.16: Crack propagation at four different snapshots highlighted in Figure 5.15.

in Ozdemir (2019).

5.5 Summary

In this chapter, a thermodynamically consistent computational framework for brittle fracture using phase-field has been outlined. Three different methods are proposed for obtaining a consistent tangent matrix necessary linearisation. A monolithic solution strategy has been utilised to simultaneously solve for displacements and the phase-field variables. In order to accurately and effortlessly trace the dissipative loading path, an arc-length procedure has been implemented that controls the incremental internal and dissipated energy with an adaptive step size. The chosen algorithm is robust and requires only two parameters provided by the user. Additionally, MoFEM's hierarchical basis functions of arbitrary polynomial order are utilised to increase the order of approximation without the need to change the finite element mesh. The investigation conducted herein demonstrates that the phase-field approach is relatively simple to implement and gives qualitatively comparable results for brittle fracture. In two presented examples, the equilibrium paths, as well as crack propagation patterns, are consistent with the literature.

The main drawback of the phase-field models is the necessity of using an enormous number of elements to approximate the sharp cracks. It is especially apparent in the three-dimensional setting, where the number of elements grows dramatically. Therefore, further development of mesh adaptive refinement techniques is crucial for the efficiency of the proposed computational approach. Another substantial disadvantage is the number of model parameters that can significantly affect the results, like length scale l_0 , choice of the degradation function or mesh element size.

In Chapter 7, phase-field is further investigated for crack propagation in heterogeneous materials and directly compared to the configurational force driven approach.

Chapter 6

Configurational force driven fracture mechanics

The objective of this chapter is to present a discrete crack propagation formulation within the context of configurational mechanics. The local form of the first law of thermodynamics provides an equilibrium condition for the crack front, expressed in terms of the configurational forces and material resistance. Application of the maximal energy dissipation principle provides the direction of the configurational forces and crack propagation. The main advantage of the presented approach is that crack release energy is expressed exclusively in terms of nodal quantities, which enables fully implicit formulation for evolving crack. Stress singularity at the crack tip is modelled accurately in an unstructured tetrahedral mesh domain by using an old concept of Quarter Point Elements. Furthermore, the approach is extended to include additional configurational force contributions originating from material heterogeneities. Performance and accuracy of the proposed framework are demonstrated by means of representative numerical simulations.

6.1 Introduction

6.1.1 Material force concept

Most of the known materials, on some scale, cannot be considered as perfect continua, because they contain numerous defects like microcracks, inclusions, voids or dislocations. To identify the interaction between these imperfections in the material manifold, the concept of a material force has been introduced. Similarly, to force acting on a body in physical space, material forces

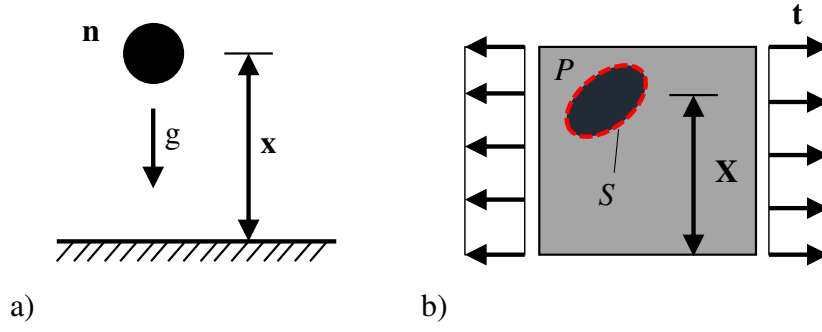


Figure 6.1: Schematic definition of physical and material spaces: a) mass under gravity in physical space; b) inclusion in solid in material space.

characterise forces acting on defects in material space. Following Kienzler and Herrmann (2012), to illustrate that concept two examples are depicted in Figure 6.1: a particle in physical space (6.1a) and inclusion in a solid undergoing deformation (6.1b)). The physical space is usually assumed to be Euclidian, homogeneous and not changing in time. The total potential of a particle at spatial position \mathbf{x} in a gravity field g is $\Psi = mg\mathbf{x}$. The physical (or often called Newtonian) force acting on that particle with mass m has the form:

$$\mathcal{F} = -\frac{\partial\Psi}{\partial\mathbf{x}}. \quad (6.1)$$

In the second example (Fig. 6.1b)) an elastic plate is subjected to tension \mathbf{t} and contains an inclusion at a distance \mathbf{X} . In this case, the total energy Ψ depends on several quantities α_i and the position in material space \mathbf{X} . The force \mathbf{G} acting on a defect is expressed as:

$$\mathbf{G} = \frac{\partial\Psi(\alpha_i, \mathbf{X})}{\partial\mathbf{X}}. \quad (6.2)$$

The concept of material forces was introduced by Eshelby (1951). In the original paper Eshelby recognised that classical theory of elasticity does not describe forces acting on defects, inclusions or crack tips. In his work he found that elastic field carries energy momentum tensor, which can be derived from variational principles like Least Action Principle (Noether, 1971). In the Eshelby's thought experiment, force \mathbf{G} can be computed by using energy momentum tensor. Let $\delta\xi$ be an infinitesimal displacement applied on an inclusion surface S as presented in Figure 6.1 while keeping the same load \mathbf{t} on the surface of the solid. The change in the energy of the system can be expressed as:

$$\delta\Psi = -\delta\xi \int_S (\Psi_{\text{II}} - \mathbf{F}^T \boldsymbol{\sigma}) \mathbf{n} \, dA, \quad (6.3)$$

where \mathbf{n} is a vector normal to inclusion surface S , Ψ is the internal strain energy, $\boldsymbol{\sigma}$ is the stress tensor (e.g. Cauchy) and \mathbf{F} - deformation gradient. It can be assumed that energy change $\delta\Psi$ is equal to work of configurational force \mathbf{G} on the infinitesimal (virtual) displacement $\delta\xi$:

$$\delta\Psi = \delta\xi \mathbf{G} \quad (6.4)$$

Furthermore, with Equations 6.3 and 6.4 at hand, force \mathbf{G} can be expressed as:

$$\mathbf{G} = - \int_S (\Psi \mathbb{I} - \mathbf{F}^T \boldsymbol{\sigma}) \mathbf{n} dA = - \int_S \boldsymbol{\Sigma} \mathbf{n} dA, \quad (6.5)$$

where $\boldsymbol{\Sigma}$ energy momentum tensor, often also called the Eshelby stress tensor. A detailed and straightforward derivation of can be found in (Eshelby, 1975). Energy momentum acts in material space and it is analogous to Cauchy stress tensor in physical space. The material forces are often also referred as quasi-force, driving force, configurational force or non-Newtonian force. When inertia effects are neglected, the Eshelby stress coincides with the J -integral (Rice, 1968), which is equal to the strain energy release rate for a crack in a homogeneous linear elastic body. The concept of the J -integral is directly related to configurational mechanics as investigated in-depth, e.g. in Gurtin (1999); Maugin (2016).

6.1.2 Material forces in fracture mechanics

The past two decades have seen a growing interest in configurational force approach for analysis of material imperfections (Maugin, 2016) and in particular for evaluating the forces driving crack advancement (Kaczmarczyk et al., 2017; Steinmann et al., 2001). In order to simulate full crack propagation, multiple thermodynamically consistent frameworks have been presented which utilise the principle of maximal dissipation at the crack tip for brittle materials (Guerses and Miehe, 2009; Kaczmarczyk and Pearce, 2011). Ozenc et al. (2016) proposed an algorithm based on the principle of local symmetry to model dynamic crack bifurcation phenomenon using configurational force approach. One of the main difficulties of nodal-force-based is the need for resolving the evolving discrete crack geometry within the finite element mesh. The topological changes in the mesh can create distorted, poor quality elements, leading to numerical errors. To mitigate this problem, initially, r-adaptive mesh alignment method was proposed, e.g. in Miehe and Gürses (2007); Guerses and Miehe (2009) with further enhancements to preserve the mesh quality proposed in Kaczmarczyk et al. (2014). More recently, a mesh cutting algorithm has been presented in Pearce (2019) in which the nodes on the crack front are always moved exactly according to the equilibrium. Subsequently, the elements in the way are cut and remeshed.

However, such discrete approach has never been used to effectively assess configurational forces in heterogeneous bodies with cracks. This work brings all together new developments in configurational mechanics framework for fracture and extends it with the capability of analysing implicit, energy consistent crack propagation in heterogeneous materials like bones.

6.2 Energy consistent framework for crack propagation

6.2.1 Preliminaries

Figure 6.2 shows an elastic body with an initial crack in the reference domain \mathcal{B}_0 . As a result of loading, the crack extends, and the body deforms elastically. Working within the framework of configurational mechanics (Kienzler and Maugin, 2014; Kaczmarczyk et al., 2014), it is convenient to decompose this behaviour into solely an extension of the crack in the material domain \mathcal{B}_t followed by elastic deformation only in the spatial domain Ω_t . The former is described by the mapping from the reference domain to the material domain Ξ , while the mapping describes the latter from the material to the spatial domain φ . The material

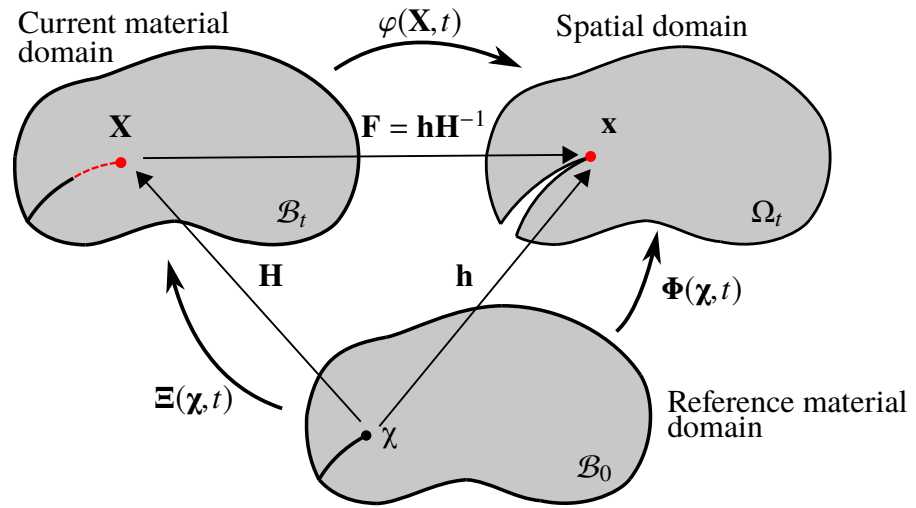


Figure 6.2: Decomposition of crack propagation in elastically deforming bone.

coordinates \mathbf{X} are mapped onto the spatial coordinates \mathbf{x} via the familiar deformation map $\varphi(\mathbf{X}, t)$. The physical displacement is:

$$\mathbf{u} = \mathbf{x} - \mathbf{X} \quad (6.6)$$

The reference material domain describes the body before the crack extension. $\Xi(\chi, t)$ maps the reference material coordinates χ onto the current material coordinates \mathbf{X} , representing a configurational change, i.e. extension of the crack due to advancement of the crack front. Φ maps the reference material coordinates χ onto the spatial coordinates \mathbf{x} . The current material and spatial displacement fields are given as:

$$\mathbf{W} = \mathbf{X} - \chi \quad \text{and} \quad \mathbf{w} = \mathbf{x} - \chi \quad (6.7)$$

\mathbf{H} and \mathbf{h} are the gradients of the material and spatial maps and \mathbf{F} the deformation gradient (Kaczmarczyk et al., 2014), defined as:

$$\mathbf{H} = \frac{\partial \Xi}{\partial \chi}, \quad \mathbf{h} = \frac{\partial \Phi}{\partial \chi}, \quad \mathbf{F} = \frac{\partial \varphi}{\partial \mathbf{X}} = \mathbf{hH}^{-1} \quad (6.8)$$

The time derivative of the physical displacement \mathbf{u} and the deformation gradient $\dot{\mathbf{F}}$ (material time derivative) are given as (Kaczmarczyk et al., 2014):

$$\dot{\mathbf{u}} = \dot{\mathbf{w}} - \mathbf{F}\dot{\mathbf{W}} \quad \dot{\mathbf{F}} = \nabla_{\mathbf{X}}\dot{\mathbf{x}} = \nabla_{\mathbf{X}}\dot{\mathbf{u}} = \nabla_{\mathbf{X}}\dot{\mathbf{w}} - \mathbf{F}\nabla_{\mathbf{X}}\dot{\mathbf{W}} \quad (6.9)$$

6.2.2 First and second laws of thermodynamics

The first law of thermodynamics can be expressed as

$$\int_{\partial \mathcal{B}_t} \dot{\mathbf{u}} \cdot \mathbf{t} dS = \int_{\partial \Gamma} \gamma \dot{A}_\Gamma + \frac{d}{dt} \int_{\mathcal{B}_t} \Psi(\mathbf{F}, \rho) dV \quad (6.10)$$

where the left-hand side is the power of external work, the first term on the right-hand side is the rate of crack surface energy, and the last term is the rate of internal energy. \mathbf{t} is the external traction vector, γ is the surface energy [Nm^{-1}], \dot{A}_Γ is the change in the crack surface area, and Ψ is the volume-specific free energy. The crack surface Γ comprises two crack faces and a crack front $\partial \Gamma$ - see Figure 6.3. In Kaczmarczyk et al. (2017), a kinematic relationship

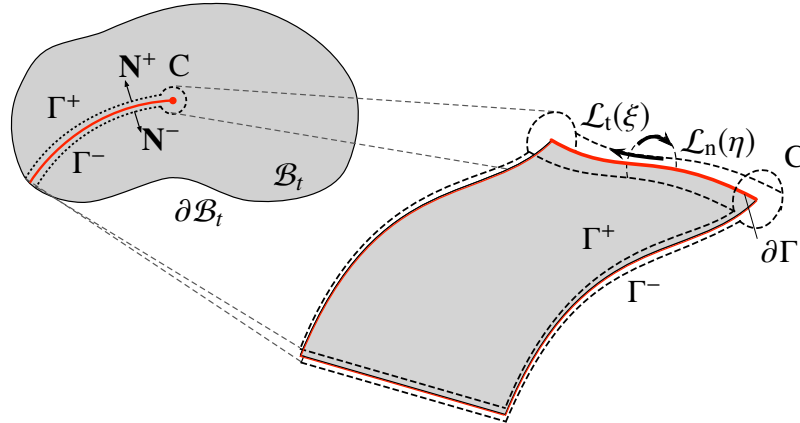


Figure 6.3: Crack construction. In 2D (left) and in more detail in 3D (right).

between the change in the crack surface area \dot{A}_Γ and the crack front velocity $\dot{\mathbf{W}}$ was derived as:

$$\dot{A}_\Gamma = \int_{\partial \Gamma} \mathbf{A}_{\partial \Gamma} \cdot \dot{\mathbf{W}} dL \quad (6.11)$$

where $\mathbf{A}_{\partial \Gamma}$ is a dimensionless kinematic state variable that defines the orientation of the current crack front that can be considered a unit vector normal to the crack front and tangential

to the crack surface. In deriving this expression, it was recognised that any change in the crack surface area \dot{A}_Γ in the current material space can only occur due to motion of the crack front. Making use of Equations 6.9 and 6.11, and given that $d\dot{V} = \nabla_{\mathbf{X}} \cdot \dot{\mathbf{W}} dV$, Eq. 6.10 can be reformulated as:

$$\int_{\partial \mathcal{B}_t} (\dot{\mathbf{w}} \cdot \mathbf{t} - \dot{\mathbf{W}} \cdot \mathbf{F}^T \mathbf{t}) dS = \int_{\partial \Gamma} \gamma \mathbf{A}_{\partial \Gamma} \cdot \dot{\mathbf{W}} dL + \int_{\mathcal{B}_t} (\mathbf{P} : \nabla_{\mathbf{X}} \dot{\mathbf{w}} + \boldsymbol{\Sigma} : \nabla_{\mathbf{X}} \dot{\mathbf{W}} + \mathbf{f}^{\text{inh}} \cdot \dot{\mathbf{W}}) dV \quad (6.12)$$

where

$$\boldsymbol{\Sigma} = \Psi(\mathbf{F}, \rho) \mathbb{I} - \mathbf{F}^T \mathbf{P}(\mathbf{F}, \rho), \text{ and } \mathbf{f}^{\text{inh}} = \left. \frac{\partial \Psi}{\partial \rho} \right|_{(\mathbf{F}=\text{const})} \frac{\partial \rho}{\partial \mathbf{X}} \quad (6.13)$$

$\boldsymbol{\Sigma}$ is the Eshelby stress tensor, and \mathbf{f}^{inh} is an additional fictitious force that drives the crack front from dense to less dense material as a result of variations in the density field. The first Piola Stress tensor \mathbf{P} , in case of heterogeneous materials has the same form as presented in Eq. 4.7: $\mathbf{P} = [\rho/\rho_0^*]^n \partial \Psi(\mathbf{F})/\partial \mathbf{F}$. The spatial conservation law of linear momentum balance is repeated here:

$$\nabla_{\mathbf{X}} \cdot \mathbf{P} = 0 \quad \forall \mathbf{X} \in \mathcal{B}_t, \quad \mathbf{P} \mathbf{n} = \mathbf{t} \quad \forall \mathbf{X} \in \partial \mathcal{B}_t^\sigma, \quad (6.14)$$

where $\partial \mathcal{B}_t^\sigma$ is the region of the boundary where tractions are applied. The equivalent material momentum balance is expressed as:

$$\nabla_{\mathbf{X}} \cdot \boldsymbol{\Sigma} = \mathbf{f}^{\text{inh}} \quad \forall \mathbf{X} \in \mathcal{B}_t, \quad \boldsymbol{\Sigma} \mathbf{n} = \mathbf{F}^T \mathbf{t} \quad \forall \mathbf{X} \in \partial \mathcal{B}_t^\sigma \quad (6.15)$$

It is important to note that $\mathbf{f}^{\text{inh}} = \mathbf{0}$ in the case of homogeneous materials, with uniform density distribution. After applying the divergence theorem to Eq. 6.12 and recognising the momentum balance laws, following Kaczmarczyk et al. (2017) a local form of Eq. 6.12 is established, which represents an expression for the equilibrium of the crack front as

$$\dot{\mathbf{W}} \cdot (\gamma \mathbf{A}_{\partial \Gamma} - \mathbf{G}) = 0 \quad (6.16)$$

where the configurational force \mathbf{G} is the driving force for crack propagation:

$$\mathbf{G} = \lim_{|\mathcal{L}| \rightarrow 0} \int_{\mathcal{L}_n} \boldsymbol{\Sigma} \mathbf{N} dL \quad (6.17)$$

From Equation 6.16, it is clear that the crack front is in equilibrium when the crack is not propagating, i.e. material velocity $\dot{\mathbf{W}}$ at the crack front is zero, or when the crack front is propagating, and the configurational force is in equilibrium with the material resistance $\gamma \mathbf{A}_{\partial \Gamma}$. It should be noted that crack front equilibrium is unaffected by material heterogeneities and does not depend on \mathbf{f}^{inh} . All terms in Eq. 6.16 are only evaluated at the crack front. However, it will be shown in Section 6.2.5 that, in a discrete setting, calculation of the nodal configurational forces involves a volume integral of the density gradient.

6.2.3 Fracture process

In the present work, bone is considered to be perfectly brittle. The likelihood of fracture is evaluated for the direction of crack propagation that results in maximum energy dissipation. Healing processes or additional dissipation arising from cohesive forces or plastic flow due to crack opening, as observed in quasi-brittle materials, are not taken into account. Future extension of the present model could include such processes, e.g. accounting for finite fracture zone.

Since Eq. 6.16 has more than one solution at equilibrium, depending on whether the crack does or does not propagate, the formulation is supplemented by a straightforward criterion for crack growth, equivalent to Griffith's criterion (Kaczmarczyk et al., 2017):

$$\phi(\mathbf{G}) = \mathbf{G} \cdot \mathbf{A}_{\partial\Gamma} - g_c/2 \leq 0, \quad (6.18)$$

where $g_c = 2\gamma$ is a material parameter specifying the critical threshold of energy release per unit area of the crack surface Γ , also known as the Griffith energy. For a point on the crack front to satisfy the crack growth criterion, either $\phi < 0$ and $\dot{\mathbf{W}} = 0$, or $\phi = 0$, $\dot{\mathbf{W}} \neq 0$ and $\gamma\mathbf{A}_{\partial\Gamma} = \mathbf{G}$. The crack will propagate only when crack release energy is equal to material toughness (and will be arrested when it is lower than toughness). The condition that the crack release energy is greater than the material toughness is an inadmissible state. The direction of fracture propagation is constrained by the second law of thermodynamics. In the context of bones, it is assumed that fracture takes place relatively fast compared to the process of adaptation (with no healing), such that non-negative dissipation at the crack front can be expressed as:

$$\mathcal{D}_{\max} = \gamma\dot{\mathbf{W}} \cdot \mathbf{A}_{\partial\Gamma} = \dot{\mathbf{W}} \cdot \mathbf{G} \geq 0 \quad (6.19)$$

For brittle fracture, from all possible crack propagation directions, the one which maximises dissipation of energy is chosen, leading to the following equation:

$$\gamma\mathbf{A}_{\partial\Gamma} = \mathbf{G}, \quad (6.20)$$

where the magnitude of \mathbf{G} can be interpreted as the crack release energy $g_c = 2\gamma$,

$$g_c/2 = \mathbf{G} \cdot \mathbf{A}_{\partial\Gamma} \quad (6.21)$$

It should be noted that the well-established stress intensity factors are not applicable in the case of heterogeneous materials since it requires the existence of an analytical solution for the stress field in the vicinity of the crack front that is independent of the arbitrary distribution of density. Similarly, the use of J -integral requires integration over the closed surface without inhomogeneities (including heterogeneous density distribution), except for the crack front itself and therefore not applicable in this case. Finally, it is worth noting that the current framework is formulated within the realm of large displacements and large strains; hence it is

generally valid under any assumption for strains and displacements.

6.2.4 Density field

The previous subsections have shown that fracture modelling of heterogeneous materials is influenced by the density distribution in the material configuration. This density field can be generated from either a) a bone adaptation analysis, solving Eq. 4.5,4.6 (see Section 4.2), or b) subject-specific data (geometry and material properties) available from, for example, computed tomography (CT) scans (see Section 3.5.1). In the numerical examples presented in Section 7.3.2, both sources of density data are used.

Previous examples in the literature of subject-specific modelling to assess the stresses and fracture risk of bones can be found in (Poelert et al., 2013; Helgason et al., 2008a; Yosibash et al., 2010). Most algorithms that use voxel data have simply averaged (Zannoni et al., 1999) or integrated data onto finite elements, thereby supplying a constant density within their volume (Taddei et al., 2007; Schileo et al., 2008) which results in a very irregular density distribution.

In order to evaluate the configurational forces at the crack front, it is necessary to have a spatially smooth density field. As shown in Eq. 6.13, the inhomogeneous force appearing in the first law of thermodynamics, requires a computation of the density gradient. Therefore, the density function has to be at least C^1 -continuous in order to provide continuous derivatives. To achieve required smoothness, discrete density data will need to be approximated as a smooth density field, and this will be achieved by adopting the Moving Weighted Least Squares (MWLS) method. This mapping approach is chosen since it offers higher regularity (i.e. higher derivatives exist) than when the field is directly approximated on the finite element mesh. More details about MWLS implementation are given in Section 3.3.2. Moreover, higher regularity is also essential for the tangent stiffness matrix, where the second derivative of the density field $\partial^2 \rho^h / \partial \mathbf{X}^2$ appears.

6.2.5 Discretisation

Three-dimensional domains are discretised with tetrahedral finite elements. Fields are approximated in the current material and current spatial spaces with hierarchical basis functions of arbitrary polynomial order, following the work of Ainsworth and Coyle (2003).

$$\mathbf{X}^h(\boldsymbol{\chi}, t) = \boldsymbol{\Phi}(\boldsymbol{\chi})\tilde{\mathbf{X}}(t), \quad \mathbf{x}^h(\boldsymbol{\chi}, t) = \boldsymbol{\Phi}(\boldsymbol{\chi})\tilde{\mathbf{x}}(t) \quad (6.22)$$

$$\mathbf{W}^h(\boldsymbol{\chi}, t) = \boldsymbol{\Phi}(\boldsymbol{\chi})\dot{\tilde{\mathbf{W}}}(t), \quad \mathbf{w}^h(\boldsymbol{\chi}, t) = \boldsymbol{\Phi}(\boldsymbol{\chi})\dot{\tilde{\mathbf{w}}}(t) \quad (6.23)$$

where Φ are shape functions, superscript h indicates approximation and (\cdot) nodal values. Moreover, the smoothed density field is approximated by MWLS shape functions:

$$\rho^{h,MWLS}(\mathbf{X}, t) = \Phi^{MWLS}(\mathbf{X})\tilde{\rho}^h(\Xi(\boldsymbol{\chi}), t) \quad (6.24)$$

It should be noted that shape functions $\Phi^{MWLS}(\mathbf{X})$ are evaluated at current material points, \mathbf{X} , rather than reference points, $\boldsymbol{\chi}$, as presented in Eq. 6.23 with the property of partition of unity. Since the density field is evaluated at \mathbf{X} , the approximation is independent of changes of the material configuration (i.e. changing mesh).

The residual force vector in the discretised spatial domain is expressed in a classical way as:

$$\mathbf{r}_s^h(\tilde{\boldsymbol{\rho}}(t), \tilde{\boldsymbol{\chi}}(t)) = \tau \mathbf{f}_{\text{ext},s}^h - \mathbf{f}_{\text{int},s}^h = \tau \int_{\partial \mathcal{B}_t^h} \Phi^T \mathbf{f}^{\text{ext}} dS - \int_{\mathcal{B}_t^h} \nabla_{\mathbf{X}} \Phi^T \mathbf{P}^{h,MWLS} dV = \mathbf{0}, \quad (6.25)$$

where τ is the unknown scalar load factor, $\mathbf{f}_{\text{ext},s}^h$ is the vector of externally applied forces and $\mathbf{f}_{\text{int},s}^h$ is the vector of internal forces. The discretisation of Eq. 6.16 establishes the material counterpart to Eq. 6.25, expressed as

$$\mathbf{r}_m^h(\tilde{\boldsymbol{\rho}}(t), \tilde{\boldsymbol{\chi}}(t)) = \mathbf{f}_{\text{res}}^h - \tilde{\mathbf{G}}^h = \mathbf{0} \quad (6.26)$$

$\tilde{\mathbf{G}}^h$ is the vector of nodal configurational forces only on nodes on the crack front, with the integration restricted to elements adjacent to the crack front:

$$\tilde{\mathbf{G}}^h = \int_{\mathcal{B}_t^h} \nabla_{\mathbf{X}} \Phi^T \Sigma^{h,MWLS} dV + \int_{\mathcal{B}_t^h} \Phi^T \frac{\partial \Psi^{h,MWLS}}{\partial \rho^{h,MWLS}} \left(\frac{\partial \rho^{h,MWLS}}{\partial \mathbf{X}} \right) dV \quad (6.27)$$

These configurational forces are the driving force for crack propagation. It should be noted that the second term of $\tilde{\mathbf{G}}^h$ reflects the influence of the spatially varying density. In the case of a homogeneous material, this second term would be zero. It should also be noted that this is only the case for the discretised configurational forces and that the continuum equivalent (Eq. 6.17) is unaffected by variation in the density field.

Let the whole surface $\partial \mathcal{B}_t^h$ of the body domain, \mathcal{B}_t^h , at current material configuration be discretised by non-overlapping triangles \mathcal{T}_i whose collection is defined as:

$$\mathcal{T} := \left\{ \mathcal{T} \in \partial \mathcal{B}_t^h : \mathcal{T}_i \cap \mathcal{T}_j = \emptyset \text{ and } \partial \mathcal{B}_t^h = \sum_i^t \mathcal{T}_i \right\} \quad (6.28)$$

where t is the total number of triangles on $\partial \mathcal{B}_t^h$. Furthermore, crack front is approximated by edges Γ^h , defined similarly to triangles, but with one dimension lower. With the above at hand, the triangulated domain can be defined with triangles that are part of body boundary and adjacent to the crack front as:

$$S_{\Gamma}^h := \{ \mathbf{X} \in \mathcal{T} : \partial \mathcal{T} \cap \Gamma^h \neq \emptyset \} \quad (6.29)$$

Next, $\mathbf{Z}^{\text{front}}$ is a matrix comprising direction vectors along the crack front that are normal to the crack front and tangent to the crack surface, and it can be defined as follows

$$\mathbf{Z}^{\text{front}} = \int_{S_{\Gamma}^h} \Phi^T \frac{\partial A_{\Gamma}^h}{\partial \tilde{\mathbf{X}}} dL \quad (6.30)$$

The crack surface tangent vector $\mathbf{Z}^{\text{front}}$ is evaluated by only integrating over S_{Γ}^h that defines the area of those triangular finite elements that discretise the crack surface Γ^h adjacent to the crack front $\partial\Gamma^h$.

$$A_{\Gamma}^h = \|\mathbf{N}(\tilde{\mathbf{X}})\| = \left\| \epsilon_{ijk} \frac{\partial \Phi_p^{\alpha}}{\partial \xi_i} \frac{\partial \Phi_r^{\beta}}{\partial \xi_j} \tilde{X}_p^{\alpha} \tilde{X}_r^{\beta} \right\| \quad (6.31)$$

where $\alpha, \beta \in \{0, \dots, N_{\text{base}}\}$ are numbers of base functions, $i, j, p, r \in \{0, 1, 2\}$ are material indices and ϵ is Levi-Civita tensor. Moreover, the total number of degrees of freedom on element is $3(N_{\text{base}} + 1)$ and the units of $\mathbf{Z}^{\text{front}}$ are $[\text{m}^{-1}]$. \mathbf{N} are the normals to the crack surface Γ . Therefore, multiplication of $\mathbf{Z}^{\text{front}}$ with nodal crack release energy \mathbf{g}_c results in the evaluation of crack configurational forces:

$$\mathbf{f}_{\text{res}}^h = \frac{1}{2} (\mathbf{Z}^{\text{front}})^T \tilde{\mathbf{g}}^h \quad (6.32)$$

where $\tilde{\mathbf{g}}^h = \mathbf{1}g_c$ is a vector of size equal to the number of nodes on the crack front. The Griffith configurational force can be considered as a crack resistance. Combining Eqs. 6.32 and 6.27 equilibrium at the crack front can be evaluated through the residual:

$$\mathbf{r}_m^h = \frac{1}{2} (\mathbf{Z}^{\text{front}})^T \tilde{\mathbf{g}}^h - \tilde{\mathbf{G}}^h = \mathbf{0} \quad (6.33)$$

Subsequently, by multiplying Eq. 6.33 on both sides with $\mathbf{Z}^{\text{front}}$ and solving for $\tilde{\mathbf{g}}^h$ the expression below is obtained:

$$\mathbf{g}^h = 2 \left[\left(\mathbf{Z}^{\text{front}} (\mathbf{Z}^{\text{front}})^T \right)^{-1} \mathbf{Z}^{\text{front}} \right] \tilde{\mathbf{G}}^h \quad (6.34)$$

The nodal configurational forces $\tilde{\mathbf{G}}^h$ are evaluated at the crack front nodes. Moreover, the dimension of the configurational nodal force is $[\text{J}/\text{m}]$, but Griffith crack release energy should be in units $[\text{J}/\text{m}^2]$. That discrepancy disappears in-plane stress analysis, where configurational forces are divided by the thickness of the body. The magnitude of nodal configurational forces at the crack front node is the value of J -integral. In the case of 3D analysis, to remove that discrepancy in units, some researchers divide adjacent edges into half (Guerses and Miehe, 2009). However, that gives the correct value for crack release energy only for straight crack fronts.

It can be noticed that by comparison of Eq. 6.34 with Theorem 1(3.) in Ainsworth (2001) nodal Griffith surface energy $\tilde{\mathbf{g}}^h$ could be interpreted as a Lagrange multiplier constraining the crack area growth. Furthermore, dimension term in square brackets on the left-hand side of Eq. 6.34 is $[1/\text{m}]$ which multiplied by the dimension of configurational force $[\text{J}/\text{m}]$ gives the

dimension of crack release energy, i.e. [J/m²]. Thereby, the main advantage of the presented approach is that crack release energy is expressed exclusively in terms of nodal quantities, which enables the implicit formulation of crack propagation algorithm.

6.2.6 Arc-length control

Following Kaczmarczyk et al. (2017), the discretised balance equations are solved iteratively using the Newton-Raphson method for the spatial and material displacements. To trace an equilibrium path which may exhibit snap-through and snap-back phenomena, an arc-length control is adopted. The global system of equations is augmented with a load control equations that constraints the crack area increment for each load step. The additional residual vector which has to be satisfied is defined as

$$\mathbf{r}_\tau = \sum_k \left(\mathbf{z}^{\text{front}} \mathbf{x}_n \right)_k - \sum_k \left(\mathbf{z}^{\text{front}} \tilde{\mathbf{X}}_{n+1}^{i+1} \right)_k - \Delta A_\Gamma = 0 \quad (6.35)$$

where ΔA_Γ is the target increment of the crack area and k is the crack front node.

6.2.7 Linearised system of equations

The residual Equations 6.26 6.25 and 6.35 are linearised in a classical procedure for the Newton-Raphson method. Since the material residual is non-zero only for nodes on the crack front, herein the material nodal positions $\tilde{\mathbf{X}}$ are decomposed into those at the crack front $\tilde{\mathbf{X}}_f$ and the rest of the mesh $\tilde{\mathbf{X}}_b$ i.e. $\tilde{\mathbf{X}} = \tilde{\mathbf{X}}_f \cup \tilde{\mathbf{X}}_b$. The resulting linear system of equations for iteration i and load step $n + 1$ is expressed as:

$$\left\{ \begin{array}{cccc} \partial_{\tilde{\mathbf{x}}} \mathbf{r}_s^h & \partial_\tau \mathbf{r}_s^h & \partial_{\tilde{\mathbf{x}}_f} \mathbf{r}_s^h & \partial_{\tilde{\mathbf{x}}_b} \mathbf{r}_s^h \\ 0 & 0 & \partial_{\tilde{\mathbf{x}}_f} \tau^h & 0 \\ \partial_{\tilde{\mathbf{x}}} \mathbf{r}_m^h & 0 & \partial_{\tilde{\mathbf{x}}_f} \mathbf{r}_m^h & 0 \\ \partial_{\tilde{\mathbf{x}}} \mathbf{f}_q^h & 0 & \partial_{\tilde{\mathbf{x}}_f} \mathbf{f}_q^h & \partial_{\tilde{\mathbf{x}}_b} \mathbf{f}_q^h \end{array} \right\} \left\{ \begin{array}{c} \delta \tilde{\mathbf{X}}^{i+1} \\ \delta \tau^{i+1} \\ \delta \tilde{\mathbf{X}}_f^{i+1} \\ \delta \tilde{\mathbf{X}}_b^{i+1} \end{array} \right\} = - \left[\begin{array}{c} \mathbf{r}_s^h \\ \mathbf{r}_\tau \\ \mathbf{r}_m^h \\ \mathbf{f}_q^h \end{array} \right] \quad (6.36)$$

where the vector \mathbf{f}_q^h is associated with material positions $\tilde{\mathbf{X}}_b$. In addition, the system in Equation 6.36 is augmented with mesh quality control and shape-preserving constraints and their corresponding degrees of freedom and Lagrange multipliers. These additional equations ensure high quality the constantly changing mesh and preserve the surfaces of the material domain, including the surfaces of the crack. For more details, see Kaczmarczyk et al. (2017).

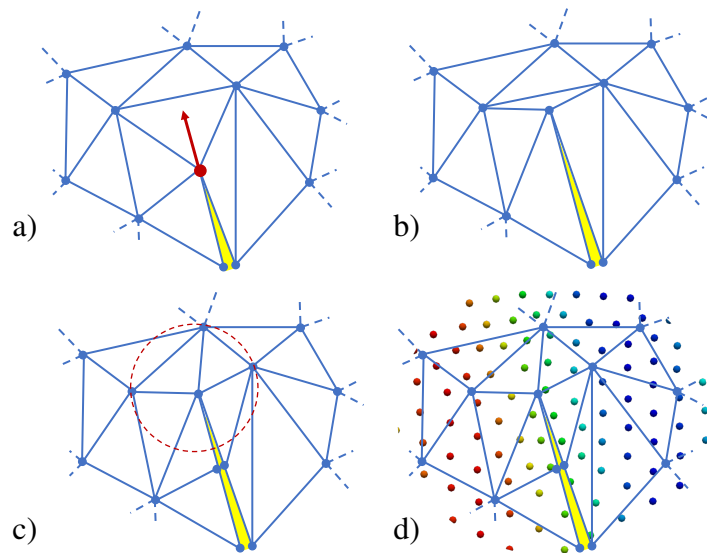


Figure 6.4: a) Nodal configurational force. b) Crack front extension. c) Mesh reconstruction around the tip. d) MWLS mapping onto new material points.

At the beginning of each new load step, the material configuration is updated to the current material configuration, utilising the Total Arbitrary Eulerian-Lagrangian approach.

6.2.8 Crack topology resolution

Continuous crack surface evolution requires constant adjustments into finite element mesh during the analysis. In this work, the new crack front is generated by moving the nodes in the direction to establish equilibrium, resulting in maximum energy dissipation (see Eq. 6.19). The mesh is not split, or the connectivity changed. Once the quality of the elements deteriorates, typically after 3-4 advancements, the mesh is cut by the resulting new crack surfaces. Subsequently, the crack surface is remeshed; the surrounding elements are trimmed and merged. These procedures are executed in an iterative manner to minimise the number of distorted elements in the new mesh. Nevertheless, the reconstructed crack surface can occasionally still contain mediocre quality elements (Jacobian $J < 0.1$), however, this deficiency is compensated by the use of higher-order and p -adaptive elements within hierarchical basis framework (Kaczmarczyk et al., 2020; Ainsworth and Coyle, 2003). Finally, after rebuilding the mesh around the crack surfaces, the field of material parameters (density) is mapped onto new elements. The data is stored on the vertices of a background mesh which does not change throughout the analysis. During the assembly process for each new step, using meshless MWLS, the data is approximated from the neighbour vertices to any considered material point of the new mesh. A schematic procedure of this process is shown in Figure 6.4.

6.2.9 Singularity element

In order to accurately determine parameters like stress intensity factors, it can be useful to reproduce the singular stress field at the crack front. However, conventional finite elements that adopt polynomial approximation functions are unable to do this. In this work, a new type of finite element with hierarchical approximation functions that overcome this problem is shortly presented. The idea is inspired by the so-called quarter-point elements, initially developed in the 1970s, whereby the mid-node of all edges connected to the crack tip node were shifted to the quarter-point (Barsoum, 1976; Henshell and Shaw, 1975). The result of such a shift is a nonlinear mapping between natural (isoparametric) and local coordinates $\xi \rightarrow \mathbf{x}$ which produces the square root singularity. Stress and strain fields are dependent on the radial function of the crack tip, reaching infinity as $r \rightarrow 0$.

An example derivation of Quarter Point Element for one dimensional case is presented in Appendix D. The influence of this approach for tetrahedral elements is investigated in Section 6.3.1.

6.3 Benchmark problems

6.3.1 Stress intensity calculations

In this section, two numerical examples are presented to examine the calculation of configurational forces. First, a simple quasi-two-dimensional plate with homogeneous material distribution is considered. The convergence study utilises an analytical solution as a reference. Second, the singularity elements are used for the same plate problem, and their influence on the rate of convergence is presented.

The stress intensity factors are commonly used in fracture mechanics to predict stress intensity at the crack tip. They identify the influence of deformation and help to provide empirical failure criteria for brittle materials. The stress intensity K from finite element solutions is typically obtained as a post-processing step in linear stress analysis and well known analytical formulas utilising the value of energy release \mathbf{G} (Zehnder, 2007). In case of plane stress, the relation looks as follows:

$$\mathbf{G} = K^2 \left(\frac{1}{E} \right) \quad (6.37)$$

where E is the Young's modulus. The energy release associated with the crack growth is then computed by using J -integral (Shih et al., 1986), which in quasi-static and homogeneous

material case is defined as follows:

$$J = \lim_{\Gamma \rightarrow 0} \int_{\Gamma} \left(\Psi_{\text{II}} - \boldsymbol{\sigma} \cdot \frac{\partial \mathbf{u}}{\partial \mathbf{x}} \right) \mathbf{n} d\Gamma \quad (6.38)$$

It can be noticed that the J -integral without inertial contributions or heterogeneities is equivalent to energy release calculated in Equations 6.13 and 6.17. In order to compute material force \mathbf{G} , a simple linear elastic problem with existing crack is solved. From resulting displacements, \mathbf{G} at the crack tip is calculated using the integral in Eq. 6.27. Finally, with the relation in Eq. 6.37 stress intensity factors can be obtained.

Finite plate with a horizontal crack

This example involves a finite plate with height, $h_{\text{pl}} = 10$, thickness $t_{\text{pl}} = 1$ and half width $b_{\text{pl}} = 2.5$ and a horizontal through-thickness crack with half width $a_{\text{pl}} = 1$, as presented in Figure 6.5a). All input parameters presented are dimensionless. The plate is spatially discretised using 1384 tetrahedral elements and subjected to uniaxial stress in the longitudinal direction, as indicated in Figure 6.5b). Displacements are constrained on three vertices of the plate to prevent rigid body motion. The purpose of this analysis is to calculate

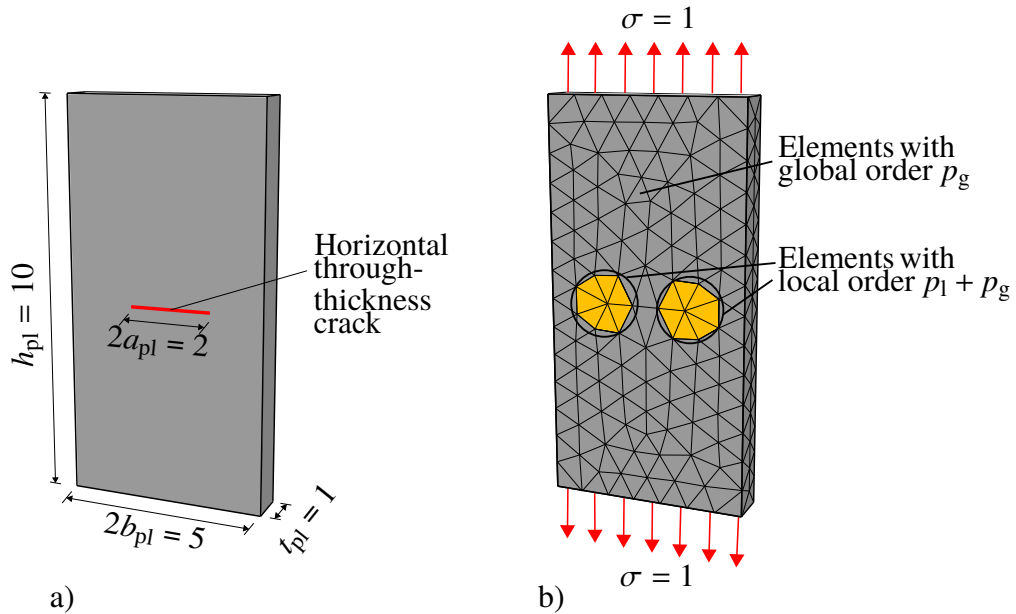


Figure 6.5: Finite plate with a horizontal crack. a) Plate geometry and through-thickness crack. b) Applied uniaxial stress σ and finite element mesh where elements presented with grey colour have the approximation order p_g and elements that have vertices at the crack tip, presented with yellow colour, have the approximation order $p_l + p_g$.

the Mode I stress intensity factor K_I and compare the results to the following analytical

solution (Rooke and Cartwright, 1976) for an infinite plate:

$$K_I = \sigma \sqrt{\pi a_{pl}} \left[\frac{1 - \frac{a_{pl}}{2b_{pl}} + 0.326 \left(\frac{a_{pl}}{b_{pl}} \right)^2}{\sqrt{1 - \frac{a_{pl}}{b_{pl}}}} \right], \quad (6.39)$$

where σ is the applied stress. Young's modulus E and Poisson's ratio ν are 1000 and 0.3, respectively. Hierarchical approximation basis functions allow for usage of elements with different orders of approximation. Hence, the influence of local and global p - refinement is investigated. In general, all tetrahedrons of the mesh have a global order of approximation, p_g , with some elements subjected to a local refinement of order p_l . $p_l + 1$ to $p_l + p_g$. When $p_l + p_g \leq 3$, two types of tetrahedral elements are considered where local order of approximation is increased to $p_l + p_g$ only at elements with vertices at the crack tip as presented in Figure 6.5b. Otherwise, a number of groups of tetrahedrons with different orders of approximation are considered. Similar to the case where $p_l + p_g \leq 3$, the first group of elements is composed of the tetrahedrons with vertices at the crack tip and have approximation order $p_l + p_g$. The second group of elements is consisted of the tetrahedrons adjacent to the first set elements, with approximation order that is one less than the previous set, i.e. $p_l + p_g - 1$. This process continues for each next adjacent group of tetrahedrons until the approximation order reaches the global order of approximation, p_g . All analyses presented were run using the same mesh with p-refinement varying from 1st-order to 6th-order so that $p_l + p_g \leq 7$. The Mode I stress intensity factor, K_I , can be calculated directly from the output configurational forces using the following relationship:

$$K_I = \sqrt{\mathbf{G}_I E} \quad (6.40)$$

where \mathbf{G}_I is the change of elastic strain energy per unit area of crack growth, calculated using Eq. 6.17. In this simple plane strain case, the configurational force vector \mathbf{G} is aligned with the crack, therefore the first component of the vector can be used to compute stress intensity in Mode I. The deformed shape of the plate is illustrated in Figure 6.6. From the graph, it is evident that, for the same coarse mesh and number of nodes, the solution can improve drastically when the order of approximation is increased. The well-known pathological nature of the 1st order solution due to shear locking is observed since a much higher error than other orders is computed. The minimum achieved error is 0.50% for all the cases with total order of approximation $p_l + p_g = 7$. Therefore, it can be observed that the same level of accuracy can be accomplished when using a low order of global approximation with only local p - refinement as with high order on the entire mesh. Moreover, by looking at the number of degrees of freedom, it can be observed that using higher-order elements locally results to the same accuracy at a much lower cost of computation time since the global matrix is much smaller.

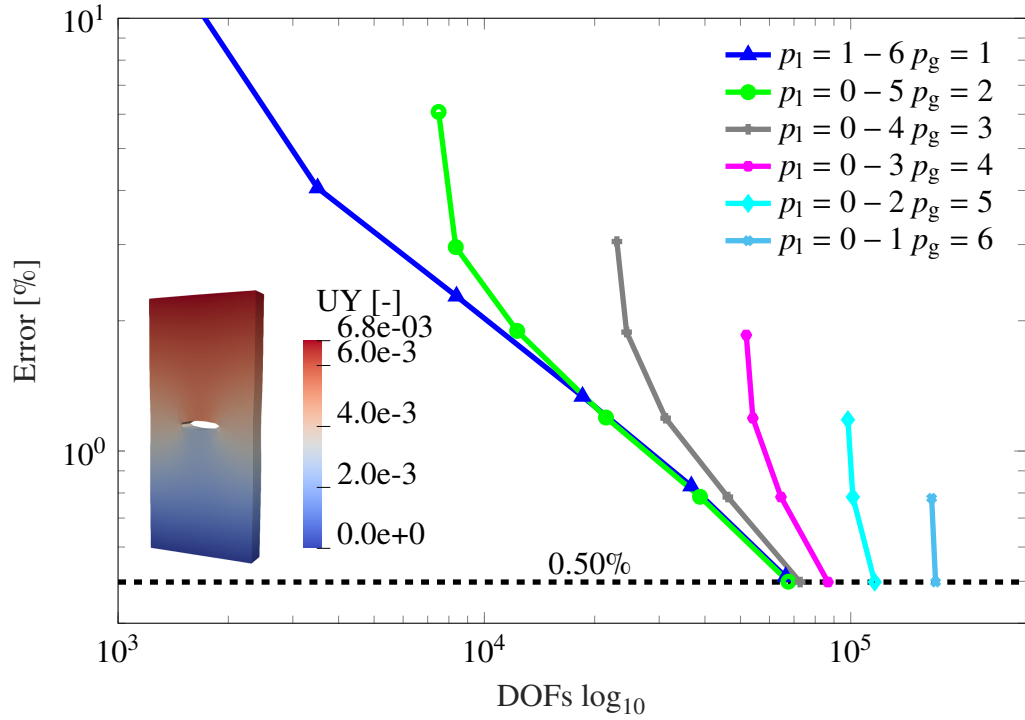


Figure 6.6: Convergence plot for stress intensity factor K_I Error (%) versus no. of DOF (log10) and deformed shape of the plate (bottom left).

Influence of singularity elements

The same problem as in Section 6.3.1 is investigated. This time, however, singularity on tetrahedral elements around the crack front are applied. Based on the results in Figure 6.7, it is evident that using singularity elements improves the convergence rate significantly and lowered the error by order of magnitude, from 0.50% down to 0.028%. However, it can be seen from the plot in Figure 6.7 that for each $p_1 + p_g$ combination, just after reaching the minimum error, it starts increasing again. This observation suggests that the solution cannot be further improved beyond that point only by enhancing the order of approximation. Possibly, by refining the mesh and changing the model length (to better replicate the infinite plate used to determine the analytical solution), the error could be decreased even more. Nevertheless, this is considered sufficiently accurate for the purpose at hand.

Overall, these results indicate that it is of great benefit to use the singularity elements since they improve the accuracy of the solution with no extra cost. Furthermore, the difference in execution time for the analysis with and without their inclusion was negligible.

6.3.2 Configurational forces in a heterogeneous body

So far, the numerical examples have assumed homogenous material properties. The next section considers the effect of heterogeneous material. Considering the same problem of the

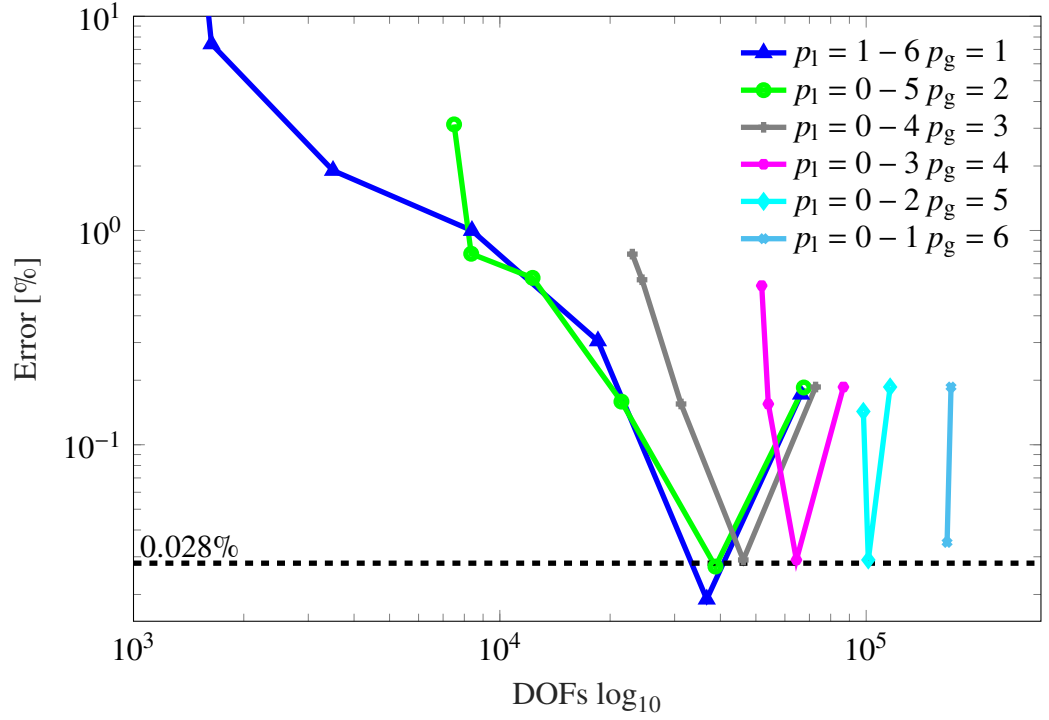


Figure 6.7: Convergence plot for stress intensity factor K_I Error (%) versus no. of DOF (log10).

finite plate with horizontal crack, a density field $\rho(x, y, z) = 0.125y + 1$ is directly assigned to the integration points of each tetrahedral element. The distribution of the density varying between 1.05 and 1.55 is depicted in Figure 6.8.

As expected, configurational forces are induced at the crack tip under load, and these are influenced by the non-uniform density distribution (see Eq. 6.15). However, the stress intensity factors or J-integral in the case of heterogeneous materials are difficult to calculate or obtain experimentally (Fischer et al., 2014). Due to the inhomogeneities the J -integral becomes path dependent and require special correction terms to be computed (Eischen, 1987; Chang-chun et al., 2002). An exception is the particular case of functionally graded materials (Kim and Paulino, 2002). A straightforward verification can be performed by using a simple numerical differentiation method like centered Finite Difference Method (FDM). Following Griffith's work (Griffith, 1921), the energy release rate for crack growth can be calculated as the change in elastic strain energy per unit area of crack growth:

$$\mathbf{G}_I = \frac{\partial \psi}{\partial a_{pl}} \quad (6.41)$$

where ψ is the elastic energy of the system, and a_{pl} is the crack length. This derivative can be calculated using FDM as:

$$\frac{\partial \psi}{\partial a_{pl}} = \lim_{\Delta a_{pl} \rightarrow 0} \frac{\psi(a_{pl} + \Delta a_{pl}) - \psi(a_{pl} - \Delta a_{pl})}{2\Delta a_{pl}} \quad (6.42)$$

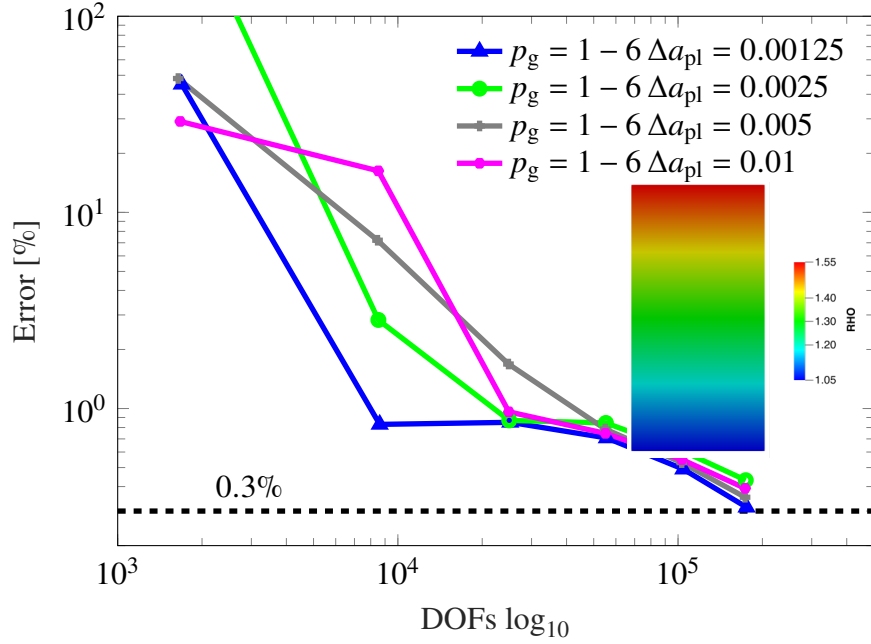


Figure 6.8: Convergence of error in release energy rate from Finite Difference Method. Density distribution (bottom right).

where the elastic strain energies $\psi(a_{pl} \pm \Delta a_{pl})$ can be obtained simply by running two additional analyses of the finite plate with horizontal cracks of lengths: $(a + \Delta a_{pl})$ and $(a - \Delta a_{pl})$, where Δa_{pl} is a very small value. Next, knowing the resulting release energy with the crack length of a_{pl} , a relative error can be calculated. Twenty-four analyses for different levels of p - refinements and values of Δa_{pl}) have been performed in order to determine the error in the release energy. The results are presented in Figure 6.8. It is apparent from the plot that with increasing levels of p -refinement, the error in release energy is converging down to 0.3%. It is worth noting that for a homogeneous case, similar accuracy was attained.

In the next test the above problem is repeated for a more difficult case - a strong horizontal gradient of the density field defined as: $\rho(x, y, z) = 10x + 1$. The distribution of the density on the plate, varying between 1.0 and 51.0, is depicted in Figure 6.9. Nevertheless, the results for three different values of Δa_{pl} , similarly to the previous case, are converging with each p -refinement to 1.8% error. Achieving higher precision with FDM validation is difficult due to the accumulation of truncation, approximation and discretisation errors. Therefore, it can be deduced that the presented implementation allows for estimation of release energy for heterogeneous domains with a satisfactory level of accuracy.

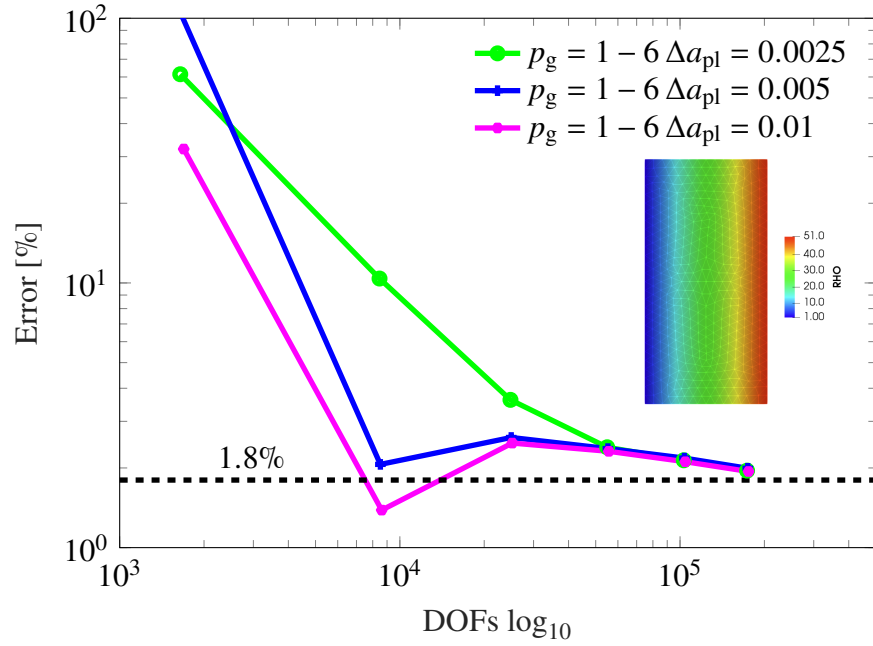


Figure 6.9: The convergence of error in release energy rate from the Finite Difference Method with horizontal gradient. Density distribution (bottom right).

6.3.3 Crack propagation in heterogeneous two-dimensional plate

To demonstrate the performance of the implementation for full crack propagation for quasi-static loading, a numerical example is presented, which considers a thin plate subjected to the 3-point loading. The dimensions of the specimen are 0.5 x 0.5 x 0.02mm. The model is spatially discretised using 2nd order tetrahedrons. The vertical force with magnitude of 1000 N is applied in the middle top of the plate applied on 0.02 x 0.02mm area. The material density is prescribed by function of spatial coordinates: $\rho(x, y, z) = 2x + 1$. Similar to bones, Young's modulus depends on the density in a power-law model of the form: $E = a\rho^n$ MPa, where coefficients a and n are chosen to be 9200 and 2, respectively. Poisson ratio ν is equal to 0.3 and critical Griffith energy release parameter $g_c = 1\text{N/mm}$. The crack is initialised in the middle bottom of the plate with length of 0.025mm. The analysis is conducted for three different meshes consisting of 1340, 5145 and 10341 elements. Figures 6.10 and 6.11a) shows that configurational forces are driving the crack in the direction opposite to the density gradient.

It should be noted that the crack path is smooth even for a coarse mesh. The load-displacement curves in Figure 6.11b) demonstrate that the results for the consecutive refinements are converging. The presented value of displacement is known as the generalised displacement and does not represent a particular point on the structure, but its value is work conjugate to the applied forces and is calculated as $\mathbf{u}_g = 2\Psi/\tau\mathbf{f}$, where $\mathbf{f} = 1\text{N}$ is the reference force, and Ψ is the total elastic energy integrated over the domain, τ is the arc-length load factor, and \mathbf{u}_g is the generalised displacement. These results indicate the ability of the formulation to accurately and robustly predict crack paths for heterogeneous bodies without bias from the original mesh.

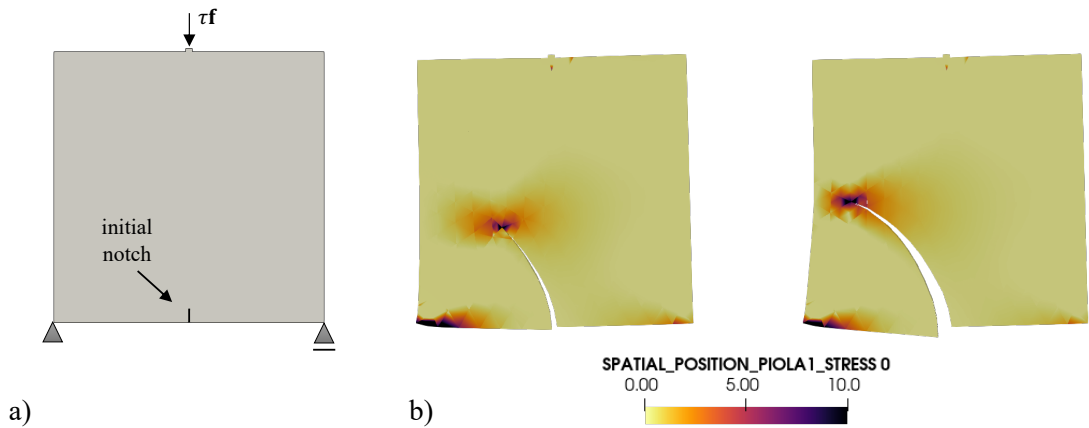


Figure 6.10: a) Geometry and boundary conditions for plate example. b) Contours of crack evolution on a map of P_{11} stress.

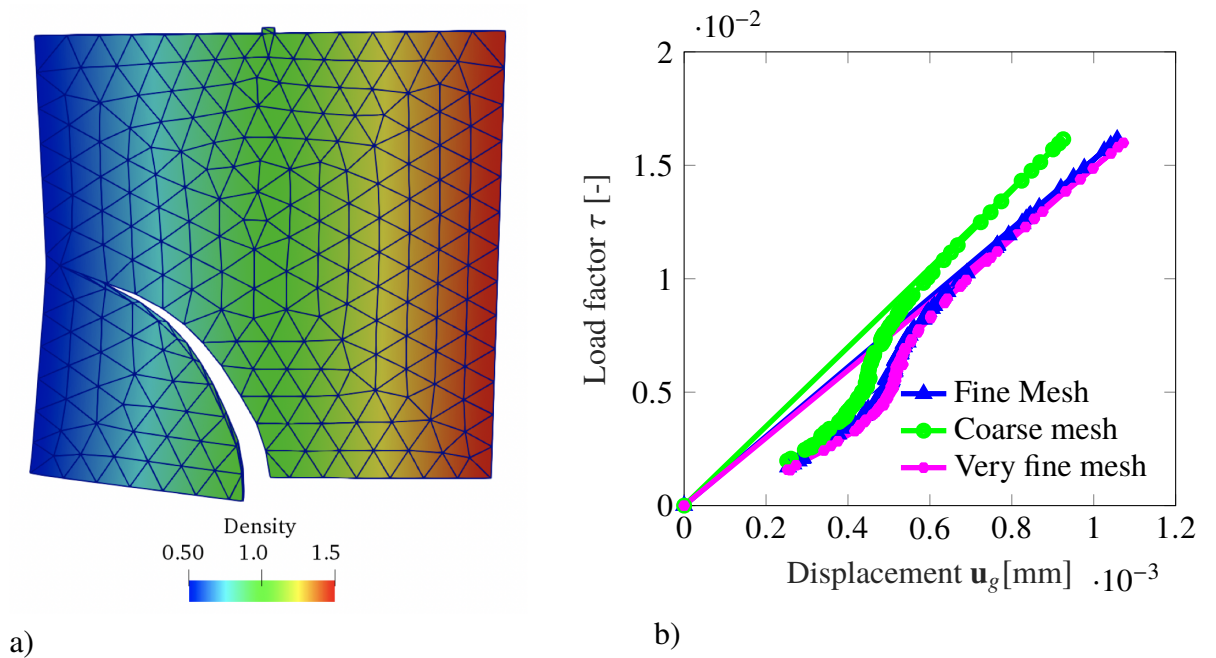


Figure 6.11: Heterogeneous 3D plate. a) model geometry with predicted crack, material distribution and coarse discretisation with 1340 tetrahedral elements. b) load-displacement response for three consecutive h-refinements.

6.4 Summary

This chapter presented a formulation for brittle fracture in elastic solids within the context of configurational mechanics that includes the influence of heterogeneous density distribution. Configurational forces are the driver for crack propagation, and it was shown that in order to evaluate these forces correctly forces at the crack front it is necessary to have a spatially smooth density field, with higher regularity than if the field is directly approximated on the finite element mesh. Therefore, density data is approximated as a smooth field using a Moving Weighted Least Squares method, that allows for the computation of higher-order derivatives. Numerical convergence was demonstrated for a simple finite plate, and the use of singularity elements was shown to further improve the rate of convergence. Furthermore, the calculated release energy rate was verified using centered FDM. The numerical example of plate heterogeneous material properties have been presented to demonstrate both the accuracy and robustness of the formulation.

In the next Chapter 7, the demonstrated configurational force driven approach is utilised for analysing release energy and crack propagation in adapted bones.

Chapter 7

Numerical investigations

The objective of this chapter is to assess the current state of development of the implemented framework in the form of numerical examples. In the first example, the remodelling of a proximal femur is considered. The developed model is utilised for assessment of the long-time response of the proximal femur bone to a hip replacement treatment. Subsequently, a comparative study of discrete and smeared approaches for approximating fracture is conducted. The presentation and discussion of the numerical results provide an insight into the potential of both methods for simulating large-scale crack propagation problems with homogeneous and heterogeneous material properties. Finally, a full framework for estimating bone fracture resistance is demonstrated. It combines all the advancements presented in Chapters 3, 4 and 6 to simulate training regime exerted on the equine MC3 bone and the following crack propagation.

7.1 Simulation of proximal femur adaptation

The proposed finite element framework has to be able to predict bone density distributions of horses undergoing specific trainings, as stated in Section 1.1. The accurate estimation of the bone stiffness is essential for calculating its resistance to fracture and possible injury prevention. In order to validate predictive capabilities of the used bone remodelling model, a well-studied hip-replacement procedure is considered and its long term influence on the density distribution. Total hip replacement is a common surgical procedure, where the damaged proximal end of the femur is replaced by a prosthesis, typically a metal ball attached to a stem inserted inside the bone. The method is very effective for fixing major fractures for elderly patients. However, long-term studies show that in active young people, such implantation can cause stress shielding in the bone (Kronick et al., 1997). When loads are carried by the

significantly more stiff metal stem, the surrounding bone tissue exhibits intense remodelling leading to the loss of the density and ultimately painful loosening of the implant. Therefore, an efficient and accurate FEM simulation of the long-term bone response can be an invaluable tool to support decision making for patient-specific treatments.

7.1.1 Proximal femur example

In this subsection, following Kuhl and Balle (2005) the functional adaptation of proximal femur without implants is considered. The previously presented bone remodelling implementation (see Chapter 4) is augmented with the option to include linear elastic elements that are not subjected to the change of material properties in time (like an implant). Bone geometry and the applied loading cases are illustrated in Figure 7.1. Since limited data is accessible for the three-dimensional loading conditions, only a 2D case is investigated (2D extruded). However, the extension to 3D is straightforward. Material and model parameters, based on

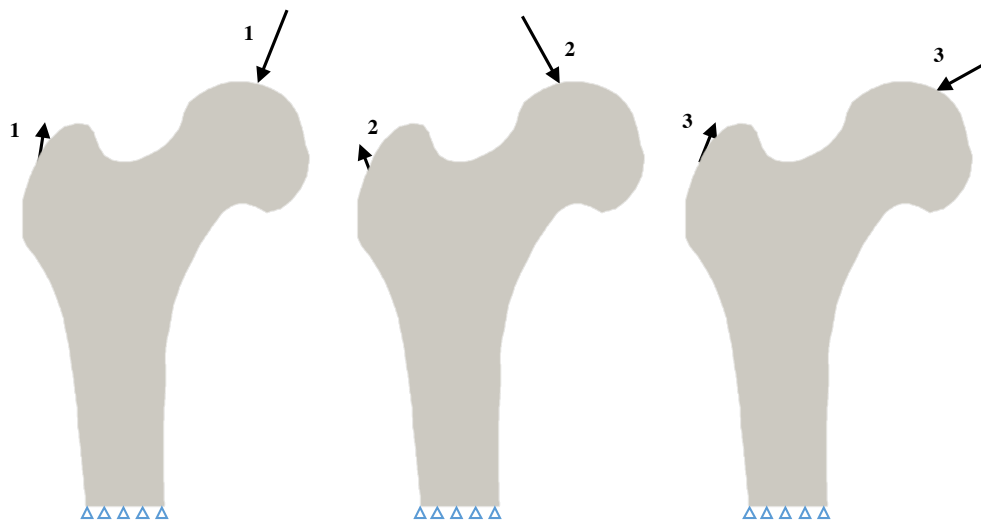


Figure 7.1: Proximal femur adaptation: geometry and loading cases. Load case 1 corresponds to the load condition for the midstance phase of gait, while load cases 2 and 3 represent the extreme cases of abduction and adduction.

Kuhl and Steinmann (2003); Kaczmarczyk and Pearce (2011), are presented in Table 7.1.

Parameter		Parameter	
E	500 MPa	c	1.0 d/cm ²
ν	0.2	m	3.0
ρ_0^*	1.2 g/cm ³	n	2.0
ψ_0^*	0.01 N/mm ²	Δt	0.1 d

Table 7.1: Material parameters used for functional adaptation of proximal femur.

The two-dimensional model is extruded in the third direction by 5 mm, and plane strain

Load case	Type of loading	Value (N)	Direction (deg)	Value (N)	Direction (deg)
1	Midstance phase of gait	2317	24	703	28
2	Extreme abduction	1158	-15	351	-8
3	Extreme adduction	1548	56	468	35

Table 7.2: Loading conditions on proximal femur.

boundary conditions are applied. The loads are applied to a small surface area to prevent the occurrence of singularities. Figure 7.2 illustrates the density distribution with respect to the prescribed loading scenario. Since all these cases never occur at the same time, final density pattern can be obtained by calculating the maximum density for all three cases separately as illustrated in Figure 7.3a). Next, as commonly reported in the literature a superposition of all three load cases is assumed to present an average daily loading. Figure 7.3b) shows the predicted density pattern at $t = 20$, when the biological equilibrium state is reached. Results illustrate the development of a region of dense trabecular bone bearing the compressive stress from the applied forces through the femoral head and neck, a second region of denser bone across the top of the femur, the formation of a lower density region with a triangular shape (Wards triangle) and a dense cortical shaft on the outer layers. Despite all the simplifications, the resulting structural arrangement is in a good agreement with the one observed from CT scans presented in Figure 7.3c). However, it is important to note that while simulating bone functional adaptation, a detailed knowledge of the actual loading situation is essential. By assuming that all three cases occur simultaneously in some loading conditions forces could balance each other, which does not take place in nature. Therefore, density patterns in Figures 7.3a) and b) are noticeably different. The representation of average daily loading exerted on the bones for numerical simulation remains an open challenged in computational biomechanics.

7.1.2 Proximal femur in presence of an implant

Finally, the proposed algorithm is utilised to predict density after total hip surgery of proximal femur presented in the previous section. Parameters of the analysis are the same as earlier (see Table 7.1). Virtually inserted prosthesis as presented in Figure 7.4 is assumed to be made of titanium, same as in Kuhl and Balle (2005), with the following elastic parameters: $E = 110000\text{MPa}$ and $\nu = 0.3$. The stiff implant tends to transfer a significant portion of the loading from the joints and muscles to the distal portion of the implant stem. At the distal tip of the stem, forces are transferred to the outer bone shaft. The resulting high stress concentration induces an increase of bone mass at the distal tip of the prosthesis.

Furthermore, since almost the entire loading is carried by the proximal regions, the femur experiences so-called stress shielding, resulting in local resorption of bone. In conclusion, the presented method is clearly capable of virtually predicting the patient's specific response to various medical strategies.

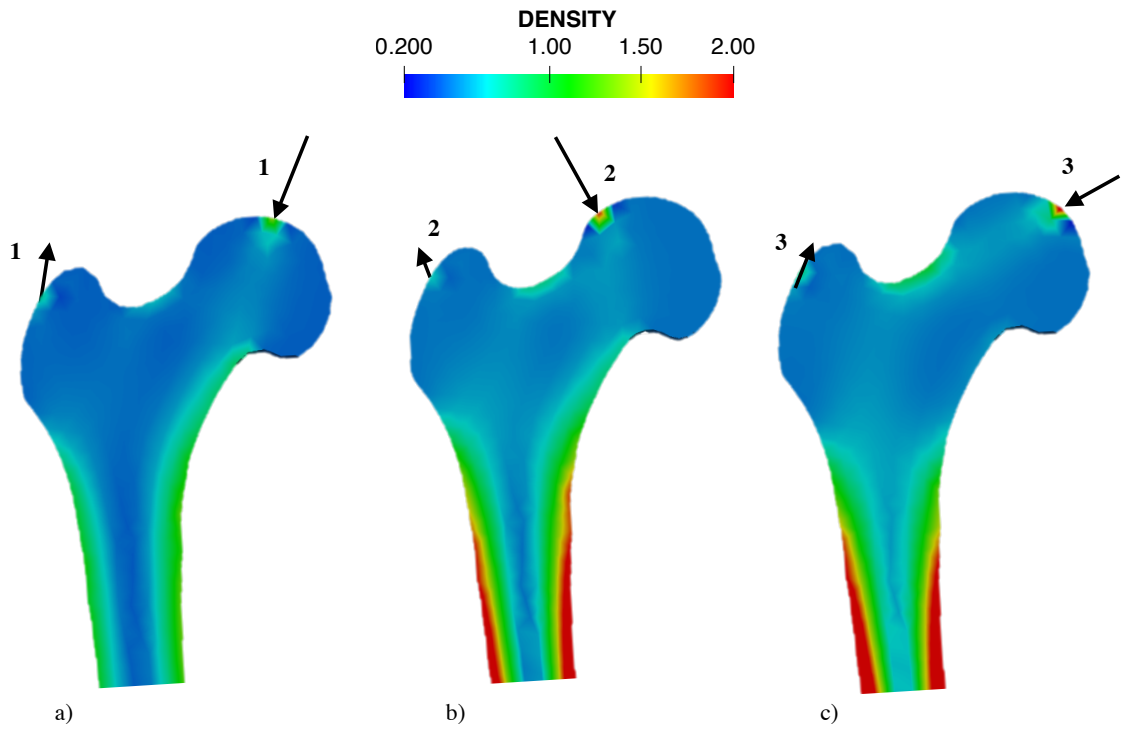


Figure 7.2: Density distribution for load cases 1, 2 and 3.

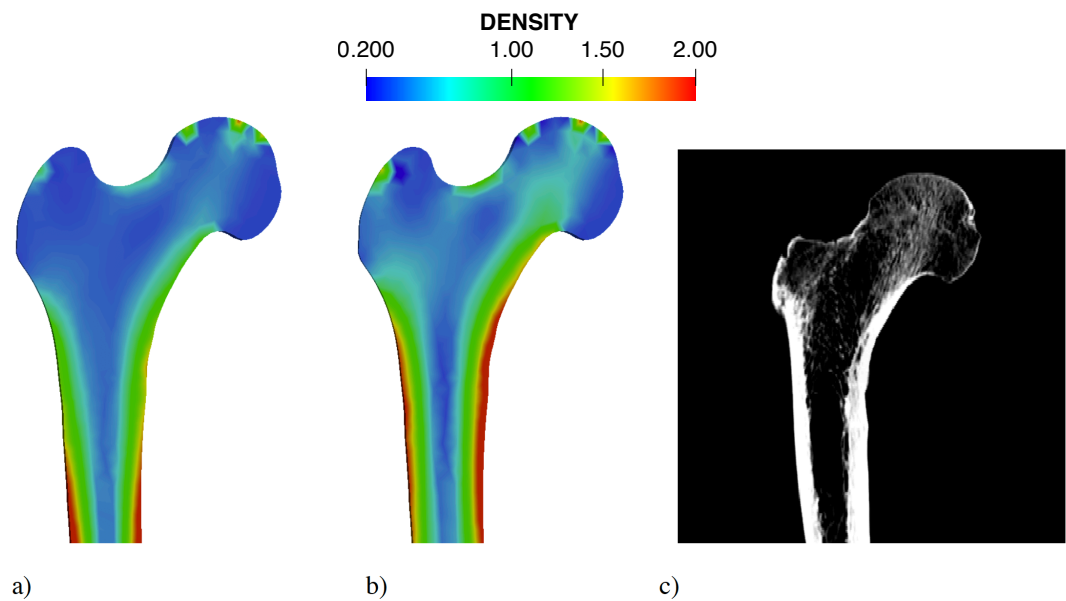


Figure 7.3: Predicted density distribution on the proximal femur. a) by calculating the maximum density form cases 1, 2 and 3 combined and b) by assuming all three load cases are applied at the same time. c) CT scan slice of a femur.

7.2 Comparison of smeared and discrete approaches for fracture

The main goal of the proposed framework is to utilise formulations that are robust, reliable and at the same time provide high accuracy for various conditions and bone geometries (as stated in Section 1.1). Such features are necessary to provide efficient tools for medical practitioners,

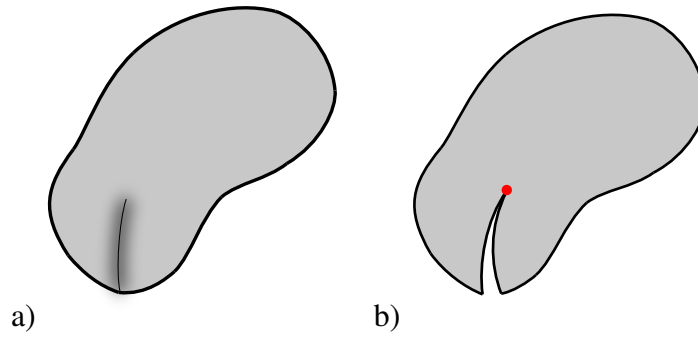


Figure 7.5: a) Phase-field smeared approximation and b) discrete representation of a crack with configurational mechanics.

7.2.1 Differences and similarities

Implementation aspect

Schematic representation of the two approaches in a continuum is depicted in Figure 7.5. Both implementations for phase-field and configurational force approach has been described in details in Chapters 5 and 6, respectively. The phase-field method belongs to the family of smeared approach methods. The crack is resolved by minimisation of the regularised energy functional by additional field variable. Thanks to this idea, it is possible to simulate phenomena like nucleation, propagation, branching and crack arrest by solving a coupled system of equations (see Eq. 5.23) on the volume without any additional equations. In configurational force method presented in this thesis, to simulate propagation, two balance equations have to be satisfied in the volume (Eq. 6.14 and 6.15) and additional constraints like Griffith criterion (Eq. 6.18) or maximum dissipation inequality (Eq. 6.19) at the crack front nodes.

The governing equations for both approaches are thermodynamically consistent. They can be solved using a monolithic scheme, augmented with arc-length equation (Eq. 5.40 and Eq. 6.35). However, as previously mentioned, due to non-convexity of the related free-energy functional in phase-field, typically a robust but slowly converging staggered solution scheme is chosen (see Section 5.2.5).

Irreversibility of the crack

To enforce the irreversible nature of the cracks, many different techniques have been developed for phase-field. In this study, the decrease of the phase-field variable, i.e. crack healing is prevented by introducing a historic variable $\mathcal{H}(t)$ (Eq. 5.24). In the discrete approach

presented herein, irreversibility is accomplished by satisfying the maximal dissipation principle (Eq. 6.19), i.e. material forces will never move crack front backwards.

Crack resolution

Any crack propagation inherently requires sufficiently fine mesh to resolve evolving discontinuity within the domain. However, discrete and smeared approaches have different demands in that regard. In phase-field, the need to resolve the small length scale l_0 to the diffusive crack approximation (ideally $l_0 \rightarrow 0$) demands extremely fine meshes. Therefore, an adaptive local mesh refinement is essential for any efficient implementation of the phase-field for fracture (Lee et al., 2016). In contrast, the configurational mechanics framework for crack propagation does not require fine meshes. Since the algorithm has to adjust the mesh anyhow, it is possible to start the analysis with a very coarse mesh. The additional mesh smoothing and mesh cutting algorithms used in the implementation presented in this work ensure that the discrete crack surface has a satisfactory resolution. Although it has not been implemented in this work, adaptive mesh refinement in phase-field is much more troublesome due to the necessity of efficient projection of the historic variables after refinement. In the configurational approach, the crack driving forces are stored at the nodes of the crack front, therefore, their calculation for adapting mesh is straightforward.

Crack initiation and branching

The theory of material forces always requires a pre-existing crack to evaluate the driving forces at the tip. In this work, a definition of an arbitrary cutting surface is required at the beginning of each analysis that will define initial crack in the considered domain (see, e.g. in Figure 7.18). Moreover, simulating the crack branching phenomenon would require a definition of additional criterion as presented in Ozenc et al. (2016) and an additional algorithm to partition the discrete crack surface. On the contrary, the smeared method like phase-field, can reproduce nucleation and branching of the cracks in a straightforward manner. No additional equations are required.

Post-processing

The material force approach avoids the need for post-processing since configurational forces and the fracture energy release rate, are expressed exclusively in terms of nodal quantities. The quantities like crack front length, crack surface or stress intensity factors area can be naturally

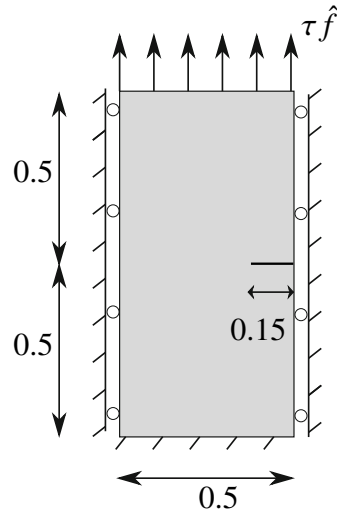


Figure 7.6: Boundary conditions for plate under tension. Thickness of the plate $t = 0.05$. Units in mm.

calculated. In smeared approaches, an additional post-processing effort is necessary to identify and measure the resulting crack geometry. Typically, an iso-volume of the phase-field is calculated (or iso-curve in 2D) using threshold values $d = 0.9, 0.95$ or 0.99 . However, it is worth to note that the obtained volume (or curve) is not always continuous. A more in-depth investigation about the resulting crack length can be found in Borst et al. (2015).

Heterogeneities

As previously mentioned, phase-field can effectively tackle various heterogeneities (see, e.g. (Nguyen et al., 2015)) or layered structures without any modifications into the formulation. Configurational mechanics approach is currently limited to smoothly spatially varying inhomogeneities (see 6.15). Moreover, since the mesh in the material domain is constantly changing to resolve new crack surfaces, it is then necessary to store data about heterogeneous material properties (Young's modulus or density) on the background mesh and approximate it onto new mesh after each mesh reconstruction.

7.2.2 Comparative numerical examples

To directly compare the performance of both methods, three numerical examples of crack propagation in brittle materials are presented. First example considers homogeneous material properties, the second one heterogeneous, and the third one includes varying Griffith energy g_c parameter. In all the cases, crack propagation for brittle fracture problem is applied to the three-dimensional plate with a notch on the right-hand side undergoing tensile loading as presented in Figure 7.6. The domain is fixed at the bottom and has constrained lateral

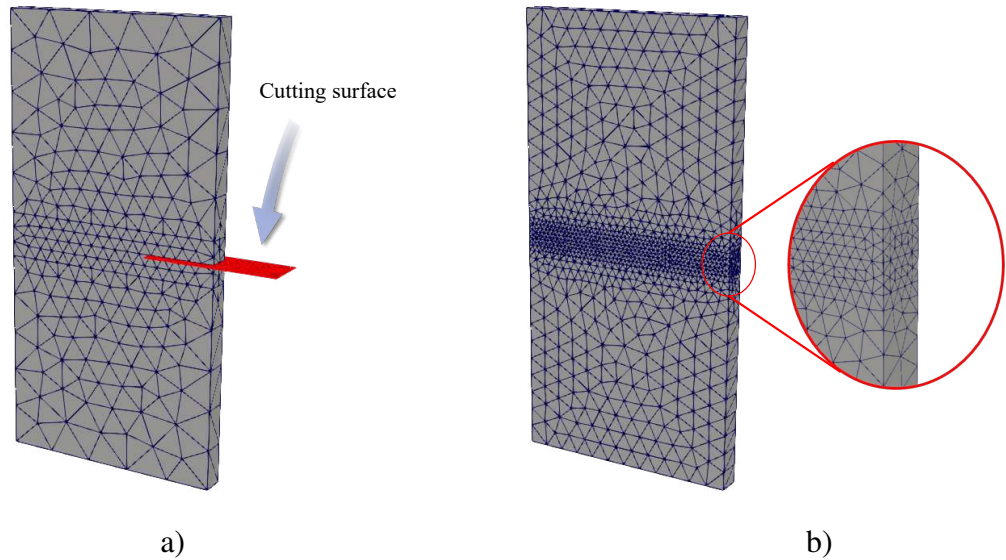


Figure 7.7: Discretisation meshes for configurational mechanics a) and phase-field approach b). Note that an initial crack is introduced by cutting the mesh with a rectangular plane. In all cases, quadratic tetrahedral elements are used. For phase-field the mesh element size is chosen such that $h \approx 0.01$ mm, i.e. $2h \approx l_0$.

movement. The material parameters are $E = 210\text{MPa}$, $\nu = 0.3$, $g_c = 1 \cdot 10^{-3}\text{N/mm}$. An additional set of parameters for phase-field are: length scale parameter $l_0 = 0.02\text{mm}$, quadratic degradation function $g(d) = (1 - d)^2$, arc-length parameters $\Delta\tau_1^F = 0.2$ and $a = 0.1$ (see Section 5.3). The only parameter necessary for configurational mechanics approach is the target increment of the crack area $\Delta A_\Gamma = 1 \cdot 10^{-4}$ for the arc-length method (see Eq. 6.35) which is a further advantage of this approach. The step size for both methods is chosen such that the typical load step takes ~ 7 Newton iterations to converge. The meshes presented in Figure 7.7 consist of 1150 and 17933 quadratic tetrahedral elements for material force driven and phase-field method, respectively.

Homogeneous case example

The load-displacement curves and the development of the approximated fractures for both methods are shown in Figures 7.9 and 7.8, respectively. As expected, the applied tensile load extends the initial notch until it reaches the opposite edge of the plate and splits it into two pieces.

From the curves in Figure 7.9, it can be observed that the structure exhibits snap-back behaviour after reaching the critical load. It is clear that phase-field dissipates energy at the onset of failure; therefore, the solution deviates from linear fracture mechanics result obtained with configurational force approach. To mitigate that difference, the cubic degradation function could be used, introducing another material parameter s , which would have to be adjusted (Vignollet et al., 2014).

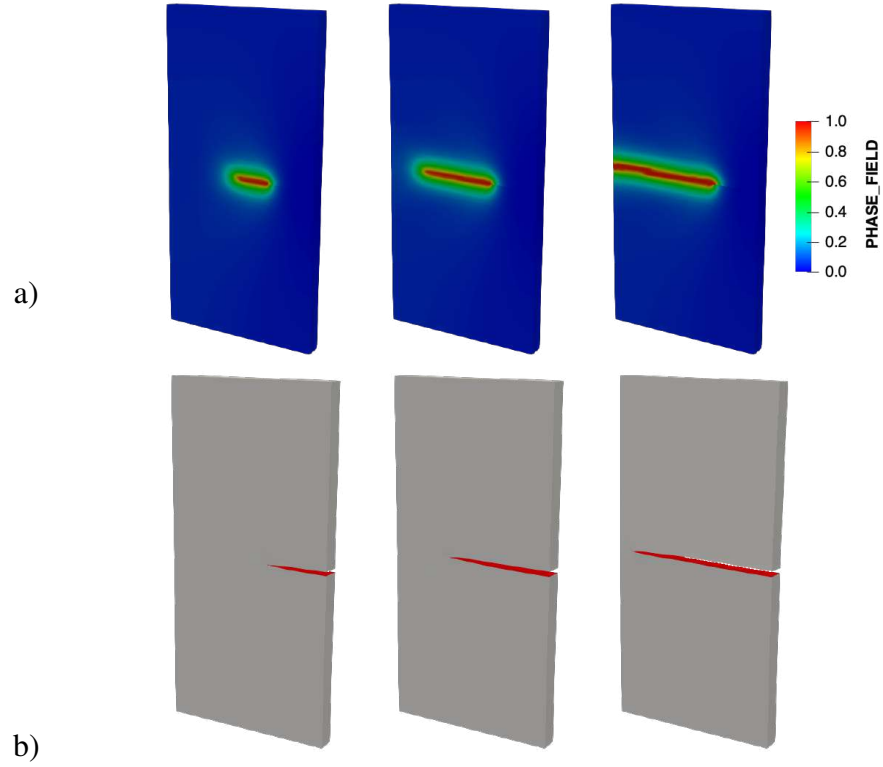


Figure 7.8: a) Propagation of the phase-field variable d for the plate and b) discrete crack surfaces obtained with configurational mechanics.

However, it was found that by switching to cubic function, the monolithic solver struggles to converge at the peak-force region. This problem is almost never mentioned in the case of 2D analyses, e.g. in May et al. (2016); de Borst and Verhoosel (2016); Liu et al. (2016). It is known that, due to non-convexity of the underlying functional in phase-field, Newton-Raphson scheme performs poorly. Several strategies have been proposed to address this (see Section 5.2.5), like, e.g. arc-length control utilised in this work. However, this example confirms that arc-length can enhance the robustness only in specific conditions and fails when e.g. 3D geometry and cubic degradation function is used, like in the example presented herein. Overall, considering the limitations of the phase-field method, the results from both approaches are in very good agreement. Note that, the value of displacement presented in Figure 7.9 (and the following examples) is known as the generalised displacement and does not represent a particular point on the structure, but its value is work conjugate to the applied forces and is calculated as $\mathbf{u}_g = 2\Psi/\tau\mathbf{f}$, where $\mathbf{f} = 1\text{N}$ is the reference force, and Ψ is the total elastic energy integrated over the domain, τ is the arc-length load factor, and \mathbf{u}_g is the generalised displacement.

Finally, the execution time for both methods is compared in Figure 7.10. Unsurprisingly, due to the requirement of much finer meshes, the smeared approximation is up to 20 times slower than configurational mechanics approach for this particular problem. The difference would possibly decrease noticeably when adaptive mesh refinement is used for phase-field. For a more fair comparison, the example with configurational mechanics is repeated using

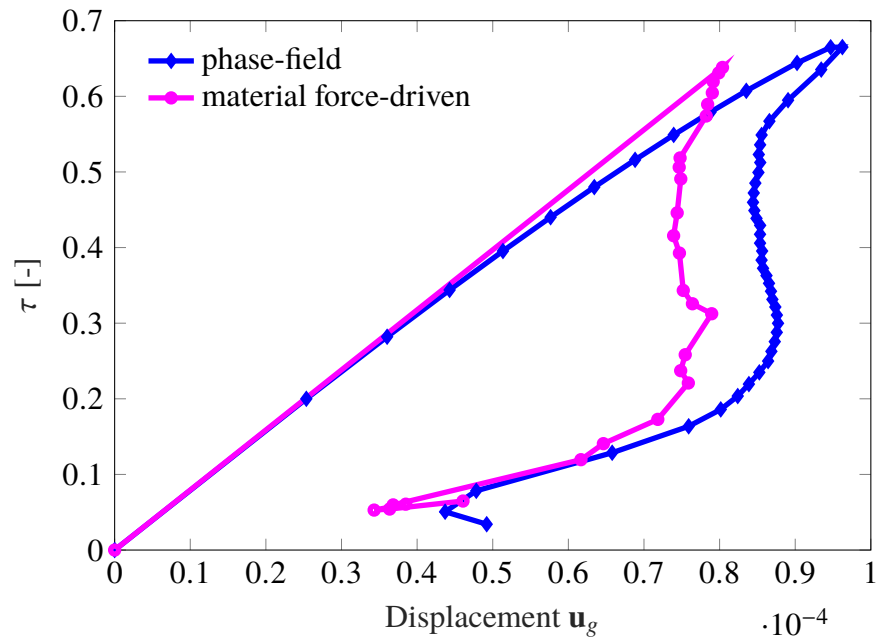


Figure 7.9: Load factor τ versus representative displacement \mathbf{u}_g for phase-field and material force driven example.

the same mesh as presented in Figure 7.7. It can be noticed that runtimes, in this case, are almost identical, proving that both implementations have similar performance and the great advantage of material force approach arises from the formulation. The numerical result was indistinguishable from the one obtained with the coarse mesh; therefore, it is not shown. It is worth to note that the solution time in material force approach depends mainly on the number of nodes at the crack front.

Heterogeneous case example

In the next example, spatially varying material properties are considered. The density field is expressed as: $\rho(x, y, z) = 9y^2 + 1$ (see Figure 7.11a) and simple correlation on the Young's modulus is introduced such that $E(\rho) = \rho E_0$, where $E_0 = 210\text{MPa}$. The remaining material and model parameters are the same as in the previous example. The influence of the heterogeneous material properties on resulting crack path and load-displacement curves is depicted in Figures 7.11 and 7.12a), respectively. The results show that the gradient of density makes the crack to slightly curve towards the softer part of the solid. Similarly to the homogeneous case, the outcomes from both methods show very good agreement.

Note that for inhomogeneous materials, the critical fracture g_c should also be varying in the domain. Several research groups in the biomechanics community have argued for a strong correlation between the density and the energy release rate (Shen et al., 2019). This has not been implemented yet in the configurational mechanics approach. In contrast, the application in phase-field is straightforward.

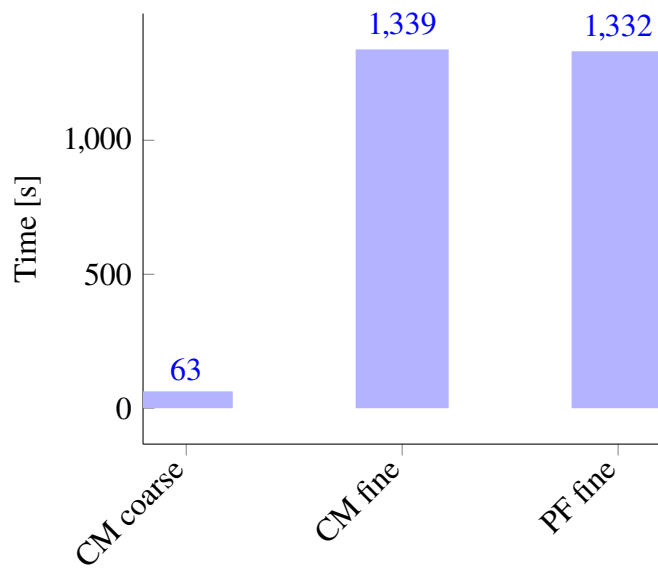


Figure 7.10: Execution time on 12 CPUs for configurational mechanics approach (CM) using coarse and fine meshes and phase-field method (PF).

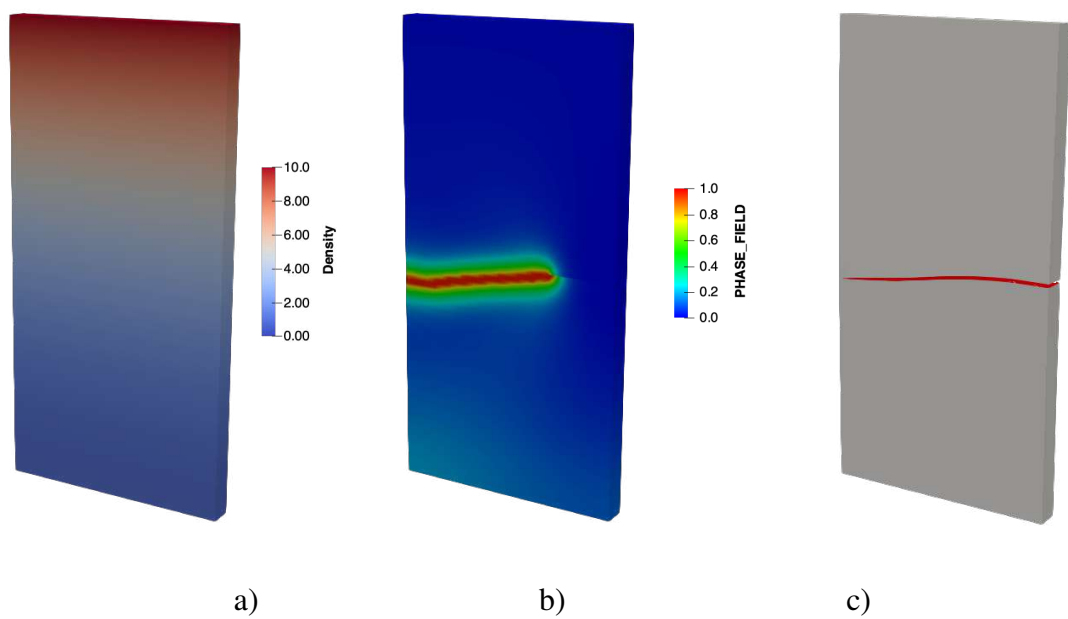


Figure 7.11: Crack propagation with heterogeneous material properties. a) Density distribution. b) Phase-field variable evolution. c) Discrete crack path.

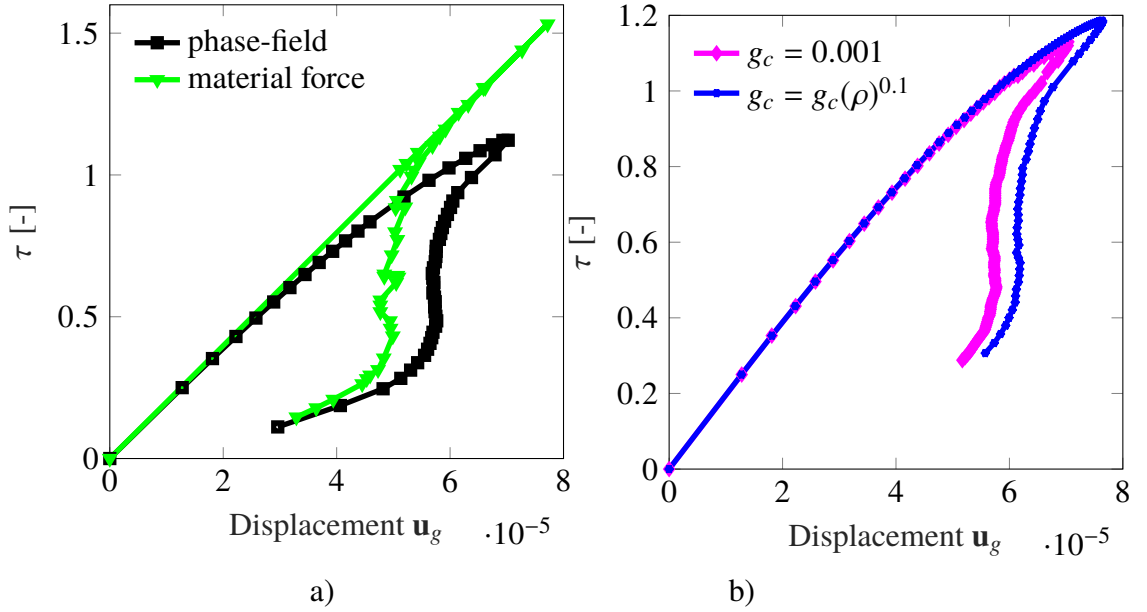


Figure 7.12: Force versus displacement curves. a) For phase-field and configurational force approach. b) Phase-field using spatially varying g_c parameter.

In the next example, once again, heterogeneous material properties are applied as in Figure 7.11a) and additionally, parameter g_c is correlated to density such that $g_c(\rho) = \rho^{0.1}$ N/mm. The results are compared with the previous case where g_c was constant in Figure 7.12b). Although the imposed correlation between Griffith energy and density is very weak, the difference in the load-displacement curves is noticeable. It was also shown recently in proximal humerus bone fracture investigation that the assumption of constant g_c led to quite different fracture patterns than the one obtained experimentally (Shen et al., 2019). Therefore, it can be concluded that for future investigation, the appropriate inhomogeneous law is necessary to accurately capture the complex bone fracture profiles.

In the spirit of using the least complex and numerically efficient methods for the developed framework, the configurational mechanics approach is chosen for a case study of MC3 bone fracture resistance assessment presented in the following section.

7.3 Fracture resistance of MC3 bone following adaptation

7.3.1 Metacarpal adaptation

This subsection considers the bone adaptation and its influence on the propensity for fracture of an equine 3rd metacarpal bone (MC3). The proposed density growth model is applied to a subject-specific three-dimensional, full-scale model of equine MC3 bone derived from CT scanning. Three cases are studied, all using the same material parameters presented in Table 7.3. Stiffness and porosity values are derived from mechanical tests (Les et al.,

1994), whereas other values are from previous studies of the human tibia (Pang et al., 2012; Waffenschmidt et al., 2012). Each case considers a different function for the parameter c that defines the rate of bone adaptation used to compute the mass source, \mathcal{R}_0 , according to Eq. 4.8. In Case 1, c is constant. For Case 2 and Case 3 different bell functions (Eq. 4.9) are used. The parameters for each case are presented in Table 7.4.

The finite element mesh used in all cases comprises 17041 tetrahedral elements. It was generated by discretising the segmented geometry from CT scan data - see Figure 7.13. The initial density is chosen to be homogeneous since, in the thermodynamic-based model, the starting density does not have a significant effect on the final bone density distribution (similar to other models at biological equilibrium (Kuhl and Steinmann, 2003)). Boundary conditions are simplified to two representative forces (5 [kN] each) spanning over a small area based on pressure film studies (Brama et al., 2001), as demonstrated in Figure 7.13. The two forces are often considered in the literature as an equivalent of joint peak force at the mid-stance of a horse gait. They are applied by linearly increasing their magnitude within the first 5 time steps and held constant thereafter. It is worth to note that the applied load should be considered as averaged long term forces mimicking mechanical load on the bone over a long time period. Furthermore, displacement degrees of freedom at the proximal end are fixed. In reality, metacarpal bone articulates with proximal phalanx bone (P1). Adaptive time-stepping scheme (using PETSc (Balay et al., 2018)) is used in all the simulations with an initial time step $\Delta t = 0.5$ [days(d)], maximum time step of $\Delta t_{\max} = 50$ [d] and minimum of $\Delta t_{\min} = 0.05$ [d].

Parameter	Description	Value
E	Young's modulus	4700 [MPa]
ν	Poisson ratio	0.3 [-]
ρ_0^*	Initial density	1.0 [g/cm ³]
ψ_0^*	Target energy density	0.0275 [MPa]
c	Density growth velocity	1.0 [d/cm ²]
m	Algorithmic exponent	3.25 [-]
n	Porosity exponent	2.25 [-] (Les et al., 1994)

Table 7.3: Material parameters used for the simulations of 3rd metacarpal bone adaptation (Waffenschmidt et al., 2012; Les et al., 1994).

Case	c	b	ρ^{\max}	ρ^{\min}
1	1	-	-	-
2	Eq. (4.9)	1000	2.5 [g/cm ³]	0.3 [g/cm ³]
3	Eq. (4.9)	30	1.8 [g/cm ³]	1.0 [g/cm ³]

Table 7.4: Presentation of three cases input parameters for the evaluation of coefficient c to compute mass source, \mathcal{R}_0 , as presented in Eq. 4.8. All cases have common material input parameters presented in Table 7.3.

Results of Case 1 are presented in Figure 7.14a), where density maps at five different points in time (0, 10, 40, 100, 700) [d] are visualised. Significant densification occurred immediately after reaching the maximum level of the loading, particularly in the proximity of the applied

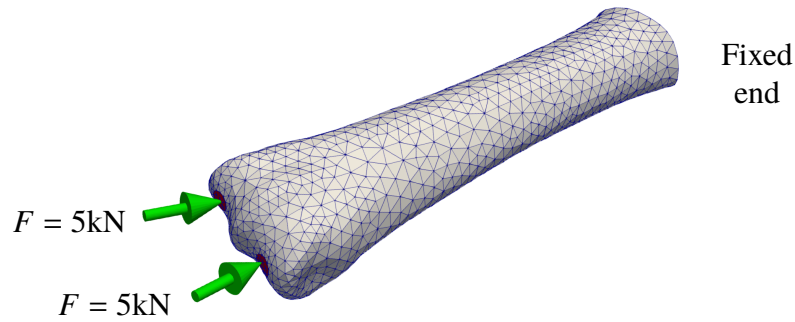
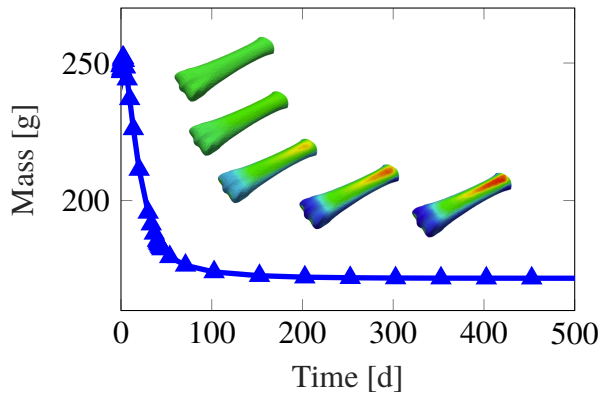


Figure 7.13: Finite element mesh of the equine 3rd metacarpal bone. The subject specific three-dimensional mesh consists of 14,041 quadratic tetrahedral elements and 70,901 degrees of freedom. To simulate the peak load of a gallop, 5 kN forces are applied on the lateral and medial side of the distal condyle.

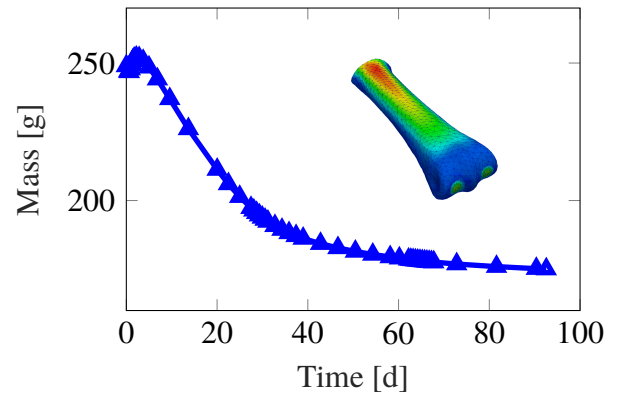
forces, associated with high levels of strain energy. Conversely, areas with low levels of strain energy experience a reduction in density. After 100 [d], biological equilibrium was achieved, and no further changes in density took place. The resulting maximum density is $2.8 \text{ [g/cm}^3\text{]}$ and the minimum is close to zero. The maximum density for Case 1 is noticeably higher than in the actual equine bones (Yamada et al., 2015), and the minimum density is unrealistically close to zero. There is clearly a need to somewhat constrain upper and lower bounds for density in order to produce more realistic outcomes. To achieve this, the bell shape function presented in Eq. 4.9 is used for the next two analyses (Case 2 and Case 3). The results for Case 2 are plotted in Figure 7.14b). The last converged step takes place at $t = 93 \text{ [d]}$. By setting a high value of b , the transition between densities is very sharp, and the algorithm encounters convergence difficulties, even with adaptive time-stepping, and biological equilibrium cannot be achieved in this case. For Case 3, a more moderate value for the exponent in the bell function was chosen along with a narrower density range than those chosen for Case 2 (see Table 7.17). The plot presented in Figure 7.14c) demonstrates how these values influence the results of the analysis. It is evident that with a much lower value for the exponent b , the algorithm no longer has problems converging. Furthermore, reducing the range between the upper and lower bounds of density has a significant impact on the results. The dense cortical shaft on the dorsal side of the bone is less dense and covers a much larger region. Furthermore, unrealistically low values of densities have been eliminated. However, as with the previous case, the overall solution converges to the same mass (and density distribution) as in Case 1, albeit requiring significantly more time steps.

To validate whether the utilised discretisation is sufficient, a convergence study is conducted. The same analysis, as presented in Case 1 (see Figure 7.14a)) is carried out using 1st and 3rd order elements. The comparison of the results in Figure 7.15a) shows the minimal difference between p-refinements.

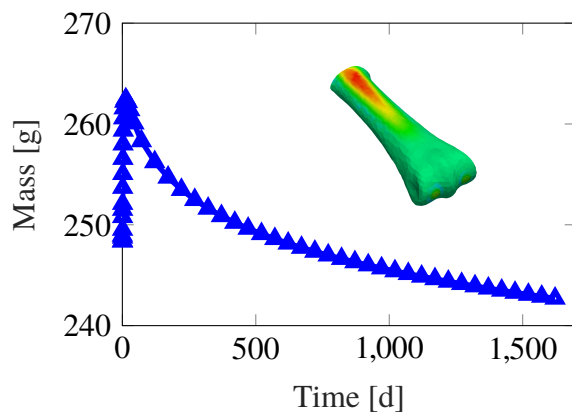
In the next example, instead of using constant initial density ρ_0^* , the data from CT-scan is mapped onto the mesh using L_2 -projection described in Section 3.2.1. The results in Figure 7.15b) show, as expected, that in the equilibrium, the resulting mass is almost exactly



(a) Case 1.



(b) Case 2.



(c) Case 3.

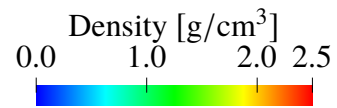


Figure 7.14: Change in bone mass over time for 3 cases (see Table 7.4). Density distribution contours in 3rd metacarpal bone at five snapshots in time in a) and at the last converged step for b) and c).

the same as in the homogeneous case. Thereby proving that the used phenomenological model is insensitive to the initial density state.

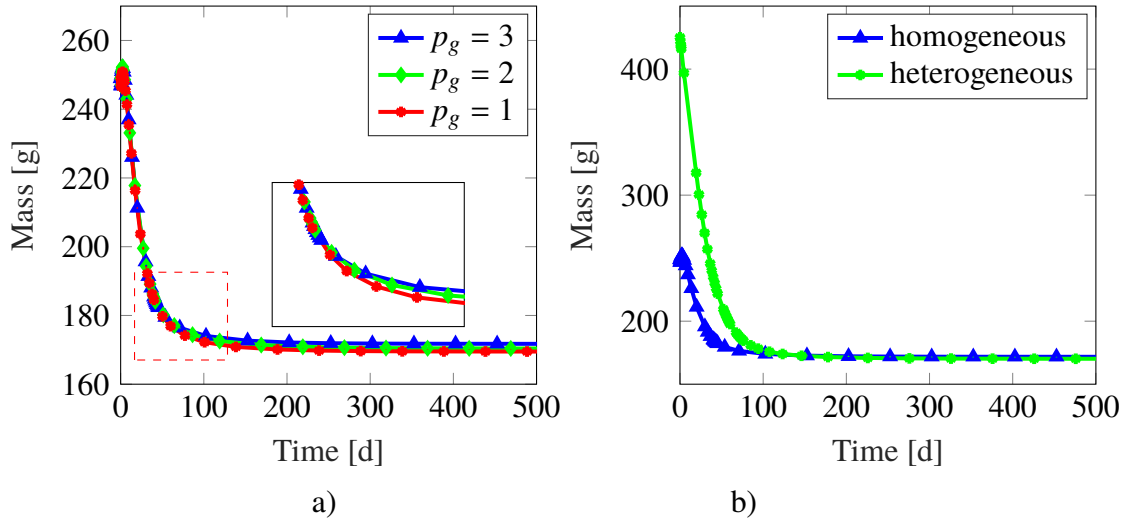


Figure 7.15: a) Convergence study. Evolution of the total mass of the bone using 1st, 2nd and 3rd order tetrahedral elements. b) Density evolution using constant initial density ρ_0^* (homogeneous) and heterogeneous initial density obtained from CT-scan data.

Furthermore, at the equilibrium stage, density was measured in the region of the sagittal grooves, as demonstrated in Figure 7.16a), the most frequent site of fracture initiation in MC3 bone. Simultaneously, the density of the bone in the same region of a cadaver horse limb was derived from the CT scan using quantitative computed tomography with calibrated dipotassium phosphate phantoms (see Chapter 2). The density profiles along the line presented in Figure 7.16 are in satisfying agreement. Although the density levels are mostly different in the entire bone, due to simplified boundary conditions, at least in the regions where the pressures are applied, i.e. sagittal grooves the density levels are quantitatively comparable with the measurements. It is particularly important since the majority of the fracture originates from these regions.

When adaptation converges to an equilibrium state, an interesting phenomenon can be observed. For each density level, there is a corresponding value of constant strain energy density ψ . This result is a direct consequence of the constitutive Eq. 4.8 i.e. when expression therein is equal to 0. This feature can be visualised by plotting the strain energy density on the contours of constant density levels, as presented in Figure 7.17.

7.3.2 Fracture risk and energy release of equine metacarpal

In this section, the configurational force driven approach for fracture is utilised for the assessment of MC3 bone's likelihood for fracture. As previously introduced in Chapter 6, to achieve this additional configurational forces arising from inhomogeneities (see Section 6.2.2)

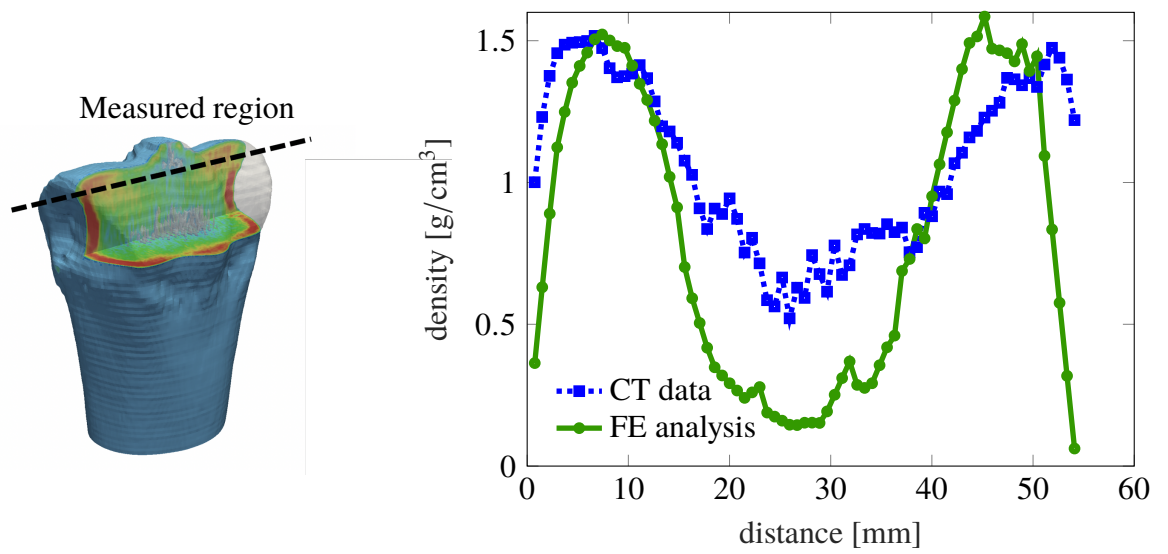


Figure 7.16: Comparison of the bone mineral density measured from CT and FEM results (right) at the region of interest (left).

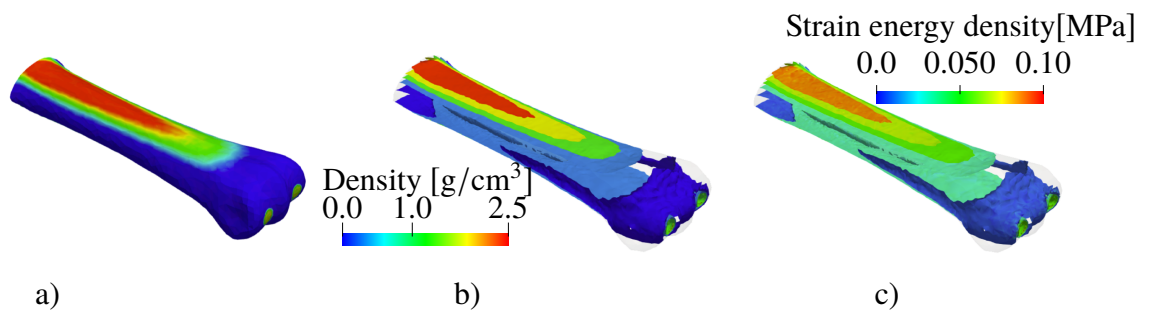


Figure 7.17: Case 1: Biological equilibrium state. a) Density map. b) Contours of density. c) Strain energy density plotted on the contours of density.

associated with spatially varying bone density are introduced into the formulation. This allows for the accurate assessment of the likelihood of a crack to propagate and to simulate the subsequent propagation of fractures in the bone.

An additional goal is to investigate bone fracture at different stages of bone adaptation, utilising the results from bone adaptation analysis. Similar concepts of combined adaptation and fracture analyses have been presented before (Hambli et al., 2013). However, it utilised a different adaptation model (Huiskes et al., 2000) and continuum damage mechanics approach for fracture, both of which require many more parameters to calibrate. The problem of bone adaptation and crack propagation or calculation of crack release energy has different boundary conditions and geometry. To solve the staggered coupled problem, initially, bone adaptation is simulated under long-term effective loads applied without initial crack. Subsequently, an initial crack is placed on the resulting mesh to compute the effect of short-term loads or extreme cycling loading. The two different remodelling and crack propagation meshes are tailored for each type of problem analysed, respectively. Note that in the presented approach, one can load initial density from CT scans, run bone adaptation analysis and subsequently introduce crack to calculate the release energy. It is also possible to load densities directly onto the mesh with a prescribed fracture. In each case, initial density is approximated using MWLS and then projected on the current material configuration.

7.3.3 Fracture energy release in bone using CT scan data

This numerical example considers the same bone as presented in Section 7.1. An initial crack was generated in the mesh using a cutting plane, as shown in Figure 7.18. A notch is situated at the origin of the most common location of lateral condyle fracture (Jacklin and Wright, 2012). The numerical analyses were undertaken using three meshes consisted of 6069, 10032 and 21189 tetrahedrons and repeated for 1st, 2nd and 3rd-order of global and local p - refinement at the crack tip. Boundary conditions and material parameters remain the same as in Table 7.3. The magnitude of the applied forces is also the same; however, in this case, the load is considered as a quasi-static case.

K_2HPO_4 calibration phantoms are used to convert the greyscale values from CT to bone mineral density. The phantoms consist of five burettes with reference densities, as shown previously in Section 3.5.1. The mechanical material properties are mapped onto the integration points of the metacarpal mesh using the MWLS method described in Section 3.3. Applying load induces configurational forces at the crack front, as shown in Figure 7.19. The direction of the vectors also indicates the direction of crack propagation. The values of numerically predicted maximal nodal energy release rates in Mode I (crack opening) for subsequent meshes are plotted in Figure 7.20. It can be seen that, for the same mesh, as the order of approximation increases, the energy release rate converges. A crack will propagate when the energy release rate G equals the material's resistance to crack extension, g_c . Assuming

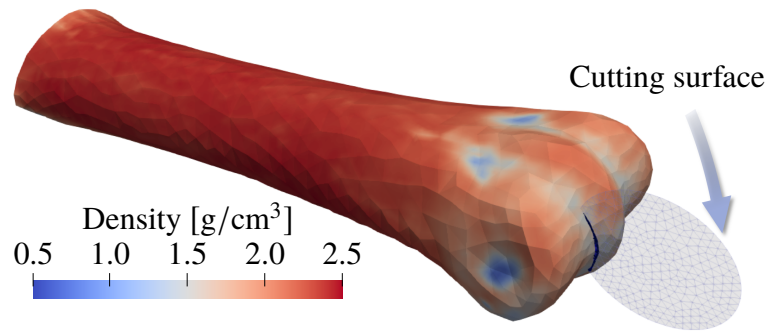


Figure 7.18: Bone geometry with mapped density from CT using MWLS approximation. In order to calculate the configurational forces, an initial crack is introduced by cutting the mesh with a circular surface. The cutting algorithm is not limited to planar cracks.

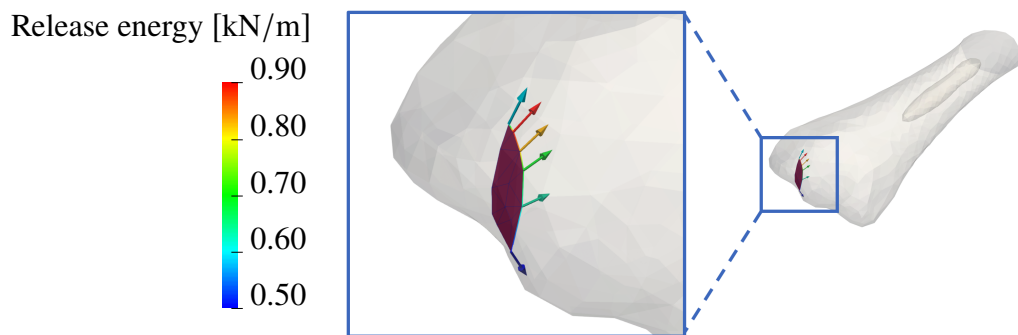


Figure 7.19: Crack surface and vectors of material (crack driving) forces at the front.

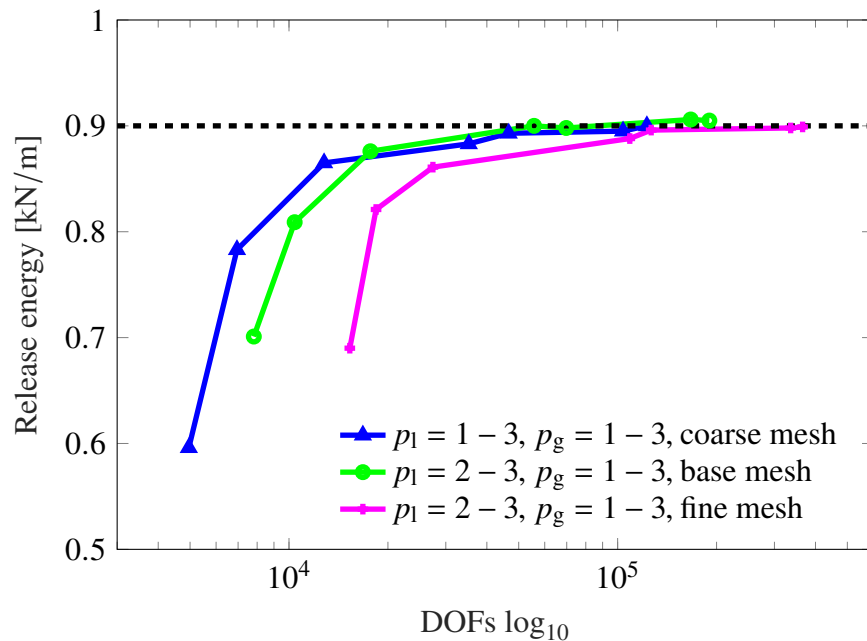


Figure 7.20: Convergence plot of maximum configurational force in Mode-I versus no of DOF (log₁₀) for subsequent discretisations and p - refinements. The results are mesh independent since they all converge to the value for energy release of approximately $G_I = 0.9$ [kJ/m²] for increasing orders of approximation.

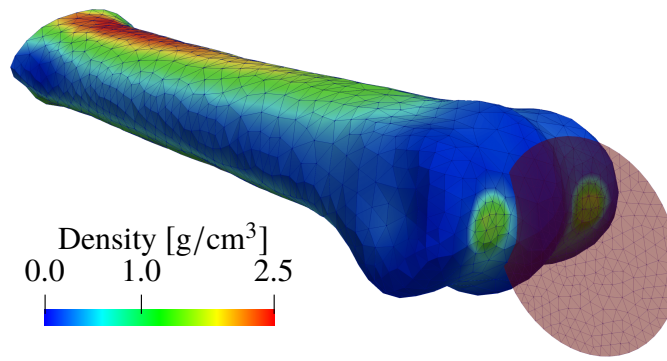


Figure 7.21: The resulting density distribution from the bone adaptation analysis is approximated directly onto integration points of the mesh used for fracture analysis using MWLS method described in Section 3.3. The cutting circular plane used to create an initial crack is also shown.

$g_c = 2.0 \text{ [kJ/m}^2\text{]}$ (Gasser and Holzapfel, 2007; Yan et al., 2008) it can be estimated that this particular metacarpal bone with this initial crack can sustain loading of approximately 2.2 times greater before a fracture starts to propagate.

7.3.4 Fracture energy release in bone using simulated density data

The previous example is extended to investigate the likelihood of fracture in an equine metacarpal bone at different phases of adaptation during training. However, this time, densities from a bone adaptation analysis (Section 7.1) are mapped onto the mesh consisting of 6069 elements, as shown in Figure 7.21. The same geometry and boundary conditions as in the previous example are used. The resulting energy release rate at different points in time of bone adaptation is illustrated in Figure 7.22 for three different local p - refinements. It can be observed that the variation in energy release rate for increased orders of approximation at the crack front is minimal. The numerical outcomes capture the general trend of increasing release energy rate over time. It can be noticed that by introducing a notch in the resorption zone, where no loading is applied, the configurational force attains larger values. This indicates that over time the bone becomes more prone to fracture in this specific region.

7.4 Crack propagation in MC3 bone

In this section, a full crack propagation for predicted density distributions is simulated. The magnitude of applied forces (Figure 7.13) is controlled by the crack area increment during each load step. The initial finite element mesh is the same as previously, as it is locally refined with the crack front advancement. The assumed bone's Griffith energy is equal to $2.0 \text{ [kJ/m}^2\text{]}$

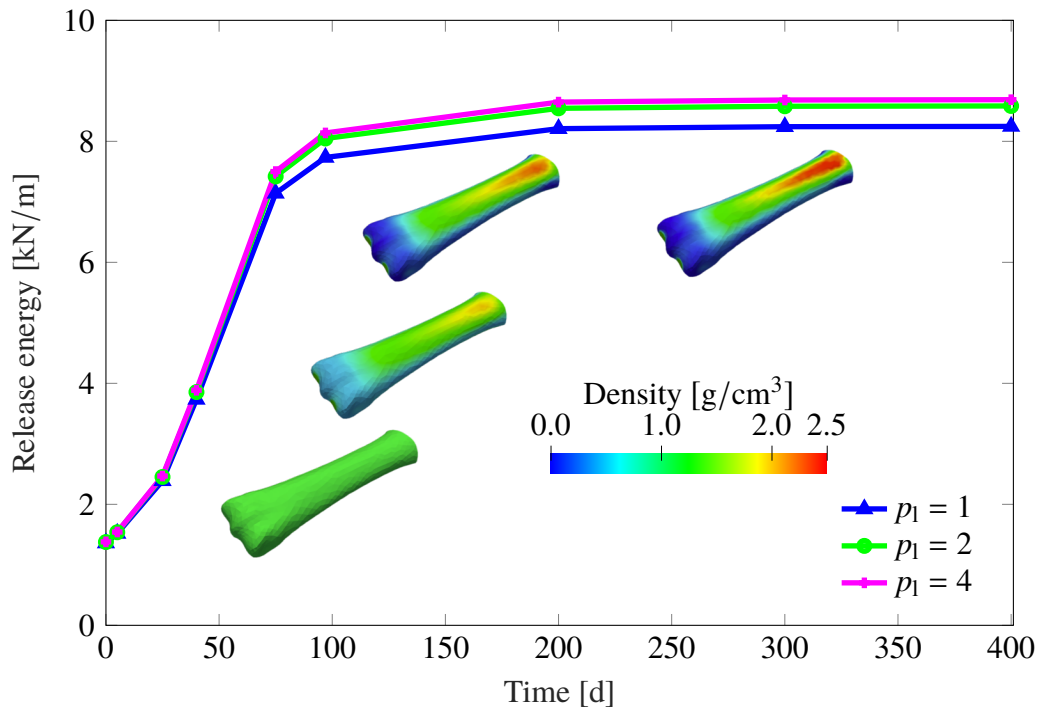


Figure 7.22: Fracture energy release rate over time during bone adaptation for three local p - refinements.

for the entire domain. The crack front nodes are moved only when the magnitude of crack driving forces is in equilibrium with the material resistance (Eq. 6.17). All five cases (time snapshots) are solved for 2nd order of approximation. The numerically predicted crack paths are shown in Figure 7.24. It can be seen that the crack has initially planar shape and then curves towards the lateral side of the bone. Load factor versus crack area plots are shown in Figure 7.23. Consistent with the previous analysis in Section 7.3.4, the metacarpal bone shows an increased propensity for fracture, i.e. for the same crack area, remodelled bone requires much lower force (load factor) to induce crack propagation. Low-density levels at the biological equilibrium ($t = 90$ and $t = 200$) also alternate the crack path, as can be observed the crack starts to curve much earlier than in the initial stages of remodelling.

As previously demonstrated (in Figure 6.7), modelling singularity can significantly improve the accuracy of the configurational forces at the crack front. In the next example, a bone with heterogeneous density distribution mapped from CT scan data is considered. The same CT scan data as in Figure 7.18 is used. In Figure 7.25a) results from crack analysis with and without Quarter Point elements are depicted. It is evident that an accurate stress state at the tip has a negligible impact on the full crack propagation analysis and the resulting load factor. From the load-crack area curves in Figure 7.25b), it can be observed that including density data from CT scans have a significant impact on the predicted load factor and crack path as well. Finally, the h and p convergence is investigated. The results presented in Figures 7.26a) and 7.26b) show good numerical convergence for consecutive refinements. It can be concluded that this formulation predicts crack path accurately with minimal effect from

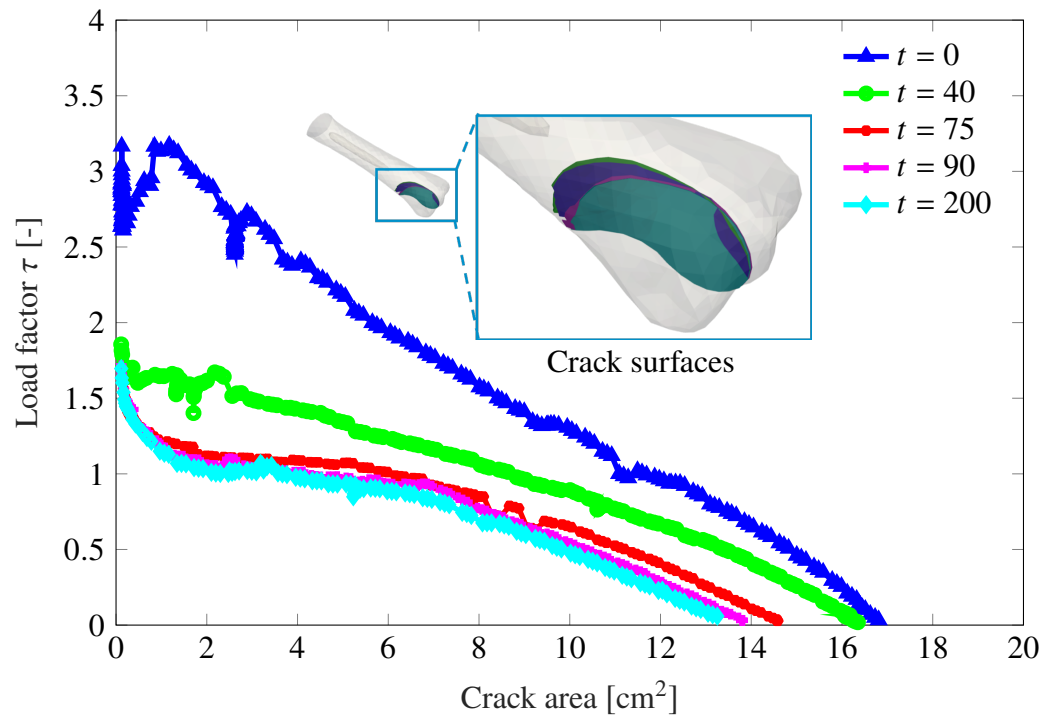


Figure 7.23: Load factor versus crack area for different moments in time during bone adaptation analysis. Bone density distribution influenced both load factor and the resulting crack surface.

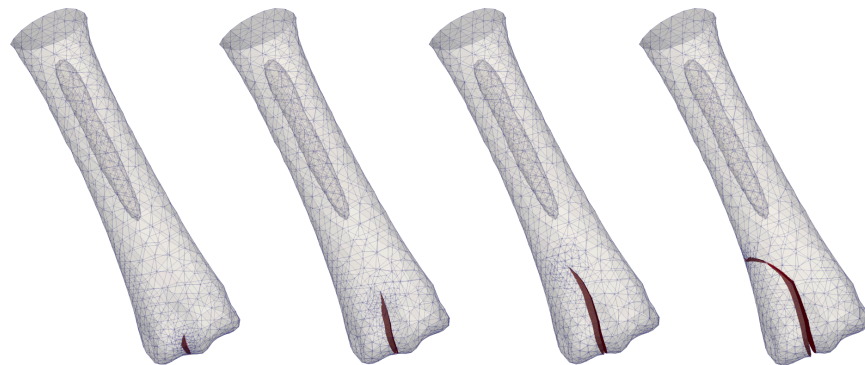


Figure 7.24: Crack surface evolution in equine 3rd metacarpal

the original mesh or order of approximation. The simulated crack path compares well with fractures observed in radiographs (Whitton et al., 2010), especially considering oversimplified loading conditions. The direct comparison of the numerically predicted crack with a crack segmented from a CT scan data and a radiograph can be found in Figure 7.27.

In the future considerations, it would be beneficial to test the sensitivity of the load-displacement curves on the placement and direction of applied forces and the initial crack.

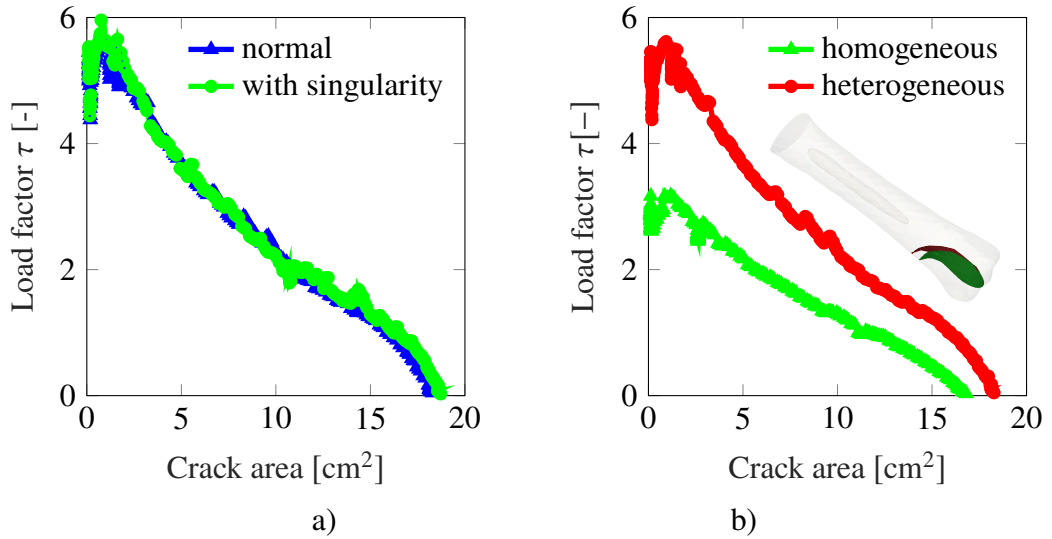


Figure 7.25: Load factor versus crack area for a) with and without singularity element and b) homogeneous versus heterogeneous density distribution.

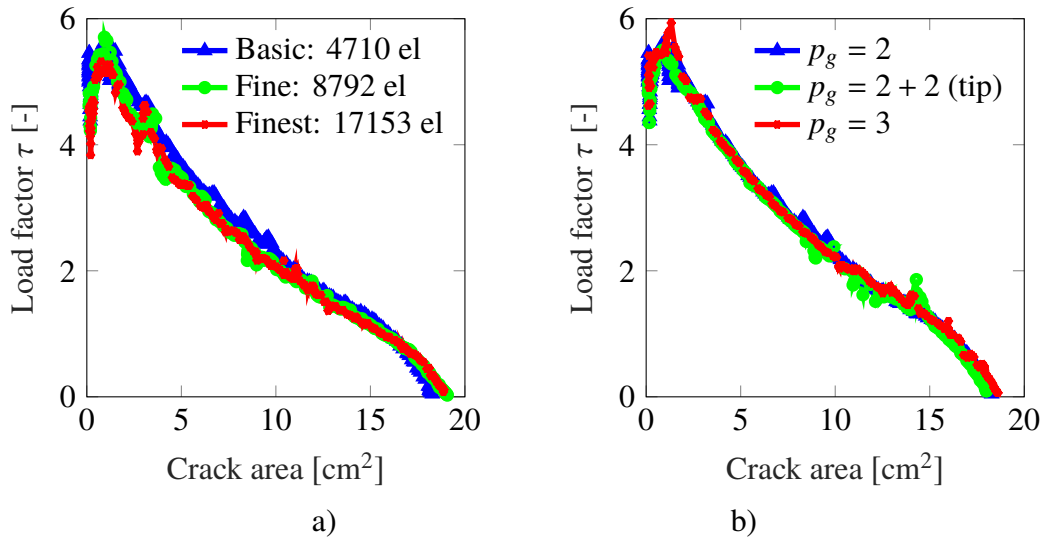


Figure 7.26: Load factor versus crack area. Global a) h - refinement and b) p -refinement.

7.5 Summary

This chapter presented FEM simulations to investigate bone adaptation model, comparative study of phase-field and configurational approaches for fracture, calculation of the fracture resistance, and crack propagation in the bone.

The first example considered bone remodelling formulation in a practical application - assessment of the proximal femur response to a hip replacement surgery. The results showed that the formulation has the capability of predicting bone density patterns and identifying potential problems with patient-specific treatments.

Subsequently, it was shown that discrete and smeared crack approximations developed in this work are able to predict fracture in heterogeneous materials. The essential aspects of both methods were compared. Although, due to its high computational cost requirements,

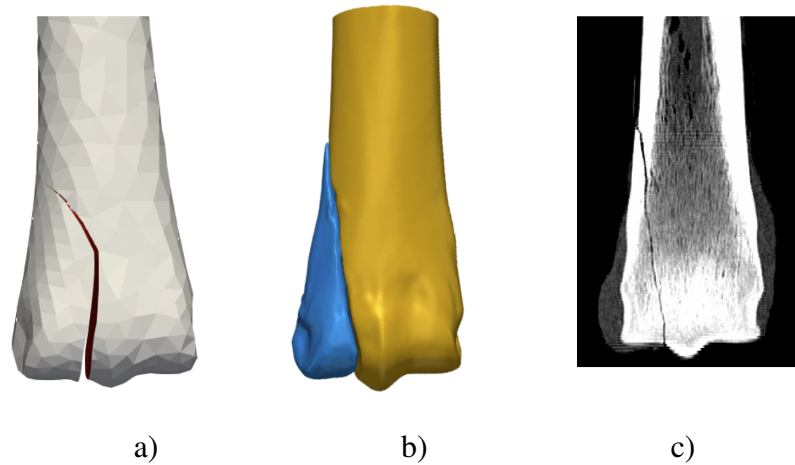


Figure 7.27: a) Numerically predicted crack. b) Bone with fracture segmented from CT scan data. c) Radiograph of a MC3 fracture.

phase-field has only been used for analysing simple problems. It can be concluded that, when perfectly brittle materials with smooth heterogeneities are considered, the proposed configurational force driven approach is superior to smeared approaches. Its computational cost is an order of magnitude lower, requires far fewer parameters and satisfies linear fracture mechanics assumptions, unlike phase-field where an additional dissipation takes place prior to failure.

In the last section, several numerical examples were presented to illustrate each aspect of the proposed framework to estimate bone fracture resistance following adaptation. The first set of analyses, considered bone remodelling of an equine 3rd metacarpal. It was found that the model accurately simulates the complex bone adaptation mechanism in bones. Application of a bell function to enforce bounds on density levels in the constitutive model did not provide rigid constraints for density levels but merely slowed down the convergence to the biological equilibrium process. Nevertheless, it may still become useful when one tries to fit the model parameters into the actual density data form CT scanning in defined periods of time. One could also constrain density bounds by introducing and calibrating mass influx to the balance of mass equation (Sharma and Robertson, 2013).

Nonetheless, bones in living organisms are never fully load adapted (Christen et al., 2014). Therefore, achieving a biological equilibrium that results in unrealistic levels of density should never take place in a real case scenario. Overall, more work has to be done towards identifying detailed boundary conditions and calibrating model parameters. Numerical convergence was demonstrated for all examples. It was also confirmed that improved accuracy of the stress at the tip thanks to Quarter Point Elements, had no impact on the crack propagation analysis and the resulting crack path. Another example demonstrated how mechanical loading and subsequent adaptation influence the resistance to bone fracture. Therefore, this framework will be a useful tool in understanding fractures in MC3 bone and ultimately preventing catastrophic fractures. The entire framework presented in this work can be executed on parallel computer systems. Supplementary data (CT scans, mesh files, command lines) necessary to reproduce the results of the numerical examples can be found in Lewandowski (2019). The

bone adaptation, phase-field and configurational fracture mechanics are submodules in the MoFEM library (Kaczmarczyk et al., 2020).

Chapter 8

Conclusions

Development of finite element models for biological applications is a very complicated process. Unlike that in typical engineering research subjects, there is still very little knowledge of the material properties. Another issue is the lack of a proper definition of the boundary conditions. Constraints are mostly explicit when analysing engineering objects such as concrete beams or steel frames under different loading conditions. However, in a living body, it is challenging to define loads accurately. Model geometry suffers from inaccuracies in scanning as well as segmentation process. Results from such models could potentially include an increasing number of errors since the data collected from each stage of the model creation encompasses high uncertainty data (Campoli et al., 2014). Available information is usually subject-specific or gathered for a relatively small population of subjects and cannot be generalised. Subsequently, even if one manages to overcome the obstacles above, there is a need for validation of such models, which will also have to deal with similar difficulties. Over the years, many frameworks have been developed to quantify such uncertainty levels, which might considerably increase the credibility of computational models (Wille et al., 2016). CT scanning on living horses limbs is still too cumbersome to be used as a standard diagnostic tool. To the best author's knowledge, there is a limited number of facilities that can perform CT scanning for horses without the necessity for anaesthesia.

Nevertheless, the outcomes of this study can bring new insight in the area of catastrophic injuries to improve the welfare of the thoroughbred racehorse. The successful application of developed framework would enable the introduction of interventions for veterinary practitioners, such as suggestions for training regimes based on known risk factors for lateral condylar fractures that could reduce the probability of fracture in racehorses.

The first task of this thesis was to build an understanding of the current state of the art of FEM techniques for analysing bone fracture resistance. The aim was to identify the key features of a patient-specific framework capable of incorporating accurate 3D data from CT-scanning,

simulating long term bone response to the proposed training regime and ultimately predicting the risk of fracture. The difficulty was to establish a balance between the essential components to provide accurate predictions and what could practically be executed in a patient-specific modelling routine within a limited time window. This was achieved by choosing efficient computational methods and the establishment of a consistently low level of complexity for the models to build a robust framework.

The procedure of building a finite element model for analysing bone always has to start with data acquisition. In Chapter 3, a three-dimensional imaging technique known as QCT scanning was applied to obtain accurate geometries of the equine bones and estimate their mineral density. Furthermore, two novel methods for mapping density data onto finite element meshes were proposed. The first method - L_2 -projection was used to investigate density gradients at a common site of fracture for three groups of equine limbs. Although the method has a potential of robustly identifying possible fracture risk factor (like high-density gradient), it was found that a small cohort of specimens was insufficient to make any meaningful conclusions. The preliminary results indicated moderate correlation between high density and density gradients at the common site of fracture. The second presented method - meshless MWLS does not use standard FEM discretisation and provides density field approximation with high regularity. This essential feature allows further for calculation of material forces in heterogeneous materials and ultimately efficient implicit crack propagation simulation within the configurational mechanics framework. Nevertheless, the accuracy of the presented approaches still has to be validated experimentally, for example, in the prediction of strains in the loaded bone specimen.

To simulate a long-term bone response to mechanical loading, a formulation for bone remodelling using open system thermodynamics framework was implemented. It has been shown that the chosen approach is capable of predicting realistic density profiles in hard tissues in response to over or underload. Benchmark examples demonstrated correctness of the implementation in comparison with the literature and also the stability and scalability of the utilised monolithic solution scheme. Two different methods of calculating consistent tangent matrix were presented. Additionally, the performance of the model was compared with a simple topology optimisation algorithm proposed in Appendix B. It was found the utilised formulation has the density predictive capabilities and necessary robustness to use it diagnostic tools like in the proposed framework.

With accurate bone density profiles and material properties derived through QCT scanning or bone remodelling simulations, the next natural step in the proposed framework is to estimate the fracture resistance. In Chapters 5 and 6, two approaches were proposed for simulating crack propagation and estimating critical load factors in heterogeneous bones.

The first one was the popular phase-field method, where the crack is represented by a smooth damage variable leading to a phase-field approximation of the variational formulation for

brittle fracture. To trace the nonlinear response, the implementation was augmented with an adaptive arc-length control method based on the rates of the internal and the dissipated energy. Furthermore, the potential of three different methods for obtaining consistent tangent matrix was explored. The heterogeneity of the material can be captured straightforwardly by using spatially varying material properties as local variables. The performance and correctness of the proposed phase-field formulation of fracture were demonstrated by means of representative numerical examples. The investigation showed that the adopted formulation gives good results in comparison with the literature. Even though the model was found to be very robust, it is also very sensitive and computationally expensive.

In the second discrete approach for fracture, configurational forces are the driver for crack propagation. The crack-driving forces, and corresponding fracture energy release rate, are expressed exclusively in terms of nodal quantities, avoiding the need for post-processing and enabling a fully implicit formulation for modelling the evolving crack front. In order to evaluate the forces correctly at the crack front for inhomogeneous materials, it was shown that it is necessary to have a spatially smooth density field, with higher regularity. Therefore, density data was approximated as a smooth field using a Moving Weighted Least Squares method. Moreover, to improve the accuracy of the calculated nodal crack driving forces, singular stress state was modelled using Quarter Point element concept. The convergence and validation tests were conducted. It was found, that with the proposed formulation, a remarkable accuracy of the calculated energy release can be achieved, even with coarse meshes. Moreover, it was also shown that the method can compute energy release in heterogeneous materials.

In the penultimate chapter of this thesis, the full potential of the developed framework was assessed in the form of practical numerical examples. The first analysis of a proximal femur with implant showed that utilised formulation for bone remodelling has the capability of predicting bone density patterns that are in good comparison with structural arrangement observed on CT scans. Subsequently, a comparative study was conducted in order to evaluate the performance of both implemented methods for approximating fracture in heterogeneous materials. It was concluded that in the current state of development, the configurational force approach is more suitable for the framework. It introduces fewer parameters and works effectively on coarse meshes. It is worth to note, that these two very different approaches gave very similar results for benchmark problems incorporating heterogeneous material properties. This outcome further proves that the proposed configurational approach correctly calculates energy release and without the bias from the original mesh. In the last section, numerical examples demonstrated the performance and accuracy of the proposed framework for analysing equine MC3 bone. Numerical convergence was demonstrated for all examples, and the use of singularity elements was shown to further improve the rate of convergence. However, it was also confirmed that improved accuracy of the stress at the tip had no impact on the crack propagation analysis and the resulting crack path. The final example demonstrated how mechanical loading and subsequent adaptation influence the resistance to fracture. The numerical results reproduced the maladaptation phenomenon, where the intense

bone remodelling increases the propensity to fracture in metacarpal bones. Moreover, the simulated crack path using density data from CT scans compared well with fractures observed in radiographs. Ultimately demonstrating that the proposed framework can be a useful tool in understanding fractures in bone and preventing catastrophic fractures.

In summary, the goal of this study was to develop a robust numerical framework for the estimation of a fracture risk of MC3 bone followed by adaptation. The main achievements of this thesis are the following:

- Incorporation of efficient and accurate mapping strategies to represent heterogeneous bone material properties for finite element models.
- Efficient implementation of bone adaptation algorithm based on open system thermodynamics to predict density levels in response to exercise.
- Deployment of three-dimensional phase-field formulation for brittle fracture with robust arc-length control.
- Novel application of configurational mechanics for modelling fracture extended to include the influence of heterogeneous bone density distribution.
- Assessment of the potential of the developed framework in evaluating bones' propensity to failure.

8.1 Limitations and future work

The methods presented in this thesis have several important limitations. Considerably more work has to be done to determine bone loading since using simplified input results in unrealistically low densities in non-load-bearing regions. Multiple load cases can be critical in modelling bone adaptation (Geraldès et al., 2016). In the future, the forces should be obtained by using gait data and musculoskeletal analysis (Delp et al., 2007) combined with, e.g. finite element mortar contact formulation (Athanasiadis et al., 2018). Another method for predicting loading conditions is to solve an inverse problem to bone adaptation. Promising results have been reported in that field by using machine learning methods like Neural Networks (Campoli et al., 2012).

Another limitation of the proposed scheme is the requirement for manual generation and meshing of bone geometry models that often requires commercial software. In future, it would be beneficial to explore methods for automatic segmentation and meshing as proposed, e.g. in Trabelsi and Yosibash (2011). The model generation should be fully automatic and require minimum human interaction to handle many specimens within a limited time frame.

The current fracture approximation approaches do not take into account nonlinear cohesive mechanisms like collagen fibre bridging at the crack tip (Yang et al., 2006). Therefore, the calculated release energy or load factor with presented approaches might be overestimated. More research is also required to calibrate material parameters, like heterogeneous Young's modulus coefficients, including bone anisotropy, or parameters regarding constitutive relations for bone adaptation.

Appendix A

Moving Weighted Least Squares basis functions

For each node, the process to evaluate the vector of unknowns $\mathbf{a}(\mathbf{X}_t) = [a_1(\mathbf{X}_t), a_2(\mathbf{X}_t), \dots, a_q(\mathbf{X}_t)]$ in Eq. 3.9 involves consideration of neighbouring points of the discrete field $v(\mathbf{X}_i)$ and a weight function $w(r)$ is constructed, where r is the normalised radial distance from the node defined as $r = \|\mathbf{X}_t - \mathbf{X}_i\|/d_{mi}$ so that $0 < r \leq 1$, where d_{mi} is a scaling parameter. An example of an arbitrary weight function for a 2D domain is presented in Figure A.1. Values of the given discrete field $v(\mathbf{X}_i)$ are presented with dots, and the positions where $v(\mathbf{X}_i)$ is mapped (i.e. nodes) are presented with circles. Furthermore, the node under consideration is located at the origin of a cylindrical local coordinate system with r and w axes. For the 2D case, the weight function is visually represented as a 3D surface (shaded area) resulting from full rotation around w axis of the 1D weight function, $w(r)$, represented as a solid line. The boundary of the domain of influence of $w(r)$ is represented by a dashed circle ($r = 1$). $w(r)$ is equal to zero outside the domain of influence. Many types of weight functions can be used for the MWLS method. A one-dimensional quartic spline, commonly used in meshless methods (Belytschko et al., 1996), was chosen for the current work:

$$w(\|\mathbf{X}_t - \mathbf{X}_i\|/d_{mi}) = w(r_i) = \begin{cases} 1 - 6r_i^2 + 8r_i^3 - 3r_i^4 & \text{for } r_i \leq 1 \\ 0 & \text{for } r_i > 0 \end{cases} \quad (\text{A.1})$$

Its derivative with respect to the material coordinates is:

$$\frac{dw}{d\mathbf{X}_t} = \frac{dw}{dr_i} \frac{dr_i}{d\mathbf{X}_t} = \frac{1}{d_{mi}} \begin{cases} (-12r_i + 24r_i^2 - 12r_i^3) & \text{for } r_i \leq 1, \\ 0 & \text{for } r_i > 0 \end{cases} \quad (\text{A.2})$$

Here $r_i = \|\mathbf{X}_t - \mathbf{X}_i\|/d_{mi}$ is the normalised radial distance of point i from the node divided by scaling parameter d_{mi} . This coefficient is governing the size of influence domain. With the

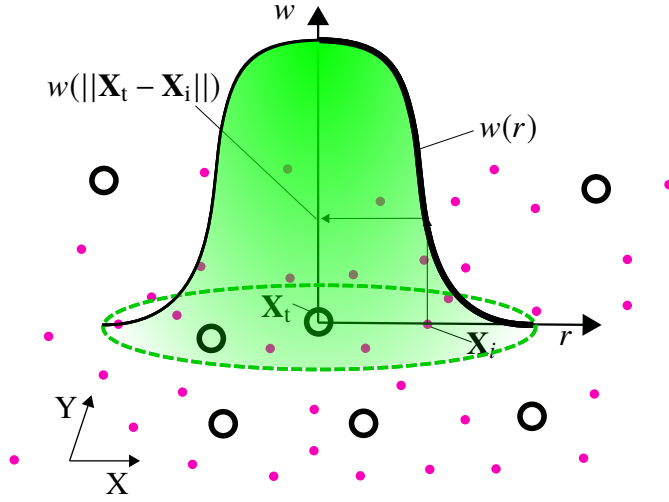


Figure A.1: 2D schematic example of arbitrary weight function of a node located with position vector \mathbf{X}_t . Points of the discrete field $v(\mathbf{X}_i)$ are presented with dots and points that $v(\mathbf{X}_i)$ is mapped are presented with circles. The function is smooth, non-negative, reaches maximum at the \mathbf{X}_t and decreases with distance $\|\mathbf{X}_t - \mathbf{X}_i\|$. The boundary of the domain of influence of the weight function is presented with dashed ellipsoid (circle on 2D plane) and the function takes a constant value of zero outside of it.

above tools at hand, the vector of unknowns $\mathbf{a}(\mathbf{X}_t)$ associated with the node can be evaluated through minimisation of the weighted L_2 norm:

$$J_c(\mathbf{X}_t) = \frac{1}{2} \sum_i^{n_w} w(r_i) \left(v^h(\mathbf{X}_t) - v(\mathbf{X}_i) \right)^2 = \frac{1}{2} \sum_i^{n_w} w(r_i) \left(\mathbf{p}^T(\mathbf{X}_i) \mathbf{a}(\mathbf{X}_t) - v(\mathbf{X}_i) \right)^2 \quad (\text{A.3})$$

where $v(\mathbf{X}_i)$ is the value of the given discrete field at point i amongst the n_w points located within the domain of influence of the node and $\mathbf{p}^T(\mathbf{X}_i)$ is the vector of shape functions of the point i . Minimisation of J_c with respect to \mathbf{a} leads to a system of linear equations as:

$$\mathbf{A}(\mathbf{X}_t) \mathbf{a}(\mathbf{X}_t) = \mathbf{B}(\mathbf{X}_t) \mathbf{v} \quad (\text{A.4})$$

where matrices $\mathbf{A}(\mathbf{X}_t)$ and $\mathbf{B}(\mathbf{X}_t)$ are of size $(q \times q)$ and $(q \times n_w)$ and defined as follows:

$$\begin{aligned} \mathbf{A}(\mathbf{X}_t) &= \sum_i^{n_w} w(r_i) \mathbf{p}(\mathbf{X}_i) \mathbf{p}^T(\mathbf{X}_i) \\ \mathbf{B}(\mathbf{X}_t) &= \left[w(r_1) \mathbf{p}(\mathbf{X}_1), w(r_2) \mathbf{p}(\mathbf{X}_2), \dots, w(r_{n_w}) \mathbf{p}(\mathbf{X}_{n_w}) \right] \end{aligned} \quad (\text{A.5})$$

and \mathbf{v} is $(n_w \times 1)$ vector of the given field values at the points within the influence domain given as:

$$\mathbf{v} = \left[v(\mathbf{X}_1), v(\mathbf{X}_2), \dots, v(\mathbf{X}_{n_w}) \right]^T \quad (\text{A.6})$$

It should be noted that parameter d_{mi} is chosen to include sufficient n_w points such that the resulting matrix \mathbf{A} is not singular. Next, Eq. 3.9 combined with Eq. A.4 can be rewritten as:

$$v^h(\mathbf{X}_t) = \sum_{i=1}^{n_w} \omega_i(\mathbf{X}_i) v_i = \omega^T(\mathbf{X}_t) \mathbf{v} \quad (\text{A.7})$$

where $\boldsymbol{\omega}(\mathbf{X}_t)$ is a resulting vector of shape functions associated with the node, defined as

$$\boldsymbol{\omega}^T(\mathbf{X}_t) = \mathbf{p}^T(\mathbf{X}_t)\mathbf{A}^{-1}(\mathbf{X}_t)\mathbf{B}(\mathbf{X}_t) \quad (\text{A.8})$$

It is also necessary to approximate the density's gradient in the material domain. Therefore, the first derivative of the shape function with respect to the material coordinates is derived in direction X_j :

$$\boldsymbol{\omega}_{,j}^T = \mathbf{p}_{,j}^T\mathbf{A}^{-1}\mathbf{B} + \mathbf{p}^T(\mathbf{A}_{,j}^{-1}\mathbf{B} + \mathbf{A}^{-1}\mathbf{B}_{,j}) \quad (\text{A.9})$$

The commas in the subscripts denote the partial derivative, and the inverse of the material derivative of matrix \mathbf{A} is evaluated as

$$\mathbf{A}_{,j}^{-1} = -\mathbf{A}^{-1}\mathbf{A}_{,j}\mathbf{A}^{-1} \quad (\text{A.10})$$

The above equations for calculating derivatives are computationally demanding. However, it was found that with the purpose at hand, i.e. considering only small strains regime where the reference material domain is indistinguishable from the current domain, a local form of the derivative is sufficient, and it can be computed as follows:

$$\boldsymbol{\omega}_{,j}^T = \mathbf{p}_{,j}^T\mathbf{A}^{-1}\mathbf{B} \quad (\text{A.11})$$

The local second derivative can be simply computed as:

$$\boldsymbol{\omega}_{,jk}^T = \mathbf{p}_{,jk}^T\mathbf{A}^{-1}\mathbf{B} \quad (\text{A.12})$$

It is worth noting that for any node located at \mathbf{X}_β , MWLS shape functions do not satisfy Kronecker delta property, i.e. $\omega_i(\mathbf{X}_\beta) \neq \delta_{i\beta}$. The values obtained from the MWLS approximation are not the same as the given field values, i.e. $v^h(\mathbf{X}_\beta) \neq v(\mathbf{X}_\beta)$ as presented with a 1D example in Figure A.2. Since the MWLS shape functions do not satisfy Kronecker-delta

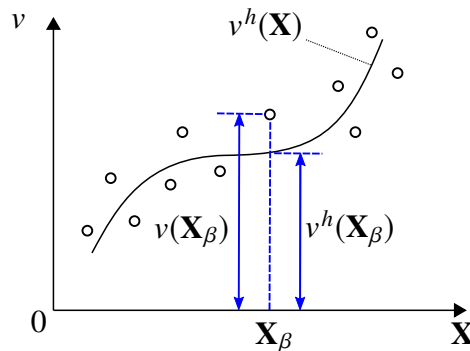


Figure A.2: 1D example of moving least squares method.

property on the boundaries of the problem; it can be quite a challenge to enforce essential boundary conditions. However, here the approximation is used for simple mapping; hence this deficiency can be neglected.

Appendix B

Topology optimisation

Topology optimisation is a mathematical method for optimising the material distribution within a domain, for a given set of boundary conditions and constraints to maximise the performance of the structure. Over the years, many different approaches have been developed, including density penalisation, level set, topological derivative, phase-field or evolutionary methods. An extensive overview can be found in Sigmund and Maute (2013).

B.1 Implementation

The topology implementation problem presented herein is based on popular *Solid Isotropic Material with Penalisation* (SIMP) (Bendsøe and Sigmund, 2003) method, where the objective is to minimise the compliance of the considered domain Ω as follows

$$\begin{aligned} \min_{\rho} : \quad & c(\rho) = \sum_{e=1}^n \mathbf{u}_e^T \mathbf{K}_e(\rho) \mathbf{u}_e \\ \text{s.t.} : \quad & \sum_{e=1}^n \int_{\Omega} \rho \, dV_e = f^{\text{top}} V \\ & : \quad 0 < \rho_{\min} \leq \rho \leq 1 \\ & : \quad \mathbf{K}(\rho) \mathbf{u} = \mathbf{f} \end{aligned} \tag{B.1}$$

where \mathbf{K} is the global stiffness matrix, \mathbf{u} vector of displacements, \mathbf{f} is the nodal force vector, ρ is the element density (design variable), V_e and V is the element volume and volume of the entire domain, respectively. f^{top} is the desired volume fraction parameter. The element

stiffness \mathbf{K}_e is calculated as follows:

$$\mathbf{K}_e = \int_{\Omega} (\rho)^{p^{\text{top}}} \nabla_{\mathbf{X}} \Phi^T \mathbb{D} \nabla_{\mathbf{X}} \Phi \, dV_e \quad (\text{B.2})$$

where p^{top} is the penalisation coefficient (typically $p^{\text{top}} = 3$), and \mathbb{D} is the 4th order elasticity tensor. The optimisation problem in Eq. B.1 is solved with the Lagrange multipliers method. The derivative of the objective function with respect to design variables has the form:

$$\frac{\partial \mathcal{L}}{\partial \rho} = -\mathbf{u}_e^T \frac{\partial \mathbf{K}_e}{\partial \rho} \mathbf{u}_e + \lambda_b V_e \quad (\text{B.3})$$

where \mathcal{L} is the Lagrangian and λ_b is the Lagrange multiplier. The condition of optimality can be expressed as follows:

$$\left\{ \begin{array}{l} \frac{\partial \mathcal{L}}{\partial \rho} \geq 0 \text{ if } \rho = \rho_{\min} \\ \frac{\partial \mathcal{L}}{\partial \rho} = 0 \text{ if } \rho_{\min} < \rho < 1 \\ \frac{\partial \mathcal{L}}{\partial \rho} < 0 \text{ if } \rho = 1 \end{array} \right. \quad (\text{B.4})$$

Furthermore, the Optimality Criteria algorithm can be applied with a heuristic iteration scheme for the design variables defined as:

$$\rho^{n+1} = \left(\frac{1}{\lambda_b V} \mathbf{u}_e^T \frac{\partial \mathbf{K}_e}{\partial \rho} \mathbf{u}_e \right)^{\eta} \rho^n \quad (\text{B.5})$$

where n is the iteration number and η is a numerical damping coefficient, typically $\eta = 0.5$. Additionally, a *move* limit is imposed (often $m^{\text{top}} = 0.2$) at each iteration to ensure the stability of the algorithm. At each iteration ρ^{n+1} has to satisfy the following inequality:

$$\max(\rho^n - m^{\text{top}}, \rho_{\min}) \leq \rho^{n+1} \leq \min(\rho^n + m^{\text{top}}, 1) \quad (\text{B.6})$$

The nonlinear solution for multiplier λ_b is obtained through bisection method. ρ_{\min} is imposed to avoid zero stiffness elements, typically $\rho_{\min} = 0.001$.

B.2 Density filtering

To prevent the checkerboard pattern and ensure mesh-independency of the solution for topology optimisation problems, typically filtering techniques on density ρ or sensitivity $\partial c / \partial \rho$ are applied (Bourdin, 2001). Most of the methods in the literature require information about the neighbour elements, which makes them difficult to partition and parallelise for efficient multiple CPU computations. Therefore, more recently, a new family of filters based on

Helmholtz-type differential equations has emerged (Lazarov and Sigmund, 2011).

The basic idea behind filters inspired by Helmholtz PDE is to solve the following differential equation:

$$-\lambda_l \nabla_{\mathbf{x}}^2 \tilde{\rho} + \tilde{\rho} = \rho \quad (\text{B.7})$$

with Neumann boundary condition imposed on the surface of the domain as follows:

$$\frac{\partial \tilde{\rho}}{\partial \mathbf{n}} = 0 \quad (\text{B.8})$$

where $\tilde{\rho}$ is nodal density and λ_l can be considered as the length scale parameter. After finding the densities ρ for each element, that satisfy the constraints in Eq. B.1 through bisection method, the PDE in Eq. B.7 can be solved with standard FEM discretisation resulting in the following system of linear equations for the unknown values of the filtered density field:

$$\mathbf{K}_f \tilde{\rho} = \mathbf{p}_f \quad (\text{B.9})$$

where the matrix \mathbf{K}_f and vector \mathbf{p}_f is obtained as follows:

$$\begin{aligned} \mathbf{K}_f &= \sum_{e=1}^n \int_{\Omega} \lambda_l \nabla_{\mathbf{x}} \Phi^T \nabla_{\mathbf{x}} \Phi + \Phi^T \Phi \, dV_e \\ \mathbf{p}_f &= \sum_{e=1}^n \int_{\Omega} \Phi^T \rho \, dV_e \end{aligned} \quad (\text{B.10})$$

Note that with the presented formulation, non-constant density within the elements can be used. The performance of this approach is demonstrated in the next section in the form of representative numerical examples.

B.3 Numerical examples

In this section, the capabilities of the discussed topology optimisation are presented. Two cantilever problems are considered: in 2D and 3D. The loads and the domain dimensions are shown in Figure B.1. The meshes consist of 1385 and 39761 structured quadratic tetrahedral elements for 2D and 3D, respectively.

Note that in the realm of hierarchical approximation basis, the order on the elastic and density filtering problems can be set independently. The problem parameters are: Young's modulus $E = 1000$ MPa, Poisson ratio $\nu = 0.1$, *move* limit $m^{\text{top}} = 0.2$, penalty parameter $p^{\text{top}} = 3$ and desired volume fraction $f^{\text{top}} = 0.3$. The results for 2D cantilever for different values of length scale parameter λ_l are shown in Figure B.2. For $\lambda_l = 0$, which basically means no filtering, as expected - an unstable checkerboard-like solution is obtained. In the following cases, it can be noticed that by decreasing λ_l finer and sharper truss-like elements can be obtained.

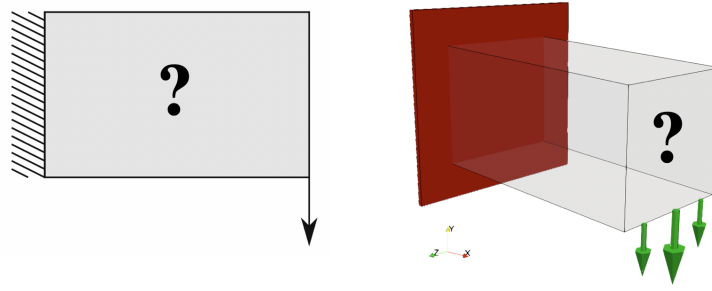


Figure B.1: Domain and boundary conditions for 2D and 3D examples. The dimensions are: 10x5mm for 2D case and 10x5x5mm for 3D case. In 2D unit nodal force is applied and in 3D spatially varying line load on bottom right edge, such that: $f(x, z, y) = 10 - z^2$ N.

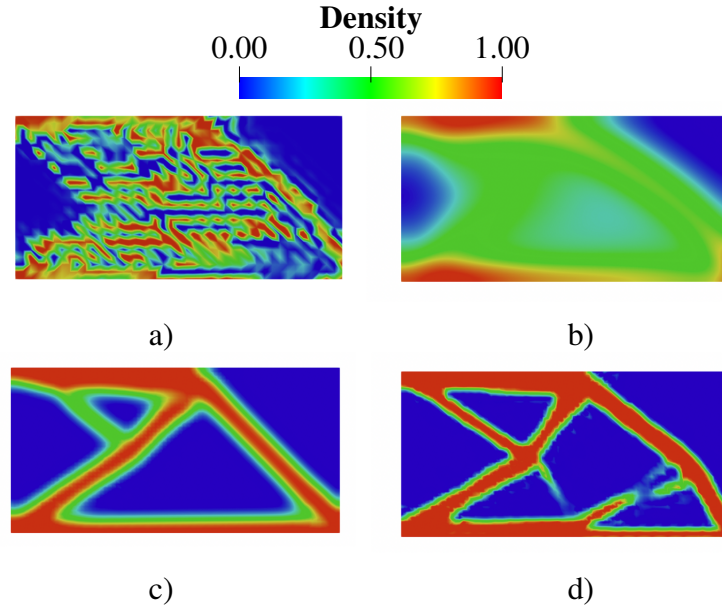


Figure B.2: Design variable for 2D cantilever after 20 iterations. a) $\lambda_l = 0$ b) $\lambda_l = 1$ c) $\lambda_l = 0.1$ d) $\lambda_l = 0.01$.

The results with $\lambda_l = 0.1$ are in good agreement with the MATLAB code demonstrated in Sigmund (2001).

In the second example, inspired by Aage and Lazarov (2013), a 3D cantilever design problem is analysed. The parameters chosen are the same as in the 2D case, apart from the length scale parameter, where $\lambda_l = 0.1$ is used. The results in Figure B.3 show every 5th iteration of the compliance minimisation steps. Note that the presented formulation can generate complex structure shapes with high resolution using relatively coarse meshes.

The examples presented before utilised isotropic filtering, i.e. λ_l is a scalar. However, it is possible to replace that quantity with a tensor that will smear the design variable ρ differently in desired directions. In order to demonstrate this feature, the same cantilever as previously is considered with scalar $\lambda_l = 0.2$ (see Fig. B.4a)) and a tensor expressed as:

$$\lambda_l = \begin{bmatrix} 0.01 & 0 & 0 \\ 0 & 0.01 & 0 \\ 0 & 0 & 0.2 \end{bmatrix} \quad (\text{B.11})$$

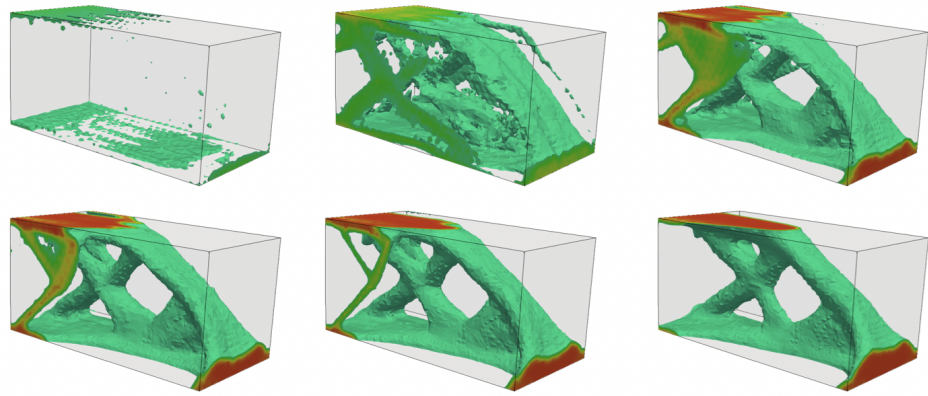


Figure B.3: Evolution of design variable ρ for every 5th iteration. Iso-volume plot showing $\rho > 0.35$.

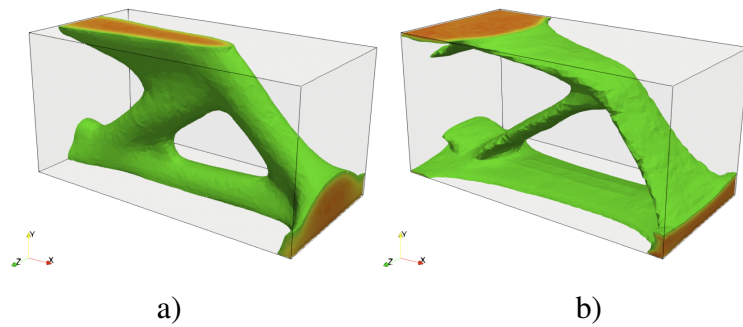


Figure B.4: Resulting topology with a) isotropic filter $\lambda_l = 0.2$ and b) anisotropic filter (Eq. B.11). Iso-volume plot showing for $\rho > 0.35$.

This will enforce filtering mainly in the z -direction. The results after 50 iterations for both filters are demonstrated in Figure B.4. The demonstrated anisotropic filtering can be beneficial in case of designing structures for extrusion or additive manufacturing methods where the strength of the parts depends highly on the direction of the material deposition.

B.4 Summary

This contribution presented a simple implementation of the topological optimisation using SIMP algorithm. A Helmholtz-type PDE anisotropic filter was utilised, allowing for efficient parallelisation of the approach. The source code can be found in Lewandowski (2020).

Appendix C

Arc-length based on the internal and the dissipated energy rates

Dissipated energy control

Following the second law of thermodynamics, the behaviour of the adiabatic dissipative process can be expressed in the local form as follows:

$$\dot{\mathcal{D}} = \boldsymbol{\sigma} \dot{\boldsymbol{\varepsilon}} - \dot{\psi} \geq 0, \quad (\text{C.1})$$

where $\dot{\mathcal{D}}$ is the rate of dissipation and ψ is the energy density stored in the bulk per unit volume. It is assumed that internal energy is dependent on damage parameter d (see Equation 5.11). Therefore, following May et al. (2016), the derivative of energy density with respect to time can be computed as:

$$\dot{\psi} = \boldsymbol{\sigma} \dot{\boldsymbol{\varepsilon}} + \frac{\partial \psi}{\partial d} \dot{d} \quad (\text{C.2})$$

and

$$\dot{\psi} = \frac{1}{2} \boldsymbol{\sigma} \dot{\boldsymbol{\varepsilon}} + \frac{1}{2} \dot{\boldsymbol{\sigma}} \boldsymbol{\varepsilon}. \quad (\text{C.3})$$

With no discontinuities in the solid, the global form of the second law of thermodynamics can be written as:

$$\dot{\mathcal{E}}^D = \int_{\Omega} \dot{\mathcal{D}} dV = \int_{\Omega} \frac{1}{2} \boldsymbol{\sigma} \dot{\boldsymbol{\varepsilon}} - \frac{1}{2} \dot{\boldsymbol{\sigma}} \boldsymbol{\varepsilon} dV = \int_{\Omega} -\frac{\partial \psi}{\partial d} \dot{d} dV \quad (\text{C.4})$$

where $\dot{\mathcal{E}}^D$ is the rate of dissipated energy. Furthermore, knowing that $\boldsymbol{\varepsilon} = \mathbf{B}_u \mathbf{u}$ and $\mathbf{f}^{\text{int}} = \int_{\Omega} \mathbf{B}_u^T \boldsymbol{\sigma} dV$, the second integral in equation C.4 can be expressed as:

$$\dot{\mathcal{E}}^D = \frac{1}{2} \dot{\mathbf{u}} \mathbf{f}^{\text{int}} - \frac{1}{2} \mathbf{u} \dot{\mathbf{f}}^{\text{int}} \quad (\text{C.5})$$

Next, the equilibrium Equation 5.39 can be applied and the dissipation rate $\dot{\mathcal{E}}^D$ is replaced with the rate parameter $\dot{\tau}^D$

$$\frac{1}{2}(\tau\dot{\mathbf{u}}^T - \dot{\tau}\mathbf{u}^T)\hat{\mathbf{f}} - \dot{\tau}^D = 0. \quad (\text{C.6})$$

Using the mid-point rule, time discretised form of the Equation C.6 can be used as the constraint in Equation 5.39 in the following way:

$$\phi^D(\mathbf{u}, \tau) = \frac{1}{2}(\tau_0\mathbf{u}^T - \tau\mathbf{u}_0^T)\hat{\mathbf{f}} - \Delta\tau^D \quad (\text{C.7})$$

where $\Delta\tau^D$ is considered as the prescribed step size, i.e. the amount of energy dissipated within one load increment. τ_0 and \mathbf{u}_0 are the converged values for the load factor and displacements of the previous step.

Internal energy control

In this subsection, another arc-length function is introduced. Typically at the beginning of the loading or unloading, before the damage mechanisms are activated, the rate of the energy dissipation is very low. In these conditions, a more suitable internal energy-based arc-length will be used.

Once again, assuming no discontinuities in the solid, the 5.39 can be expressed in the global form of the second law to render the rate of the internal energy $\dot{\mathcal{U}}$:

$$\dot{\mathcal{U}} = \int_{\Omega} \dot{\psi} dV = \frac{1}{2}(\tau\dot{\mathbf{u}}^T + \dot{\tau}\mathbf{u}^T)\hat{\mathbf{f}} \quad (\text{C.8})$$

Next, similar to Equation C.7 the mid-point rule is applied and $\dot{\mathcal{U}}$ is replaced with parameter $\Delta\tau^F$, which yields the following arc-length function:

$$\phi^U(\mathbf{u}, \tau) = \frac{1}{2}(\tau\mathbf{u}^T - \tau_0\mathbf{u}_0^T)\hat{\mathbf{f}} - \Delta\tau^U \quad (\text{C.9})$$

where $\Delta\tau^U$ is considered as the prescribed step size, i.e. the amount of internal energy which has to be introduced in one load increment. τ_0 and \mathbf{u}_0 are the converged values for the load factor and displacements of the previous step. The Equation C.9 is utilised when there is no increase in the dissipation.

In the algorithmic setting, it is worth noting that in the very first iteration of the analysis, the displacement $\mathbf{u} = \mathbf{u}_0 = 0$ rendering the tangent stiffness matrix to be singular. Therefore, in the first increment, the following simple constraint function is used:

$$\phi_1^F = (\tau - \Delta\tau_1^F) = 0 \quad (\text{C.10})$$

where $\Delta\tau_1^F$ is the parameter that has to be specified. Such constraint is equivalent to $\tau = \Delta\tau_1^F$, similarly to force control increment. From the first iteration, u_1 and τ_1 are known, therefore,

the rate of the internal energy can be evaluated as follows:

$$\Delta\tau_1^U = \frac{1}{2}\tau_1\mathbf{u}_1^T\hat{\mathbf{f}}. \quad (\text{C.11})$$

Furthermore, $\Delta\tau_1^U$ is used in the consecutive load increments. The second parameter, after $\Delta\tau_1^F$, is the ratio a that needs to be prescribed. This parameters determine whether the arc-length algorithm has to switch from internal energy-based to the dissipation based constraint function. The ratio a is defined as follows:

$$a = \frac{\Delta\tau^D}{\Delta\tau^U}. \quad (\text{C.12})$$

In order to find the suitable value of this parameter, May et al. (2016) suggest starting the analysis assuming a large value of a and subsequently assign to a a value that is smaller than $\Delta\tau^D/\Delta\tau^U$ from the last converged increment. Fortunately, this procedure can be easily automatised; therefore, practically only one parameter is necessary to start the calculation with the arc-length control. The fully detailed derivation of the procedure presented above can be found in May (2016).

C.0.1 Algorithmic treatment

The final form of the global system of equations (see Equation 5.27) augmented with the arc-length control for phase-field fracture has the following form:

$$\begin{bmatrix} \mathbf{K}^{dd} & \mathbf{K}^{du} & 0 \\ \mathbf{K}^{ud} & \mathbf{K}^{uu} & -\hat{\mathbf{f}} \\ 0^T & \mathbf{h}^T & w \end{bmatrix}_i \begin{bmatrix} \delta d \\ \delta \mathbf{u} \\ \delta \tau \end{bmatrix}_{i+1} = \begin{bmatrix} -\mathbf{f}_d^{\text{int}} \\ \tau \mathbf{f}^{\text{ext}} - \mathbf{f}_u^{\text{int}} \\ \phi(\tau, \mathbf{u}) \end{bmatrix}_i, \quad (\text{C.13})$$

where

$$w = \frac{\partial \phi}{\partial \tau}, \quad \mathbf{h} = \frac{\partial \phi}{\partial \mathbf{u}}. \quad (\text{C.14})$$

The algorithm presented in the previous section is summarised in Figure 1 below. In order to improve the robustness of the algorithm, an adaptive step size is applied. In subsequent load steps the initial constraint $\Delta\tau_1^U$ is multiplied by the following factor:

$$\Delta\tau_1^U = \Delta\tau_1^U \sqrt{\frac{i^d}{i+1}}, \quad (\text{C.15})$$

where i is the number of previously converged iterations and i^d is the optimal number of iterations for the Newton-Raphson method, typically 5 (Gutiérrez, 2004). The parameter i^d is usually adjusted by the user.

```

Load  $\Delta\tau_1^F$  and ratio  $a$  from input parameters;
 $n = 0$ ;
InternalEnergyArclength = true;
while  $n < n_{\max}$  do
   $i = 0$ ;
  while  $error > 10^{-8}$  do
    if  $n == 1$  then
       $\phi_1^F = \tau_1 - \Delta\tau_1^F$ ;
    else
      if InternalEnergyArclength == true then
         $\phi^U = \frac{1}{2} (\tau_{n+1}^i \mathbf{u}_{n+1}^{iT} - \tau_n \mathbf{u}_n^T) \hat{\mathbf{f}}$ ;
      else
         $\phi^D = \frac{1}{2} (\tau_n^i \mathbf{u}_{n+1}^{iT} - \tau_{n+1} \mathbf{u}_n^T) \hat{\mathbf{f}}$ ;
      end
    end
     $error = error(\mathbf{u}_{n+1}^{i+1}, \tau_{n+1}^{i+1})$ ;
     $i = i + 1$ ;
  end
  if  $n == 1$  then
     $\Delta\tau_1^U = \frac{1}{2} \tau_1 \mathbf{u}_1^T \hat{\mathbf{f}}$ ;
     $\Delta\tau^U = \Delta\tau_1^U$ ;
  else
    if InternalEnergyArclength == true then
       $\Delta\tau^D = \frac{1}{2} (\tau_n \mathbf{u}_{n+1}^T - \tau_{n+1} \mathbf{u}_n^T) \hat{\mathbf{f}}$ ;
      if  $\Delta\tau^D > a\Delta\tau_1^U$  then
        InternalEnergyArclength = false;
        InternalEnergyNegative = false;
         $\Delta\tau^D = a\Delta_1^U$ ;
      end
    else
       $\Delta\tau^U = \frac{1}{2} (\tau_{n+1} \mathbf{u}_{n+1}^T - \tau_n \mathbf{u}_n^T) \hat{\mathbf{f}}$ ;
      if  $\Delta\tau^U < 0$  and InternalEnergyNegative == false then
        InternalEnergyNegative = true;
      else
        if  $\Delta\tau^U > \Delta\tau_1^U$  and InternalEnergyNegative == true then
          InternalEnergyArclength = true;
           $\Delta\tau^U = \Delta\tau_1^U$ ;
        end
      end
    end
     $\Delta\tau_1^U = \Delta\tau^{U,D} \sqrt{\frac{i^d}{i+1}}$ ; // Scale step size for adaptivity;
  end
   $n = n + 1$ ;
end

```

Algorithm 1: Algorithm for the arc-length control.

The algorithm begins with assigning prescribed parameters: ratio a and $\Delta\tau_1^F$. After the first simple force control step, the resulting internal energy $\Delta\tau_1^U$ is computed and used as a step size for the energy-based arc-length control ϕ^U . When the amount of dissipated energy $\Delta\tau^D$ surpasses the value of $a\Delta_1^U$ which occurs in the vicinity of a failure, the loading process

switches to dissipation based (ϕ^D) control. In case of complex problems with multiple snap-backs and snap-throughs, the arc-length can switch back to energy control when $\Delta\tau^U < 0$ flag is triggered and subsequently when increment in internal energy becomes greater than in the initial step: $\Delta\tau^U > \Delta\tau_1^U$. Additionally, after each converged step, the initial step $\Delta\tau_1^U$ is adjusted based on the number of previous iterations (see Eq. C.15).

Appendix D

One-dimensional Quarter Point Element

For simplicity, the concept of the quarter-point element is briefly described by means of 1D 2-nd order finite element with hierarchical base shape functions. Global configuration of 2-nd order element with nodes 0, 2 and 1 is schematically presented in Figure D.1a) where node 0 coincides with the crack tip. Furthermore, the natural coordinate system of the element is presented in Figure D.1c), and the corresponding standard shape functions N_0 , N_2 and N_1 are presented in Figure D.1b). Let the demonstrated element be a quarter-point type; the distance

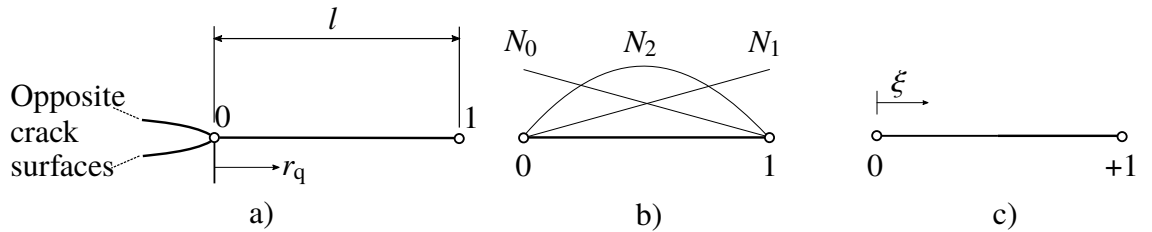


Figure D.1: 1D 2-nd order quarter-point element with standard shape functions: a) global configuration, b) base shape functions, c) natural coordinates.

between node 0 with nodes 2 and 1 is given by radial coordinate r_q (see Figure D.1a)). The position of the middle node 2 is controlled by the parameter κ . In this section, the concept of 2-nd order quarter-point element formulation with standard shape function is extended to the case of hierarchical shape functions. A more detailed description for higher dimensions can be found in, for example, (Nejati et al., 2015). For elements adjacent to the crack tip in the material configuration, the approximated material displacement field \mathbf{W} , using hierarchical shape functions (up to 2nd order), is expressed as:

$$\mathbf{W}(\xi) = \sum_{a=0}^2 N_a(\xi) \mathbf{W}^{(a)} = (1 - \xi) \mathbf{W}^{(0)} + \xi \mathbf{W}^{(1)} + \kappa(1 - \xi) \xi \mathbf{W}^{(2)} \quad (\text{D.1})$$

where the natural coordinate $0 \leq \xi \leq 1$ and $N_2 = \kappa N_0 N_1 = \kappa \xi(1 - \xi)$. The introduction of the parameter κ leads to a nonlinear mapping between the natural and physical coordinates and results in the desired singular stress and strain field at the crack tip. In standard isoparametric formulation, the element geometry can also be interpolated using the same approximation functions. Thus, the physical distance from the crack tip is expressed as:

$$r_q(\xi) = \sum_{a=0}^2 N_a(\xi) r_q^{(a)} = \xi l + \kappa \xi(1 - \xi) l \quad (\text{D.2})$$

where $r_q(\xi = 0) = 0$ at the crack tip and $r_q(\xi = 1) = l$. Setting $\kappa = -1$ results in the following relationship:

$$r_q = \xi l - \xi(1 - \xi) l = \xi l \quad \Rightarrow \quad \xi = \sqrt{\frac{r_q}{l}}, \quad (\text{D.3})$$

This yields the following radial dependence for displacements and strains:

$$\begin{aligned} \mathbf{W}(r_q) &= \mathbf{W}^{(0)} + \left(-\mathbf{W}^{(0)} + \mathbf{W}^{(1)} - \mathbf{W}^{(2)} \right) \sqrt{\frac{r_q}{l}} - \mathbf{W}^{(2)} \frac{r_q}{l} \\ \boldsymbol{\varepsilon}(r_q) &= \frac{\partial \mathbf{W}}{\partial r_q} = \left(\mathbf{W}^{(0)} + \mathbf{W}^{(1)} - \mathbf{W}^{(2)} \right) \frac{1}{2} \sqrt{\frac{l}{r_q}} + \mathbf{W}^{(2)} \frac{1}{l} \end{aligned} \quad (\text{D.4})$$

Expressions in Eq. D.4 have the necessary terms to reproduce rigid body motion and pass the patch tests, as well as the desired singularity at the crack tip due to the existence of the term $1/\sqrt{r_q}$. This will enable the elements adjacent to the crack front to reproduce the strain singularity resulting in an accurate finite element solution.

Bibliography

- N. Aage and B. S. Lazarov. Parallel framework for topology optimization using the method of moving asymptotes. *Structural and Multidisciplinary Optimization*, 47(4):493–505, 2013.
- J. E. Adams. Quantitative computed tomography. *European Journal of Radiology*, 71(3):415–424, 2009.
- J. Ahrens, B. Geveci, and C. Law. Paraview: An end-user tool for large data visualization. *The visualization Handbook*, 717, 2005.
- M. Ainsworth. Essential boundary conditions and multi-point constraints in finite element analysis. *Computer Methods in Applied Mechanics and Engineering*, 190(48):6323–6339, 2001.
- M. Ainsworth and J. Coyle. Hierarchic finite element bases on unstructured tetrahedral meshes. *International Journal for Numerical Methods in Engineering*, 58(14):2103–2130, 2003.
- D. Ambrosi, G. Ateshian, E. Arruda, S. Cowin, J. Dumais, A. Goriely, G. A. Holzapfel, J. D. Humphrey, R. Kemkemer, E. Kuhl, and others. Perspectives on biological growth and remodeling. *Journal of the Mechanics and Physics of Solids*, 59(4):863–883, 2011.
- P. R. Amestoy, I. S. Duff, J. Koster, and J.-Y. L'Excellent. A Fully Asynchronous Multifrontal Solver Using Distributed Dynamic Scheduling. *SIAM Journal on Matrix Analysis and Applications*, 23(1):15–41, 2001.
- H. Amor, J.-J. Marigo, and C. Maurini. Regularized formulation of the variational brittle fracture with unilateral contact: Numerical experiments. *Journal of the Mechanics and Physics of Solids*, 57(8):1209 – 1229, 2009.
- I. Athanasiadis, Z. Ullah, Ł. Kaczmarczyk, and C. Pearce. *Mortar contact formulation for hierarchical basis functions*. June 2018.
- S. Balay, S. Abhyankar, M. F. Adams, J. Brown, P. Brune, K. Buschelman, L. Dalcin, V. Eijkhout, W. D. Gropp, D. Kaushik, M. G. Knepley, D. A. May, L. C. McInnes, R. T. Mills, T. Munson, K. Rupp, P. Sanan, B. F. Smith, S. Zampini, H. Zhang, and H. Zhang. *PETSc Web page*. 2018.

- R. S. Barsoum. On the use of isoparametric finite elements in linear fracture mechanics. *International Journal for Numerical Methods in Engineering*, 10(1):25–37, 1976.
- Z. P. Bažant. Size effect on structural strength: a review. *Archive of applied Mechanics*, 69(9-10):703–725, 1999.
- Z. P. Bazant. Size effect. *International Journal of Solids and Structures*, 37:69–80, 2000.
- G. Beaupre, T. Orr, and D. Carter. An approach for time-dependent bone modeling and remodeling-application: A preliminary remodeling simulation. *Journal of Orthopaedic Research*, 8(5):662–670, 1990.
- T. Belytschko and T. Black. Elastic crack growth in finite elements with minimal remeshing. *International Journal for Numerical Methods in Engineering*, 45(5):601–620, 1999.
- T. Belytschko and M. Tabbara. Dynamic fracture using element-free Galerkin methods. *International Journal for Numerical Methods in Engineering*, 39(6):923–938, 1996.
- T. Belytschko, Y. Krongauz, D. Organ, M. Fleming, and P. Krysl. Meshless methods: an overview and recent developments. *Computer Methods in Applied Mechanics and Engineering*, 139(1-4):3–47, 1996.
- M. P. Bendsøe. Optimal shape design as a material distribution problem. *Structural optimization*, 1(4):193–202, Dec. 1989.
- M. P. Bendsøe and O. Sigmund. Theory, methods and applications. *Topology optimization*. Springer, Berlin, 2003.
- A. Bettamer, R. Hambli, S. Allaoui, and A. Almhdi-Imjabber. Using visual image measurements to validate a novel finite element model of crack propagation and fracture patterns of proximal femur. *Computer Methods in Biomechanics and Biomedical Engineering: Imaging & Visualization*, 5(4):251–262, 2017.
- S. H. Bogers, C. W. Rogers, C. Bolwell, W. Roe, E. Gee, and C. W. McIlwraith. Quantitative comparison of bone mineral density characteristics of the distal epiphysis of third metacarpal bones from Thoroughbred racehorses with or without condylar fracture. *American Journal of Veterinary Research*, 77(1):32–38, 2016.
- J. Bolander and S. Saito. Fracture analyses using spring networks with random geometry. *Engineering Fracture Mechanics*, 61(5-6):569–591, 1998.
- M. J. Borden. *Isogeometric analysis of phase-field models for dynamic brittle and ductile fracture*. Thesis, Aug. 2012.
- D. Borst, S. May, and J. Vignollet. A numerical assessment of phase field models for brittle and cohesive fracture : G -Convergence and stress oscillations. 52:72–84, 2015.

- B. Bourdin. Filters in topology optimization. *International Journal for Numerical Methods in Engineering*, 50(9):2143–2158, 2001.
- B. Bourdin. The variational formulation of brittle fracture: numerical implementation and extensions. In A. Combescure, R. De Borst, and T. Belytschko, editors, *IUTAM Symposium on Discretization Methods for Evolving Discontinuities*, IUTAM Bookseries, pages 381–393. Springer Netherlands, 2007.
- B. Bourdin, G. A. Francfort, and J.-J. Marigo. The Variational Approach to Fracture. *Journal of Elasticity*, 91(1):5–148, 2008.
- P. Brama, D. Karssenberg, A. Barneveld, and P. Van Weeren. Contact areas and pressure distribution on the proximal articular surface of the proximal phalanx under sagittal plane loading. *Equine Veterinary Journal*, 33(1):26–32, 2001.
- A. M. Bruaset and A. Tveito, editors. *Numerical solution of partial differential equations on parallel computers*. Number 51 in Lecture notes in computational science and engineering. Springer, Berlin, 2006.
- K.-D. Budras, W. O. Sack, and S. Rock. *Anatomy of the Horse: An Illustrated Text*. Schlütersche, 2003.
- G. Campoli, H. Weinans, and A. A. Zadpoor. Computational load estimation of the femur. *Journal of the Mechanical Behavior of Biomedical Materials*, 10:108–119, June 2012.
- G. Campoli, B. Bolsterlee, F. van der Helm, H. Weinans, and A. A. Zadpoor. Effects of densitometry, material mapping and load estimation uncertainties on the accuracy of patient-specific finite-element models of the scapula. *Journal of The Royal Society Interface*, 11(93):20131146, 2014.
- C. E. Cann and H. K. Genant. Precise measurement of vertebral mineral content using computed tomography. *Journal of Computer Assisted Tomography*, 4(4):493–500, 1980.
- D. Carter, M. Van der Meulen, and G. Beaupre. Mechanical factors in bone growth and development. *Bone*, 18(1):S5–S10, 1996.
- W. Chang-chun, H. Peixiang, and L. Ziran. Extension of j integral to dynamic fracture of functional graded material and numerical analysis. *Computers & Structures*, 80(5):411–416, 2002. doi: 10.1016/S0045-7949(02)00013-5.
- G. Chen, B. Schmutz, D. Epari, K. Rathnayaka, S. Ibrahim, M. Schuetz, and M. Pearcy. A new approach for assigning bone material properties from CT images into finite element models. *Journal of Biomechanics*, 43(5):1011–1015, 2010.
- P. Christen, K. Ito, R. Ellouz, S. Boutroy, E. Sornay-Rendu, R. D. Chapurlat, and B. Van Rietbergen. Bone remodelling in humans is load-driven but not lazy. *Nature communications*, 5:4855, 2014.

- J. D. Clayton and J. Knap. A geometrically nonlinear phase field theory of brittle fracture. *International Journal of Fracture*, 189(2):139–148, 2014.
- S. Cowin and D. Hegedus. Bone remodeling I: theory of adaptive elasticity. *Journal of Elasticity*, 6(3):313–326, 1976.
- C. Crijs, A. Martens, H.-J. Bergman, H. van der Veen, L. Duchateau, H. van Bree, and I. Gielen. Intramodality and intermodality agreement in radiography and computed tomography of equine distal limb fractures. *Equine Veterinary Journal*, 46(1):92–96, 2014.
- M. A. Crisfield. Accelerated solution techniques and concrete cracking. *Computer Methods in Applied Mechanics and Engineering*, 33(1):585–607, Sept. 1982.
- H. Davies and J. Merritt. Surface strains around the midshaft of the third metacarpal bone during turning. *Equine Veterinary Journal*, 36(8):689–692, 2004.
- R. de Borst and C. V. Verhoosel. Gradient damage vs phase-field approaches for fracture: Similarities and differences. *Computer Methods in Applied Mechanics and Engineering*, 312:78–94, 2016.
- R. de Borst, J. Remmers, A. Needleman, and M.-A. Abellan. Discrete vs smeared crack models for concrete fracture: Bridging the gap. *International Journal for Numerical and Analytical Methods in Geomechanics*, 28(7-8):583–607, 2004.
- S. L. Delp, F. C. Anderson, A. S. Arnold, P. Loan, A. Habib, C. T. John, E. Guendelman, and D. G. Thelen. OpenSim: Open-Source Software to Create and Analyze Dynamic Simulations of Movement. *IEEE Trans. Biomed. Engineering*, 54(11):1940–1950, 2007.
- M. Doblaré and J. Garcia. Anisotropic bone remodelling model based on a continuum damage-repair theory. *Journal of Biomechanics*, 35(1):1–17, 2002.
- M. Doblaré, J. Garcia, and M. Gómez. Modelling bone tissue fracture and healing: a review. *Engineering Fracture Mechanics*, 71(13-14):1809–1840, 2004.
- M. G. Drum, C. M. Les, R. D. Park, R. W. Norrdin, C. W. McIlwraith, and C. E. Kawcak. Correlation of quantitative computed tomographic subchondral bone density and ash density in horses. *Bone*, 44(2):316–319, 2009.
- K. L. Easton. *Effect of bone geometry on stress distribution patterns in the equine Metacarpophalangeal joint*. Thesis, Colorado State University, 2012.
- K. L. Easton and C. E. Kawcak. Evaluation of increased subchondral bone density in areas of contact in the metacarpophalangeal joint during loading in horses. *American Journal of Veterinary Research*, 68(8):816–821, 2007.
- S. Eberle, M. Göttlinger, and P. Augat. An Investigation to Determine if a Single Validated Density-Elasticity Relationship Can Be Used for Subject Specific Finite Element Analyses of Human Long Bones. *Med Eng Phys*, 35(7):875–83, 2013.

- R. Eberlein, G. A. Holzapfel, and C. A. J. Schulze-Bauer. An Anisotropic Model for Annulus Tissue and Enhanced Finite Element Analyses of Intact Lumbar Disc Bodies. *Computer Methods in Biomechanics and Biomedical Engineering*, 4(3):209–229, Jan. 2001.
- D. Eberly. A Robust Eigensolver for 3x3 Symmetric Matrices. page 22, Dec. 2014.
- A. Egger, U. Pillai, K. Agathos, E. Kakouris, E. Chatzi, I. A. Aschroft, and S. P. Triantafyllou. Discrete and Phase Field Methods for Linear Elastic Fracture Mechanics: A Comparative Study and State-of-the-Art Review. *Applied Sciences*, 9(12):2436, Jan. 2019.
- J. W. Eischen. Fracture of nonhomogeneous materials. *International Journal of Fracture*, 34(1):3–22, 1987. doi: 10.1007/BF00042121.
- J. Eshelby. The elastic energy-momentum tensor. *Journal of elasticity*, 5(3-4):321–335, 1975.
- J. D. Eshelby. The force on an elastic singularity. *Phil. Trans. R. Soc. Lond. A*, 244(877):87–112, 1951.
- Z. Fan, J. G. Swadener, J. Y. Rho, M. E. Roy, and G. M. Pharr. Anisotropic properties of human tibial cortical bone as measured by nanoindentation. *Journal of Orthopaedic Research*, 20(4):806–810, 2002.
- E. M. Feerick, X. C. Liu, and P. McGarry. Anisotropic mode-dependent damage of cortical bone using the extended finite element method (XFEM). *Journal of the Mechanical Behavior of Biomedical Materials*, 20:77–89, 2013.
- E. C. Firth, M. Doube, and A. Boyde. Changes in mineralised tissue at the site of origin of condylar fracture are present before athletic training in Thoroughbred horses. 0169(April), 2016.
- F. D. Fischer, J. Predan, R. Müller, and O. Kolednik. On problems with the determination of the fracture resistance for materials with spatial variations of the young's modulus. *International Journal of Fracture*, 190(1):23–38, 2014.
- G. A. Francfort and J. J. Marigo. Revisiting brittle fracture as an energy minimization problem. *Journal of the Mechanics and Physics of Solids*, 46(8):1319–1342, Aug. 1998.
- H. M. Frost. Bone "mass" and the "mechanostat": a proposal. *The Anatomical record*, 219(1):1–9, 1987.
- T. C. Gasser and G. A. Holzapfel. A numerical framework to model 3-D fracture in bone tissue with application to failure of the proximal femur. In *IUTAM Symposium on Discretization Methods for Evolving Discontinuities*, pages 199–211. Springer, 2007.
- D. M. Geraldes, L. Modenese, and A. T. M. Phillips. Consideration of multiple load cases is critical in modelling orthotropic bone adaptation in the femur. *Biomechanics and Modeling in Mechanobiology*, 15(5):1029–1042, Oct. 2016.

- T. Gerasimov and L. De Lorenzis. A line search assisted monolithic approach for phase-field computing of brittle fracture. *Computer Methods in Applied Mechanics and Engineering*, 312:276–303, 2016.
- L. J. Gibson. Biomechanics of cellular solids. *Journal of Biomechanics*, 38(3):377–399, 2005.
- I. M. Gitman, H. Askes, E. Kuhl, and E. C. Aifantis. Stress concentrations in fractured compact bone simulated with a special class of anisotropic gradient elasticity. *International Journal of Solids and Structures*, 47(9):1099–1107, 2010.
- P. Grassl and M. Jirásek. Meso-scale approach to modelling the fracture process zone of concrete subjected to uniaxial tension. *International Journal of Solids and Structures*, 47(7-8):957–968, 2010.
- A. A. Griffith. The Phenomena of Rupture and Flow in Solids. *Philosophical Transactions of the Royal Society of London A: Mathematical, Physical and Engineering Sciences*, 221(582-593):163–198, 1921.
- A. Grigoryan. Measure theory and probability. *Lecture Notes, October*, page 122, 2008.
- E. Guerses and C. Miehe. A computational framework of three-dimensional configurational-force-driven brittle crack propagation. *Computer Methods in Applied Mechanics and Engineering*, 198(15-16):1413–1428, 2009.
- H. Gupta and P. Zioupos. Fracture of bone tissue: the 'hows' and the 'whys'. *Medical Engineering & Physics*, 30(10):1209–1226, 2008.
- M. E. Gurtin. *Configurational Forces as Basic Concepts of Continuum Physics*. Springer Science & Business Media, 1999.
- M. A. Gutiérrez. Energy release control for numerical simulations of failure in quasi-brittle solids. *Communications in Numerical Methods in Engineering*, 20(1):19–29, 2004.
- P. Hajela and E. Lee. Genetic algorithms in truss topological optimization. *International Journal of Solids and Structures*, 32(22):3341–3357, Nov. 1995.
- R. Hambli. Micro-ct finite element model and experimental validation of trabecular bone damage and fracture. *Bone*, 56(2):363 – 374, 2013a.
- R. Hambli. A quasi-brittle continuum damage finite element model of the human proximal femur based on element deletion. *Medical & Biological Engineering & Computing*, 51(1-2):219–231, Feb. 2013b.
- R. Hambli, A. Bettamer, and S. Allaoui. Finite element prediction of proximal femur fracture pattern based on orthotropic behaviour law coupled to quasi-brittle damage. *Medical Engineering & Physics*, 34(2):202 – 210, 2012.

- R. Hambli, E. Lespessailles, and C.-L. Benhamou. Integrated remodeling-to-fracture finite element model of human proximal femur behavior. *Journal of the Mechanical Behavior of Biomedical Materials*, 17:89–106, Jan. 2013.
- T. P. Harrigan and J. J. Hamilton. Finite element simulation of adaptive bone remodelling: A stability criterion and a time stepping method. *International Journal for Numerical Methods in Engineering*, 36(5):837–854, 1993.
- T. P. Harrigan, J. J. Hamilton, J. D. Reuben, A. Toni, and M. Viceconti. Bone remodelling adjacent to intramedullary stems: an optimal structures approach. *Biomaterials*, 17(2): 223–232, 1996.
- N. M. Harrison, P. McDonnell, L. Mullins, N. Wilson, D. O’Mahoney, and P. E. McHugh. Failure modelling of trabecular bone using a non-linear combined damage and fracture voxel finite element approach. *Biomechanics and Modeling in Mechanobiology*, 12(2): 225–241, 2013.
- S. M. Harrison, R. C. Whitton, C. E. Kawcak, S. M. Stover, and M. G. Pandy. Relationship between muscle forces, joint loading and utilization of elastic strain energy in equine locomotion. *The Journal of experimental Biology*, 213:3998–4009, 2010.
- S. M. Harrison, R. C. Whitton, C. E. Kawcak, S. M. Stover, and M. G. Pandy. Evaluation of a subject-specific finite-element model of the equine metacarpophalangeal joint under physiological load. *Journal of Biomechanics*, 47(1):65–73, Jan. 2014.
- S. J. Hazelwood, R. Bruce Martin, M. M. Rashid, and J. J. Rodrigo. A mechanistic model for internal bone remodeling exhibits different dynamic responses in disuse and overload. *Journal of Biomechanics*, 34(3):299–308, 2001.
- B. Helgason, E. Perilli, E. Schileo, F. Taddei, S. Brynjolfsson, and M. Viceconti. Mathematical relationships between bone density and mechanical properties: a literature review. *Clinical biomechanics*, 23(2):135–146, 2008a.
- B. Helgason, F. Taddei, H. Palsson, E. Schileo, L. Cristofolini, M. Viceconti, and S. Brynjolfsson. A modified method for assigning material properties to FE models of bones. *Medical Engineering & Physics*, 30(4):444–453, 2008b.
- R. Henshell and K. Shaw. Crack tip finite elements are unnecessary. *International Journal for Numerical Methods in Engineering*, 9(3):495–507, 1975.
- Hirshikesh, S. Natarajan, R. K. Annabattula, and E. Martínez-Pañeda. Phase field modelling of crack propagation in functionally graded materials. *Composites Part B: Engineering*, 169:239–248, July 2019.
- S. Hosseini, J. J. C. Remmers, C. V. Verhoosel, and R. d. Borst. An isogeometric continuum shell element for non-linear analysis. *Computer Methods in Applied Mechanics and Engineering*, 271:1 – 22, 2014.

- H. Hovagimian, C. Molica, and K. Billiar. Osteoporotic equine bone modeling: 3-point bending of deer metacarpal bone. *2011 IEEE 37th Annual Northeast Bioengineering Conference NEBEC*, (1):1–2, 2011.
- J. M. Hughes, K. L. Popp, R. Yanovich, M. L. Boussein, and R. W. Matheny Jr. The role of adaptive bone formation in the etiology of stress fracture. *Experimental Biology and Medicine*, 242(9):897–906, 2017.
- R. Huiskes, R. Ruimerman, G. H. van Lenthe, and J. D. Janssen. Effects of mechanical forces on maintenance and adaptation of form in trabecular bone. *Nature*, 405(6787):704–706, 2000.
- G. Irwin. Fracture strength relative to onset and arrest of crack propagation. In *Proc ASTM*, volume 58, pages 640–657, 1958.
- B. Jacklin and I. Wright. Frequency distributions of 174 fractures of the distal condyles of the third metacarpal and metatarsal bones in 167 Thoroughbred racehorses (1999–2009). *Equine Veterinary Journal*, 44(6):707–713, 2012.
- C. R. Jacobs, M. E. Levenston, G. S. Beaupré, J. C. Simo, and D. R. Carter. Numerical instabilities in bone remodeling simulations: the advantages of a node-based finite element approach. *Journal of Biomechanics*, 28(4):453–459, 1995.
- L. Kaczmarczyk and C. J. Pearce. Efficient numerical analysis of bone remodelling. *Journal of the Mechanical Behavior of Biomedical Materials*, 4(6):858 – 867, 2011.
- Ł. Kaczmarczyk, M. M. Nezhad, and C. Pearce. Three-dimensional brittle fracture: configurational-force-driven crack propagation. *International Journal for Numerical Methods in Engineering*, 97(7):531–550, 2014.
- Ł. Kaczmarczyk, Z. Ullah, and C. J. Pearce. Energy consistent framework for continuously evolving 3d crack propagation. *Computer Methods in Applied Mechanics and Engineering*, 324:54–73, Sept. 2017.
- Ł. Kaczmarczyk, Z. Ullah, K. Lewandowski, X. Meng, X.-Y. Zhou, I. Athanasiadis, H. Nguyen, C.-A. Chalons-Mouriesse, E. Richardson, E. Miur, A. Shvarts, M. Wakeni, and C. Pearce. MoFEM: an open source, parallel finite element library. *The Journal of Open Source Software*, 2020. <http://mofem.eng.gla.ac.uk>.
- J. H. Keyak, T. S. Kaneko, J. Tehranzadeh, and H. B. Skinner. Predicting proximal femoral strength using structural engineering models. *Clinical Orthopaedics and Related Research®*, 437:219–228, 2005.
- R. Kienzler and G. Herrmann. *Mechanics in Material Space: with Applications to Defect and Fracture Mechanics*. Springer Science & Business Media, Dec. 2012.

- R. Kienzler and G. A. Maugin. *Configurational mechanics of materials*, volume 427. Springer, 2014.
- J.-H. Kim and G. H. Paulino. Finite element evaluation of mixed mode stress intensity factors in functionally graded materials. *International Journal for Numerical Methods in Engineering*, 53(8):1903–1935, Mar. 2002.
- N. K. Knowles, J. M. Reeves, and L. M. Ferreira. Quantitative computed tomography (QCT) derived bone mineral density (BMD) in finite element studies: a review of the literature. *Journal of Experimental Orthopaedics*, 3, 2016.
- J. Kronick, M. Barba, and W. Paprosky. Extensively coated femoral components in young patients. *Clinical Orthopaedics and related research*, (344):263–274, 1997.
- E. Kuhl. *Theory and Numerics of Open System Continuum Thermodynamics: Spatial and Material Settings*. UKL LTM / T. Techn. Univ., 2004.
- E. Kuhl and F. Balle. Computational modeling of hip replacement surgery: Total hip replacement vs. hip resurfacing. *Technische Mechanik*, 25(2):1–8, 2005.
- E. Kuhl and P. Steinmann. Theory and numerics of geometrically non-linear open system mechanics. *International Journal for Numerical Methods in Engineering*, 58(11):1593–1615, 2003.
- E. Kuhl, A. Menzel, and P. Steinmann. Computational modeling of growth. A critical review, a classification of concepts and two new consistent approaches. *Computational Mechanics*, 32(1-2):71–88, 2003.
- C. Kuhn and R. Müller. A continuum phase field model for fracture. *Engineering Fracture Mechanics*, 77(18):3625–3634, Dec. 2010.
- C. Kuhn and R. Müller. A discussion of fracture mechanisms in heterogeneous materials by means of configurational forces in a phase field fracture model. *Computer Methods in Applied Mechanics and Engineering*, 312:95–116, 2016.
- C. Kuhn, A. Schlüter, and R. Müller. On degradation functions in phase field fracture models. *Computational Materials Science*, 108:374–384, Oct. 2015.
- M. Kuna. Basics of Fracture Mechanics. In M. Kuna, editor, *Finite Elements in Fracture Mechanics: Theory - Numerics - Applications*, Solid Mechanics and Its Applications, pages 21–151. Springer Netherlands, Dordrecht, 2013.
- P. Lancaster and K. Salkauskas. Surfaces generated by moving least squares methods. *Mathematics of computation*, 37(155):141–158, 1981.
- B. S. Lazarov and O. Sigmund. Filters in topology optimization based on Helmholtz-type differential equations. *International Journal for Numerical Methods in Engineering*, 86(6):765–781, 2011.

- P. D. Leahy, B. S. Smith, K. L. Easton, C. E. Kawcak, J. C. Eickhoff, S. S. Shetye, and C. M. Puttlitz. Correlation of mechanical properties within the equine third metacarpal with trabecular bending and multi-density micro-computed tomography data. *Bone*, 46(4): 1108–1113, 2010.
- S. Lee, M. F. Wheeler, and T. Wick. Pressure and fluid-driven fracture propagation in porous media using an adaptive finite element phase field model. *Computer Methods in Applied Mechanics and Engineering*, 305:111–132, 2016.
- C. M. Les, J. H. Keyak, S. M. Stover, K. T. Taylor, and A. J. Kaneps. Estimation of material properties in the equine metacarpus with use of quantitative computed tomography. *Journal of Orthopaedic Research*, 12(6):822–833, 1994.
- K. Lewandowski. Supplement data for Numerical investigation into fracture risk of bone following adaptation. Dec. 2019.
- K. Lewandowski. MoFEM-TopologyOptimization-Module-v0.1.0. Feb 2020.
- H. Liedtke, A. McBride, S. Sivarasu, and S. Roche. Computational simulation of bone remodelling post reverse total shoulder arthroplasty. *arXiv preprint arXiv:1705.08324*, 2017.
- G. Liu, Q. Li, M. A. Msekh, and Z. Zuo. Abaqus implementation of monolithic and staggered schemes for quasi-static and dynamic fracture phase-field model. *Computational Materials Science*, 121:35–47, Aug. 2016.
- J. Londono, L. Berger-Vergiat, and H. Waisman. An equivalent stress-gradient regularization model for coupled damage-viscoelasticity. *Computer Methods in Applied Mechanics and Engineering*, 322:137 – 166, 2017.
- E. Lorentz and P. Badel. A new path-following constraint for strain-softening finite element simulations. *International Journal for Numerical Methods in Engineering*, 60(2):499–526, 2004.
- A. Loughridge, A. Hess, T. Parkin, and C. Kawcak. Qualitative assessment of bone density at the distal articulating surface of the third metacarpal in Thoroughbred racehorses with and without condylar fracture. *Equine Veterinary Journal*, 49(2):172–177, 2017.
- E. Martínez-Pañeda, A. Golahmar, and C. F. Niordson. A phase field formulation for hydrogen assisted cracking. *Computer Methods in Applied Mechanics and Engineering*, 342:742–761, Dec. 2018.
- G. A. Maugin. *Configurational forces: thermomechanics, physics, mathematics, and numerics*. Chapman and Hall/CRC, 2016.
- S. May. *Splines for damage and fracture in solids*. Thesis, University of Glasgow, Aug. 2016.

- S. May, J. Vignollet, and R. de Borst. A new arc-length control method based on the rates of the internal and the dissipated energy. *Engineering Computations*, 33(1):100–115, Mar. 2016.
- N. Mc Turlough. Condylar fractures in horses – a review. *Veterinary Ireland Journal*, 4(4): 205–211, 2014.
- C. McIlwraith. Use of synovial fluid and serum biomarkers in equine bone and joint disease: a review. *Equine Veterinary Journal*, 37(5):473–482, 2005.
- A. Menzel and E. Kuhl. Frontiers in growth and remodeling. *Mechanics Research Communications*, 42:1–14, 2012.
- J. S. Merritt, C. R. Burvill, M. G. Pandy, and H. M. S. Davies. Determination of mechanical loading components of the equine metacarpus from measurements of strain during walking. *Equine Veterinary Journal*, 38(SUPPL.36):440–444, 2006.
- J. S. Merritt, M. G. Pandy, N. A. T. Brown, C. R. Burvill, C. E. Kawcak, C. W. McIlwraith, and H. M. S. Davies. Mechanical loading of the distal end of the third metacarpal bone in horses during walking and trotting. *American Journal of Veterinary Research*, 71(5): 508–514, 2010.
- C. Miehe. Computation of isotropic tensor functions. *Communications in Numerical Methods in Engineering*, 9(11):889–896, 1993.
- C. Miehe. Comparison of two algorithms for the computation of fourth-order isotropic tensor functions. *Computers and Structures*, 66(1):37–43, 1998.
- C. Miehe and E. Gürses. A robust algorithm for configurational-force-driven brittle crack propagation with r-adaptive mesh alignment. *International Journal for Numerical Methods in Engineering*, 72(2):127–155, 2007.
- C. Miehe, M. Hofacker, and F. Welschinger. A phase field model for rate-independent crack propagation: Robust algorithmic implementation based on operator splits. *Computer Methods in Applied Mechanics and Engineering*, 199(45-48):2765–2778, 2010a.
- C. Miehe, F. Welschinger, and M. Hofacker. Thermodynamically consistent phase-field models of fracture: Variational principles and multi-field FE implementations. *International Journal for Numerical Methods in Engineering*, 83(10):1273–1311, 2010b.
- C. Miehe, F. Aldakheel, and A. Raina. Phase field modeling of ductile fracture at finite strains: A variational gradient-extended plasticity-damage theory. *International Journal of Plasticity*, 84:1–32, Sept. 2016.
- D. S. Milo. *Good Enough: The Tolerance for Mediocrity in Nature and Society*. Harvard University Press, June 2019.

- D. Mumford and J. Shah. Optimal approximations by piecewise smooth functions and associated variational problems. *Communications on Pure and Applied Mathematics*, 42 (5):577–685, 1989.
- M. Nejati, A. Paluszny, and R. W. Zimmerman. On the use of quarter-point tetrahedral finite elements in linear elastic fracture mechanics. *Engineering Fracture Mechanics*, 144: 194–221, 2015.
- D. Ngo and A. Scordelis. Finite element analysis of reinforced concrete beams. In *Journal Proceedings*, volume 64, pages 152–163, 1967.
- L. Nguyen, S. Stoter, T. Baum, J. Kirschke, M. Ruess, Z. Yosibash, and D. Schillinger. Phase-field boundary conditions for the voxel finite cell method: Surface-free stress analysis of CT-based bone structures. *International Journal for Numerical Methods in Biomedical Engineering*, 33(12):e2880, 2017.
- T. T. Nguyen, J. Yvonnet, Q. Z. Zhu, M. Bornert, and C. Chateau. A phase field method to simulate crack nucleation and propagation in strongly heterogeneous materials from direct imaging of their microstructure. *Engineering Fracture Mechanics*, 139:18–39, 2015.
- E. Noether. Invariant variation problems. *Transport Theory and Statistical Physics*, 1(3): 186–207, 1971.
- D. M. Nunamaker and A. J. Ruggles. The Bucked-Shin Complex. *Diagnosis and Management of Lameness in the Horse: Second Edition*, pages 953–960, 2010.
- J. O’Connor, L. A. Borges, F. P. Duda, and A. G. da Cruz. Bone density growth and the biomechanics of healthy and prosthetic femur. *Journal of the Brazilian Society of Mechanical Sciences and Engineering*, 39(10):3743–3756, 2017.
- I. Ozdemir. An alternative implementation of the incremental energy/dissipation based arc-length control method. *Theoretical and Applied Fracture Mechanics*, 100:208–214, Apr. 2019.
- K. Ozenc, G. Chinaryan, and M. Kaliske. A configurational force approach to model the branching phenomenon in dynamic brittle fracture. *Engineering Fracture Mechanics*, 157: 26–42, 2016.
- D. H. Pahr and P. K. Zysset. Influence of boundary conditions on computed apparent elastic properties of cancellous bone. *Biomechanics and Modeling in Mechanobiology*, 7(6): 463–76, 2008.
- A. Pakdel, J. Fialkov, and C. M. Whyne. High resolution bone material property assignment yields robust subject specific finite element models of complex thin bone structures. *Journal of Biomechanics*, 49(9):1454–1460, 2016.

- H. Pang, A. P. Shiwalkar, C. M. Madormo, R. E. Taylor, T. P. Andriacchi, and E. Kuhl. Computational modeling of bone density profiles in response to gait: a subject-specific approach. *Biomechanics and modeling in mechanobiology*, 11(3-4):379–390, 2012.
- T. Parkin, P. Clegg, N. French, C. Proudman, C. Riggs, E. Singer, P. Webbon, and K. Morgan. Analysis of horse race videos to identify intra-race risk factors for fatal distal limb fracture. *Preventive Veterinary Medicine*, 74(1):44–55, 2006.
- T. D. H. Parkin, P. D. Clegg, N. P. French, C. J. Proudman, C. M. Riggs, E. R. Singer, P. M. Webbon, and K. L. Morgan. Horse-level risk factors for fatal distal limb fracture in racing Thoroughbreds in the UK. *Equine Veterinary Journal*, 36(6):513–519, 2004.
- T. D. H. Parkin, P. D. Clegg, N. P. French, C. J. Proudman, C. M. Riggs, E. R. Singer, P. M. Webbon, and K. L. Morgan. Risk factors for fatal lateral condylar fracture of the third metacarpus/metatarsus in UK racing. *Equine Veterinary Journal*, 37(3):192–199, 2005.
- C. Pearce. Crack propagation in nuclear graphite. 2019.
- E. Peleg, R. Herblum, M. Beek, L. Joskowicz, M. Liebergall, R. Mosheiff, and C. Whyne. Can a partial volume edge effect reduction algorithm improve the repeatability of subject-specific finite element models of femurs obtained from CT data? *Computer methods in biomechanics and biomedical engineering*, 17(3):204–209, 2014.
- K. Pham, H. Amor, J.-J. Marigo, and C. Maurini. Gradient Damage Models and Their Use to Approximate Brittle Fracture. *International Journal of Damage Mechanics*, 20(4):618–652, May 2011.
- L. Podshivalov, A. Fischer, and P. Z. Bar-Yoseph. *On the Road to Personalized Medicine: Multiscale Computational Modeling of Bone Tissue*, volume 21. 2014.
- S. Poelert, E. Valstar, H. Weinans, and A. A. Zadpoor. Patient-specific finite element modeling of bones. *Proceedings of the Institution of Mechanical Engineers, Part H: Journal of Engineering in Medicine*, 227(4):464–478, 2013.
- J. Y. Rho. An ultrasonic method for measuring the elastic properties of human tibial cortical and cancellous bone. *Ultrasonics*, 34(8):777–783, 1996.
- J. R. Rice. A path independent integral and the approximate analysis of strain concentration by notches and cracks. *Journal of applied mechanics*, 35(2):379–386, 1968.
- C. Riggs, G. Whitehouse, and A. Boyde. Structural variation of the distal condyles of the third metacarpal and third metatarsal bones in the horse. *Equine Veterinary Journal*, 31(2): 130–139, Mar. 1999.
- C. M. Riggs and a. Boyde. Effect of exercise on bone density in distal regions of the equine third metacarpal bone in 2-year-old thoroughbreds. *Equine Veterinary Journal. Supplement*, 30:555–60, 1999.

- C. M. M. Riggs and A. Boyde. Effect of exercise on bone density in distal regions of the equine third metacarpal bone in 2-year-old thoroughbreds. *Equine Veterinary Journal.*, 30 (555-60), July 1991.
- E. Riks. An incremental approach to the solution of snapping and buckling problems. *International Journal of Solids and Structures*, 15(7):529–551, Jan. 1979.
- R. O. Ritchie, J. H. Kinney, J. J. Kruzic, and R. K. Nalla. A fracture mechanics and mechanistic approach to the failure of cortical bone. *Fatigue & Fracture of Engineering Materials & Structures*, 28(4):345–371, 2005.
- D. P. Rooke and D. J. Cartwright. Compendium of stress intensity factors. *Procurement Executive, Ministry of Defence. H. M. S. O. 1976*, 1976.
- E. Schileo, F. Taddei, L. Cristofolini, and M. Viceconti. Subject-specific finite element models implementing a maximum principal strain criterion are able to estimate failure risk and fracture location on human femurs tested in vitro. *Journal of Biomechanics*, 41(2):356–367, 2008.
- R. Scholz, F. Hoffmann, S. von Sachsen, W. G. Drossel, C. Klöhn, and C. Voigt. Validation of density-elasticity relationships for finite element modeling of human pelvic bone by modal analysis. *Journal of Biomechanics*, 46(15):2667–2673, 2013.
- J. J. Setterbo, T. C. Garcia, I. P. Campbell, J. L. Reese, J. M. Morgan, S. Y. Kim, M. Hubbard, and S. M. Stover. Hoof accelerations and ground reaction forces of Thoroughbred racehorses measured on dirt, synthetic, and turf track surfaces. *American Journal of Veterinary Research*, 70(10):1220–1229, 2009.
- A. Sharir, M. M. Barak, and R. Shahar. Whole bone mechanics and mechanical testing. *Veterinary Journal*, 177(1):8–17, 2008.
- G. B. Sharma and D. D. Robertson. Adaptive scapula bone remodeling computational simulation: Relevance to regenerative medicine. *Journal of Computational Physics*, 244: 312–320, July 2013.
- R. Shen, H. Waisman, Z. Yosibash, and G. Dahan. A novel phase field method for modeling the fracture of long bones. *International Journal for Numerical Methods in Biomedical Engineering*, 35(8):e3211, 2019.
- C. Shih, B. Moran, and T. Nakamura. Energy release rate along a three-dimensional crack front in a thermally stressed body. *International Journal of fracture*, 30(2):79–102, 1986.
- O. Sigmund. A 99 line topology optimization code written in matlab. *Structural and Multidisciplinary Optimization*, 21(2):120–127, 2001.
- O. Sigmund and K. Maute. Topology optimization approaches: A comparative review. *Structural and Multidisciplinary Optimization*, 48(6):1031–1055, Dec. 2013.

- W. Squire and G. Trapp. Using Complex Variables to Estimate Derivatives of Real Functions. *SIAM Review*, 40(1):110–112, Jan. 1998.
- C. Steinke, K. Ozenc, G. Chinaryan, and M. Kaliske. A comparative study of the r-adaptive material force approach and the phase-field method in dynamic fracture. *International Journal of Fracture*, 201(1):97–118, 2016.
- P. Steinmann, D. Ackermann, and F. Barth. Application of material forces to hyperelastostatic fracture mechanics. II. Computational setting. *International Journal of Solids and Structures*, 38(32-33):5509–5526, 2001.
- Z. Tabor and E. Rokita. Quantifying anisotropy of trabecular bone from gray-level images. *Bone*, 40(4):966–972, 2007.
- F. Taddei, E. Schileo, B. Helgason, L. Cristofolini, and M. Viceconti. The material mapping strategy influences the accuracy of CT-based finite element models of bones: an evaluation against experimental measurements. *Medical Engineering & Physics*, 29(9):973–979, 2007.
- T. J. Tautges, R. Meyers, K. Merkle, C. Stimpson, and C. Ernst. MOAB: a mesh-oriented database. SAND2004-1592, Sandia National Laboratories, Apr. 2004. Report.
- R. Taylor, C. Zheng, R. Jackson, J. Doll, J. Chen, K. Holzbaur, T. Besier, and E. Kuhl. The phenomenon of twisted growth: humeral torsion in dominant arms of high performance tennis players. *Computer Methods in Biomechanics and Biomedical Engineering*, 12(1):83–93, 2009.
- J. J. Thomason and M. L. Peterson. Biomechanical and Mechanical Investigations of the Hoof-Track Interface in Racing Horses. *Veterinary Clinics of North America: Equine Practice*, 24(1):53–77, 2008.
- A. Tovar, N. M. Patel, G. L. Niebur, M. Sen, and J. E. Renaud. Topology Optimization Using a Hybrid Cellular Automaton Method With Local Control Rules. *Journal of Mechanical Design*, 128(6):1205–1216, Nov. 2006.
- N. Trabelsi and Z. Yosibash. Patient-specific finite-element analyses of the proximal femur with orthotropic material properties validated by experiments. *Journal of Biomechanical Engineering*, 133(6):061001, 2011.
- N. Trabelsi, Z. Yosibash, and C. Milgrom. Validation of subject-specific automated p-FE analysis of the proximal femur. *Journal of Biomechanics*, 42(3):234–241, 2009.
- C. Tranquille, R. Murray, and T. Parkin. Can we use subchondral bone thickness on high-field magnetic resonance images to identify Thoroughbred racehorses at risk of catastrophic lateral condylar fracture? *Equine Veterinary Journal*, 49(2):167–171, 2017.
- Z. Ullah and C. Augarde. Finite deformation elasto-plastic modelling using an adaptive meshless method. *Computers & Structures*, 118:39–52, 2013.

- A. Ural and S. Mischinski. Multiscale modeling of bone fracture using cohesive finite elements. *Engineering Fracture Mechanics*, 103:141–152, 2013.
- S. van den Munckhof and A. A. Zadpoor. How accurately can we predict the fracture load of the proximal femur using finite element models? *Clinical Biomechanics*, 29(4):373–380, 2014.
- M. Viceconti, M. Davinelli, F. Taddei, and A. Cappello. Automatic generation of accurate subject-specific bone finite element models to be used in clinical studies. *Journal of Biomechanics*, 37(10):1597–1605, 2004.
- J. Vignollet, S. May, R. De Borst, and C. V. Verhoosel. Phase-field models for brittle and cohesive fracture. *Meccanica*, 49(11):2587–2601, 2014.
- T. Waffenschmidt and A. Menzel. Application of an anisotropic growth and remodelling formulation to computational structural design. *Mechanics Research Communications*, 42:77–86, 2012.
- T. Waffenschmidt, A. Menzel, and E. Kuhl. Anisotropic density growth of bone - A computational micro-sphere approach. *International Journal of Solids and Structures*, 49(14):1928–1946, 2012.
- A. Walther. Getting Started with ADOL-C. In U. Naumann, O. Schenk, H. D. Simon, and S. Toledo, editors, *Combinatorial Scientific Computing*, Dagstuhl Seminar Proceedings, Dagstuhl, Germany, 2009. Schloss Dagstuhl - Leibniz-Zentrum fuer Informatik, Germany.
- X. Wang, C. D. L. Thomas, J. G. Clement, R. Das, H. Davies, and J. W. Fernandez. A mechanostatistical approach to cortical bone remodelling: an equine model. *Biomechanics and Modeling in Mechanobiology*, 15(1):29–42, 2016.
- H. Weinans, R. Huiskes, and H. Grootenboer. The behavior of adaptive bone-remodeling simulation models. *Journal of Biomechanics*, 25(12):1425–1441, 1992.
- R. C. Whitton, G. D. Trope, A. Ghasem-Zadeh, G. A. Anderson, T. D. Parkin, E. J. Mackie, and E. Seeman. Third metacarpal condylar fatigue fractures in equine athletes occur within previously modelled subchondral bone. *Bone*, 47(4):826–831, 2010.
- T. Wick. Modified newton methods for solving fully monolithic phase-field quasi-static brittle fracture propagation. *Computer Methods in Applied Mechanics and Engineering*, 325:577–611, 2017.
- H. Wille, M. Ruess, E. Rank, and Z. Yosibash. Uncertainty quantification for personalized analyses of human proximal femurs. *Journal of Biomechanics*, 49(4):520–527, 2016.
- J. Wolff. The classic on the inner architecture of bones and its importance for bone growth. *Clinical Orthopaedics and Related Research*, 50:389–450, 1870.

- K. C. Wong, L. Wang, H. Zhang, H. Liu, and P. Shi. Meshfree implementation of individualized active cardiac dynamics. *Computerized Medical Imaging and Graphics*, 34(1):91–103, 2010.
- J.-Y. Wu. A unified phase-field theory for the mechanics of damage and quasi-brittle failure. *Journal of the Mechanics and Physics of Solids*, 103:72–99, June 2017.
- J.-Y. Wu, V. P. Nguyen, C. T. Nguyen, D. Sutula, S. Bordas, and S. Sinaie. Phase field modeling of fracture. *Advances in Applied Mechancis: Multi-scale Theory and Computation*, 52, 2018.
- K. Yamada, F. Sato, T. Higuchi, K. Nishihara, M. Kayano, N. Sasaki, and Y. Nambo. Experimental investigation of bone mineral density in Thoroughbreds using quantitative computed tomography. *Journal of Equine Science*, 26(3):81–87, 2015.
- J. Yan, A. Daga, R. Kumar, and J. J. Mecholsky. Fracture toughness and work of fracture of hydrated, dehydrated, and ashed bovine bone. *Journal of Biomechanics*, 41(9):1929 – 1936, 2008.
- Q. Yang, B. N. Cox, R. K. Nalla, and R. Ritchie. Fracture length scales in human cortical bone: the necessity of nonlinear fracture models. *Biomaterials*, 27(9):2095–2113, 2006.
- A. Yildiz, N. Oztürk, N. Kaya, and F. Oztürk. Integrated optimal topology design and shape optimization using neural networks. *Structural and Multidisciplinary Optimization*, 25(4): 251–260, Oct. 2003.
- Z. Yosibash, D. Tal, and N. Trabelsi. Predicting the yield of the proximal femur using high-order finite-element analysis with inhomogeneous orthotropic material properties. *Philosophical Transactions of the Royal Society of London A: Mathematical, Physical and Engineering Sciences*, 368(1920):2707–2723, 2010.
- A. A. Zadpoor. Open forward and inverse problems in theoretical modeling of bone tissue adaptation. *Journal of the mechanical behavior of biomedical materials*, 27:249–261, 2013.
- C. Zannoni, R. Mantovani, and M. Viceconti. Material properties assignment to finite element models of bone structures: a new method. *Medical Engineering & Physics*, 20(10):735–740, 1999.
- A. T. Zehnder. Lecture notes on fracture mechanics. *Cornell University*, 20:22, 2007.
- O. C. Zienkiewicz, R. L. Taylor, R. L. Taylor, and R. L. Taylor. *The Finite Element Method: Solid mechanics*. Butterworth-Heinemann, 2000.